Technische Universität Graz
Institut für Thermische Turbomaschinen und Maschinendynamik

# Unsteady Combustion Phenomena in Current and Future Aero Engines

Dissertation

zur Erlangung des akademischen Grades eines
Doktors der technischen Wissenschaften,
eingereicht an der Fakultät für Maschinenbau der Technischen
Universität Graz

von

Dipl.-Ing. Andreas Lang

*Erstgutachter:* Univ.-Prof. Dr.-Ing. Franz Heitmeir
*Zweitgutachter:* Univ.-Prof. Dipl.-Ing. Dr.techn. Helmut Eichlseder

Graz, September 2011

Diese Arbeit wurde von der Europäischen Kommission (EC) als Teil des Forschungsprogramms NEWAC (New Aeroengine Core Concepts; AIP5-CT-2006-030876) gefördert.

Try not. Do or do not, there is no try.

- Yoda, Jedi Grand Master -

## Statutory Declaration

*I declare that I have authored this thesis independently, that I have not used other than the declared sources / resources, and that I have explicitly marked all material which has been quoted either literally or by content from the used sources.*

| Place | Date | Signature |
|---|---|---|

## Eidesstattliche Erklärung

*Ich erkläre an Eides statt, dass ich die vorliegende Arbeit selbstständig verfasst, andere als die angegebenen Quellen/Hilfsmittel nicht benutzt, und die den benutzten Quellen wörtlich und inhaltlich entnommene Stellen als solche kenntlich gemacht habe.*

| Ort | Datum | Unterschrift |
|---|---|---|

## Danksagung

Die vorliegende Arbeit entstand während meiner Zeit als Wissenschaftlicher Mitarbeiter am Institut für Thermische Turbomaschinen und Maschinendynamik an der Technischen Universität Graz. Ich möchte mich daher besonders beim Institutsvorstand, Univ.-Prof. Dr.-Ing. Franz Heitmeir, der auch Erstgutachter dieser Arbeit ist, bedanken.

Weiters möchte ich mich bei Univ.-Doz. Dipl.-Ing. Dr. Fabrice Giuliani bedanken, der mein Interesse an der Verbrennung geweckt hat und mich während meiner Arbeit immer wieder motiviert und tatkräftig unterstützt hat.

Dank gilt auch Herrn Dipl.-Ing. Thomas Leitgeb, ohne dessen Engagement im Labor die Steuerung des Prüfstandes in dieser Art und Weise nicht möglich gewesen wäre.

Bei meinen ehemaligen Diplomanden, den Herren Dipl.-Ing. Andreas Lechner und Dipl.-Ing. Christian Faustmann möchte ich mich ebenfalls bedanken, die mich während meiner Versuche besonders engagiert unterstützt haben.

Natürlich möchte ich auch allen Kollegen des Institutes Dank aussprechen, die eine gemütliche Arbeitsatmosphäre geschaffen haben und immer Zeit für einen Kaffee hatten.

Stefanie gebührt ganz besonderer Dank, da sie mich immer angetrieben hat meine Dissertation, trotz aller Rückschläge, fortzuführen und zu einem guten Ende zu bringen.

Graz, September 2011 Andreas Lang

# Kurzfassung

Das stetige Wachstum des Luftverkehrs und die damit einhergehenden strengeren Richtlinien für Flugtriebwerke führen zu schadstoffarmen Antrieben, die immer innovativere Technologien verwenden.
Instabile bzw. unstetige Verbrennung spielt dabei in zweierlei Hinsicht eine Rolle. Einerseits wird die unstetige Verbrennung im Bereich der Pulse Detonation Engines bewusst genutzt und könnte bei Triebwerken für den Zeitraum nach 2020 eingesetzt werden.
Jetzige Triebwerke arbeiten mit stationärer Verbrennung. Der Zwang zur Schadstoffarmut führt zu Konzepten mit magerer Verbrennung, die jedoch anfällig für Verbrennungsinstabilitäten (Brennkammer-Schwingungen) sind. Dies ist, im Gegensatz zur bewusst gepulsten Verbrennung ein Effekt der zu vermeiden ist.
In dieser Arbeit wird zuerst das Potential der gepulsten Verbrennung am Konzept eines Hybrid Turbofan Triebwerks gezeigt. Dafür wurde ein Tool zur Berechnung der Leistungsdaten eines solchen Triebwerks entwickelt und für zwei Triebwerkskonzepte angewandt.
Im zweiten Teil der Arbeit wurde die instabile Verbrennung anhand eines Mager-Brennkammer-Konzepts, der Lean Premixed Prevaporized (LPP) Technologie experimentell untersucht. Eine für die Anwendung in Brennkammern neue laseroptische Messtechnik (Laser Vibrometery -LV), wurde am Institut für Thermische Turbomaschinen und Maschinendynamik (ITTM) entwickelt. Im Rahmen dieser Arbeit wurde sie bei zwei Brennkammer-Konzepten angewendet.
Als erste Brennkammer wurde dabei ein, für Laboranwendungen übliches Design mit nur einem Einspritzmodul gewählt, welches mit Gas (vorgemischt mit Luft) betrieben wird. An diesem Brenner wurde zuerst die instabile Verbrennung unter moderatem Druck untersucht. In einem weiteren Schritt wurde die Laser Vibrometry an einem Testsektor einer Flug-Gasturbinen-Brennkammer eingesetzt. Dieser mit flüssigem Kraftstoff betriebene Testsektor wurde mit einer neu entwickelten "Sirene", unter hohem Druck und Temperatur, künstlich zum Schwingen angeregt. Für die Sirene wurden neue Methoden und Routinen entwickelt um Brennkammern nach resonanten Frequenzen zu scannen. Zusätzlich wurde die Möglichkeit implementiert die Amplitude der Pulsation frei einzustellen.
Mittels Laser Vibrometry wurden schließlich Verbrennungsinstabilitäten messtechnisch erfasst und anschließend graphisch dargestellt, ausgewertet und interpretiert.

## Abstract

The increase in air traffic and the demand of the certifying authorities for low emission engines lead to the development of advanced and innovative aero engine technologies.
These new technologies have to deal with unsteady combustion processes. The use of unsteady combustion in terms of pulsed detonation combustion is leading to innovative jet engines beyond the time frame of 2020.
State of the art engines are using conventional steady combustion processes. The necessity for low pollutant concept is leading to combustion technologies operated in the lean domain. However, lean combustion concepts are susceptible to combustion instabilities (combustion oscillations). Compared to pulsed combustion such effects have to be avoided.
In this work, first the potential of using pulse detonation combustion in a hybrid turbofan engine concept is shown. A system level performance estimation tool, capable to simulate pulsed detonation is developed and used on two engine concepts.
The second part of this work is dealing with the experimental analysis of unsteady combustion phenomena on a lean combustor, using a technology called Lean Premixed Prevaporized (LPP). A novel laser based measurement technique for use in combustion technology, called Laser Vibrometry (LV), was developed at the Institute for Thermal Turbomachinery and Machine Dynamics (ITTM). In the frame of this work the Laser Vibrometry was used on two combustor concepts. First a laboratory (dump) combustor operated with a premixed methane air mixture was used. On this combustor the Laser Vibrometry was adapted to detect combustion instabilities in a flame operated at elevated pressure conditions. Next a combustor test sector, based on the design of an aero engine combustor, was developed. This sector used liquid fuel as propellant and was artificially excited by a novel flow exciter of the siren type, designed at the Institute. New methods and routines were developed for the siren to scan the combustor for resonant frequencies. In addition the option of varying amplitude of excitation was implemented to receive a versatile as possible flow exciter. By making use of Laser Vibrometry combustion instabilities were detected, displayed and evaluated.

# Contents


**1 Introduction** **1**

**2 Conventional aero engines** **5**

**3 Innovative aero engine core concepts** **11**
3.1 Pulse Detonation Engine - Overview . . . 12
3.2 Hybrid Turbofan Engine Concept . . . 14
3.3 Basic operation principle . . . 18
3.4 Thermodynamic modeling . . . 19
3.5 Evaluation of the PDE code . . . 22
3.6 Validation of the standard gas turbine parts . . . 28
3.7 Results on hybrid turbofan engine simulation . . . 29

**4 Advanced aero engines** **35**
4.1 Gas turbine combustor technology . . . 37
4.2 Gas turbine combustion . . . 39
4.3 Fuel injection technology . . . 40
4.4 Low Emission Concepts . . . 41
4.5 LPP combustor technology . . . 43

**5 Aspects of combustion instabilities** **45**
5.1 Reaction mechanism . . . 45
5.2 Thermodynamics of the reaction . . . 46
5.3 Continuous ignition of the flame . . . 48
5.4 Thermo acoustic coupling . . . 51
5.5 Simple combustion instability model . . . 53
5.6 Combustion instabilities in LPP combustors . . . 54

**6 Measurement techniques and specific methods** **57**
6.1 Laser Doppler Anemometry . . . 57
6.2 Laser Vibrometry . . . 61
6.3 High temperature resistant pressure transducer . . . 64
6.4 Specific methods and routines . . . 65
6.4.1 Spectrographical representation of scanning for resonant frequencies 66
6.4.2 Treatment of data for mapping the density fluctuation inside the combustor . . . 67
6.4.3 Computation of the Gladstone-Dale Constant . . . 70

**7 Model combustor design** **73**
7.1 Flow Exciter . . . 74
7.1.1 Type of flow exciters . . . 74
7.1.2 Design of the TUG siren . . . 76

7.2 Dump Combustor . . . 81
7.3 Single LPP combustor . . . 82
7.4 Industrial type LPP test sector . . . 83
7.4.1 Design guidelines for the LPP test sector . . . 84
7.4.2 Liner of the LPP test sector . . . 86
7.4.3 Combustor air feed of the LPP test sector . . . 88
7.4.4 Pressure casing of the LPP test sector . . . 90
7.4.5 Ignition device of the LPP test sector . . . 91

**8 Experimental Setup 95**
8.1 Setup for dump combustor experiments . . . 95
8.2 Setup for isothermal flow characterization . . . 96
8.3 Setup used to characterize the siren . . . 97
8.4 Experimental setup during single injector stability analysis . . . 100
8.5 Setup for isothermal flow stability analysis using the LPP test sector . . . 102
8.6 Setup for reactive flow stability analysis using the LPP test sector . . . 105

**9 Results and Discussion 107**
9.1 Mapping of density fluctuations inside the dump combustor . . . 107
9.2 Isothermal flow characterization of the test sector at atmospheric conditions 112
9.3 Characterization of the flow exciter . . . 115
9.3.1 Flow exciter without combustion chamber . . . 115
9.3.2 Flow exciter attached to the NEWAC combustion chamber at atmospheric conditions . . . 116
9.4 Single LPP injector stability analysis . . . 122
9.5 Isothermal stability analysis of the LPP test sector . . . 123
9.6 Reactive stability analysis of the LPP test sector . . . 127
9.6.1 Transient stability analysis . . . 127
9.6.2 Fixed frequency analysis . . . 129
9.6.3 Mapping of density fluctuations . . . 134

**10 Summary and Conclusion 145**

**11 Published articles 149**
11.1 Articles on Pulse Detonation engines . . . 149
11.2 Articles on Laser Vibrometry Measurements . . . 149
11.3 Others . . . 150

**Appendices 153**

**A Thermodynamical expressions for pulse detonation engine modeling 153**

**B Results on second test case evaluation 159**

**C Hybrid Engine Concepts 161**

**D Instrumentation of the flame tube of the NEWAC combustor 165**

**E Additional results on reactive stability analysis 167**

**F Refractive indices for computation of the Gladstone-Dale constant 169**

**G Images of the flame during reactive experiments** **171**

**H Characterization of the LPP injectors** **173**
H.1 Flow number . . . . . 173
H.2 Pressure loss coefficient . . . . . 174

**I Mathematical derivation of the time derivative of the density fluctuation** **175**

# List of Figures


1.1 Impact of air traffic growth on $CO_2$ emission . . . 1
1.2 ACARE Vison 2020 . . . 2
1.3 NEWAC contribution to improvement of $CO_2$ and $NO_x$ Emission . . . 3

2.1 Thermodynamic gas turbine cycle . . . 5
2.2 Thermal efficiency of aero engines . . . 8
2.3 Propulsive efficiency of various engine types . . . 9
2.4 Qualitative characteristics of thermal efficiency as function of overall pressure ratio for selected engine technolgoies . . . 10

3.1 Constant Volume Combustor . . . 13
3.2 Hybrid Turbofan Engine concept . . . 14
3.3 Hybrid Turbofan Engine scheme . . . 15
3.4 Pulse Detonation Engine Cycle . . . 19
3.5 Temperature entropy diagram of the detonation process . . . 20
3.6 Mach-number at initial conditions . . . 23
3.7 Temperature ratios and thermal efficiency as function compression temperature ratio . . . 24
3.8 Thrust as function of compression temperature ratio . . . 25
3.9 Results obtained from computation of reference engine (case 1) . . . 29
3.10 Temperature Entropy Diagram of HTE concept 1 . . . 30
3.11 Temperature Entropy Diagram of HTE concept 2 . . . 31

4.1 Engine Concepts to lift the thermal efficiency . . . 36
4.2 Fuel injection technology for different engine concepts as function of OPR . . . 36
4.3 Representation of three main combustor concepts . . . 37
4.4 Reverse flow type combustor . . . 38
4.5 Schematic of a conventional combustor . . . 39
4.6 Spatial location of emission formation . . . 40
4.7 Fuel injector types . . . 41
4.8 Emissions of gas turbine combustors . . . 42
4.9 LPP combustor technology . . . 43
4.10 Design point for main burner and pilot stage of the LPP concept . . . 44

5.1 Free enthalpy of a chemical reaction . . . 47
5.2 Energy balance for successful ignition as function of temperature . . . 49
5.3 Unsteady reaction rate . . . 51
5.4 Feedback loop responsible for combustion instabilities . . . 52
5.5 Rijke tube . . . 53
5.6 Variation of $p'$, $q'$ and $v'$ with time . . . 53
5.7 Disturbances responsible for combustion driven oscillations . . . 55

6.1 LDA system in fringe mode . . . 58
6.2 Fringe pattern of LDA system . . . 59
6.3 Doppler burst . . . 60
6.4 Scattering intensity distribution on a water droplet of 1 $\mu$m . . . 60
6.5 Components of a LDA system operating in back scattering mode . . . 61
6.6 Laser Vibrometery (LV) setup . . . 62
6.7 Light wave . . . 63
6.8 Properties of $GaPO4$ crystal . . . 65
6.9 Data structure for spectrographical representation . . . 66
6.10 Histogram of pulsation periods . . . 68
6.11 Time signals of LV data . . . 68
6.12 Ensemble averaged time signals at good and foul SNR . . . 69
6.13 Gladstone Dale constant for combustion with ethanol . . . 71

7.1 IRA core scheme . . . 73
7.2 LPP module . . . 74
7.3 Design principle of the TUG siren . . . 76
7.4 Cross section of the TUG siren . . . 76
7.5 Design of the sonic nozzle . . . 77
7.6 Mass flow through a sonic nozzle . . . 78
7.7 Different ensembles of critical nozzle/sprocket wheel . . . 79
7.8 Precision of excitation frequency . . . 79
7.9 Pulsation of the siren as function of tilt angle . . . 80
7.10 Dump combustor design . . . 81
7.11 Single LPP injector test stand . . . 82
7.12 Hot flow test facility . . . 83
7.13 Cross section of the test sector . . . 84
7.14 Design input parameter for the NEWAC test sector . . . 85
7.15 2D cross section through the liner of the NEWAC test sector . . . 86
7.16 3D cross section through the liner of the NEWAC test sector . . . 87
7.17 Air box with installed NEWAC LPP injector . . . 89
7.18 Alignment of the LPP injectors . . . 89
7.19 Pressure vessel of the LPP test sector . . . 90
7.20 Optical access for the pressure vessel . . . 91
7.21 Torch igniter . . . 92
7.22 Schematic of the ignition control . . . 93

8.1 LV measurement grid during dump combustor experiments . . . 96
8.2 Measurement setup during isothermal flow characterization . . . 97
8.3 Measurement setup during validation of the siren . . . 99
8.4 Location of measurement points for validation of the siren . . . 99
8.5 Experimental setup for single LPP injector combustion experiments . . . 101
8.6 Experimental setup during isothermal stability analysis . . . 104
8.7 Experimental setup during reactive stability analysis . . . 106

9.1 Phase resolved density fluctuation at 540 Hz excitation frequency . . . 109
9.2 Phase resolved density fluctuation at 540 Hz excitation frequency . . . 110
9.3 Images of flame structure during dump combustor experiments . . . 111
9.4 Flow field at lateral view of the combustor . . . 112
9.5 Flow field at bottom view of the combustor . . . 113

9.6 Swirl number at different cross sectional areas . . . 114
9.7 Flow field at frontal view of the combustor . . . 115
9.8 LDA measurement during validation of the siren at 452 Hz . . . 117
9.9 LDA measurements at LDA1 with varying amplitude of excitation . . . 118
9.10 LDA measurements at LDA2 with varying amplitude of excitation . . . 119
9.11 Influence of the vibrating optical access to the LV measurement . . . 120
9.12 Frequency spectra at excitation with 340 Hz, 350 Hz and 360 Hz during validation of the siren . . . 121
9.13 Signal strength as function of amplitude for excitation at 226 Hz . . . 122
9.14 Signals recorded during transient behavior of the single LPP experiment . . 123
9.15 Signals recorded during transient isothermal stability analysis . . . 124
9.16 Frequency spectra of CP502 and Laser Vibrometer at excitation frequencies of 526 Hz, 572 Hz and 854 Hz . . . 126
9.17 Signals recorded during transient reactive stability analysis . . . 128
9.18 Frequency spectra of CP502 and Laser Vibrometer at excitation frequencies of 176 Hz, 624 Hz and 900 Hz . . . 131
9.19 Frequency spectra of CP502 and Laser Vibrometer at excitation frequency of 854 Hz at different operating conditions . . . 133
9.20 Phase plot at center axis during excitation with 176 Hz . . . 135
9.21 Luminosity analysis of a high speed video at 176 Hz excitation frequency . . 136
9.22 Phase resolved density fluctuation at $176Hz$ excitation frequency . . . 137
9.23 Phase resolved density fluctuation at $624Hz$ excitation frequency . . . 139
9.24 Phase resolved density fluctuation at $854Hz$ excitation frequency . . . 141
9.25 Phase resolved density fluctuation at $900Hz$ excitation frequency . . . 143

A.1 Detailed Temperature Entropy Diagram of the Detonation Process . . . 156

B.1 Results obtained from computation of reference engine (case 1) . . . 159

C.1 Temperature Entropy Diagram of the reference engine . . . 161
C.2 Temperature and pressure history for HTE concept 1 . . . 162
C.3 Temperature and pressure history for HTE concept 2 . . . 162

D.1 Instrumentation of the NEWAC liner, top view . . . 165
D.2 Instrumentation of the NEWAC liner, back view . . . 166
D.3 Instrumentation of the NEWAC liner, bottom view . . . 166

E.1 Signals recorded during second transient reactive stability analysis . . . 167
E.2 Signals recorded during third transient reactive stability analysis . . . 168

G.1 Flame structure during excitation with 176 Hz . . . 171
G.2 Flame structure during excitation with 624 Hz . . . 171
G.3 Flame structure during excitation with 854 Hz . . . 172
G.4 Flame structure during excitation with 900 Hz . . . 172

H.1 Flow number of the NEWAC LPP's . . . 173
H.2 Characterization of the NEWAC LPPs . . . 174

# List of Tables


3.1 Input-data for reference case . . . . . 16
3.2 Difference in hybrid turbofan cases 1 and 2 . . . . . 17
3.3 Input data for ideal PDE calculation . . . . . 22
3.4 Comparison of ideal PDE cycle calculation . . . . . 27
3.5 Results of cycle evaluation for conventional turbofan engine reference case 1 28
3.6 Difference in test cases 1 and 2 for standard turbofan validation . . . . . 29
3.7 Results of HTE efficiency analysis . . . . . 32
3.8 Results of HTE performance analysis . . . . . 33

7.1 Operating conditions of the NEWAC IRA core combustor . . . . . 83

8.1 Operating conditions for dump combustor experiments . . . . . 95
8.2 Operating conditions during evaluation of the siren . . . . . 98
8.3 Location of measurement points for optical measurement . . . . . 100
8.4 Operating conditions for single LPP injector experiments . . . . . 102
8.5 Operating conditions for isothermal stability analysis . . . . . 103

9.1 Measurement techniques used at different experimental setups . . . . . 107
9.2 Mean and min. /max. of velocity components at excitation with 452 Hz . . 116
9.3 Mean and min. /max. of velocity components at excitation with 226 Hz . . 119
9.4 Operating conditions for first transient reactive stability analysis . . . . . 128
9.5 Operating conditions for first transient reactive stability analysis . . . . . 129
9.6 Operating conditions for first transient reactive stability analysis . . . . . 129
9.7 Operating conditions for perturbations at fixed frequency . . . . . 130
9.8 Operating conditions during excitation with 854 Hz . . . . . 132

B.1 Results of cycle evaluation for conventional turbofan engine reference case 2 159

C.1 PDE stats at configuration HTE1 . . . . . 163
C.2 PDE stats at configuration HTE2 . . . . . 163

F.1 Refractive indices for several species . . . . . 169

# Nomenclature

| | **Latin symbols** |
|---|---|
| $\Delta f$ | Frequency Shift Added by the Bragg Cell |
| $\Delta x$ | Width of the Fringe Pattern |
| $\Delta y$ | Height of the Fringe Pattern |
| $\Delta z$ | Depth of the Fringe Pattern |
| $\dot{m}$ | Mass Flow |
| $\bar{}$ | Average |
| $\prime$ | Conditions at Stationary Shock Wave, Fluctuating, Time Derivative |
| $\Re$ | Rayleigh's Criterion |
| $\tilde{q}$ | Non Dimensional Heat |
| $c_c$ | Correction Coefficient |
| $c_p$ | Specific Heat at Constant Pressure |
| $d_f$ | Spacing of the Fringe Pattern |
| $E_a$ | Activation Energy |
| $H_f$ | Lower Heating value |
| $k^f$ | Forward Reaction |
| $k^r$ | Reverse Reaction |
| $R_G$ | Gladstone Dale Constant |
| $R_m$ | Universal Gas Constant |
| A | Area |
| c | Velocity, Speed of Sound, Concentration |
| D | Diameter |
| d | Diameter |
| e | Eccentricity |
| F | Thrust |
| f | Frequency |
| FN | Flow Number |
| G | Gibbs Energy |
| I | Intensity |
| K | Rate of Reaction |
| k | Calibration Factor |
| l, L | Length |
| M | Mach-Number |
| n | Number of Samples, Refractive Index, Amount of Substance |
| p | Pressure |

| | |
|---|---|
| q, Q | Heat |
| r | Radius |
| S | Signal, Entropy |
| T | Temperature, Cycle Duration |
| t | Time |
| U | Voltage, Velocity, Internal Energy |
| u | Axial Velocity, Velocity |
| V | Volume |
| v | Specific Volume, Radial Velocity |
| X | Mole Fraction |
| x | A Single Recorded Signal Sample |
| z | Geometric bath of laser beam, Number of Teeth |

**Greek symbols**

| | |
|---|---|
| $\eta$ | Efficiency |
| $\gamma$ | Ratio of specific heats |
| $\lambda$ | Wave Length |
| $\mu$ | Chemical Potential |
| $\nu$ | Viscosity, Stoichiometric Coefficient |
| $\phi$ | Equivalence Ratio, Phase Angle |
| $\Pi$ | Pressure Ratio |
| $\Psi$ | Tilt Angle |
| $\psi$ | Temperature Ratio |
| $\rho$ | Density |
| $\tau$ | Period Length, Time Lag |
| $\Theta$ | Beam Angle |
| $\zeta$ | Pressure Loss Coefficient |

**Subscripts**

| | |
|---|---|
| 0 | Ambient, Emitting |
| 9 | Nozzle |
| A,B | Precursors |
| add | Added |
| C | State After Constant Pressure Combustion |
| c | Carnot |
| CJ | Chapman Jouget |
| conv | Convective |
| core | Core |
| D | State at End of Detonation Process, Doppler Shifted |
| down | Downstream |
| E | State After Expansion to Ambient |
| e | End |

| | |
|---|---|
| E,F | Products |
| eq | Equivalent |
| f | at Fixed Frequency, Fluid |
| free | Free |
| i | Counter, Emitting Optics |
| j | Counter |
| L | Loss |
| LEC | Low Emission Concepts |
| max | Maximum |
| mech | Mechanical |
| min | Minimum |
| N | Net |
| o | Overall, Reference |
| obj | Object |
| opt | Optical |
| OTDF | Overall Temperature Distribution Factor |
| P | Produced |
| p | Particle |
| PDC | Pulse Detonation Combustor |
| prop | Propulsive |
| ref | Reference |
| rej | Rejacted |
| s | Receiving |
| s | Sample, Receiving Optics |
| st | stoichiometric |
| sub | Sub Sample |
| th | Thermal |
| trans | Transfer |
| up | Upstream |
| X | State at Start of Detonation Process |
| x | State at start of Detonation Process |
| Y | State at End of Shock Induced Compression |
| Z | State at End of Rayleigh Heat Release Process |

**Vectors**

| | |
|---|---|
| $\overrightarrow{e}$ | Unit Vector |
| $\overrightarrow{U}$ | Velocity |

**Abbreviations**

| | |
|---|---|
| $CO$ | Carbon Monoxide |
| $CO_2$ | Carbon Dioxide |
| $NO_x$ | Nitride Oxides |

| | |
|---|---|
| ACARE | Advisory Council of Aeronautical Research in Europe |
| AFR | Air to Fuel Ratio |
| BPR | Bypass Ratio |
| BSA | Burst Spectrum Analyzer |
| CAC | Cooling Air Compressor |
| CAD | Computer Aided Design |
| CFD | Computational Fluid Dynamics |
| CJ | Chapman Jouget |
| CVC | Constant Volume Combustion |
| DDT | Deflagration to Detonation Transition |
| DLR | Deutsches Zentrum für Luft und Raumfahrt - German Aerospace Center |
| ESA | European Space Agency |
| FAR | Fuel to Air Ratio |
| FFT | Fast Fourier Transform |
| FT | Fourier Transform |
| GE | General Electric |
| GT | Gas Turbine |
| HeNe | Helium Neon |
| HEX | Heat Exchanger |
| HPC | High Pressure Compressor |
| HPT | High Pressure Turbine |
| HTE | Hybrid Turbofan Engine |
| IAE | International Aero Engines |
| IATA | International Air Transport Association |
| ICAO | International Civil Aviation Organisation |
| IPC | Intermediate Pressure Compressor |
| IRA | Intercooled Recuperative Aero Engine |
| ITTM | Institute for Thermal Turbomachinery and Machine Dynamics |
| LDA | Laser Doppler Anemometry |
| LDI | Lean Direct Injection |
| LDV | Laser Doppler Velocimetry |
| LPC | Low Pressure Compressor |
| LPP | Lean Premixed Prevaporized |
| LPT | Low Pressure Turbine |
| LV | Laser Vibrometry |
| NACA | National Advisory Committee for Aeronautics |
| NEWAC | New Aero Engine Core Concepts |
| ONERA | Office National d'Etudes et de Recherches Aérospatiales - The French Aerospace Lab |
| OPR | Overall Pressure Ratio |
| P&W | Pratt & Whitney |
| PDC | Pulse Detonation Combustor |

| | |
|---|---|
| PDE | Pulse Detonation Engine |
| PERM | Partially Evaporated Rapid Mixing |
| PIV | Particle Image Velocimetry |
| PM | Performance Model |
| PR | Pressure Ratio |
| RTDF | Radial Temperature Distribution Factor |
| SFC | Specific Fuel Consumption |
| TET | Turbine Entry Temperature |
| TM | Turbomeca |
| TRL | Technology Readiness Level |
| TSFC | Thrust Specific Fuel Consumption |
| TTL | Transistor Transistor Logic |
| TUG | Graz University of Technology |
| UHB | Ultra High Bypass |
| UHC | Unburnt Hydro Carbons |
| WR | Wave Rotor |
| ZND | Zel'dovich/vonNeumann/Döring |

# Chapter 1

# Introduction

With the dawn of aviation a drastic change in transportation happened. Large distances, like transatlantic routes could be covered in hours with an aircraft, compared to the weeks it took by ship. Although very expensive in the early years of air transportation, due to the steep technological development especially with the beginning of the jet age, traveling by plane is affordable for everybody today and is thus an economic factor. Business meetings all over the world are also common today, as well as air cargo for important goods that have to be delivered on time.
A continuous growth in air traffic since the start of aviation can be noticed. The only two events in the last decade with a negative growth rate were the aftermath of 9/11 in 2001 and the financial crisis in 2009 [1]. Although air traffic slowed down for almost a year due to this events, a mean growth rate of air traffic by 4 % for the decade 2000 to 2010 is given and the ICAO (International Civil Aviation Organization) forecasts a growth in air traffic by 4.6 % p.a. as most likely up to 2025 (2.6 % lowest and 6.2 % highest growth rate respectively) [2].

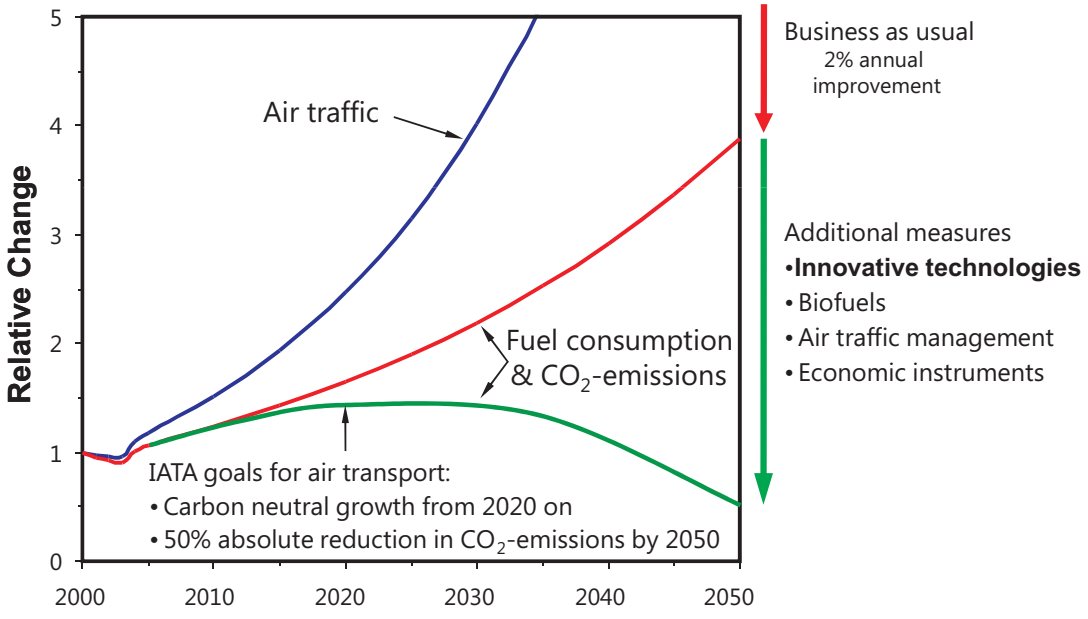


Figure 1.1: Impact of air traffic growth on $CO_2$ emission; [3] modified

The impact of air transportation on the environment is therefore of importance as the absolute demand on fuel for aviation is increasing together with the output on pollutant emissions. Figure 1.1 shows that even with an annual improvement of 2 % p.a. on fuel

efficiency (business as usual; red curve), the $CO_2$ emissions will triple until 2050 [3].
To achieve the IATA (International Air Transport Association) goals of carbon neutral growth of the air traffic, starting from 2020 and finally reduce $CO_2$ emissions by 50 % until 2050, despite the increase in air traffic, additional measures (green curve), like advanced and innovative technologies, have to be used. The terminology advanced and innovative can be categorized when using the Technology Readiness Level (TRL) as measure.
The TRL is giving the development status of a technology. Here the ninefold scale, defined by the European space agency (ESA), is used. TRL levels from 1 to 3 are related to the creative concept phase. Innovative technologies fall within this category (the basic principle of a technology has been described). TRL 4 to 6 is dedicated to component tests and testing of subsystems. Advanced technologies have a TRL of more than three (the functionality of a technology has been shown and first laboratory experiments are started) and fall thus in this category. For prototype testing up to start of production the, TRL levels of 7 to 9 have to be achieved [4].
Based on the impact of air transport on the environment the ACARE (Advisory Council of Aeronautical Research in Europe) has defined the Vision 2020. The European aeronautical industry has set up a visionary goal:

> "*Aircraft and an air transport system that are responding to society's needs, despite a three-fold increase in air transport*".[5]

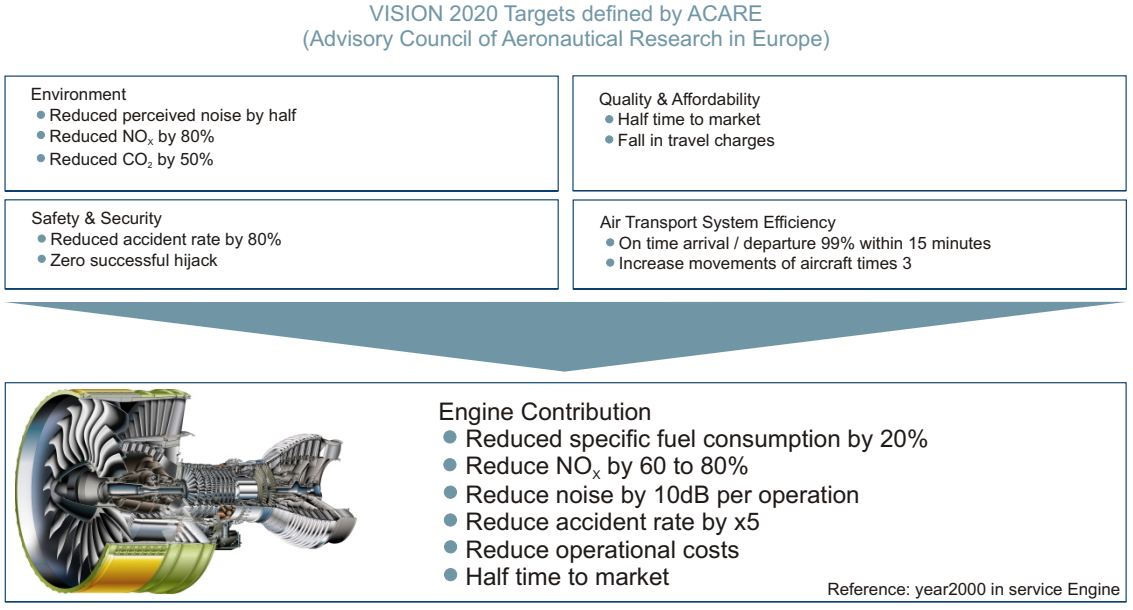


Figure 1.2: ACARE Vision 2020; [6] modified

This vision for the year 2020 stands on 4 pillars, shown in figure 1.2. The society's needs effect the whole air transportation system. The contribution that can be made by the engine are, despite economic aspects (operational costs, time to market) and safety (accident rate) the environmental impact of aviation. Engines have to be designed to produce less noise, have lower fuel consumption and emit less pollutant emissions. Several activities in the frame of European framework programs have been started to get towards fulfilling the vision 2020. Previous programs like SILENCER (main focus on noise reduction), EEFAE-ANTLE, EEFAE-CLEAN (efficient, eco-friendly aircraft engines) have made main

contributions. The next step however was started with the project NEWAC[1] (**NEW A**ero engine **C**ore concepts) with its targets to receive a further reduction in $CO_2$ by 6 % and $NO_x$ by 16 % compared to the above mentioned programs (see figure 1.3).

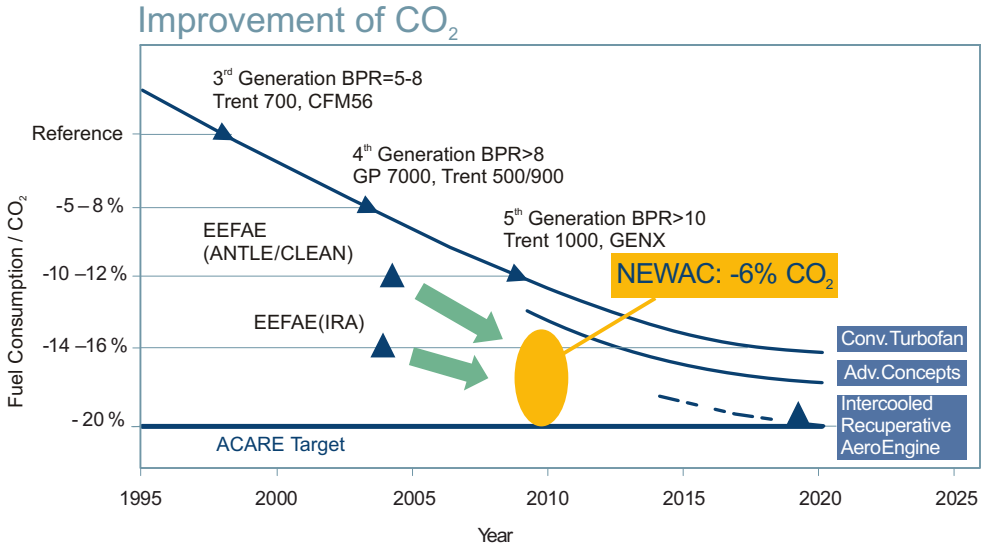


(a) NEWAC contribution to improvement of $CO_2$ Emission

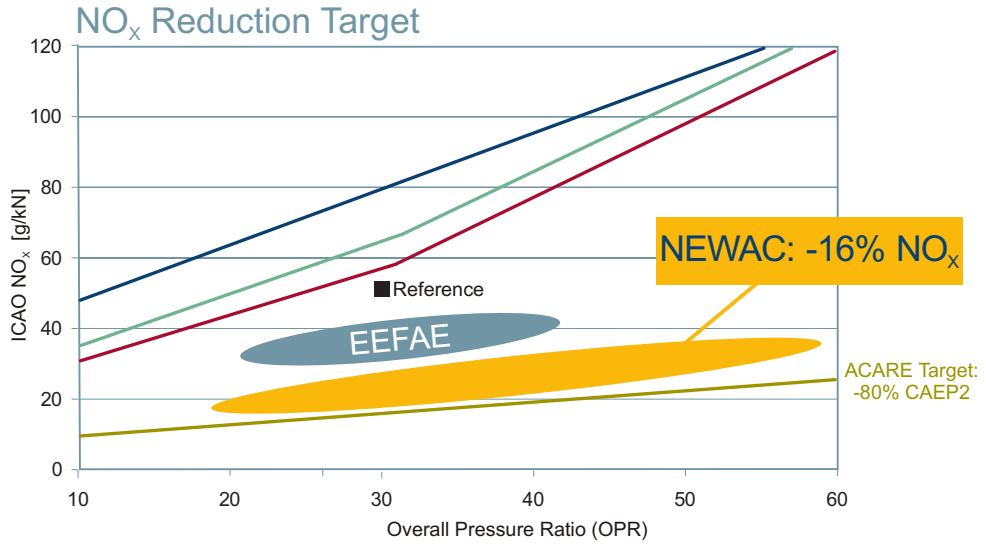


(b) NEWAC contribution to improvement of $NO_x$ Emission

Figure 1.3: NEWAC contribution to improvement of $CO_2$ and $NO_x$ Emission [6]

The new technologies to reach the targets of NEWAC can be split in two categories. The first one deals with completely new promising technologies like innovative combustion. These technologies are for the time frame beyond 2020 and are dealing for example with unsteady combustion processes. The engines for future aircrafts might use unsteady combustion in terms of pulsed combustion.
The second category is improving the well established continuous combustion process used

[1]NEWAC is an Integrated Project co-funded by the European Commission within the Sixth Framework Programm; FP6-030876

in conventional aero engines. Improvements are done in terms of pollutant emissions by forcing the combustion to take place in the very lean operating range of combustors.
In the following chapters first the background on aero engine technology is given to show the fundamentals on which the new engine concepts are based on. This is followed by a description of the use of unsteady combustion in future aero engines on a theoretical basis. It is shown that by using pulsed detonation as a replacement for conventional combustion (continuous combustion is replaced by a detonative intermittent combustion) the thermal efficiency of an aero engine can be lifted. A tool to compute the performance of a hybrid turbofan engine, having a core engine with an increased power density, on system level was developed.
However, the pulsed combustion is on a rather low technology readiness level. Meanwhile existing concepts being in operation have to reach for the goals of ACARE. Currently available combustor technologies are thus operated in a way to emit low levels of emissions. But such advanced combustion technologies have to deal with unsteady combustion. Advanced combustion technologies for the near future tend to get unsteady as the combustion is operated at the lean regime and thus get prone to combustion instabilities. These instabilities, or sometimes called combustion oscillations, are unsteady combustion processes that are harmful to the operation and have thus to be avoided. First a description of combustion technologies for the lean operating range is given and the the problem of combustion instabilities is described.
To experimentally detect in-situ combustion instabilities, the laser vibrometry was adapted to combustion processes. The previous work by Mayerhofer [7], Hampel [8] and Giuliani [9] was continued. In addition the laser vibrometry is accompanied by a measurement of the unsteady pressure inside the combustor. Therefore a high temperature resistant pressure transducer was used.
Three combustion chambers, for a laser optical investigation, were developed. To perform measurements, first a simple dump combustor design was used for the examination of laser vibrometry measurements at elevated pressure conditions. A single laboratory axial swirler injector was designed and fed with a premixed air-methane mixture. The design of the injector is similar to the design by Wagner [10]. The combustor was first investigated at atmospheric conditions and finally pressurized up to 2.5 bar.
The same injector design was used by Köberl [11] for a detailed investigation of the flame flame interaction of an arrangement of three injectors using dual laser vibroemtry.
The combustor laboratory at the Institute for Thermal Turbomachinary and Machine Dynamics (ITTM) at Graz University of Technology (TUG) offers the possibility to investigate combustor test sectors using liquid fuels. By using the 3 MW compressor facility air mass flows from $2.5 \div 15$ kg/s at pressure ratios from 2.9 up to 10 are possible. As a thermal air heater with a thermal power of 5 MW is available combustor entry conditions with temperature levels up to 823 K can be set. The air supply system is capable of splitting the air mass flows into primary air for combustion (preheated) and cooling air. More on the capabilities of the versatile test rig of the ITTM can be found in the papers by Leitgeb [12, 13].
A test sector using the geometry of an industrial type reverse-flow combustor, consisting of two main injectors (lean premixed prevaporized type) and a pilot stage (flat spray type) was designed and artificially excited by using a newly developed flow exciter of the siren type. The initiated density fluctuations (which are potential markers for combustion instabilities) can be detected and visualized by using laser vibrometry, frequency and spatially resolved. The necessary algorithms for evaluation and visualization were developed.

# Chapter 2

# Conventional aero engines - fundamentals

Nowadays commonly gas turbines (GT) are used as aero engines. The most simple gas turbine is the turbojet, shown in figure 2.1 left.

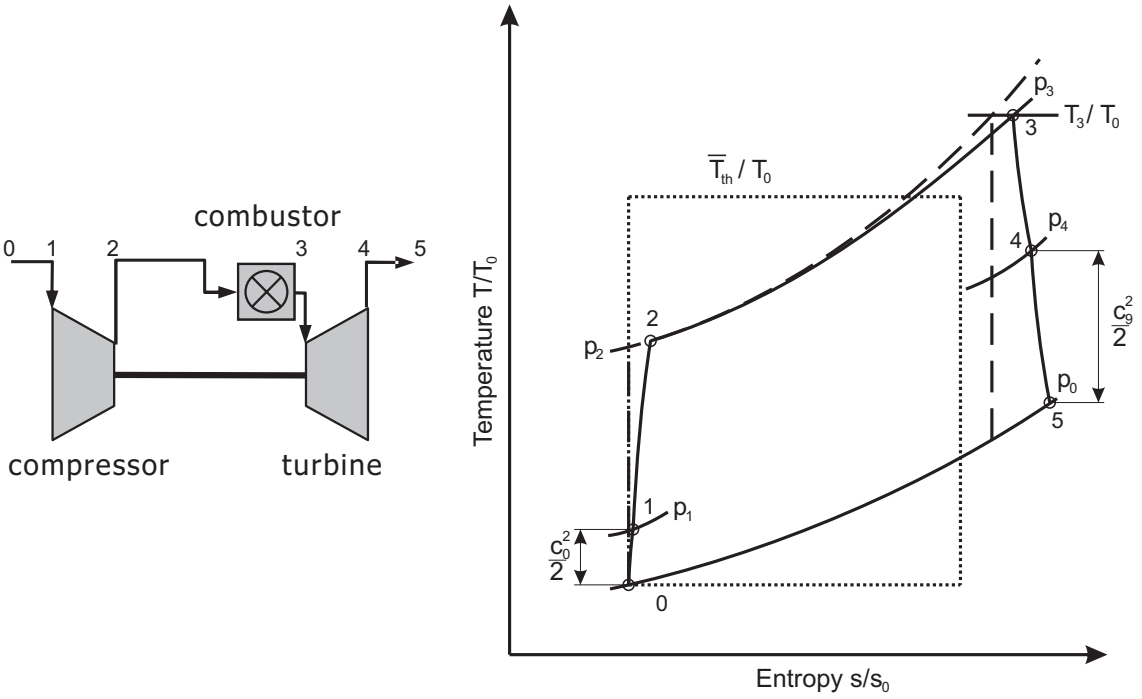


Figure 2.1: Thermodynamic gas turbine cycle (left: engine scheme, right: qualitative T-s diagram); solid line: Joule process, dashed line: isentropic change of state; dotted line: Carnot process

From a thermodynamic point of view the gas turbine cycle is a Joule process (shown in figure 2.1 right). As the GT is a continuous working machine the working media (air) is changing its conditions of state throughout the engine. These states are labeled from zero to five in figure 2.1. The compression of the air is done from state 0 to 2, where the compression is partially achieved by retention at the engine's inlet (depending on the flight speed $c_0$) and aerodynamically by the compressor. This is followed by a heat addition due to the combustion of fuel together with the compressed air from state 2 to 3. Due to the design of the combustor a slight pressure drop occurs. The power needed to drive the compressor is extracted from the hot gases by the turbine through an expansion process from 3 to 4. The remaining energy of the exhaust flow is expanded in the nozzle to generate thrust (velocity of the exhaust jet $c_9$).

To compute the efficiency of such an engine one has to compare the useful power generated by the engine and compare it to the effort put into the engine. Generally speaking two efficiencies can be computed. The outer, or propulsive efficiency and the inner or thermal efficiency. For the discussion of the efficiencies an ideal (lossless) engine is considered.
The propulsive efficiency compares the useful work of the engine to the energy available in the exhaust jet. This is illustrated by equation 2.1.

$$\begin{aligned}\eta_{prop} &= \frac{\text{useful work of the engine}}{\text{energy of the exhaust jet}} = \frac{\dot{m}\cdot(c_9-c_0)\cdot c_0}{\dot{m}\left(\frac{c_9^2}{2}-\frac{c_0^2}{2}\right)} \\ &= \frac{2\cdot c_0}{c_9+c_0} = \frac{2}{1+\frac{c_9}{c_0}}\end{aligned} \tag{2.1}$$

It can be seen that the propulsive efficiency is a function of the exhaust jet velocity to the cruise speed ratio.
To compute the thermal efficiency two formulations are possible. For the first one, being similar to the discussion of the propulsive efficiency, one has to compare the energy of the exhaust jet to the energy added by the fuel.

$$\begin{aligned}\eta_{th} &= \frac{\text{energy of the exhaust jet}}{\text{energy added by the fuel}} = \frac{\dot{m}\left(\frac{c_9^2}{2}-\frac{c_0^2}{2}\right)}{\dot{m}_f\cdot H_f} \\ &\text{with } FAR = \frac{\dot{m}_f}{\dot{m}} \\ &= \frac{c_0^2}{2}\cdot\frac{(c_9/c_0)^2-1}{FAR\cdot H_f}\end{aligned} \tag{2.2}$$

In this constellation the thermal efficiency is a function of the same velocity ratio as given in the propulsive efficiency, the cruise speed, the fuel to air ratio (FAR) and the lower heating value of the fuel. However, as mainly kerosene of type Jet-A is used in aviation, the heating value of the fuel can be considered as constant.
Another definition of the thermal efficiency can be given by applying an energy balance of the Joule process. Equation 2.3 is showing the mathematical expression for this definition.

$$\begin{aligned}\eta_{th} &= \frac{\text{heat added - heat rejected}}{\text{heat added}} = \frac{q_{add}-q_{rej}}{q_{add}} \\ &= \frac{c_p\cdot(T_3-T_2)-c_p\cdot(T_5-T_0)}{c_p\cdot(T_3-T_2)} = \frac{(T_3-T_5)-(T_2-T_0)}{(T_3-T_2)} \\ &= \frac{T_3\cdot\left(1-\frac{T_5}{T_3}\right)-T_2\cdot\left(1-\frac{T_0}{T_2}\right)}{T_3-T_2} = \frac{T_3\cdot\left(1-\frac{1}{\Pi^{\frac{\gamma-1}{\gamma}}}\right)-T_2\cdot\left(1-\frac{1}{\Pi^{\frac{\gamma-1}{\gamma}}}\right)}{T_3-T_2} \\ &= 1-\frac{1}{\Pi^{\frac{\gamma-1}{\gamma}}}\end{aligned} \tag{2.3}$$

Here the thermal efficiency is only a function of the (overall )pressure ratio (OPR; $\Pi$) of the engine.
When going for the best thermal efficiency possible for a thermodynamic cycle, one will end up with the Carnot efficiency $\eta_c$. Assuming an ideal gas, it arises from equation 2.3 that for the OPR one can use the temperature ratio $T_2/T_0 = \Pi^{\frac{\gamma-1}{\gamma}}$. To maximize the efficiency, the highest temperature difference between the level where heat is added and

rejected has to be considered. By minimizing $T_0$ and maximizing $T_2$, and assuming a heat addition / rejection at constant temperature the Carnot efficiency is given (see figure 2.1 right). This is illustrated by equation 2.4. Although it is impossible to realize a Carnot process, it is commonly used for optimization and comparison. Thus for cycles where the heat is added via a temperature interval, rather than at constant temperature, the thermodynamic mean temperature $\overline{T_{th}}$ is used ($T_{max} = \overline{T_{th}}$) [14].

$$\eta_c = 1 - \frac{T_{min}}{T_{max}} = 1 - \frac{T_0}{\overline{T_{th}}} \text{ with } \overline{T_{th}} = \frac{T_{t3} - T_{t2}}{ln\frac{T_{t3}}{T_{t2}}} \tag{2.4}$$

The overall efficiency can be computed as the product of propulsive and thermal efficiency and is giving the ratio of propulsive power to the heat that has to be added to the cycle.

$$\begin{aligned} \eta_0 &= \frac{\text{useful work of the engine}}{\text{energy of the exhaust jet}} \cdot \frac{\text{energy of the exhaust jet}}{\text{energy added by the fuel}} \\ &= \frac{\text{useful work of the engine}}{\text{energy added by the fuel}} \\ &= \frac{\dot{m} \cdot (c_9 - c_0) \cdot c_0}{\dot{m_f} \cdot H_f} = \frac{F_N \cdot c_0}{\dot{m_f} \cdot H_f} = \frac{c_0}{SFC \cdot H_f} \end{aligned} \tag{2.5}$$

In equation 2.5 the thrust specific fuel consumption (SFC) is the ratio of fuel mass flow to the net thrust generated.
From the definition of the efficiencies one can see that mainly four engine parameters are effecting the performance.

- **Velocity ratio** $c_9/c_0$; setting the propulsive and thermal efficiency.
  The propulsive efficiency is tending towards unity for $c_9 = c_0$. However, this is not possible as for an air breathing engine the principle of momentum states that the net impulse has to be positive to receive thrust.
  Furthermore component losses at high flight speeds degenerate the propulsive efficiency (as this fact is more complex it will be described later on in more detail).
  On the other hand an increase in $c_9/c_0$ ($c_9 > c_0$) would lift the thermal efficiency as equation 2.2 has shown. But with higher exhaust jet velocity the noise of the engine will drastically increase and also the propulsive efficiency would decrease.

- **OPR**; setting the thermal efficiency. The larger the OPR the higher the thermal efficiency. To achieve a higher OPR more compressor stages are necessary. Beside the increase in weight of the engine the compressor exit temperature is increased too. Materials that can withstand this higher level of temperature are thus necessary. As these materials do have usually a higher density, additional weight is added. An increase in 1 % weight means an increase in 0.1 % fuel burn for long range and 0.11 % for short range air crafts respectively [15].
  With increasing OPR the power density of the engine is increased, so that more energy at the exhaust jet is available. In order to reduce the exhaust jet velocity the exhaust jet energy is converted by an additional turbine stage into mechanical work and is used to drive additional low pressure ratio compressors (so called fans; more on this will also be shown later).

- **FAR**; setting the thermal efficiency. An other option for an increase in $\eta_{th}$ would be to set the combustor operating at a lower FAR, which is leading to lean combustion technologies.

- **Turbine entry temperature (TET)** $T_3$; setting the Carnot efficiency. When maximizing the TET the highest thermal efficiency possible is achieved. However, restriction to the TET are given by the engine parts facing the hot exhaust gases. This is mainly the stator of the high pressure turbine (HPT) and the first rotor. Raising the temperature is only possible when using high temperature resistant materials (nickel-based alloys) in combination with highly sophisticated cooling technologies. The cooling technology can be set by using cooling air, bleed off from the compressor and routed alongside the stator blades and / or using coating layers on the blades. When more cooling air is required the efficiency of the engine is reduced as well as the thrust, due to the fact that bleed air from the compressor is used for cooling, which will not participate in the combustion process or expansion in the turbine. By coating the high temperature facing parts, the effort and complexity gets higher as well as the weight of these parts increases.

The impact of FAR and speed ratio $c_9/c_0$ is visualized in figure 2.2. From the same figure it can also be seen that aero engines are designed for high flight speeds, as the thermal efficiency increases with $c_0$ (see equation 2.2).

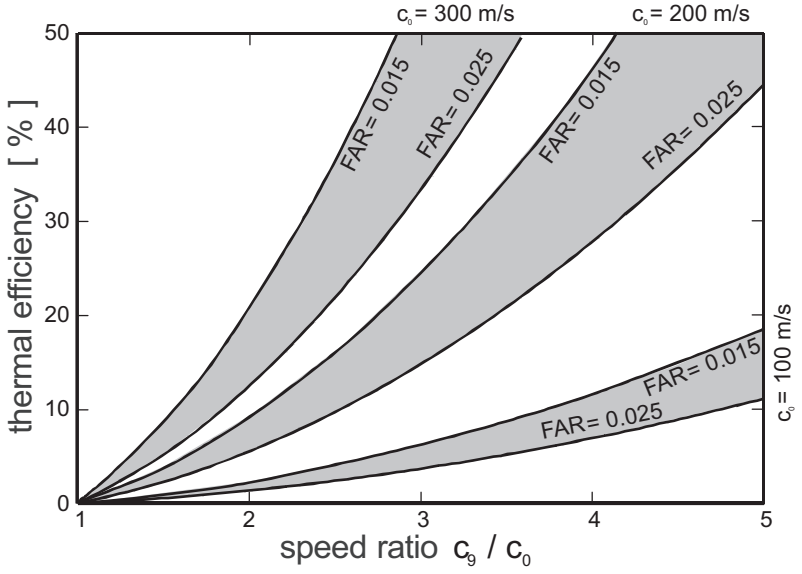


Figure 2.2: Thermal efficiency of aero engines as function of flight speed to exhaust jet velocity ratio and air to fuel ratio; [14] modified

From the discussion above it arises that a multidimensional optimization has to be done to find an optimum solution. The outcome of the optimization process leads to several engine types for different applications (flight speeds or "missions"). Figure 2.3a shows the propulsive efficiency as a function of flight speed. It can be seen that the propulsive efficiency reaches an optimum at flight speeds dependent on the engine type used. Therefore several "basic" engine types have been developed.
In the early days of aviation the basic concept of an aero engine was of the turbojet type (see figure 2.1 left for the engine scheme). Nowadays the principle of the turbojet is found in the core of an engine. In addition a so called fan, or low pressure ratio compressor, is used to bypass a high quantity of air to generate thrust at a higher efficiency, whereas the core of the engine is mainly used to drive the fan.

However, basically one can say that the best fitted engine type can be determined on the flight speed the aircraft shall reach. In the low speed range (up to roughly 600 km/h) the turboprop is more efficient than the turbojet or turbofan due to its better propulsive efficiency. At higher speeds the component efficiency of the propeller decreases drastically as the blade-tips reach the speed of sound [14]. For higher flight speeds up to Mach-numbers of $Ma = 0.85$ (roughly 900 km/h), which is the usual cruise speed for civil air crafts, the turbofan engine is the most promising. When going into supersonic speed the pure turbojet engine or a low bypass turbofan is performing better (usually military application, but also the civil super sonic airliner Aérospatiale-BAC Concorde 101/102 or the Tupolew Tu-144 Charger). The qualitative progress of $\eta_{prop}$ for the four main engine types given in figure 2.3a is accompanied by representative engines depicted in figure 2.3b. Sketched in figure 2.3b are the turboprop TP400 engine from Europrop international [16], the turbofan V2500 from International Aero Engines (IAE)[17] as well as the low bypass turbofan EJ200 from Eurojet[18] and finally the turbojet Olympus 593 Mk. 610 from Rolls-Royce [19]. Figure 2.3a also indicates that the higher the bypass ratio (BPR; ratio of bypass air mass flow to core air mass flow) the higher the propulsive efficiency. For in-service engines like the CFM56 from CFM international (first run in 1974) or the V2500 from P&W (first run in 1984) the bypass ratio is in the order of 5 to 6. Newer engines like the GP7200 from engine alliance (2004), powering the huge Airbus A-380, or the GE90 from General Electric (1995) used on the Beoing 777 have a bypass ratio of roughly 9 and next generation turbofans will have bypass ratios of up to ten or eleven [20], like for the Rolls Royce Trent

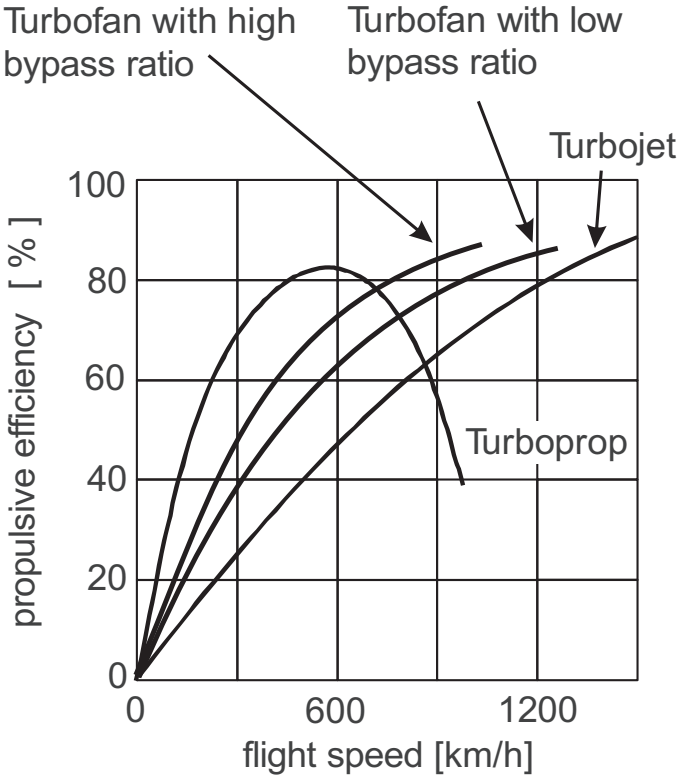


(a) Propulsive efficiency as function of cruise speed; [14] modified

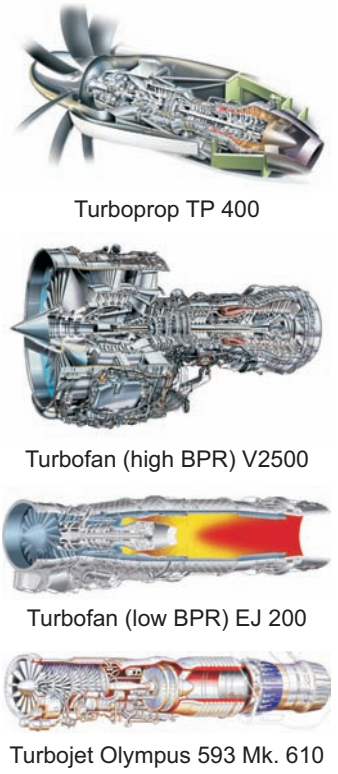


(b) Different conventional aero engines

Figure 2.3: Propulsive efficiency of various engine types

1000 [21]. The limiting factor in the design of high or ultra high bypass turbofan engines however is, like before with the turboprop engines, the efficiency of fan-blades at higher blade tip speeds. Furthermore the larger diameter of the fan induces further problems in terms of engine installation on the aircraft. Engines with larger diameter produce more engine specific drag during flight. Additionally the ground clearance is reduced making it necessary to lift the undercarriage.
However, an increase in propulsive efficiency (e.g. via the BPR) brings the necessity of a core engine with a higher power density (e.g. higher OPR), which will also increase the thermal efficiency.
This thesis is dealing with combustion and therefore the focus is set on core engine technologies. As earlier said the new technologies under investigation in this thesis can be split into technologies with an TRL of less than three (innovative technologies) and higher than three (advanced technologies). First an highly innovative combustion technology is presented, followed by advanced engine concepts.
Figure 2.4 is showing the potential of one innovative and four advanced engine concepts compared to a conventional propulsion system.

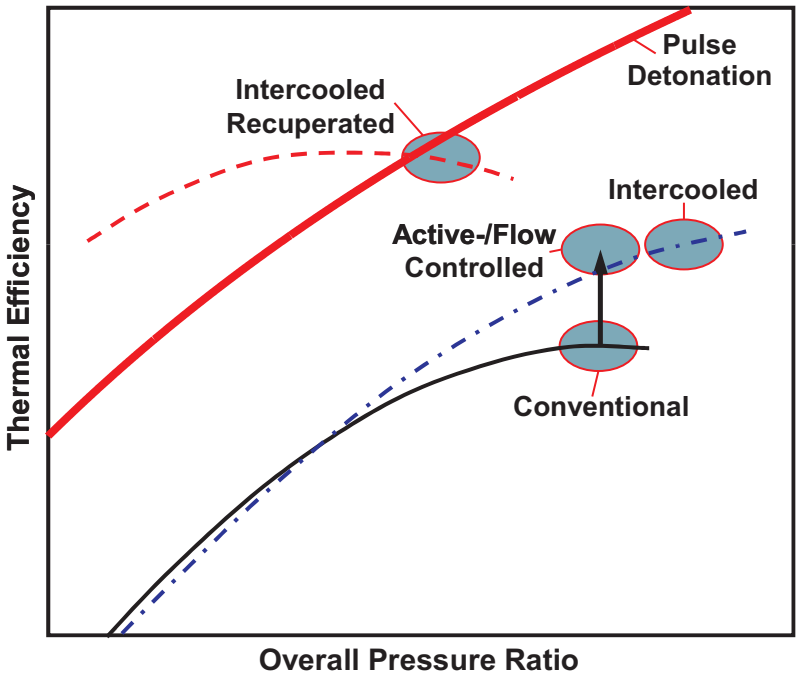


Figure 2.4: Qualitative characteristics of thermal efficiency as function of overall pressure ratio for selected engine technolgoies; [3] modified

# Chapter 3

# Innovative aero engine core concepts

In this section the focus in terms of new innovative core engine concepts is on technologies with a TRL of two ("*Technology concept and/or application formulated*" [4]). Four promising concepts, closely investigated by the NEWAC project, are [15, 22]:

- **Variable Core Cycle**; Conventional aero engines are designed to deliver the maximum power at take off and hence the OPR is here maximized too. At part load or during cruise the power of the engine is throttled and thus the OPR is decreased. As it has been shown, with an decreased OPR the thermal efficiency decreases. However, the cruise phase is where the engine is operated most of the time. An increase in OPR during the cruise phase with throttled power is thus favorable. This can be achieved by using a variable core. The power of the engine and the core mass flow are coupled. Thus, for an increase in OPR with reduced air mass flow the choking cross sectional area of the engine (usually at the turbine entry) has to be varied during operation. This inheres the issue of variable core mass flow for the combustion chamber. A combustor concept with the capability of variable air flow at different loadings is thus needed.

- **Contra Rotating Core Architecture**; This technology is focusing on lifting the specific work of the high pressure compressor and turbine (HPC and HPT respectively) by using every blade row available. The commonly used static stator blades are contra rotating to the rotor blades. By doing so, especially the compressor is reduced in size. The core of the engine is building smaller, the part count is reduced and an overall reduction in engine weight can be achieved. Furthermore less cooling air for the turbine is needed, thus increasing the efficiency of the engine.

- **Unconventional Heat Management**; In an engine a lot of waste heat is generated. By using the heat sink capacity of the fuel tank a "lossless" heat exchanging system can be exploited (compared to conventional air-based heat exchanging devices).

- **Innovative Combustion Technologies**; One very promising technology is innovative combustion, where the conventional combustion process is substituted by an unstable combustion process, more precisely a detonation. The basic idea is to implement a detonation based combustion process into an aero engine. This will in turn bring a better thermal efficiency for engines with high OPR, or a fairly good efficiency for intermediate OPR machines, but with a smaller (and thus lightweight) core, as the increase in efficiency is linked to an increase in pressure during the combustion process.

The fourth concept (innovative combustion) is covered in more detail in this thesis. In a detonation based combustor the continuous combustion process of a conventional combustion chamber is replaced by an intermittent detonative combustion sequence. The following section is giving a survey on this topic.

## 3.1 Pulse Detonation Engine - Overview

The most simple way to use detonation based combustion for an aero engine is the Pulse Detonation Engine (PDE). This device is similar to the pulse jet used in the Fieseler Fi 103. Like a pulse jet the PDE does not need any turbomachinery parts (e.g. compressor or turbine) to generate thrust. Its design is consisting only of a straight tube forming the combustor, usually a rotating valve at the closed end (inlet), a fuel injector and a nozzle at the open end (exhaust).
The configuration of a PDE can be in single tube or multi tube arrangement. A multi tube configuration consists of several PDE tubes arranged can-annular around a center axis.
However, for a jet engine application a pure thruster configuration seems not to be applicable. The major problems of a thruster engine configuration would be the lack of bleed air that can be taken out of the cycle to pressurize the cabin or deice the slats. Also a generation of electricity is due to the lack of rotating parts not possible.
To overcome this hurdle, a concept for making use of pulsed detonation can be the replacement of the conventional combustion chamber by a Pulse Detonation Combustor (PDC). By doing so the proposed higher thermal efficiency of the detonative combustion process is combined with standard turbo machinery components. However, several problems of the PDC technology are still present:

- **Detonation initiation**; Problematic for all detonation based combustion processes is the fact that most of the fuels used in aviation do not detonate quite easily (unconventional fuels like $H_2$ are more easily to detonate and are therefore commonly used as surrogate fuel in the literature). A process called deflagration to detonation transition (DDT) is necessary to achieve detonative combustion. Furthermore detonative combustion is operated at a rather high frequency (up to 100 Hz). Thus ignition devices capable of delivering ignition energy at this high frequency are necessary.

- **Complexity of detonation control**; Combined with the problem of detonation initiation, the control of stable detonation processes during transition from design to off design points might be problematic.

- **High peak temperatures**; During the detonation process high peak temperatures occur. Although these temperatures persist only for a few milliseconds, the problem of dissociation of the fuel and formation of pollutant emissions at this high temperatures might occur.

- **Pressure gain**; During the detonative combustion the pressure raises. Sealing of the rotating parts is thus more complex as bleed air can enter into the center of the engine and damage temperature sensitive parts such as discs. Furthermore cooling of the turbine stages is problematic as the pressure ratio of the cooling vents is insufficient to blow out the cooling air.

- **Noise**; The noise level of a pure PDE is extremely high. The authors in [23] give a soundpressure level of roughly 212 dB(!) near the closed end of the tube and around 170 dB further downstream of the tube.
- **Flow intermittency**; As the PDE process is of the intermittent type, the implementation into a steady working machine implies further problems. The compressor is delivering a constant volume flow. During a part of the PDE cycle the tubes are shut from the inflow of the compressor, so that the compressed air has to be stored in some kind of reservoir. Furthermore the turbines are optimized to work in an steady flow environment, so that the turbine efficiency will degrade in an intermittent flow system.

To overcome some of the above mentioned hurdles two main concepts for a PDC are found in the literature. The first one being a static arrangement of detonation tubes, the second one is a rotating configuration.
For the rotating concept the often used terminology of Constant Volume Combustor (CVC) is used. The concept of a PDE is combined with a Wave Rotor (WR). The design of a CVC engine [24–26] consists of a large number of PDE tubes, like small channels, arranged annular around a center axis. Such a device, designed by authors in [27], is shown in figure 3.1a.

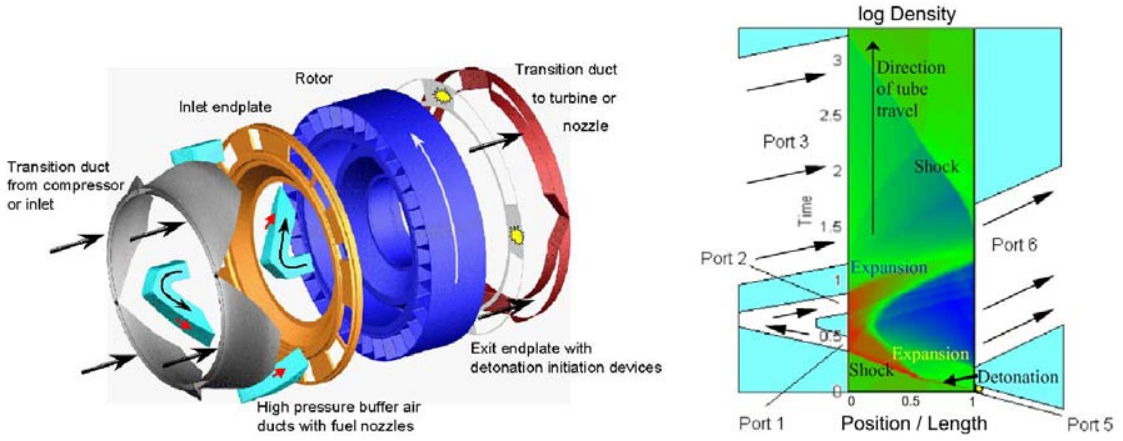


(a) CVC combustor concept (b) Wave diagram

Figure 3.1: Constant Volume Combustor, [25] modified

A wave diagram (figure 3.1b) shows the time history of density inside the rotor, rotating around the center axis.
Considering a tube at the bottom of figure 3.1b, it is filled with fresh reactants on the right side (near Port 5) and pure air on the left (opposite of Port 5). Detonation is initiated through port five, labeled with "Exit endplate with detonation initiation device" in figure 3.1a, by hot gas or any other method (e.g. spark or laser). Due to the detonation a shock wave is formed and travels to the left side of the tube and compresses the fresh air along its path. When the tubes are opening to port six an expansion wave is formed, accelerating the exhaust towards the turbine. When opening to port one the fresh air is pushed by the shockwave into a transition duct. In this duct the fuel is injected to the flow and the so formed fuel air mixture is entering the rotating tubes via port two again. The hot gases are still discharging towards the turbine thus enabling the fresh mixture to enter. As the

tubes open to port three fresh air is entering into the tube pushing the fuel air mixture towards the right side of the rotor. By closing port six a hammer shock is formed thus compressing the fresh air entering. When port three closes the process is repeated again. [24]
The rotation of the device can either be self propelled via aerodynamic forces or set by using magnetic bearings. The advantage of magnetic bearings would be the possibility to adapt the rotational speed to design and off design points.
For the static configuration rotating valves at the inlet of the PDE tubes are used, while the tubes itself are static.
Although CVC seems, due to its homogeneous flow field generated, favorable for application in a gas turbine, the parts needed to build a CVC are more complex compared to the PDE. And as the CVC is rotating, additional bearing (with all necessary systems) have to be installed too. Also the timing of detonation initiation in respect to the rotational speed is more demanding. So the combustion system is building more complex compared to a conventional one.
The most important fact for choosing either CVC or PDE for future aero engines is, beside the efficiency and feasibility of the technology itself, the integration into the rest of the core and thus the flow field for the following turbine.
To solve the problem of unsteady flow generated when using a PDE is the possibility of introducing a phase shift in the firing sequence of the tubes, thus forcing a homogenous flow field downstream the PDE tubes [28, 29].
In the following more attention is paid on the "static" PDE technology as it is more promising due to its simplicity compared to CVC.

## 3.2 Hybrid Turbofan Engine Concept

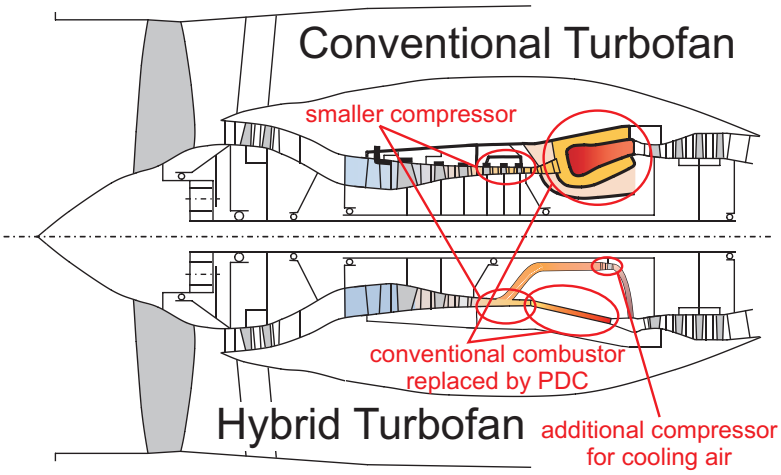


Figure 3.2: Hybrid Turbofan Engine concept (bottom), compared to a two spool turbofan engine (top); based on sketches from reference [3]

The simplest way, inspired by the work of Goldmeer et al. [30], for introducing pulsed combustion, and thus unsteady combustion, into an aero engine, is by replacing the conventional gas turbine combustion chamber by a set of PDE tubes. The detonation process

is pressure gain, so in addition a part of the core can thus be removed (e.g. the high pressure compressor and the part of the turbine that drives the HPC). A schematic diagram of such a hybrid turbofan engine (HTE) is compared to a standard two-spool turbofan engine with booster configuration in figure 3.2.
As shown in figure 3.2 top (base line engine), the fan and booster are driven by the LP turbine. The HPT is only driving a HPC. The engine scheme for the reference engine as well as for the HTE concept is shown in figure 3.3, giving also the labeling for the conditions of state throughout the turbomachine.
This booster configuration is kept for the HTE concept, only the combustor type is changed. To deliver cooling air for the HPT, a fraction of the core air mass flow is further compressed by using an additional small compressor (CAC). This cooling air is used to reduce the exhaust temperature of the PDE by using a mixing chamber.
However, to show the potential of the HTE a generic two-spool engine of the 120 kN (27,000 $lb_f$) thrust class is used as a reference. Table 3.1 is showing the detailed input data that was used to model the engine in GasTurb11 (GasTurb$^{TM}$[31]). The operating conditions were set to represent take-off.

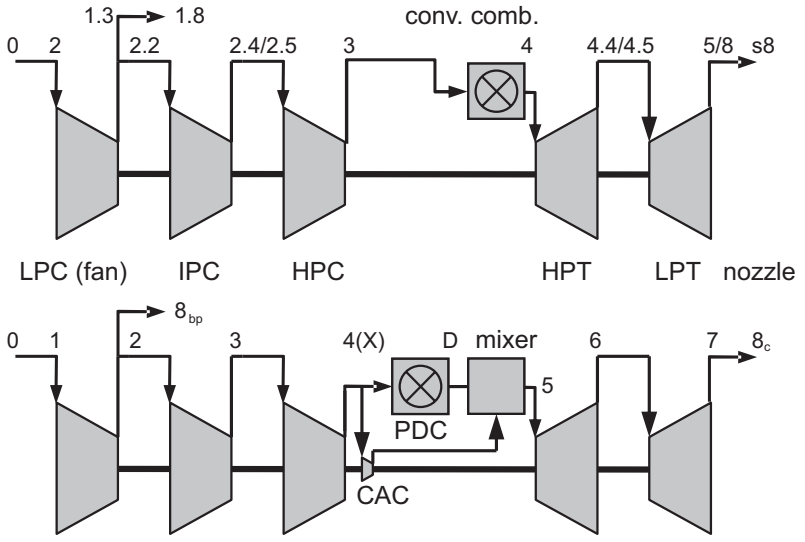


Figure 3.3: Hybrid Turbofan Engine scheme (bottom), compared to a two spool turbofan engine (top); including the necessary labeling for conditions of state of the working fluid; based on sketches from reference [3]

Table 3.1: Input-data for reference case; Validation vs. GasTurb11

| | | | | | | | |
|---|---|---|---|---|---|---|---|
| General Conditions | Altitude | [m] | 0 | Design Input | Rel. Enthalpy of Recirc Bleed | [-] | 1 |
| | Delta T from ISA | [K] | 0 | | HPT NGV Cooling | [-] | 0 |
| | Rel. Humidity | [%] | 0 | | HPT Rotor Cooling Air | [-] | 0 |
| | Mach Number | [-] | 0.25 | | HPT Cooling Air Pump D. | [-] | 0 |
| Design Data | | | | | LPT NGV Cooling | [-] | 0 |
| | Intake Press. Ratio | [-] | 1 | | Rel. Enth. LPT NGV Cooling | [-] | 0.6 |
| | Average core dP/P | | Yes | | LPT Rotor Cooling Air | [-] | 0 |
| | Inner Fan Press. Ratio | [-] | 1.45 | | Rel. Enth of LPT Cooling | [-] | 0.6 |
| | Outer Fan Press. Ratio | [-] | 1.45 | | Rel. HP Leakage to LPT Ex. | [-] | 0 |
| | Core Inlet Duct Press. Ratio | [-] | 1 | | Rel. Fan Overb. Bleed | [-] | 0 |
| | IP Compr. Press. Ratio | [-] | 1.53 | Mass Flow | | | |
| | Compr. Interd. Press. Ratio | [-] | 1 | | Inlet Corr. Flow | [kg/s] | 440 |
| | HP Compr. Press. Ratio | [-] | 14.78 | LPC Efficiency | | | |
| | Bypass Duct Press. Ratio | [-] | 1 | | Isentr. Inner LPC Efficiency | [-] | 0.925 |
| | Turb. Interd. Ref. Press. Ratio | [-] | 1 | | Isentr. Outer LPC Efficiency | [-] | 0.925 |
| | Design Bypass Ratio | [-] | 5.4 | LPC Design | | | |
| | Burner Exit Temperature | [K] | 1600 | | Nominal LP Spool Speed | [rpm] | 4,000 |
| | Burner Design Efficiency | [%] | 100 | IPC Efficiency | | | |
| | Burner Partload Constant | [-] | 1 | | Isentr. IPC Efficiency | [-] | 0.9163 |
| | Fuel Heating Value | [kJ/kg] | 43,124 | HPC Efficiency | | | |
| | Overboard Bleed | [kg/s] | 0 | | Isentr. HPC Efficiency | [-] | 0.8842 |
| | Power Offtake | [kW] | 0 | HPC Design | | | |
| | HP Spool Mech. Efficiency | [%] | 100 | | Nominal HP Spool Speed | [rpm] | 18,000 |
| | Gear Ratio | [-] | 1 | HPT Efficiency | | | |
| | LP Spool Mech. Efficiency | [%] | 100 | | Isentr. HPT Efficiency | [-] | 0.91 |
| | Burner Press. Ratio | [-] | 0.95 | LPT Efficiency | | | |
| | Turbine Exit Duct Press. Ratio | [-] | 1 | | Isentr. LPT Efficiency | [-] | 0.9238 |
| Air System | | | | Nozzle | | | |
| | Rel. Handling Bleed to Bypass | [-] | 0 | | Core Nozzle Thrust Coeff. | [-] | 0 |
| | Rel. HP Leakage to Bypass | [-] | 0 | | Bypass Nozzle Thrust Coeff. | [-] | 1 |
| | Rel. Overboard Bleed | [-] | 0 | | Design Core Nozzle Angle | [] | 0 |
| | Rel. Enthalpy of Overb. Bleed | [-] | 1 | | | | |
| | Recirculating Bleed | | Off | | | | |

For the hybrid engine concept two main strategies are of interest.
The first one is to design a lighter engine with the same performance at a lower OPR (case 1 - **Reduced Engine Weight**). This type of engine would be of interest for short range aircraft applications, as the engine weight is of more importance than the thrust specific fuel consumption (TSFC).
As boundary condition the diameter of the engine as well as the BPR are kept constant (same as reference engine), only the HPC pressure ratio is changed to $\Pi_{mech} = 16.4$. The efficiency of the HPT is changed in accordance with [29] to take into account the loss in turbine efficiency due to the unsteady flow field of the PDC. Furthermore the pressure after the detonation process should not exceed 6,000 kPa (PDC collector) as well as the turbine entry temperature (TET) should be below 1,700 K and the temperature level at the LPT should be limited to 1,350 K to avoid the need for LPT cooling.
For a long range aircraft application the TSFC is of main importance. Therefore an engine with improved TSFC is of interest (case 2 - **More Efficient Engine**). Here the PR achieved via the compressors is kept constant and the thermal efficiency is further lifted by implementing a PDC as additional source of compression ratio. By doing so the weight of the engine is increased, but is of minor importance for such an application. Here too the above mentioned restriction regarding bypass ratio and TET are effective.
Table 3.2 is summarizing the engine data for both HTE concepts.

Table 3.2: Difference in hybrid turbofan cases 1 and 2

| | | | Reduced Engine Weight | More Efficient Engine |
|---|---|---|---|---|
| Fuel | Kerosene Jet A-1 | | | |
| | Lower Heating Value | [kJ/kg] | 43,124 | |
| General Conditions | | | | |
| | Altitude | [m] | 0 | |
| | Delta T from ISA | [K] | 0 | |
| | Relative Humidity | [%] | 0 | |
| | Mach Number | [-] | 0.25 | |
| | Mass Flow Rate | [kg/s] | 456.7 | |
| Design Parameter | | | | |
| | Thrust | [kN] | 122.53 | |
| | Bypass Ratio | [-] | 5.4 | |
| | Fan Pressure Ratio | [-] | 1.45 | |
| | Booster Press. Ratio | [-] | 1.53 | |
| | HP Compr. Press. Ratio | [-] | 7.39 | 14.78 |
| | HP Turbine Efficiency | [-] | 0.872 | |
| Others | | | | |
| | Equiv. Ratio per PDC cycle | [-] | 0.5 | 0.4 |
| | Equiv. Ratio of fresh mixture | [-] | 1 | |

Although the pulsed detonation technology is not new to the aero engine community, the thermodynamics of such an device are not implemented into commercial system level performance tools, like for example GasTurb$^{TM}$. However, a method used by Goldmeer [30] first uses a 1d CFD simulation tool to generate a transfer function. This transfer function is used as an input for the system level performance estimation done in gate

cycle (GateCycle - Heat Balance Software for Power Plant Simulation by General Electric; GE) to represent the thermodynamics of the PDE. By doing so, first the nature of the PDE is analyzed on its own and is than incorporated into the system level tool. With this approach the effort for modeling a HTE is rather high.

In this work therefore a performance model (PM) to estimate the system level performance of a hybrid turbofan engine was developed to give quick results on the performance of these type of engines. The performance model was developed using MATLAB vR2009b (The MathWorks). Standard gas turbine components (inlet, compressor, conventional combustor, turbine and nozzle) are modeled using the standard equations for the variables of state (e.g. see Walsh & Fletcher [32] for details).
For the calculation of specific heat, the polynomials by Burcat and Ruscic [33] are used.
The thermodynamics used to model the PDE process are described in the next section.

## 3.3 Basic operation principle

Before modeling the thermodynamic cycle of a PDE the basic operation will be explained. First of all the difference between deflagration (the usual continuous combustion process used in gas turbine combustion) and detonation is described.
In the process of **deflagration** the fuel is preheated in the flame and thus ignited, so that the fuel air-mixture is burned at velocities in the order of several m/s (usual 1 m/s). During the combustion process the pressure inside the combustor slightly drops (combustion induced pressure drop) [34].
Compared to the standard form of combustion the **detonation** process is more brutal. A shock induced combustion wave propagates at a velocity of 1 to 4 km/s through the reactants, heating them up and finally triggering the combustion. The shock wave is coupled with a thin reaction zone where the actual chemical reaction is taking place. Here the reactants are consumed $10^3 - 10^8$ times faster than by a deflagration process [35]. The chemical reaction is resulting in an energy release thus generating an expansion wave that drives the previously mentioned shock wave [36]. So the detonation is one of the most rapid chemical energy release processes with release rates of up to $10^{10}\,\mathrm{W/m^2}$ [37].

To use detonation in a technical application the previously mentioned detonation tubes are used. The operation of such a device is described in [38] within the following 8 steps (the description is further illustrated by figure 3.4):

a) Detonation initiation at the closed end of the tube, which is filled with reactants only.

b) Propagation of the detonation wave towards the open end at velocity[2] $U_{cj}$. The reactants are heated up within the detonation front. The chemical reaction takes place shortly after the detonation front in the following reaction zone, which is than followed by a Taylor expansion wave. After the detonation process the whole tube is filled with products only.

c) The detonation wave diffracts outside the tube as a decaying shock. An expansion wave is reflected at the open end and travels back to the closed end starting the blow down process. The blow down process is initiated due to an interaction of the reflected shock

[2] velocity at conditions to match the Chapman Jouguet detonation process

wave with the Taylor wave inside the tube. The interaction of both waves accelerates the fluid towards the open end.

d) After the shock interaction the tube contains products at rest and the pressure inside the tube drops below ambient. This "state" lasts 20 times longer than the detonation front needs to travel from closed to open end of the tube (static case).

e) By opening the valves the purging/filling process is triggered. Shock waves are sent into the burned gases by opening the valves. Before reactants are fed to the tube a slug of air is injected to build a contact surface of air/products.

f) This slug of air is called purge-air and is used to prevent pre-ignition of fresh reactants due to the hot burned products. The purging-air than pushes out the burned gases of the tube.

g) Fresh reactants are injected after the purge-air.

h) The tube is than filled with reactants completely and the valve is closed.

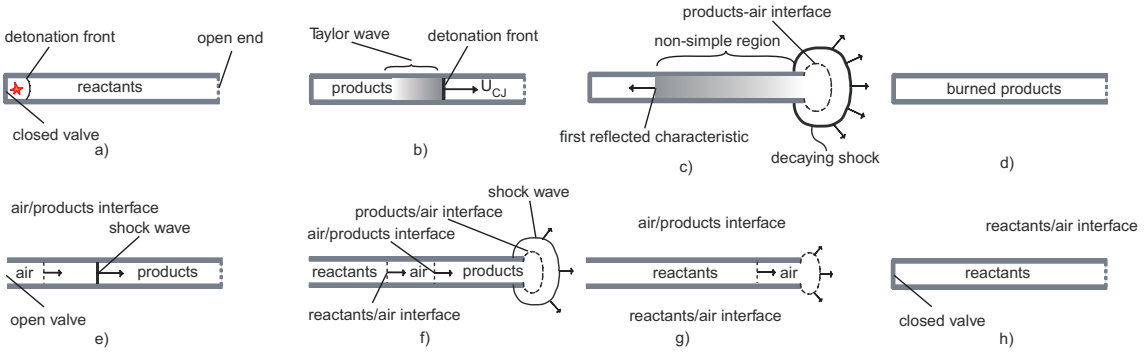


Figure 3.4: Pulse Detonation Engine Cycle [38]

## 3.4 Thermodynamic modeling

From the above given description of the operation of a PDE, the cycle of such a device seems to be rather complicated. To cover the unsteady nature of a PDE, computational fluid dynamics (CFD) is commonly used. The outcome of the CFD computation delivers the input to compute the conditions of state after a detonation cycle to use it for a following cycle analysis (see [30]). However, the authors in [39] used a simple thermodynamic closed cycle analysis to give an easy to follow methodology to calculate the cycle. The detonation wave model commonly used is of the Zel'dovic/vonNeumann/Döring type, which was described by Foa [40] and used by Kentfield [41] for a simple thermodynamic model. In addition usually the following assumptions are made, as stated by Fickett [35]:

- The detonation wave (jump discontinuity) is steady (independent of time)
- planar
- one dimensional
- modeled as a hydrodynamic discontinuity along which the energy release occurs

- all species emerging from the discontinuity are assumed to be in thermodynamical equilibrium

And further the authors in [39] (Heiser & Pratt - H&P) assume that every fluid particle passes through the same detonation process, the expansion of the detonated mixture is isentropic and no energy penalty due to detonation initiation is made.
With these assumptions, a description of the thermodynamic cycle of a pure detonation tube operated at ambient conditions can be done.

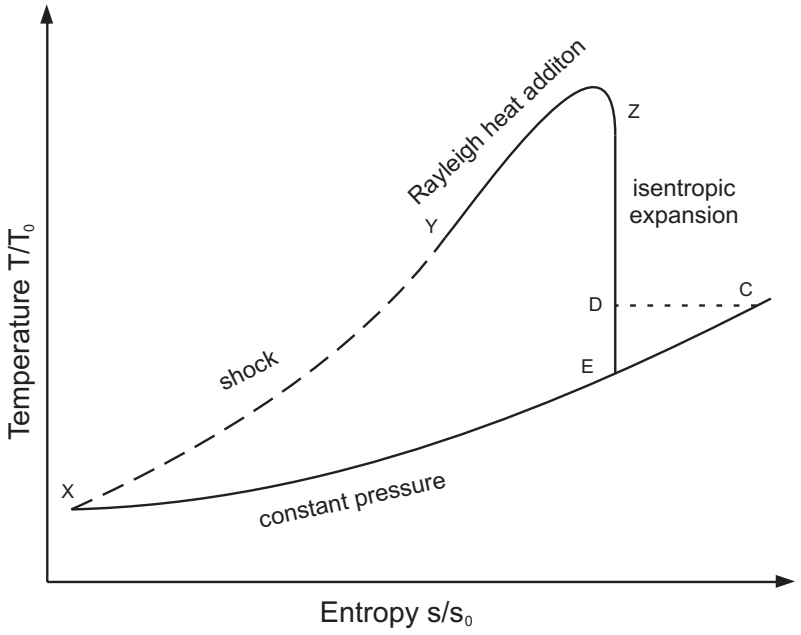


Figure 3.5: Temperature entropy diagram of the detonation process; [41] modified

For the following explanations the model by Kentfield was set as baseline.
The description starts with the explanation for a detonation with a stationary shock wave. A transformation to a moving one is applied afterwards.
The detonation is initiated at state $X$ ($T_X = T_0$, $p_X = p_0$, $M'_x$; for a PDE operating at ambient conditions). A shock wave (with stationary shock front) is formed and compresses the reactive mixture to state $Y$ ($T_Y$, $p_Y$, $M'_Y$). By using the normal shock tables from NACA [42] (more precisely the equations given) the conditions at point $Y$ are computed. As the mixture is heated in the shock front to conditions where combustion can take place the mixture burns at a uniform cross sectional area (the detonation tube), which implies that it is of the Rayleigh type [40]. As the flow, relative to the detonation wave is sonic (see [43]), a temperature drop occurs before state $Z$ ($T_Z$, $p_Z$, $M'_Z = 1$), which is due to the heat addition at Mach 1 (drop in static temperature). This point of state, where the Mach-number is unity and combustion is completed, is known as the Chapman-Jouguet (CJ) point. A detonation process can only be achieved if the conditions are set to match the CJ point.
For the Rayleigh heat addition the relationships for pressure and temperature (see equations A.8 to A.11) are computed and further applied to calculate the state point $Z$ with the boundary condition that the Mach-number is one.
For the transformation of the variables of state from the stationary to the moving shock wave, the Mach-number at the initial condition (state $X$) is computed and deducted form

the Mach-numbers at stations $Y$ and $Z$. As the relations for pressure and temperature are functions of the Mach-numbers, the conditions of state at $Y$ and $Z$ have to be evaluated once more, using the new Mach-numbers for the moving shock wave.
The expansion process of the detonated gases from $Z$ to $D$ ($T_D$, $p_D$; assumed to be isentropic) delivers energy to drive the shock wave from state $X$ to $Y$. The final temperature of the PDE process reached (conditions of state at point $D$), is the same that would be achieved after a constant pressure combustion ($T_D = T_C$). This results when looking at the energy balance of equation 3.1, showing the relation of energy released by the fuel to the temperature increase of the exhaust gases.

$$\dot{m}_f \cdot H_f = \dot{m} \cdot c_p \cdot (T_D - T_X) \tag{3.1}$$

As one can see from figure 3.5, when using a PDE process less entropy is generated compared to the constant pressure combustion commonly used. The final expansion from $D$ to $E$ ($T_E$, $p_E = p_0$) is only of interest for a pure thruster application.

The model developed by Kentfield is enhanced in this thesis by introducing the following modifications:

- The specific heat of the fluids involved is iterated over the detonation process (state $X$ to $Z$). The same specific heat is than applied to the isentropic expansion for driving the shock wave. Hence the isentropic exponent $\gamma$ used in the equations is adapted to match the enthalpy balance. This is also different to the calculations done by the authors in [39]. However, the specific heat for the shock wave, Rayleigh heat addition and isentropic expansion has to be the same so that the equations given by Foa [40] can be used.
  By iterating the isentropic exponent more realistic performance data will result as the temperature increase during the detonation process alters $\gamma$ drastically from its usual initial value of roughly 1.4 at ambient conditions. For the calculation of the specific heat the database by Burcat and Ruscic [33] is used.
- The initial Mach-number at station point $X$ is set as a function of the equivalence ratio (see equation 3.2). This is done as usually gas turbine combustion is modeled as a function of equivalence ratio.

$$M_x = \left[2 \cdot \left(1 + \frac{\gamma + 1}{T_X \cdot c_p \cdot FAR_{st}} \cdot \phi \cdot H_f\right)\right]^{1/2} \tag{3.2}$$

- The equations 10 and 11 of Kentfield [41] were corrected as a misprint in both equations was found.
- The PDE is integrated into a gas turbine cycle to model hybrid engine concepts.

With this new, enhanced mathematical model for the PDE process, more precise estimates of the thermodynamics of a pulse detonation engine, introduced into a gas turbine cycle, can be gathered.
The detailed mathematical expressions to compute the thermodynamics of a PDE can be found in annex A.

Heiser & Pratt [39] have also done system level performance estimations of a hybrid engine concept. However, the authors used an approach of computing only the increase in entropy

of the whole cycle. Thus the temperatures and pressures of the cycle are not computed per se and subsequent all compression and expansion processes are treated with the same efficiency. Furthermore the expansion of the hot gases to drive the shock wave of the PDE process is not separately modeled.
Compared to H&P the performance model developed is more flexible as compression and expansion processes can be modeled in various steps (e.g. LPC, IPC, HPC, ...). Furthermore all conditions of state are computed, thus providing input data for detailed component design.

## 3.5 Evaluation of the PDE code

After developing the performance model, several test cases from the literature were used for a benchmark of the code.
For benchmark of the thermodynamics of the PDE the work by Kentfield was used. As this work is based on a pure thruster application other aspects of the code (compression, expansion, ...) are isolated and only the PDE is validated. Four distinctive cases are given in paper [41]. The input parameters are shown in table 3.3.

Table 3.3: Input data for ideal PDE calculation; cases taken from [41]

| **Test Case** | **Isentropic Exponent** | **Equivalence Ratio** |
|---|---|---|
| 1 | 1.4 | 1.00 |
| 2 | 1.4 | 0.75 |
| 3 | 1.4 | 0.50 |
| 4 | 1.286 | 0.75 |

As Kentfield is computing the cycle with a constant isentropic exponent the PM was adapted accordingly.
Table 3.4 is giving a comparison of the results obtained with the performance model with the results of [41]. The deviation in computation is given in terms of Mach-numbers, pressure ratios and temperature ratios along the detonation process for the four cases. The temperature and pressure ratio for state point $D$ are not given in the paper, so they were derived by using the equations A.32 to A.37 (see annex A for a detailed description). However, table 3.4 on page 27 indicates that the results obtained with the newly developed code, set at constant isentropic exponent, is giving the same results as the model by Kentfield. The largest deviation observed is 3.68 % and the RMS value of deviation, computed over all results obtained, does not exceed 0.57 %.

As the performance of a HTE shell be estimated and Kentfield does only compute a thruster application, other test cases from the literature had to be found. Heiser and Pratt do system level estimations of a HTE [39], with the restriction that they do not evaluate all the conditions at the various state points during the detonation process. This is due to the method used, being based on an entropy evaluation. It was therefore not possible to use the data given for a cycle with losses implied as the compression by retention and mechanical work can not be split.
The computation of the lossless cycle however is less problematic. Therefor the parametric

study of H&P was used for comparison of results of a simple HTE concept. The compression pressure ratio of the HTE was set as function of the temperature ratio ($\psi$) achieved by compression, either mechanical or aerodynamical or a combination of both.
For the parametric study H&P have given the initial Mach-number for introducing a detonation process as a function of temperature ratio. Furthermore the authors in [39] have defined the chemical energy of the fuel as a non dimensional heat $\tilde{q}$. Thus the initial Mach-number by H&P is written as:

$$M_{cj}^2 = (\gamma+1)\cdot\frac{\tilde{q}}{\psi} + 1 + \sqrt{\left[(\gamma+1)\cdot\frac{\tilde{q}}{\psi}+1\right]^2 - 1} \tag{3.3}$$

When using the definition for the non dimensional heat $\tilde{q} = (FAR \cdot H_f)/(c_p \cdot T_0)$ and substituting it into equation 3.3 one will find that the $M_{cj}$ is still a function of the initial temperature of the detonation process (see equation 3.4).

$$M_{cj} = \left\{(\gamma+1)\cdot\frac{FAR\cdot H_f}{c_p\cdot T_0\cdot\psi} + 1 + \left\langle\left[(\gamma+1)\cdot\frac{FAR\cdot H_f}{c_p\cdot T_0\cdot\psi}+1\right]^2 - 1\right\rangle^{\frac{1}{2}}\right\}^{\frac{1}{2}} \tag{3.4}$$

However, equation 3.4 is still differing from the one used in the performance model. To compare the results obtained with the own code (PM) to the results from H&P, first the Mach numbers of both codes were compared. This is mandatory as all subsequent computations rely on the initial Mach-number. Figure 3.6 is showing initial Mach-numbers

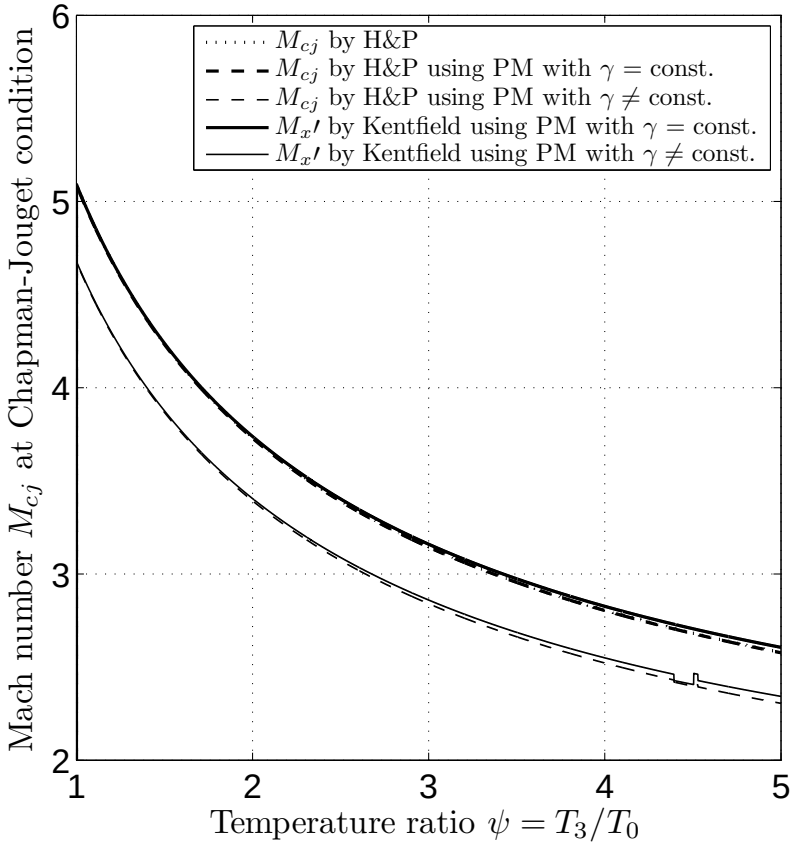


Figure 3.6: Mach-number at initial conditions for different temperature ratios

computed with different mathematical expressions. The dotted line represents equation 3.4 evaluated for a constant isentropic exponent of $\gamma = 1.4$ and non dimensional head $\tilde{q} = 5$ for temperature ratios $\psi$ of 1 to 5.
The bold dashed line represents the same equation with modified energy term, meaning that equation 3.4 was further adapted so that the non dimensional heat will result in a dependency of the equivalence ratio set. However, the equivalence ratio was set accordingly to match $\tilde{q} = 5$, leading to the same result as for the original formula.
Next the definition of the Mach-number used in the performance model, derived from Kentfield [41] (equation 3.2), with $\gamma = 1.4$ and $\tilde{q} = 5$ was computed, represented by the bold solid line.
The results are fairly close to the Heiser & Pratt results, with a slightly higher Mach-number using the Kentfield equation at higher initial temperature ratio. Finally the Mach-number using both definitions was evaluated where the specific heat was set as a function of the temperature ratio over the detonation process (thin dashed line for H&P and thin solid line for Kentfield). Due to the lower isentropic exponent the initial Mach-number is lowered by roughly 0.4 - 0.2. The hump at $\psi = 4.5$ in both cases where $\gamma$ is iterated is due to the used polynomial which actually consists of two polynomials linked at 1,000 K [33].

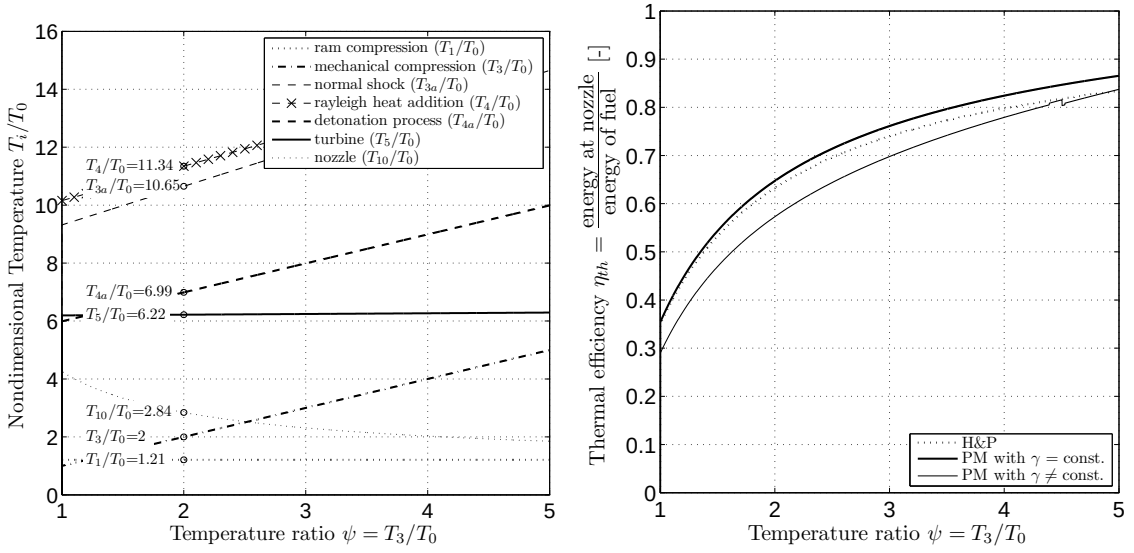


(a) Temperature ratios at $\gamma = const.$

(b) Thermal efficiency

Figure 3.7: Temperature ratios and thermal efficiency as function compression temperature ratio; comparison of Kantfield [41] vs. Heiser & Pratt [39]

Next the thermodynamic cycle of the simple HTE was computed with the own code (PM) and compared to the results of H&P. The input parameters are in accordance with the ideal cycle using a varying $\psi$ from 1 to 5 and a non dimensional heat $\tilde{q} = 5$. No losses are implied. As the temperature ratios are not given in paper [39] directly, they are extracted from the figures given in the paper.
Figure 3.7 is showing the comparison of results. First in (a) the non dimensional temperatures at the various engine positions are presented. It can be seen that the results obtained with the PM model, using a constant isentropic exponent, are in some points different than the results received by H&P. For example the temperature ratio after the

normal shock predicted by the PM ($T_{3a}/T_0 = 10.65$) is higher than by H&P ($\sim 7.4$). The temperature ratio after the heat addition however (PM: $T_4/T_0 = 11.34$) is rather close to H&P ($\sim 10.7$). From figure 3 of H&P [39] one will find that the temperature ratio at the end of the detonation process (the same as for a constant pressure combustion) is 6.99 which was also calculated with the PM. Figure 2 of [39] however shows the end of the detonation process at station point 4 (after the Rayleigh heat addition) with a following expansion in the turbine to 5. This is not possible as the energy needed to drive the shock wave has not been deducted.
Figure 3.7b is showing the thermal efficiency of such an hybrid engine as function of compression temperature ratio. The figure indicates that there is a deviance between the PM and H&P. Generally the performance model (bold solid line) predicts a higher efficiency than H&P (dotted) does. This deviation ranges from 1.5 % at $\psi = 1$ to 3.7 % for $\psi = 5$. However, the technically relevant temperature ratio lies between $\psi = 2$ (deviation 2.3 %) and $\psi = 3$ (deviation 2.8 %).
The performance model is intended to iterate the isentropic exponent as function of temperature increase during the detonation process. By enabling this function in the code the thermal efficiency of the HTE (thin solid line) decreases drastically due to the change in the isentropic exponent (a lower isentropic exponent results in an higher specific heat so that more fuel is necessary to achieve the same increase in temperature). Although the trend of all three curves is alike (showing that the PM is capable of computing the performance of a PDE), the PM shows now a more realistic performance of a HTE, compared to Heiser and Pratt.
Finally the specific thrust (in imperial units for comparison) is evaluated. As reference figure 5 of [39] is used with a flight Mach-number of 1 at an altitude of 11 km. H&P is computing the thrust only as a function of initial Mach-number and amount of heat added, whereas in the performance model uses the classical approach of exhaust nozzle calculation (with a fully expanding nozzle).

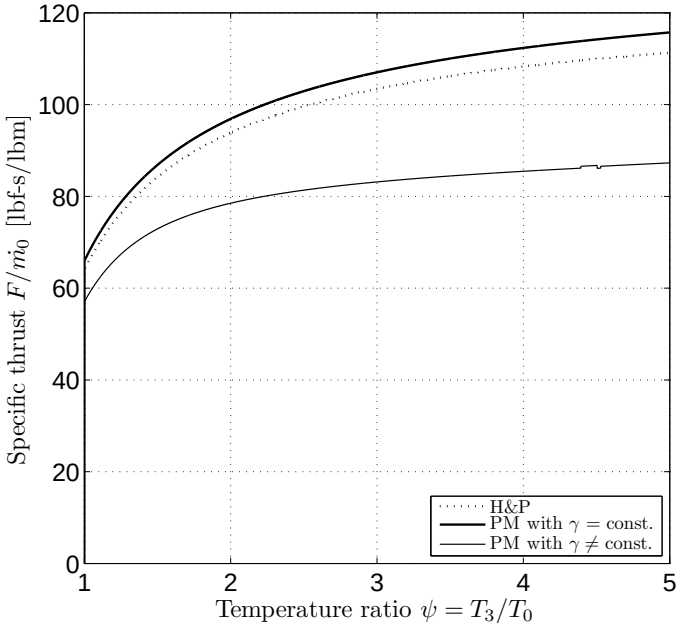


Figure 3.8: Thrust as function of compression temperature ratio

Figure 3.8 is showing a similar trend as figure 3.7b. The results obtained with an iterated

isentropic exponent show a decreased thrust, which is obvious as the thermal efficiency is decreased too.
After using several test cases with different approaches for computation of the performance of a PDE, one can say that the the performance model developed in this thesis is giving reasonable results. Furthermore the PM is iterating the isentropic exponent of the detonation process, which is new compared to the literature, resulting in a more realistic performance of a hybrid turbofan engine.

Table 3.4: Comparison of ideal PDE cycle calculation; comparison against Kentfield [41] for the four given cases

| | $\gamma = 1.4;\phi = 1.0$ | | | $\gamma = 1.4;\phi = 0.75$ | | | $\gamma = 1.4;\phi = 0.5$ | | | $\gamma = 1.286;\phi = 0.75$ | | |
|---|---|---|---|---|---|---|---|---|---|---|---|---|
| | Kentfield | PM | % | Kentfield | PM | % | Kentfield | PM | % | Kentfield | PM | % |
| $M'_X$ | 7.197 | 7.197 | 0.00 | 6.275 | 6.273 | -0.03 | 5.186 | 5.186 | 0.00 | 5.468 | 5.499 | -0.35 |
| $M_Y$ | 1.771 | 1.772 | 0.10 | 1.737 | 1.738 | 0.06 | 1.673 | 1.675 | 0.14 | 2.034 | 2.031 | -0.14 |
| $M_z$ | 0.692 | 0.691 | -0.14 | 0.684 | 0.684 | -0.04 | 0.672 | 0.670 | -0.31 | 0.733 | 0.732 | -.011 |
| $P_Y/P_X$ | 60.400 | 60.266 | -0.22 | 45.800 | 45.741 | -0.13 | 31.200 | 31.216 | 0.05 | 33.500 | 33.281 | -0.65 |
| $P_{0Y}/P_X$ | 331.700 | 331.955 | 0.08 | 239.300 | 239.146 | -0.07 | 143.200 | 148.471 | 3.68 | 270.800 | 267.705 | -1.14 |
| $P_Z/P_X$ | 30.300 | 30.633 | 1.10 | 23.300 | 23.371 | 0.30 | 15.900 | 16.108 | 1.31 | 17.200 | 17.140 | -0.35 |
| $P_{0Z}/P_X$ | 41.700 | 42.152 | 1.08 | 31.800 | 31.954 | 0.49 | 21.600 | 21.763 | 0.75 | 24.000 | 5.144 | -0.44 |
| $T_Y/T_X$ | 11.030 | 11.014 | -0.15 | 8.610 | 8.592 | -0.21 | 6.180 | 6.170 | -0.17 | 5.170 | 8.179 | -0.50 |
| $T_{0Y}/T_X$ | 17.950 | 17.933 | -0.09 | 13.800 | 13.783 | -0.12 | 9.640 | 9.633 | -0.07 | 8.220 | 9.895 | -0.50 |
| $T_Y/T_X$ | 18.090 | 18.116 | 0.14 | 13.890 | 13.880 | -0.07 | 9.620 | 9.646 | 0.27 | 9.950 | 10.654 | -0.55 |
| $T_{0Z}/T_X$ | 19.830 | 19.846 | 0.08 | 15.190 | 15.178 | -0.08 | 10.490 | 10.512 | 0.21 | 10.720 | 7.057 | -0.62 |
| $T_D/T_X$ | 11.375 | 11.375 | 0.00 | 8.781 | 8.781 | 0.00 | 6.187 | 6.187 | 0.00 | 7.057 | 3.749 | 0.00 |
| $p_D/p_X$ | 5.960 | 6.009 | 0.83 | 4.670 | 4.707 | 0.78 | 3.400 | 3.405 | 0.15 | 3.660 | 5.260 | 2.42 |

## 3.6 Validation of the standard gas turbine parts

GasTurb11$^{TM}$[31] is a system level evaluation tool commonly used in the preliminary design stage of aero engines. However, although it is a versatile standard tool, it is not capable of estimating the performance of engines containing a pulse detonation combustor.
In the following it will be used as benchmark for the standard turbomachinery code introduced into the performance model (e.g. compressors, turbines, ...). To check the results obtained with the PM, the generic turbofan engine used as reference, given in table 3.1, was modeled in the PM tool as well as in GasTurb11$^{TM}$.
A further problem that arose from using GasTurb11$^{TM}$was that a turbofan of the booster type was not in the included library. The closest engine configuration was the geared turbofan, set to a gear ratio of one. With the performance model developed during this thesis one will not depend on predefined engine configurations as only the linking between subfunction (turbomachinery components) has to be done to design an engine configuration of interest.
Two similar reference test cases were evaluated. The major results in terms of thrust, fuel consumption and efficiencies of the first generic reference engine are presented in table 3.5. The deviation in results is well below 2 %.

Table 3.5: Results of cycle evaluation for conventinal turbofan engine reference case 1; PM vs. GasTurb11$^{TM}$

| | | **GasTurb11** | **PM** | **deviation [%]** |
|---|---|---|---|---|
| $FN$ | [kN] | 122.07 | 122.53 | 0.38 |
| $w_f$ | [kg/s] | 1.634 | 1.621 | -1.15 |
| $TSFC$ | [mg/Ns] | 13.386 | 13.231 | -0.78 |
| $\eta_{th}$ | [-] | 0.3474 | 0.3537 | 1.63 |
| $\eta_{prop}$ | [-] | 0.3902 | 0.3892 | -0.26 |
| $\eta_o$ | [-] | 0.1355 | 0.1377 | 1.57 |
| $\eta_{core}$ | [-] | 0.5210 | 0.5295 | 1.63 |
| $\eta_{trans}$ | [-] | 0.6620 | 0.6681 | 0.91 |

In addition the conditions of state, defined by temperature and pressure ratios are graphically represented in figure 3.9. It can be seen that the calculation by using the PM is giving the same results as GasTurb11$^{TM}$.
All engine parameters (pressure and temperature) are well matched. The deviation is below 4 %. The compression is very well captured, also the combustion is modeled well. The expansion however is more susceptible to minor variation in the specific heat[3]. The largest deviations can thus be found in the hot exhaust path of the engine.
The second reference case is a slight modification of the first one. The Bypass ratio was lowered as well as the IPC and HPC pressure ratio. Table 3.6 is showing the difference of the two test cases. The graphical representation of the deviation in results (below 3 %) of the PM compared to GasTurb11$^{TM}$can be found in annex B.

[3] GasTurb$^{TM}$is using the polynomials of Gordon and McBride [44], whereas the PM uses the polynomials by Burcat and Ruscic [33]

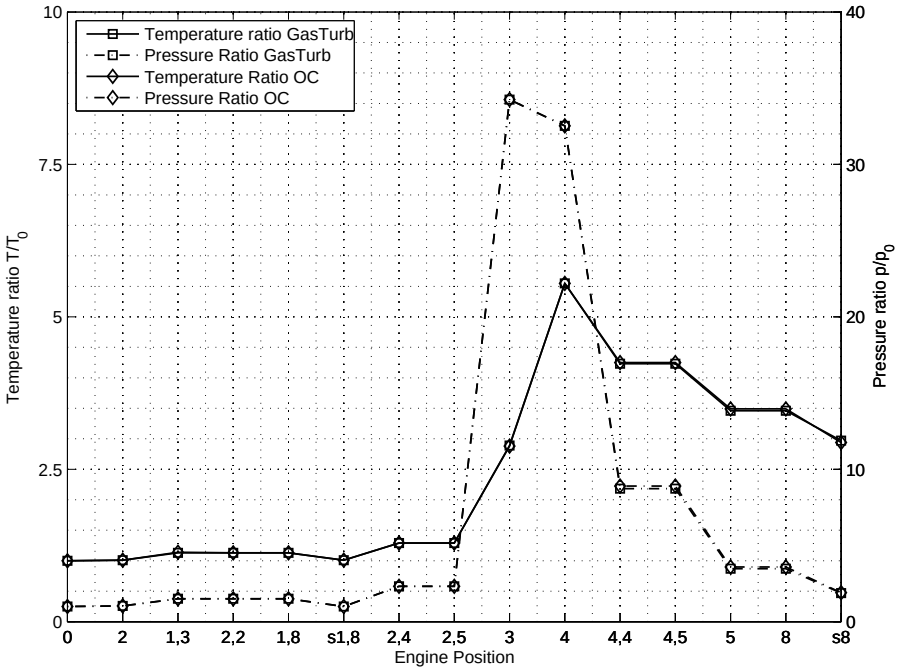


Figure 3.9: Results obtained from computation of reference engine (case 1)

Table 3.6: Difference in test cases 1 and 2 for standard turbofan validation

| | Case 1 | Case 2 |
|---|---|---|
| Bypass ratio | 5.4 | 4.5 |
| IPC pressure ratio | 1.53 | 1.30 |
| HPC pressure ratio | 14.78 | 12.00 |

Based on the low deviance in results obtained with the PM, one can say that the performance model developed is working as expected and will give reasonable results when applying it to an combined cycle engine using conventional aero engine parts. This fact, in combination with the newly developed thermodynamic code for the pulse detonation combustion, gives the possibility of computing the system level performance of a hybrid turbofan engine. This is a very new feature within this thesis since GasTurb11$^{TM}$is not capable of doing so. Furthermore Heiser and Pratt have model the HTE quite simple and Goldmeer is dependent on 1D CFD simulations of the PDE prior computing the system level performance.

## 3.7 Results on hybrid turbofan engine simulation

The previously mentioned two concepts for a hybrid turbofan engine were modeled with the PM code. The boundary conditions are those stated in section 3.2. Recalled, the concepts are:

- **Case1**: lighter engine with same performance at lower OPR
- **Case2**: high OPR engine with improved fuel burn

Detailed information on the parameters set can be found in table 3.2.
Both engine concepts are compared to the generic base line (reference) engine. Therefore the target thrust of the HTE was set to match 122.53 kN. As variable engine parameters the split of the core air mass flows was adapted to match the target thrust. With the split of core air mass flows the following three mass flows are meant:

- **combustion air**: Part of the core air mass flow used for mixing with fuel and following combustion.
- **buffer air**: To prevent pre-ignition of the fresh mixture a slug of air is injected after the blow down process.
- **cooling air**: The exhaust gases are cooled down to an acceptable level for the HPT by mixing them with cooling air from the additional cooling air compressor.

To match the target thrust, for the HTE Case1 (*lighter engine with same performance at lower OPR*), the variable air split was found found to be:

- combustion air: $1/3 \cdot m_{core}$
- buffer air: $1/3 \cdot m_{core}$
- cooling air: $1/3 \cdot m_{core}$

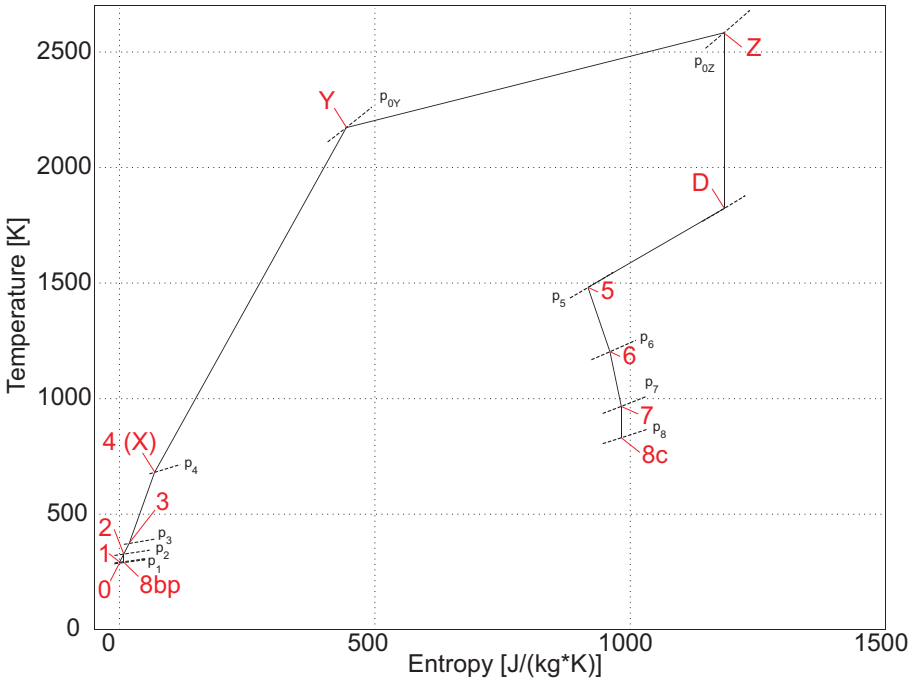


Figure 3.10: Temperature Entropy Diagram of HTE concept 1: lighter engine at same TSFC

For the detonation cycle (using 2/3 of the core air mass flow) the local equivalence ratio for the detonation was set to one. But as half of this air is used as buffer air the global equivalence ratio for the detonation is $\phi = 0.5$. The pressure gain due to the detonation process in this case is found to be $\Pi_{PDC} = 1.6$. Figure 3.10 presents the resulting temperature entropy (T-s) diagram of this concept, indicating that at a lower OPR (26 compared to the 32 of the reference engine) the same thrust can be achieved

when using a PDC instead of a conventional combustor. This can be achieved as at a lower pressure level a rather high temperature level can be reached. Thus the same amount of energy can be extracted from the exhaust gases, although a lower PR was necessary to get to the temperature level. For Case 1 the overall efficiency and the TSFC are slightly inferior compared to the reference engine. However, as the engine is building smaller, in turn reducing the engines weight, this type of power plant would be the best choice for a short range application. For short range aircrafts the weight of the engine is more of interest than its efficiency, so that such a trade off can be of interest.

For the high OPR engine ($OPR = 46.13$ with $\Pi_{mech} = 32.79$, $\Pi_{PDC} = 1.3$), figure 3.11 is presenting the T-s diagram giving a reduction in TSFC of 5.4%. This could be achieved by using the following air split to reach the target thrust:

- combustion air: $0.32 \cdot m_{core}$
- buffer air: $0.47 \cdot m_{core}$
- cooling air: $0.21 \cdot m_{core}$

In this case the global equivalence ratio for combustion will be $\phi = 0.4$.
When comparing both T-s diagrams (figure 3.10 and 3.11) one has to keep in mind that the air mass flows are not constant throughout the whole cycle operation. Furthermore the additional compression of the cooling air mass flow is not shown. This is important as the case for the lighter engine needs more cooling air and thus drains off more power from the HP shaft. This results in a reduced engine efficiency as said above.

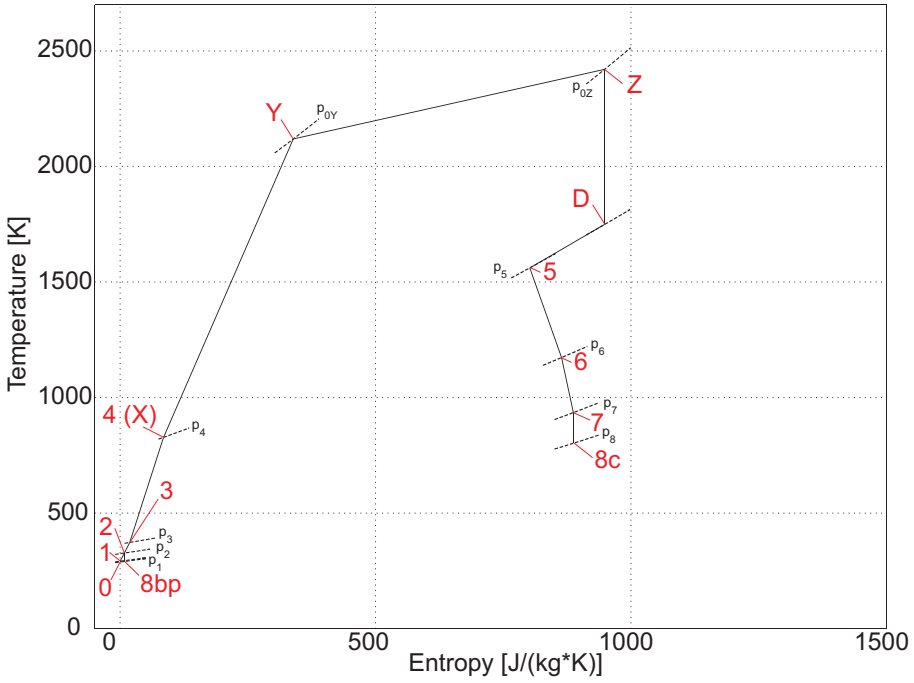


Figure 3.11: Temperature Entropy Diagram of HTE concept 2: reduced TSFC at high OPR

Table 3.8 is summarizing the facts for both engine types. Additional charts on pressure and temperature distribution throughout the engines as well as the T-s diagram of the

reference engine can be found in annex C. Furthermore the conditions of state throughout the PDE process of both engines are also given in annex C. The efficiencies of both concepts can be found in table 3.7 showing as expected a better thermal, core and overall efficiency of the second concept. The propulsive efficiency of both engines is alike but the transfer efficiency (efficiency to drive the LPC - fan) of the first core is slightly higher than the one from the second case.
However, as the model is not optimized for specific missions there is still room for improvement in terms of cooling air and adaption of the BPR. An engine core using a PDC has a higher power density than a conventional one, given the engineer the choice for making use of ultra high bypass turbofan engines.

Table 3.7: Results of HTE efficiency analysis

| | | **Concept 1** | **Concept 2** |
|---|---|---|---|
| $\eta_{th}$ | [-] | 0.3454 | 0.3586 |
| $\eta_{prop}$ | [-] | 0.3892 | 0.3892 |
| $\eta_o$ | [-] | 0.1344 | 0.1395 |
| $\eta_{core}$ | [-] | 0.5344 | 0.5663 |
| $\eta_{trans}$ | [-] | 0.6462 | 0.6332 |

From the discussion of the results achieved for the two engine concepts one can say that unsteady combustion in aero engines is a very promising phenomena. The engines efficiency can be lifted and the TSFC lowered. This implies a reduction in fuel burn and therefore a reduction in pollutant emissions ($CO_2$).
On the other hand there are still some problems to cope with. From the modeling of pulsed detonation a more precise code was developed in this work. However, the computation of the thermodynamics of the PDE process is still idealized and the whole engine model not optimized for specific missions.
Furthermore the feasibility of a PDE introduced into a turbofan engine is still an open question. There are several technical problems to be solved (e.g. sealing, valving, ...).
With this work a next small step on the long journey from TRL 2 to TRL 9 is done.

Table 3.8: Results of HTE performance analysis

| | | | Conventional Engines | Hybrid Engines | | | |
|---|---|---|---|---|---|---|---|
| | | | Reference 1 | Concept 1: less weight | | Concept 2: improved TSFC | |
| | | | | | rel. to Ref. | | rel. to Ref. |
| Performance | Thrust Specific Fuel Consumption | [g/kN/s] | 13.23 | 13.20 | -0.23% | 12.52 | -5.37% |
| | Overall Equivalence-ratio | [-] | 0.33 | 0.33 | 0.00% | 0.32 | -3.03% |
| | Fuel burn | [kg/s] | 1.621 | 1.618 | -0.19% | 1.533 | -5.43% |
| Mass flows | Cor mass flow | [kg/s] | 71.36 | | | | |
| | % combustion air | [-] | 66.7 | 33.3 | - | 31.6 | - |
| | % buffer air | [-] | 0 | 33.3 | - | 47.4 | - |
| | % cooling air | [-] | 33.3 | 33.3 | - | 21 | - |
| Combustor conditions | Inlet pressure | [bar] | 34.7 | 17.35 | -50.00% | 34.7 | 0.00% |
| | Outlet pressure | [bar] | 32.97 | 27.91 | -15.35% | 46.13 | +39,92% |
| | Inlet temperature | [K] | 830 | 681 | -17.95% | 830 | 0.00% |
| | Outlet temperature | [K] | 1600 | 1481 | -7.44% | 1561 | -2.44% |
| Detonation specific Data | Nondimensional heat added | [-] | - | 5.07 | - | 4.06 | - |
| | Peak pressure after Rayleigh heat addition | [bar] | - | 132.36 | - | 193.42 | - |
| | Peak temp. after Rayleigh heat addition | [K] | - | 2584 | - | 2421 | - |
| | PDC Pressure Ratio | [-] | - | 1.61 | - | 1.33 | - |

# Chapter 4

# Advanced aero engines

As the previously described technology of pulse detonation is dedicated for the time frame far beyond 2020, more current technologies with a TRL of three ("*Analytical and experimental critical function and/or characteristic proof-of concept*" [4]) or higher, are of great interest and are intended to contribute largely towards the ACARE targets.
Regarding the core of the engine, with the intention to improve mainly the thermal efficiency, the following concepts are promising [22]:

- **Core cycle improvements by heat management**; using intercooled and recuperative technologies to maximize the use of heat flux available in the engine (e.g. intercooled HPC, recuperative heat from the exhaust nozzle for lifting the combustor entry temperatures) for low OPR engines. Or pure intercooling of the HPC for high OPR engines to improve fuel burn and reduce $NO_x$ emissions.
- **Active core engine system**; adapt the engine core to the operating conditions (improvement at part load conditions). Thus the operability of the engine is enhanced and the fuel burn at off design is lowered.
- **Core engine technology for ultra high bypass (UHB) engines**; having a higher component efficiency for high power density core engines.
- **Innovative combustion technologies**; based on lean combustion configuration. Combustion chambers in single annular combustor design with fuel injection technologies suitable for different OPRs.

These concepts are closely investigated by the project NEWAC and results in four main engine concepts, designed for different thrust classes and missions (short range / long range application). Figure 4.1 is showing the engine concepts and is giving information which technology is implemented (investigated). Starting from the baseline engine (conventional turbo fan), the improvements in terms of thermal efficiency for the four engine types can be found in figure 2.4.
An active-, flow- controlled core will lift the efficiency at the same OPR.
The improvements of the intercooled core can be found when going to higher OPR by cooling the air flow between intermediate and high pressure compressor (less work is needed for compression and thus more work is available at the exhaust), resulting in a higher efficiency at high OPR.
An even better management of heat can be found by introducing an intercooled recuperative engine. In addition to the intercooling of the air flow, the exhaust gases of the core are used to pre-heat the air used for combustion. This will drastically lift the thermal efficiency at lower OPR [6].
In this work the focus is on innovative combustion technologies using new fuel injection technologies.

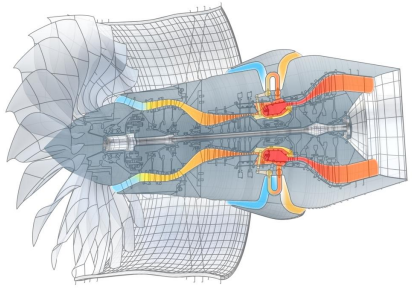

(a) Active Core; active cooling air cooling, smart HPC, PERM[4]combustor technology

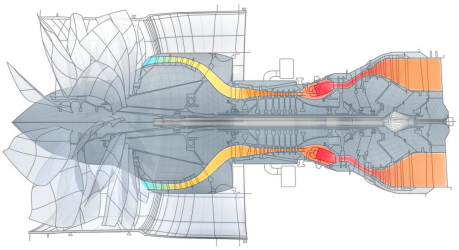

(b) Flow Controlled Core; flow controlled HPC, LDI[4]/PERM combustor technology

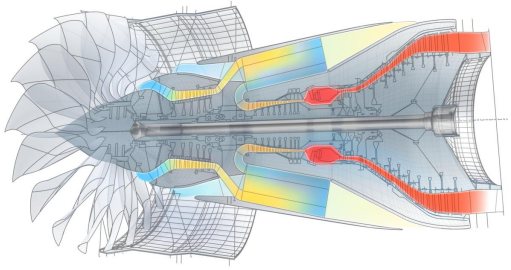

(c) Intercooled Core; intercooler and dedicated ducting, HPC for intercooling, LDI combustor technology

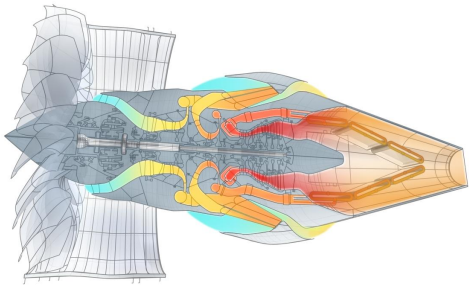

(d) Intercooled Recuperative Aero Engine; recuperator and dedicated ducting, radial HPC, LPP[4]combustor technology

Figure 4.1: Engine Concepts to lift the thermal efficiency [45]

For every engine type, designed for a specific OPR, a specific fuel injection system is used, to minimize pollutant emissions. Figure 4.2 is showing the fuel injection concepts of LPP (Lean Premixed Prevaporized), PERM (Partially Evaporated and Rapid Mixing) and LDI (Lean Direct Injection) as function of OPR and the engine concepts they are used in.

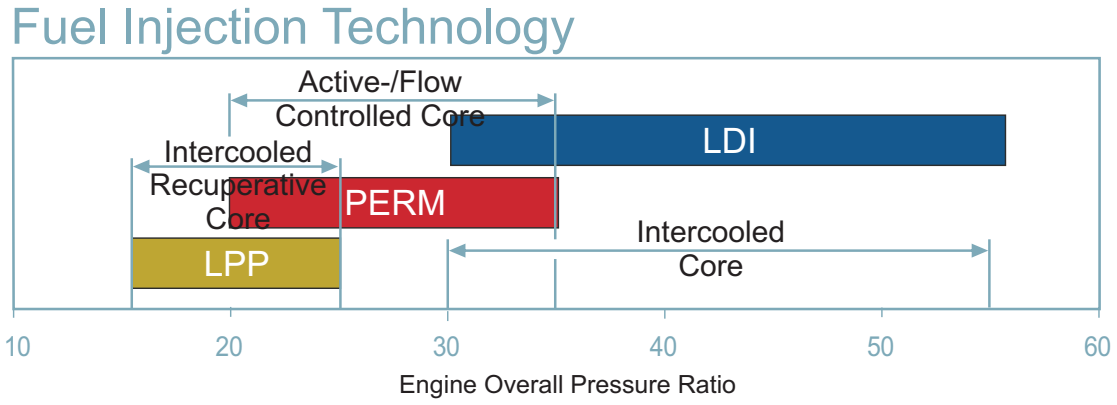


Figure 4.2: Fuel injection technology for different engine concepts as function of OPR; [6] modified

The combustor technologies used in advanced aero engines are accountable for the reduction in pollutant emissions. In the following section a short discussion of historical

[4]A description of the combustion thechnology is given in section 4.4

development, actual combustion systems and possible concepts for the future is given. The explanations are partly derived from [14, 34, 46].

## 4.1 Gas turbine combustor technology

The gas turbine combustor is responsible for the heat addition in the cycle. A fuel air mixture has to be combusted with high efficiency by emitting pollutants at the lowest level possible.

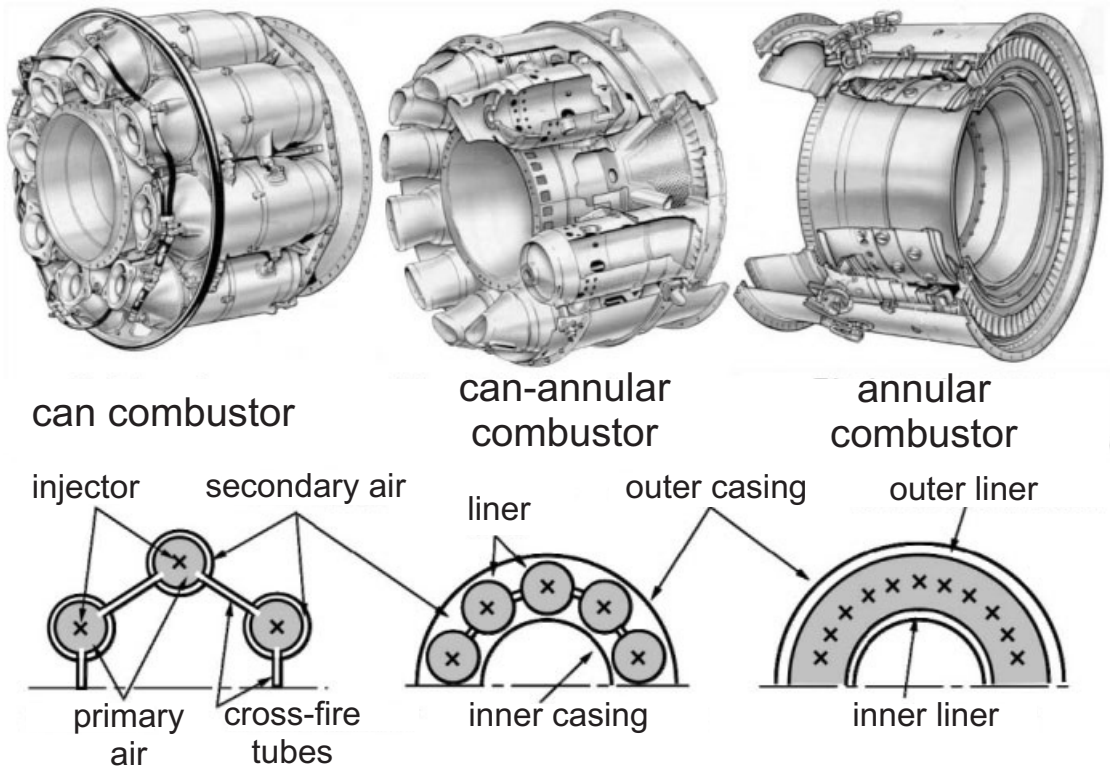


Figure 4.3: Representation of three main combustor concepts; top: conducted combustor concepts; bottom: schematic combustor concepts; [14] modified

By keeping this in mind from the early days of development up till now three main combustor concepts have been designed. Figure 4.3 is giving the schematics of these combustor types. The oldest one is of the can type (**can combustor**), which is basically an arrangement of cylindrical tubes around the center axis of the engine (usually 6 or 8 tubes are used). The effort for development and manufacturing of this type of combustor is rather low, but it is not a lightweight design. A further development of this combustor type, due to increasing OPR, is the **can-annular combustor**. Although these combustors are more compact they have a high stiffness, which is mandatory for increased pressure ratios. Even more compact is the latest combustor design known as **annular combustor**. The design consists of two centrical arranged ring segments, where the inner one is used as thermal shielding and the outer to persist the high pressure in modern aero engines. From an aero dynamical point of view this type of combustor is also giving the lowest aerodynamic pressure drop in the combustion chamber. A fourth type of combustor, actually being a

subspecies of the annular combustor is the **reverse flow type combustor**. A reverse flow type combustor (annular reverse-flow combustor; see figure 4.4) is usually used in small engines (e.g. PW JT-15D turbofan, PWC PT-6A-34 turboprop and Avco Lycoming T-53/55 turboshaft [14]). It offers the advantages of a shorter core and thus a lighter engine. Furthermore the air flows over the combustor liner prior entering the combustion zone. By doing so the liner walls are cooled and the air is preheated thus aiding the combustion process [14, 34] .
The main drawback of such combustors is the rather high surface to volume ratio, which increases the amount of cooling air needed for liner wall cooling. Furthermore the requirement for high combustor efficiency and low emissions lead to a large number of fuel injectors. But as this combustor type is generally small the high number of injectors lead to small devices. This is problematic as small orifices and passages are usually prone to blockage and erosion [34].

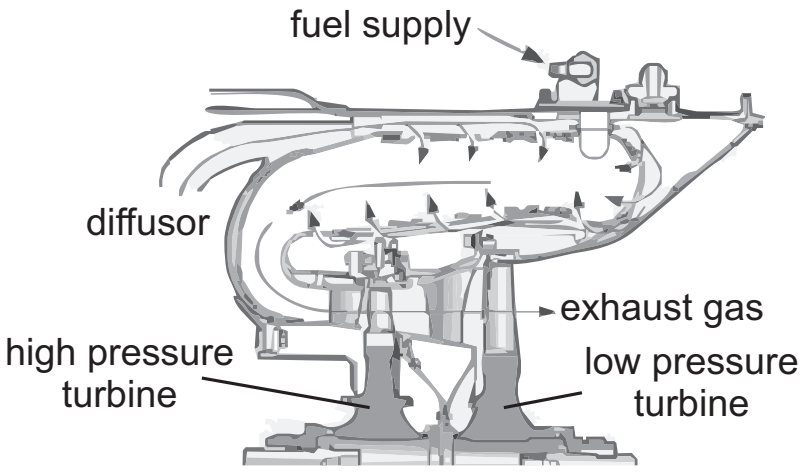


Figure 4.4: Reverse flow type combustor; [14] modified

However, beside the adaption to a specific OPR (leading to the different design strategies), Joos [46] also gives general requirements for modern gas turbine combustors:

- Low level of emissions ($NO_x$, $CO$, $UHC$ and soot)
- High combustor efficiency over the whole operation envelope
- Reliable ignition at all operating conditions (also relight in high altitude)
- Stable operation at rich as well as at lean operating conditions
- low stagnation pressure loss
- Temperature profile at the combustor exit matches the requirements of the turbine
- Low manufacturing and maintenance costs
- Overall dimensions match the engine concept (short, lightweight, small surface area)
- high lifetime
- versatile to various fuels

Nowadays one of the most important requirement for a gas turbine combustor is to produce a low level of pollutant emissions. Section 4.2 is first giving the general aspects on the combustion process in a gas turbine, before showing low emission concepts in section 4.4.

## 4.2 Gas turbine combustion

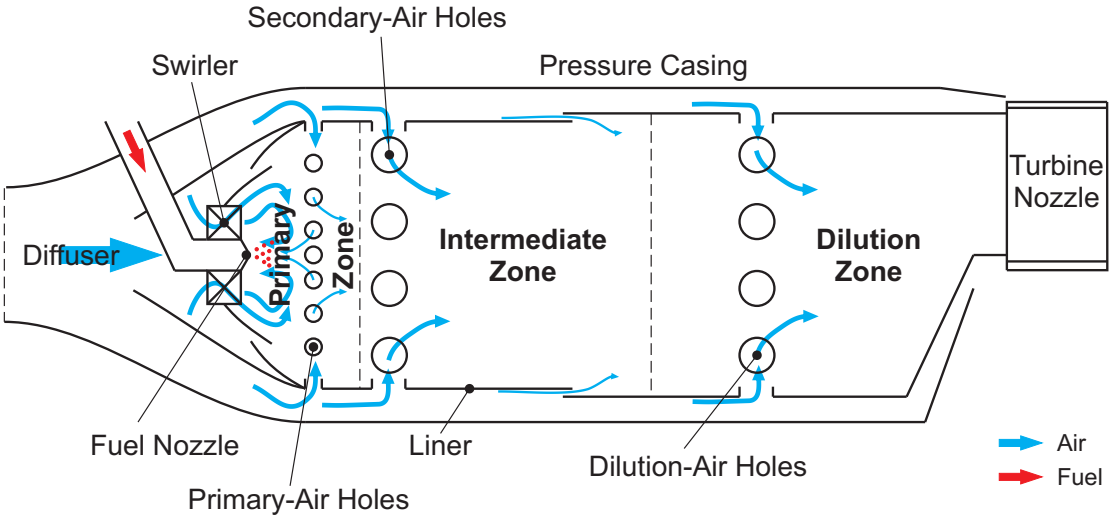


Figure 4.5: Schematic of a conventional combustor; [34] modified

Common to all three combustor types mentioned in chapter 4.1 above is the split of the combustor into separate combustion zones (see figure 4.5). Most important to form a sustainable flame is the **primary zone**. The residence time of the fuel-air mixture in this zone has to be long enough for full combustion. To achieve this the turbulence and temperature of the flow field have to be high. A method to receive this is to form a toroidal flow pattern (recirculation zone). The first combustors used air jets to form such a flow pattern, but in modern engines the injection system is designed to generate a swirl stabilized flame by using air swirlers. By using a swirl stabilized flame the operating range is enhanced and the start up characteristic is improved. In the first combustors typically $10 \div 20\,\%$ of the total air flow was injected via the fuel injection system only. Further air for the combustion process was routed to the flame by orifices in the primary zone.
The largest problem of the primary zone however is the peak temperature during combustion that can reach up to 2500 K so that mainly $NO_x$ is formed. But as also dissociation can occur, the formation of $CO$ and $H_2$ is possible too.
To reduce pollutant emissions formed in the primary zone a second **intermediate** combustion **zone** is introduced. Here the flame temperature is reduced by adding air through orifices in the liner walls. The intermediate products like $CO$ and all kind of unburned hydro carbons ($UHC$) are further oxidized. This is important not only to reduce emissions, but as $UHC$'s can be treated as unburned fuel, a further oxidization will increase the combustor efficiency. As modern engines are designed compact to reduce the weight of the engine, the combustion chamber has to be designed rather short. Therefore in modern gas turbine combustors the classical intermediate zone is not present any more. The compactness of the combustor is not the only reason for removing this zone. More air is nowadays needed for cooling of the combustor liner as the temperature in the combustors are higher.

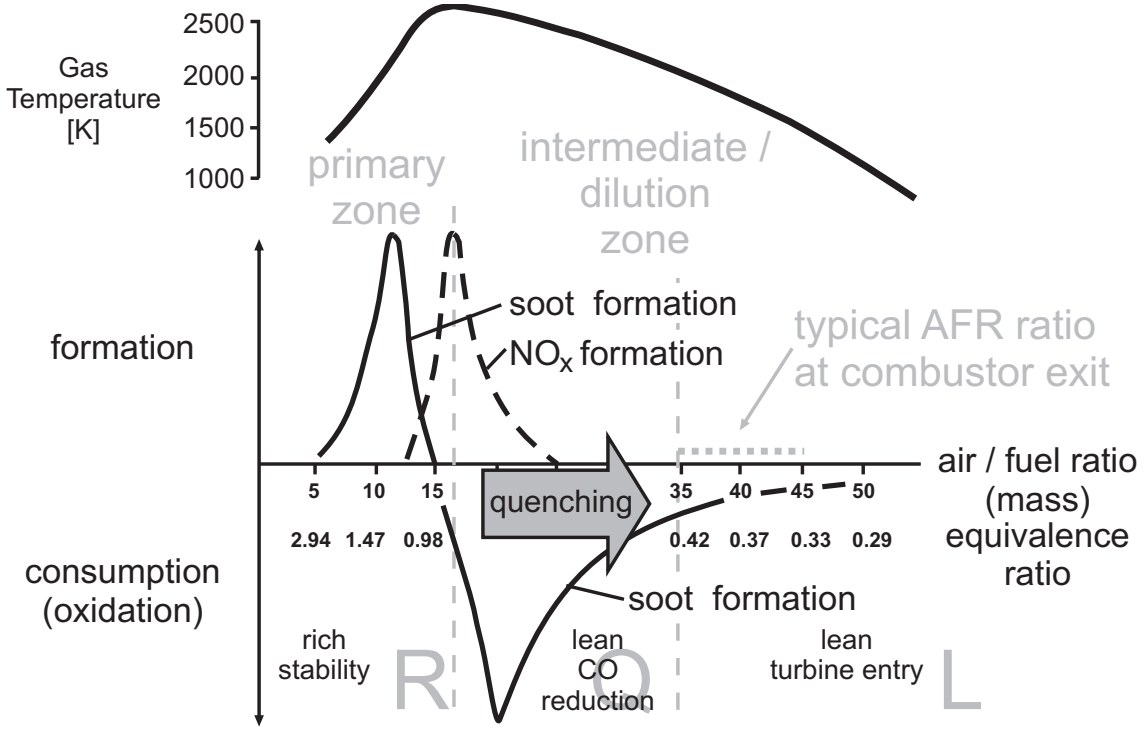


Figure 4.6: Spatial location of emission formation; [46] modified

Finally at the combustor exit a **dilution zone** is located to set the temperature profile for the turbine. A pattern of orifices is defining the overall temperature distribution factor (OTDF) and the radial temperature distribution factor (RTDF). The purpose of both factors is to specify the temperature profile that should be homogenous in circumferential direction (OTDF - no hot spots) and well set in radial direction (RTDF). For the RTDF the temperatures at hub and tip of the following turbine stage should be low to reduce the thermal load. At mid span the temperature is set to the maximum allowable temperature the vanes can withstand with an acceptable life time. Figure 4.6 is showing the formation of emissions as function of the above mentioned combustion zones as well as of the air-fuel-ratio in the specific zones. The figure shows that the formation of emissions is mainly done in the primary zone and any action taken to reduce pollutants can only be done by a well designed combustion process. In section 4.4 some concepts for low emission combustors are presented.

## 4.3 Fuel injection technology

Besides the subdivision of the combustor into several zones, the injection technology used is of importance. The combustor efficiency as well as the formation of pollutant emissions are effected by the selected injection system. Two main technologies are used for injection in common gas turbine engines. The first, being the most simple technology, is to make use of pressure swirl atomizers. With this design the fuel is injected at high pressure via a small orifice into the primary combustion zone. Although the design is mechanically simple, the small orifices pose the risk of getting blocked by contaminants in the fuel. The main drawback with this type of injectors however is that the injected mass flow is

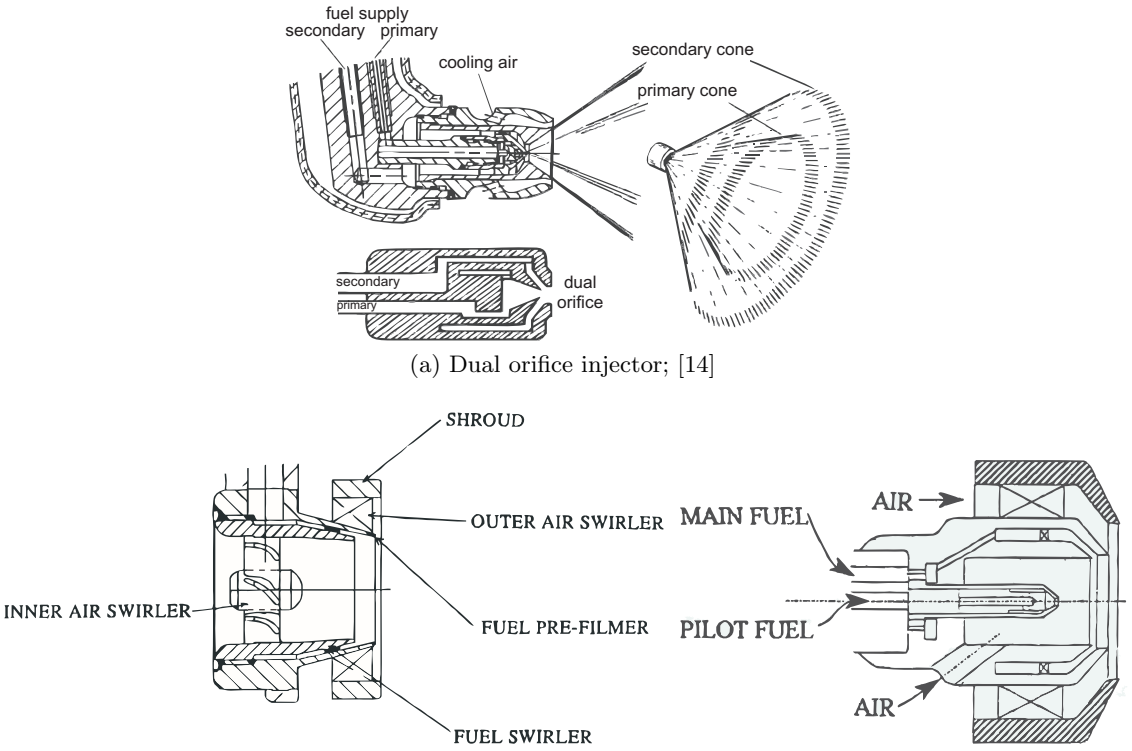


(a) Dual orifice injector; [14]

(b) Air blast injector; [34]

(c) Piloted air blast injector; [34]

Figure 4.7: Fuel injector types

quadratic proportional to the pressure delivered by the fuel pump. For doubling the fuel mass flow a fourfold in fuel pressure is necessary. To improve the concept first instead of one orifice, an injector using two orifices was designed. However, the mechanical design is more complex. To overcome the general disadvantage of high fuel pressure, the air assisted fuel injector and air blast atomizer were developed. The kinetic energy needed to atomize the fuel is here delivered by the air flow from the compressor so that the fuel system is now operating at lower pressures. With the air blast atomizer the liquid fuel is injected onto a pre-filming surface first. The air flow, usually a swirling one, is entraining the film and finally atomizes the fuel. With this technology soot formation is vastly suppressed so that the temperatures at the combustor liner, especially at the primary zone, are lowered (no radiation of the soot particles). However, at part load, where the air is having lower kinetic energy, the atomization is not as good as at full load. To increase the part load performance of air blast atomizers, the pilot assisted air blast atomizer was introduced, where a pressure atomizer, as pilot stage, is used for base load operation. Nowadays the pilot stage is integrated into the air blast system thus building smaller and simplifying the fuel system. Figure 4.7 is showing all three mentioned concepts.

## 4.4 Low Emission Concepts (LEC)

As the combustion chamber is the only contributor to pollutant emissions, the combustion process has to be designed to reduce emissions without influencing the functionality of the device. Whereas figure 4.5 has shown the formation of emissions as function of the spatial location inside the combustion chamber, figure 4.8 shows qualitatively the emission levels

of a gas turbine combustor as function of the equivalence ratio $\phi$ (defined as the actual to the stoichiometric fuel-to-oxidizer ratio).
Major importance in terms of emissions is dedicated to $NO_x$. The main problem with $NO_x$ is its impact on formation of ground-level ozone. Furthermore it is harmful to the mucosa membrane and the respiratory system [46]. As figure 4.8 indicates, a formation of $NO_x$ can be limited significantly when operating the combustor at the lean operating range.

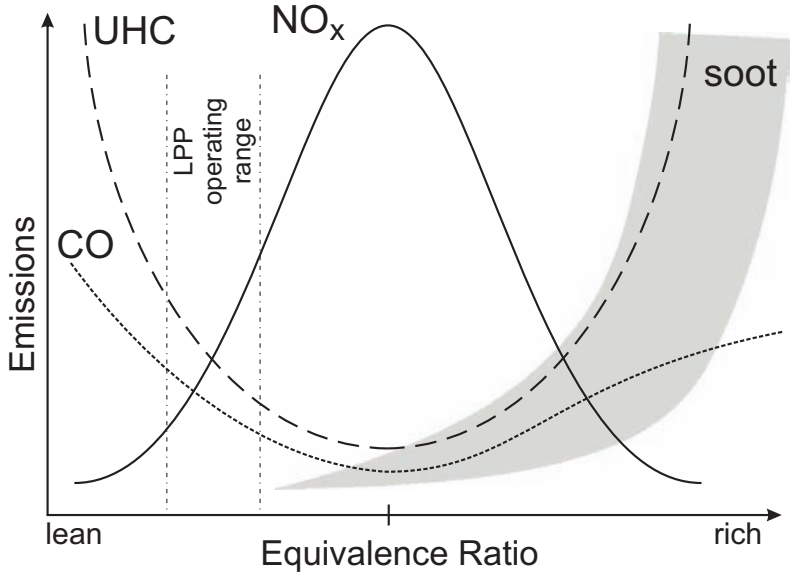


Figure 4.8: Emissions of gas turbine combustors as function of equivalence ratio

This is mainly due to lower temperatures of the flame (reduction in thermal $NO_x$). The discussion above leads to the main three drivers for environmentally friendly combustors:

- lean combustion
- lower flame temperature
- staged combustion (rich-lean combustion zones)

Lean combustion and low flame temperature are closely related to each other. A fuel-air mixture operated at the lean region lowers the flame temperature. This is due to the fact that the reaction rates at $\phi = 1$ are at a maximum, so that the heat release per volume is a maximum too. Thus, as $NO_x$ is formed exponential with an increase in flame temperature, this pollutant can be reduced by lowering the flame temperature. A homogeneous mixture of fuel is mandatory to avoid hot gas streaks and receive a lean combustion throughout the flame. Three concepts are mainly dealing with lean combustion. **LPP** (Lean Premixed Prevaporized) and **PERM** (Partially Evaporated Rapid Mixing) are used for liquid fuels, whereas **DLE** (Dry Low Emission) uses gaseous fuels. The difference in LPP and DLE is the physical condition of the fuel at injection. Nevertheless are both technologies operated in the very lean combustion domain. PERM is similar to the LPP technology, but here the fuel is not fully evaporated thus avoiding the possibility of flashback.
Regarding staged combustion mainly **RQL** (Rich Burn Quick Quench Lean Combustion) and **LDI** (Lean Direct Injection) are used to reduce emissions. For RQL the primary zone

is operated in a rich region to receive a stable flame and guarantee complete combustion of the fuel. The following second combustion zone is operated in the lean domain so that by adding secondary air for quenching, the formation of $NO_x$ at $\phi = 1$ is suppressed. This also implies that the primary zone is uncooled, making it necessary to use special materials and coatings to reduce wall temperatures. LDI on the other side is using a different methodology. The injection system is built as a matrix of several sub injectors. A radial and circumferential pattern of a large number of small injectors is generated. By injecting the fuel in this way the residence time in the primary zone can be reduced so that $NO_x$ formation is suppressed as the combustor itself is shortened. Due to the large number of small injectors the fuel system is more complex compared to conventional fuel systems.

One of the most promising concepts with the largest potential of reducing emissions is the LPP concept. However, the largest drawback of this technology is that LPP combustors tend to get unstable. For the investigation of unsteady combustion phenomena, the LPP technology is eligible. Therefore this thesis focus on this topic and a more detailed description of the technological challenges and hurdles will be given.

## 4.5 LPP combustor technology

For lean injection it is important that the fuel is premixed with the air to form a uniform mixture that will burn lean all over the flame. When using liquid fuels it is therefore mandatory that the fuel has time to first evaporate and then to mix with the combustor air to provide a uniform equivalence ratio within the entire mixture. The basic concept of a LPP combustor to form such a uniform mixture is shown in figure 4.9a. In addition the figure also shows the control range of such a combustion chamber. A sketch of an actual built LPP injector system, from Rolls-Royce Deutschland, is given in figure 4.9b

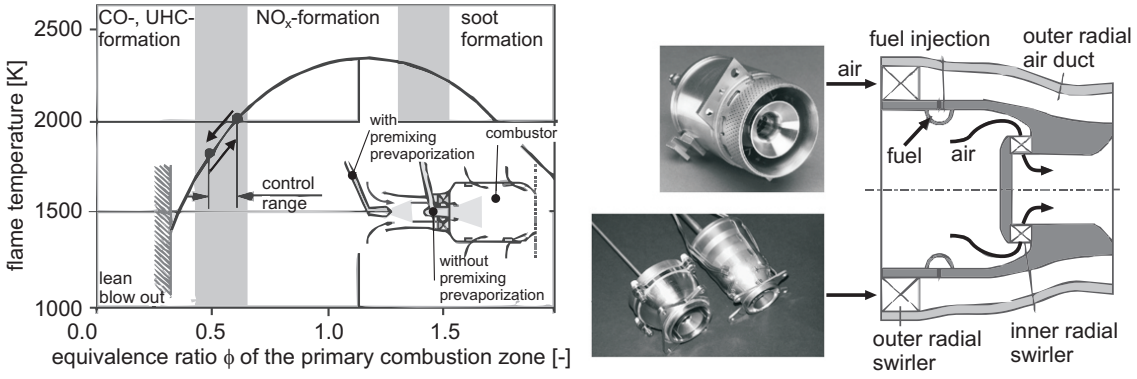


(a) Basic concept of LPP combustion technology (b) LP(P) burner by Rolls-Royce Deutschland

Figure 4.9: LPP combustor technology; [46] modified

It can be seen that the fuel is injected upstream of the combustor interface so that evaporation and mixing can take place.
By doing so a major drawback of this system gets evident. Inside the injector, in the so called premixing tube (or air duct as labeled in figure 4.9b), a highly combustible mixture is formed that is susceptible to auto ignition or flashback.

The length of the premixing tube as well as the velocity of the flow inside the tube are thus of great importance. Furhtermore the risk of auto ignition gets more and more pronounced the higher the OPR of the engine is [34]. Therefor LPP combustors are intended to be operated at rather low OPR's (see figure 4.2). The risk of flashback can be reduced by lifting the velocity of the flow. However, by doing so the time to form a homogeneous mixture might be insufficient. At the present there is now LPP system working that is fully prevaporizing. Thus homogeneous premixing of fuel with air is limited.
Beside the risk of auto ignition and flashback, LPP injectors are subject to combustion instabilities, favored due to the operation near the lean blow out limit.
To stabilize the combustion process, usually pilot burners are used. The hot exhaust gases of the pilot flame stabilizes the lean operating LPP injectors. Beside the stabilization effect, the pilot burners are also used for staged combustion. At part load only the pilot stage is active whereas at full load all injection modules are supplied with fuel. Such a staged operation, in respect to the production of $NO_x$, is shown qualitatively in figure 4.10.

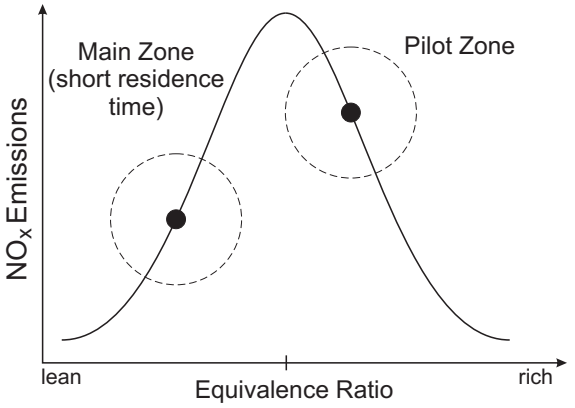


Figure 4.10: Design point for main burner and pilot stage of the LPP concept

Although more $NO_x$ is formed in the pilot flame, beside the stabilizing effect of the pilot burner, the burning of $CO$ and $UHC$ throughout the whole combustor is enhanced. For the LPP concept the pilot stage is used as a separate group of injectors, like for the double annular combustor or axial staged combustor concept. This adds weight to the engine and lifts the complexity (especially for the fuel supply).
A system investigated, where the pilot stage is integrated into the main burner is the twin annular premixing swirler (TAPS) concept used in the Tech56/CFM or GE90 engines [46] (here the fuel is premixed but not fully pre-vaporized in the injector).
However, LPP combustors are, despite the intention to stabilize the flame with the help of pilot burners, still subject to combustion instabilities.

# Chapter 5

# Aspects of combustion instabilities

In this chapter the basic mechanism involved in flame stability will be presented.
Therefore the basic reaction mechanism are first described, by using the methodology of [46], followed by the constraints for successful continuous ignition of the fresh fuel-air mixture, using [47]. Based on these survey the aspects of flame stability are presented. Subsequently the physics of combustion instabilities are shown and described on a simple model (Rijke tube) and an advanced combustion chamber technology (LPP combustor).

## 5.1 Reaction mechanism

A combustion process is a chemical reaction where the aerial oxygen reacts with the fuel. The products of this reaction are the exhaust gases.

$$\begin{gathered} \text{fuel} + \text{air} \;\rightleftarrows\; \text{exhaust gases} \\ \nu_A \cdot [A] + \nu_B \cdot [B] + \ldots \underset{k^r}{\overset{k^f}{\rightleftarrows}} \nu_E \cdot [E] + \nu_F \cdot [F] + \ldots \end{gathered} \tag{5.1}$$

$$\sum_{i=1}^{l} \nu_i \cdot P_i = 0 \tag{5.2}$$

With $\nu_A, \nu_B, \ldots$ being the stoichiometric coefficients (number of moles) of precursors $A, B, \ldots$ and $\nu_E, \nu_F, \ldots$ for the products $E, F, \ldots$ respectively. Furthermore $k^f$ is used to describe the forward reaction and $k^r$ is giving the reverse reaction.
For the reaction rate the following approach is used

$$\frac{\partial c_i}{\partial t} = -k \cdot \prod c_i^{a_i} \tag{5.3}$$

where $\partial c_i / \partial t$ represents the change in concentration of a substance $c_i$ with time, $k$ is an empirical factor and the exponent $a_i$ denotes the order of the reaction. Thus the forward reaction of substance $[A]$ from equation 5.1 can be written as

$$\frac{\partial [A]}{\partial t} = -k^f \cdot [A]^a \cdot [B]^b \cdot [C]^c \ldots \tag{5.4}$$

The minus sign is used as during the reaction the substance $[A]$ is consumed.
For the reverse reaction one can write

$$\frac{\partial [A]}{\partial t} = k^r \cdot [D]^d \cdot [E]^e \cdot [F]^f \ldots \tag{5.5}$$

For a reaction at chemical equilibrium the forward and reverse reaction proceed identical.

$$\frac{\partial[A]}{\partial t} = -k^f \cdot [A]^{|a|} \ldots + k^r \cdot [D]^d \ldots \tag{5.6}$$

$$k^f \cdot [A]^{|a|} \cdot [B]^{|b|} \cdot [C]^{|c|} \ldots = k^r \cdot [D]^d \cdot [E]^e \cdot [F]^f \ldots \tag{5.7}$$

$$\frac{k^f}{k^r} = \frac{[D]^d \cdot [E]^e \cdot [F]^f}{[A]^{|a|} \cdot [B]^{|b|} \cdot [C]^{|c|}} = K_c \tag{5.8}$$

The quotient of $k^f/k^r = K_c$ is known as the rate of reaction.

## 5.2 Thermodynamics of the reaction

Using the first law of thermodynamics for the reaction

$$\mathrm{d}U = \mathrm{d}Q - p \cdot \mathrm{d}V \tag{5.9}$$

with the definition for the reversal heat

$$\mathrm{d}S \geq \frac{\mathrm{d}Q}{T} \tag{5.10}$$

one will find

$$\mathrm{d}U - p \cdot \mathrm{d}V - T\mathrm{d}S \leq 0 \tag{5.11}$$

In equation 5.11 the equal sign stands for reversible processes, whereas a irreversible process is determined by an unequally character. For systems at equilibrium the above given equation can thus be written as (*Gibbs Equation*)

$$\mathrm{d}U - p \cdot \mathrm{d}V - T\mathrm{d}S = 0 \tag{5.12}$$

By making use of

$$T\mathrm{d}S = \mathrm{d}(T \cdot S) - S\mathrm{d}T \tag{5.13}$$

it follows that

$$\begin{aligned} \mathrm{d}U + p \cdot \mathrm{d}V - \mathrm{d}(T \cdot S) &= 0 \\ \mathrm{d}(\underbrace{U - T \cdot S + p \cdot V}_{U+p\cdot V-T\cdot S=H-T\cdot S\equiv G}) - V \cdot \mathrm{d}p + S\mathrm{d}T &= 0 \end{aligned} \tag{5.14}$$

with $G$ being the Gibbs Enthalpy. To reach a chemical equilibrium the pressure and temperature must not change. With these restriction applied to equation 5.14 it follows that

$$\begin{aligned} V \cdot \mathrm{d}p &= 0 \\ S \cdot \mathrm{d}T &= 0 \end{aligned}$$

and thus

$$(\mathrm{d}G)_{p,T} = 0 \tag{5.15}$$

From equation 5.15 it follows that at chemical equilibrium the Gibbs energy reaches a minimum. For multi-component systems the minimum for the Gibbs Energy can be written

as the gradient of the free Enthlpy $\Delta G$ with respect to the amount of substance $\Delta n$ (see figure 5.1).

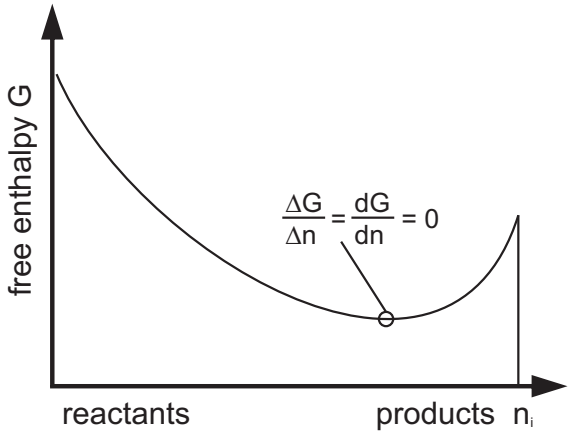


Figure 5.1: Free enthalpy of a chemical reaction

$\Delta G/\Delta n$ is identified as the chemical potential. For a multi-component system it is written as the partial deviation of the free enthalpy $G$ with respect to the amount of substance $n_i$.

$$\mu_i = \left(\frac{\partial G}{\partial n_i}\right)_{p,t,n_j} \tag{5.16}$$

To compute the chemical potential of a substance one can now use the definition for the Gibbs enthalpy and split it into shares with constant pressure and temperature respectively.

$$\mathrm{d}G = \mathrm{d}H - d(T \cdot S) = \mathrm{d}U + d(p \cdot V) - \mathrm{d}(T \cdot S) \tag{5.17}$$

$$\mathrm{d}G(p,T) = (\mathrm{d}G)_T + (\mathrm{d}G)_p \tag{5.18}$$

With the constraints for constant temperature it follows that $\mathrm{d}T = 0$ and thus $\mathrm{d}U = 0$. Furthermore to receive equilibrium $p \cdot \mathrm{d}V - T \cdot \mathrm{d}S = 0$. Thus the free Gibbs energy can be computed as

$$(\mathrm{d}G)_T = V \cdot \mathrm{d}p \tag{5.19}$$

For the temperature dependence $(\mathrm{d}G)_T$ the standard enthalpy $G^0(T)$ can be used. Thus, for an ideal gas ($p \cdot V = n \cdot R_m \cdot T$), one can write

$$G(T,p) = G^0(T) + \int_{p^0}^{p} V \cdot \mathrm{d}p' = G^0(T) + \int_{p^0}^{p} n \cdot R_m \cdot T \cdot \frac{\mathrm{d}p'}{p} = G^0(T) + n \cdot R_m \cdot T \cdot ln\left(\frac{p}{p_0}\right) \tag{5.20}$$

The chemical potential can be computed by forming the partial derivative of equation 5.20 in respect to the species $n$.

$$\mu_i = \frac{\partial G}{\partial n} = \mu_i^0(T) + R_m \cdot T \cdot \ln\left(\frac{p_i}{p^0}\right) \tag{5.21}$$

The equation for the Gibbs energy (equation 5.14) as function of pressure, temperature and substances $G = G(p, T, n_i)$ can thus be written as

$$\mathrm{d}G = V \cdot \mathrm{d}p - S \cdot \mathrm{d}T + \sum \left(\frac{\partial G}{\partial n_i}\right)_{p,T,n_j} \cdot \mathrm{d}n_i \tag{5.22}$$

With the previously stated constrain of $\sum \nu_i \cdot P_i = 0$ and for $(\mathrm{d}G)_{T,p} = 0$ (equilibrium) it follows that

$$\sum \mu_i \cdot \mathrm{d}n_i = 0 \tag{5.23}$$

At equilibrium the concentration of the substances is equal to the moles of the species and thus $\nu_i = n_i$. Therefore equation 5.23 can be written as

$$\sum \nu_i \cdot \mu_i = 0 \tag{5.24}$$

Subsequent equation 5.20 can be transformed to

$$\begin{aligned} \sum \nu_i \cdot \mu_i + R_m \cdot T \cdot \sum \nu_i \cdot ln\left(\frac{p_i}{p_0}\right) &= 0 \\ \sum \nu_i \cdot \mu_i + R_m \cdot T \cdot ln \underbrace{\prod \left(\frac{p_i}{p_0}\right)^{\nu_i}}_{K_p} &= 0 \end{aligned} \tag{5.25}$$

with $K_p$ the low of mass action. Similar for the concentration, when an ideal gas is assumed, one can write

$$K_c = \prod \left(\frac{c_i}{c_0}\right)^{\nu_i} \tag{5.26}$$

due to the fact that the partial pressure of the substances is equal to the concentration of species of the mixture.
Evaluation of equation 5.25 and using $K_c$ instead of $K_p$ will give

$$R_m \cdot T \cdot ln(K_c) = -\underbrace{\sum \nu_i \cdot \mu_i^0}_{\Delta_R \bar{G}^0} \tag{5.27}$$

with $\Delta_R \bar{G}^0$ being the standard enthalpy change of formation

$$K_c = e^{-\frac{\Delta_R \bar{G}^0}{R_m \cdot T}} \tag{5.28}$$

The above given $K_c$ is equivalent to the previously defined rate of reaction for forward and backward reaction. Generally the terminology of Arrhenius is used.

$$k = A \cdot e^{-\frac{E_a}{R_m \cdot T}} \tag{5.29}$$

with $A$ as pre-exponential factor, $E_a$ the activation energy to start the chemical reaction, $R_m$ the molar gas constant and $T$ the temperature of the mixture.

## 5.3 Continuous ignition of the flame

For successful combustion the mixture has first to be heated up to a certain temperature so that ignition of the fuel is possible. The energy balance of such an event, giving the temperature raise of the system, is a function of heat release by the fuel and the heat losses over the system.

$$\rho \cdot V \cdot c_p \cdot \frac{\partial T}{\partial t} = \dot{Q}_P - \dot{Q}_L \tag{5.30}$$

The heat due to the chemical reaction, by making use of equation 5.29, can be written as

$$\dot{Q}_P = \dot{q} \cdot V \cdot [B]^b \cdot A \cdot e^{-\frac{E_a}{R_m \cdot T}} \tag{5.31}$$

with $\dot{q}$ the heat release rate of the chemical reaction, $V$ the system volume and $[B]$ the concentration of the hydrocarbons (fuel). The exponent $b$ gives the order of reaction, defining how many molecules are transformed.
For the losses in a lean combustor the additional amount of air is of importance. As more air is fed to the combustor as necessary, the flame has to deliver enough energy to raise the temperature of the whole mixture to the same level.

$$\dot{Q}_L = \dot{m} \cdot c_p \cdot (T - T_0) \tag{5.32}$$

It can be seen from equation 5.31 and 5.32 that the heat release is depending exponential and the losses linearly from the temperature. Figure 5.2 shows the energy balance (heat release as solid line and heat losses as dashed lines) as function of temperature.

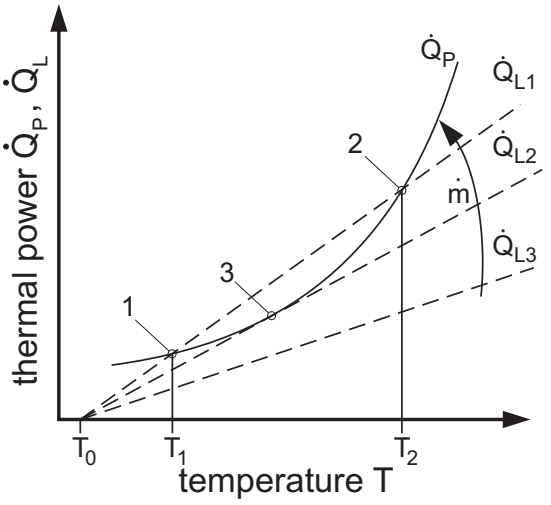


Figure 5.2: Energy balance for successful ignition as function of temperature

For the stability of the flame, in terms of possibility to continuously enlightening the fuel, three cases can be distinguished, also shown in figure 5.2. All three cases have in common that the same heat release is used. The losses, described by $\dot{Q}_L$ are constantly decreased. The first case is representing a flame with a high excess of air. The losses are depicted by the curve labeled with $\dot{Q}_{L1}$. Two intersections with the heat release curve $\dot{Q}_P$ can be found in figure 5.2. For an increase in temperature starting from $T_0$, the system will be heated up to $T_1$. If the temperature increases above $T_1$ the losses start to increase and the temperature of the system will drop till it reaches $T_1$ again. Point 1 can be defined as stable. The other point of intersection at 2 is unstable as small deviations from the temperature $T_2$ will lead to either successful ignition ($T > T_2$) or a temperature drop which will lead to flame out.
When decreasing the excess of air, leading to a richer flame, one can assume the curve represented by $\dot{Q}_{L2}$. Ignition is possible except at point 3 where the heat release equals the heat losses.
Operating the flame at a rather rich fuel to air ratio will lead to the loss curve given by $Q_{L3}$. The heat release due to the chemical reaction is high enough to lead to successful

ignition anyway.

From the above given description the following problems in term of flame stability occur:

- **Temperature dependence of reaction rate**; is shown in equation 5.29. It can be seen that at low temperatures the reaction rate is lowered too. When looking at figure 5.3b one can see that the raise in temperature and thus in temperature of the flame inside a combustor is a function of the equivalence ratio. With a decrease in equivalence ratio the flame temperature drops also (with a decrease in equivalence ratio the flame temperature slightly drops as the excess of fuel drains off more energy of the system to get heated up). This in turn implies that the reaction rate (figure 5.3a) may thus vary as function of equivalence ratio too. As the reaction rate is exponentially dependent on the temperature, a decrease in $T$ leads to an exponential decrease in the reaction rate. Furthermore small variations in equivalence ratio (and or temperature) will lead thus to large variations in reaction rate.
  An other impact of the variation of flame temperature and thus reaction rate is on the general stability of the flame. If the reaction rate is lowered due to an decrease in temperature the velocity of the air flow may be too high so that the fresh mixture can not be ignited, and blow out occurs. Vice versa for a high temperature at low air velocity will lead to flashback as the mixture is consumed faster than it approaches into the combustion chamber.

- **Concentration of the fuel**; accountable for the energy release of the chemical reaction (equation 5.31). The fuel should be distributed uniform inside the mixture to set the heat release as uniform as possible. Otherwise changes in heat release might lead to local flame out. Premixing of fuel and air is thus preferable. However, the main drawback of premixing is the risk of auto-ignition, as a highly combustible mixture is formed in the premixing tube. When looking at engines with an OPR of $30 \div 40$ the compressor exit temperatures reach 600-800 K. In such cases the ignition delay time is below 0.1 ms and auto-ignition inside the premixing tube is possible. The design of the premixing tube and the achievable velocity of the air flow are therefore of great importance [46]. With flow velocities higher than the flame speed a flash back is very unlikely and the residence time of the fuel is lowered so that the risk of auto-ignition is lowered too (see constraints above).
  An other problem of fuel concentration is given when using liquid combustibles. Before combustion the liquid has to be vaporized. To do so energy (heat) is needed. Pockets with a high concentration of liquid fuel need more energy to be vaporized, thus lowering the temperature at this point and leading to so called "rich blow out" as the temperature for successful ignition can not be reached.

- **excess of air**; is determined by the energy balance given by equation 5.30. With an drastic increase in air, the losses in terms of heat needed to lift the temperature of the "inert" air to the temperature of the systems are increasing too. Thus the system will tend to unstable operation as shown in figure 5.2.

- **Turbulence**; increases the mixing of fuel and air, as well as the recirculation of radicals and heat too. Thus ignition of the fresh mixture is enhanced if the turbulence is high. However, if the turbulence is too high, the recirculation of exhaust gases might dilute the fresh mixture to a point where combustion is not possible.

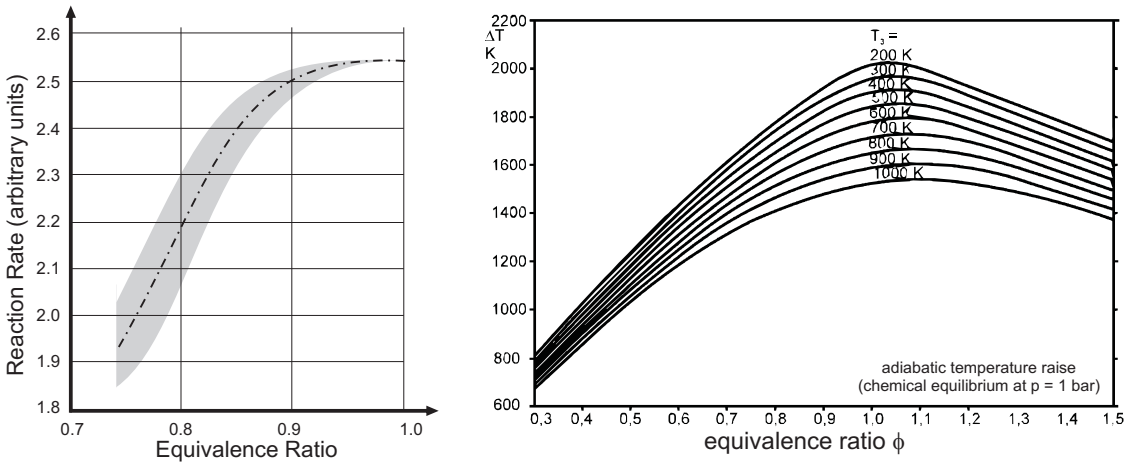


(a) Reaction rate as function of equivalence ratio; [48] modified

(b) Temperature raise as function of equivalence ratio; [46]

Figure 5.3: Unsteady reaction rate due to changes in flame temperature and equivalence ratio

From the above given description it arises that at high flame temperatures, located at an equivalence ratio of roughly one, the flame is more stable than at lean or very rich operating conditions. However, high flame temperatures also imply a high formation of $NO_x$. Furthermore by introducing a recirculation zone the flame is not only stabilized by aerodynamic forces, but also ignition of the fresh mixture is enhanced by adding energy from the exhaust gases.
A combustor operating in the lean operating range is thus susceptible to unsteady combustion phenomena. If the unsteady flame is now excited, a so called combustion instability or combustion oscillation occurs. The mechanisms are described below.

## 5.4 Thermo acoustic coupling

A thermo acoustic instability is a closed loop coupling between unsteady heat release and pressure fluctuations [46, 49].
Fluctuations in density are induced by fluctuations in heat release and are transported with the velocity of the flow to the exhaust of the combustor. Here they are reflected as fluctuations in pressure and are transported backwards towards the inlet of the combustor. Thus fluctuations in density are induced by fluctuations in pressure and entropy [46].
Following the methodology of Leitgeb [50], the mathematical expressions for the above given description are as follows:

$$\frac{\mathrm{D}\rho}{\mathrm{D}t} = \underbrace{\frac{\mathrm{d}\rho}{\mathrm{d}t}}_{\rho'} = \left.\frac{\partial\rho}{\partial p}\right|_s \cdot \underbrace{\frac{\mathrm{d}p}{\mathrm{d}t}}_{p'} + \left.\frac{\partial\rho}{\partial s}\right|_p \cdot \underbrace{\frac{\mathrm{d}s}{\mathrm{d}t}}_{s'} \tag{5.33}$$

with the density fluctuation denoted as $\rho'$, the fluctuation in pressure given by $p'$ and the entropy fluctuation $s'$.

For the partial derivatives in equation 5.33 one can write:

$$\left.\frac{\partial \rho}{\partial p}\right|_s = \frac{1}{c^2} \tag{5.34}$$

$$\left.\frac{\partial \rho}{\partial s}\right|_p = \frac{(\gamma - 1) \cdot \rho}{c^2} \tag{5.35}$$

The deviation of density by the pressure at constant entropy is proportional to the velocity of sound of the system. Furthermore the derivative of entropy at constant pressure is proportional to the isentropic exponent multiplied by the density and divided by the velocity of sound. A detailed mathematical derivation of both partial derivatives can also be found in annex I.
After some mathematical treatment of equation 5.33 one will finally receive the time derivative of density fluctuation given below.

$$\frac{\partial \rho'}{\partial t} = \frac{1}{c^2} \cdot \frac{\partial p'}{\partial t} - \frac{(\gamma - 1) \cdot \rho}{c^2} \cdot \dot{q}' \tag{5.36}$$

The detailed mathematics to receive equation 5.36 can be found in annex I.
With equation 5.36 the thermo-acoustic (closed loop) coupling between the unsteady heat release and the acoustic energy of a system (pressure fluctuations) is described [49]. This feedback loop is sketched in figure 5.4. Although equation 5.36 describes the thermo-

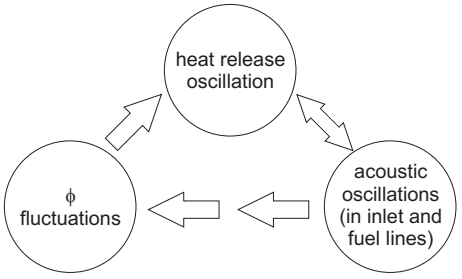


Figure 5.4: Feedback loop responsible for combustion instabilities [51]

acoustic coupling, a combustion instability will only appear if a specific criterion is fulfilled. Rayleigh [52] has stated (in words) that the thermo-acoustic coupling will only arise if the pressure fluctuation and the unsteady heat release are in phase, so that the heat release is adding power to the system at an opportune moment. Equation 5.37 is mathematically representing Rayleigh's criterion (see [53]).

$$\Re = \frac{1}{T} \cdot \oint p' \cdot \dot{q}' \mathrm{d}t \tag{5.37}$$

When evaluating the equation one will find that energy is added to the system only if $p'$ and $\dot{q}'$ are in phase, resulting in $\Re > 0$. For $\Re < 0$ energy is extracted from the system and for $\Re = 0$ energy is neither added nor extracted.

The simplest demonstrative description of the above presented mechanisms is to use the Rijke tube, which is described in the following section.

## 5.5 Simple combustion instability model

A Rijke tube is basically a straight tube with two open ends. If an energy source, like a flame, is placed in the lower half of the tube the air column above the energy source starts to oscillate. Thereby sound waves start to move towards the open end and some of these acoustic waves are reflected back into the tube. The reflected waves interact with the arriving waves to form a stationary (or standing) wave.
The boundary conditions for this are such that at both ends of the tube a pressure node is given. Thus the fundamental mode that is formed will have a wave length of $\lambda = 2 \cdot L$, with $L$ the length of the tube [52] (see figure 5.5). The energy source inside the tube is just to maintain the standing wave. The wave itself would also be formed if any source is present to excite it. However, as said before, to sustain the oscillation the Rayleigh criterion, given in equation 5.37, has to be satisfied. This can only be achieved if the heat source is located in the lower half of the tube. Furthermore figure 5.5 shows the heat source at a fourth of the tube length ($L/4$), which is the position with the highest amplification of the oscillation (evaluation of equation 5.37).
This can be confirmed when considering the following. For the standing wave, anywhere in the lower half of the tube, figure 5.6 bottom shows the variation of acoustic pressure, heat release and velocity as function of time. On the left the situation is shown in an amplitude time diagram and on the right it is shown as a vector diagram with $A(t) = \hat{A} \cdot sin(\omega \cdot t)$, where $A$ stands representative for the above mentioned variables. From the figure it is shown that the velocity fluctuation is at a maximum where

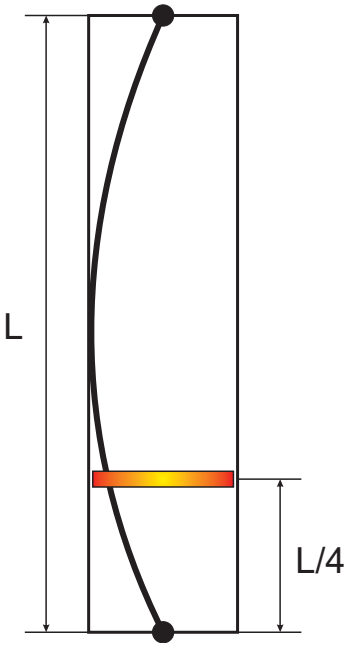


Figure 5.5: Rijke tube

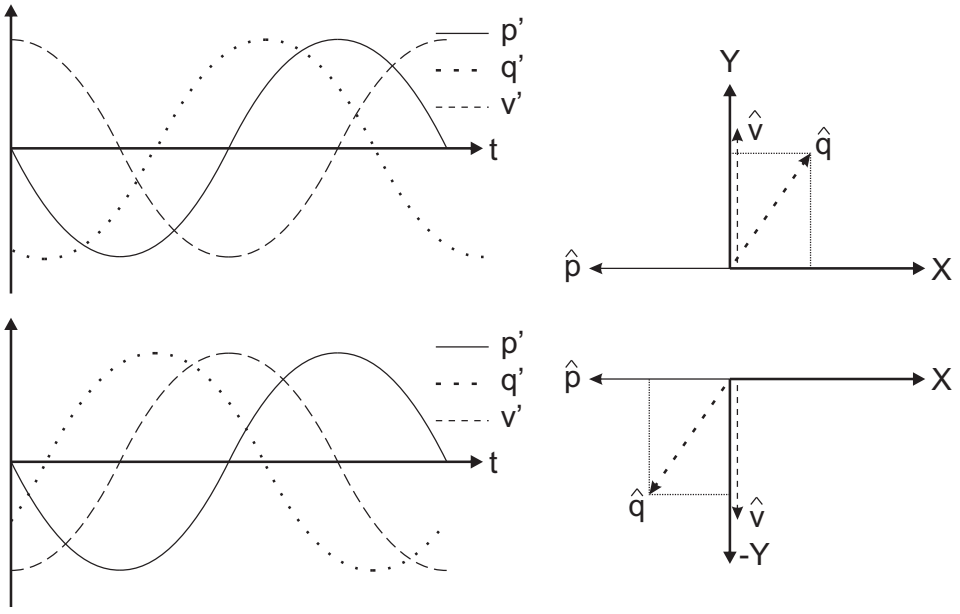


Figure 5.6: Variation of $p'$, $q'$ and $v'$ with time [54]; top: any location in the upper half of the Rijke tube; bottom: any location in the lower half of the Rijke tube

the pressure fluctuation has a node. Furthermore the velocity has an impact on the heat release rate as the heat transfer is eased at higher velocities of flow and vice versa. As the change in heat transfer is not instantaneous the fluctuation in heat release lags behinds the velocity fluctuation. As the Rayleigh criterion states that $q'$ and $p'$ have to be in phase, this is only possible in the lower half of the tube (see the right side of figure 5.6; bottom: a part of $\dot{q}'$ acts in direction of $p'$; top: $\dot{q}'$ acts in opposite direction of $p'$.

## 5.6 Combustion instabilities in LPP combustors

When adapting the simple relations of the Rijke tube to LPP combustors one will find several similarities. In a LPP combustor the flame is usually located in the lower half of the combustor. In addition, due to lean operation, almost all the air is injected via the LPP modules. To avoid flashback the velocity of air injection is rather high. Thus the flame is usually situated at a pressure maximum [51], which will ease to fulfill the Rayleigh criterion.
In combustion chambers the excitation is usually given due to oscillations in pressure, velocity or temperature, or in some cases by the composition of the mixture [51]. Still the oscillations of pressure and heat release have to be in phase.
As LPP combustors are operating near the blow out limit they are susceptible to variations in the equivalence ratio. Thereby the oscillations can be due to variations in fuel or air mass flow. With the following example the interaction of fluctuation in acoustic pressure and unsteady heat release rate in a LPP combustor (figure 5.7a) are described.
Considering a combustor operating at low Mach numbers in the primary zone with chocked fuel injectors, the following mechanism can be applied.
Pressure fluctuations in the flame will be transferred to the injector. Due to the low Mach numbers, both oscillations will be in phase (see figure 5.7b). Velocity oscillations are phase shifted by $\pi/4$ and the corresponding oscillations in air mass flow are slightly lagging the velocity fluctuation. As said no fluctuation in fuel mass flow is present, so the equivalence ratio fluctuation is shifted by $\pi/2$. The mixture with varying equivalence ratio $\phi'$ is now convected with the flow and enters the combustor base after the time lag $\tau_{conv}$. As the fuel is not consumed instantaneous the oscillation in heat release rate will suffer an additional time lag of $\tau_{eq}$. If the heat release oscillation $q'$ is now again in phase with the pressure fluctuation $p'$ at the flame, a combustion instability occurs. Regions of unstable combustion can than be found when applying

$$\frac{\tau_{conv} + \tau_{eq}}{T} = n - \frac{1}{4} \qquad \text{with } n = 1, 2, \ldots \tag{5.38}$$

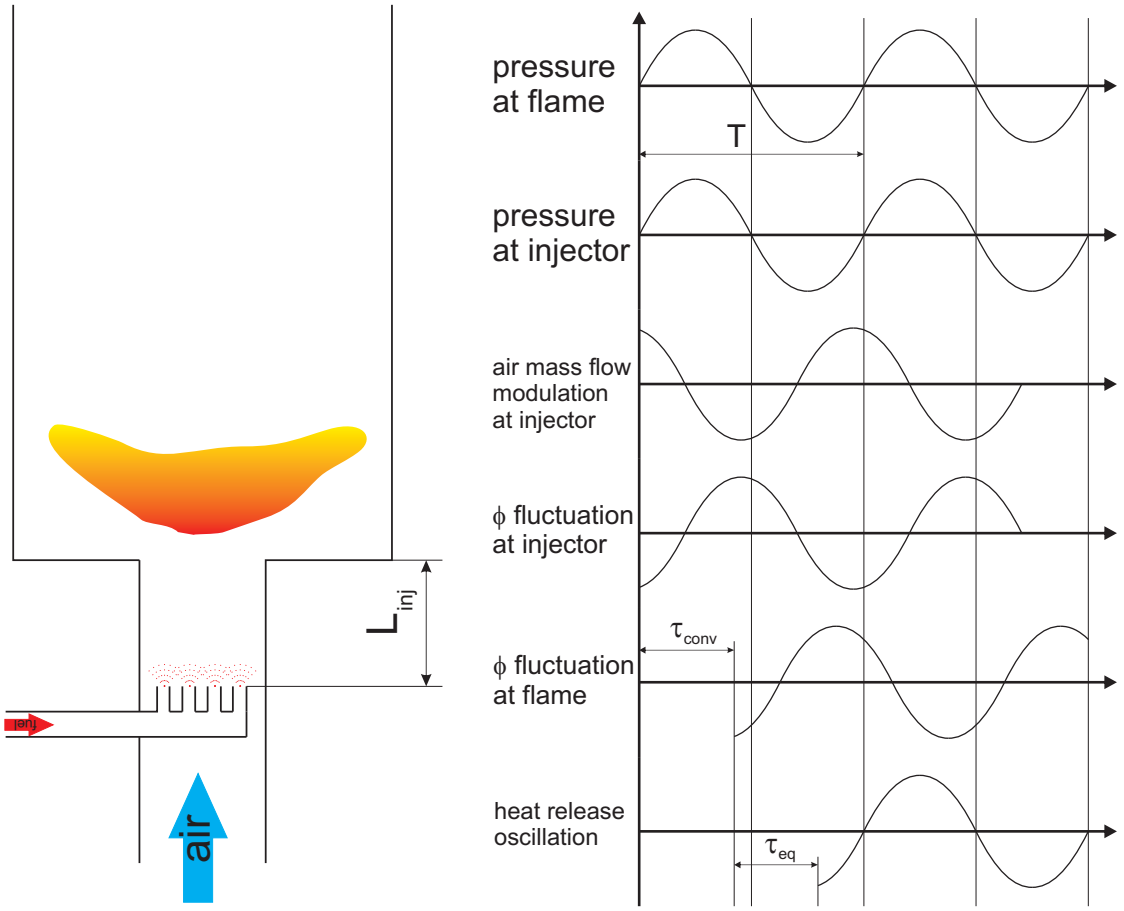


(a) Sketch of LPP combustor

(b) Oscillation mechanism

Figure 5.7: Disturbances responsible for combustion driven oscillations [51]

# Chapter 6

# Measurement techniques and specific methods

## 6.1 Laser Doppler Anemometry

Laser Doppler Anemometry (LDA) or Laser Doppler Velocimetry (LDV) is a non intrusive measurement technique to record spatially resolved velocity data from the fluid flows under investigation.
The measurement principle is based on the Doppler shift of light scattered by moving particles. To be precise, one will actually measure the velocity of particles in the flow rather than the velocity of the flow itself. By adding so called "seeding particles" (or "tracer particles") to the flow it is possible to measure velocities in small combustion chambers as well as in large scale wind tunnel experiments. The velocities that can be detected ranges from centimeters per hour up to supersonic Mach-numbers. The system has a linear response and does not need a calibration (compared to Particle Image Velocimetry - PIV) [55].
Two type of LDA systems had been developed:

- Reference beam system
- Crossed beam or fringe mode

The usually used systems nowadays are of the fringe mode type as the detected frequency (so called "Doppler burst") is independent from the direction of the scattered light. Thus collecting the light over a wide angle is possible [55].
To generate a fringe pattern a coherent light source is needed. By using a laser as light source and a beam splitter, two beams ($i,1$ and $i,2$) of coherent light (with frequencies $f_0$ and wavelengths $\lambda_0$ pointing in the direction with unit vectors $\overrightarrow{e_{i,1}}$ and $\overrightarrow{e_{i,2}}$ respectively) can be crossed to form the measurement volume (fringe pattern). If a particle with velocity $\overrightarrow{U}$ passes the pattern it is illuminated at the bright fringes and scatters light in all directions. Considering the unit vector $\overrightarrow{e_s}$ pointing in the direction of the receiver, the relative velocity of the laser beam and the particle will be depending on which laser beam the light is scattered (see also figure 6.1)

$$c - \overrightarrow{U} \cdot \overrightarrow{e_{i,j}} \qquad \text{with j=1,2} \tag{6.1}$$

$$\text{where } c = \lambda_0 \cdot f_0 \tag{6.2}$$

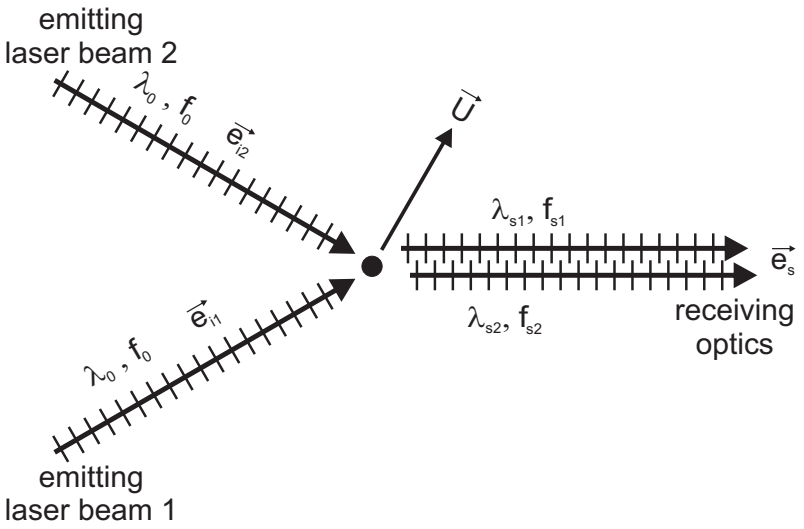


Figure 6.1: LDA system in fringe mode

The frequency at which the wavefronts are interrupted by the particle can be computed as

$$f'_j = \frac{c - \overrightarrow{U} \cdot \overrightarrow{e_{i,j}}}{\lambda_0} = f_0 - \frac{\overrightarrow{U} \cdot \overrightarrow{e_{i,j}}}{\lambda_0} \tag{6.3}$$

The receiving optic is getting scattered light only from direction $\overrightarrow{e_s}$, so the wave fronts are interrupted at frequency

$$\begin{aligned} f_{s,j} &= \frac{c + \overrightarrow{U} \cdot \overrightarrow{e_{s,j}}}{\lambda_s} = f'_j + \frac{\overrightarrow{U} \cdot \overrightarrow{e_{s,j}}}{\lambda_s} \\ f_{s,j} &= f_0 + \overrightarrow{U} \cdot \left( \frac{\overrightarrow{e_{s,j}}}{\lambda_s} - \frac{\overrightarrow{e_{i,j}}}{\lambda_0} \right) \\ &\text{with } \lambda_s \simeq \lambda_0 \\ f_{s,j} &= f_0 + \frac{\overrightarrow{U}}{\lambda_0} \cdot (\overrightarrow{e_{s,j}} - \overrightarrow{e_{i,j}}) \end{aligned} \tag{6.4}$$

The change in frequency by the two parallel light waves, obtained by the receiver, is the doppler shifted frequency

$$f_D = f_{s,2} - f_{s,1} = \frac{\overrightarrow{U}}{\lambda_0} \cdot (\overrightarrow{e_{i,1}} - \overrightarrow{e_{i,2}}) \tag{6.5}$$

By applying this system it is not possible to distinguish the direction of the flow. To overcome this directional ambiguity an acousto-optical modulator, a so called Bragg cell, is used to add a constant frequency shift on one of the incident laser beams, causing a beating frequency within the measurement volume. The fringe pattern is now moving at a constant velocity. Thus equation 6.5 changes to

$$f_D = \Delta f + \frac{\overrightarrow{U}}{\lambda_0} \cdot (\overrightarrow{e_{i,1}} - \overrightarrow{e_{i,2}}) \tag{6.6}$$

where $\Delta f$ is the frequency shift added by the Bragg cell. The measurement volume formed by the two laser beams is shown in figure 6.2 and can be computed as

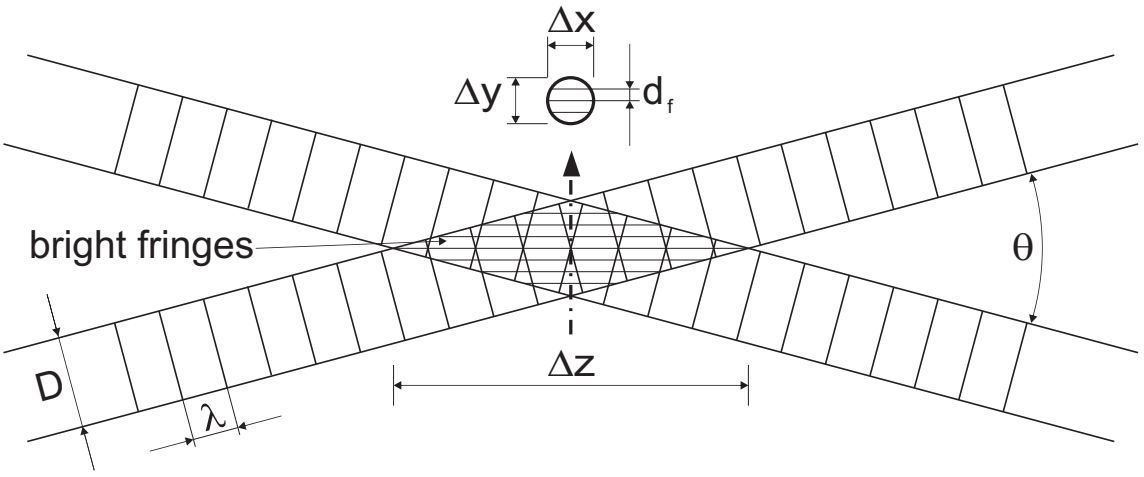


Figure 6.2: Fringe pattern of LDA system; center top: cross section of the measurement volume; bottom: crossing laser beams establishing a fringe pattern

$$\Delta x = D_0 \tag{6.7}$$

$$\Delta y = \frac{D_0}{cos(\Theta/2)} \tag{6.8}$$

$$\Delta z = \frac{D_0}{sin(\Theta/2)} \tag{6.9}$$

$$\text{with } D_0 = \frac{4}{\pi} \cdot \frac{F_l}{D} \cdot \lambda_0$$

The measurement volume is given by the beam angle $\Theta$ and the size of the beam diameter $D_0$. As every laser beam has a Gaussian intensity distribution the emitted laser beam will form a fringe pattern with a Gaussian intensity distribution where $D$ is transformed to $D_0$.
The fringe pattern formed has a spacing of

$$d_f = \frac{\lambda_0}{2 \cdot sin(\Theta/2)} \tag{6.10}$$

Thus the velocity of the particle can be computed to

$$u = \lambda_0 \cdot f_D \tag{6.11}$$

The signal of such an event, when a particle passes the measurement volume, is called a Doppler burst. Figure 6.3 shows such an event. As a lot of particles are flowing through the fringe pattern, Burst Spectrum Analyzer (BSA) are used to keep up with a high data rate.

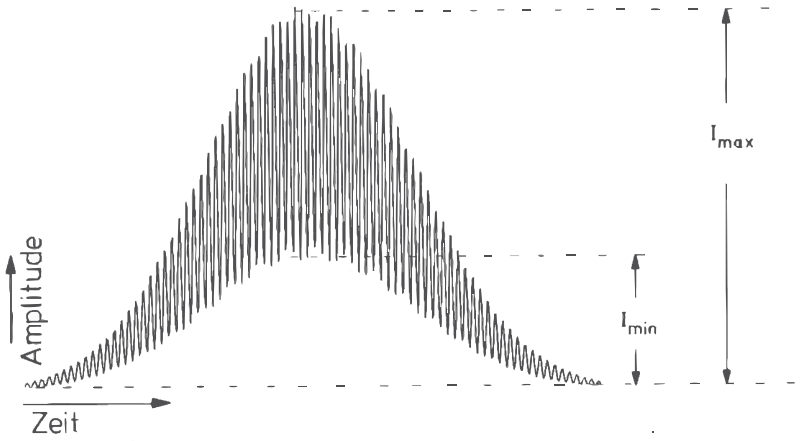


Figure 6.3: Doppler burst [56]

Particles are used to scatter the light. The size of the particles ($u_p$) is usually in the micrometer size so that they can follow the flow without lag (see equation 6.12) and give a good frequency resolution in turbulent flows. The velocity of the particle or better to say the time the particle needs to finally reach the velocity of the flow is a function of the density ratio of fluid ($\rho_f$) to particle ($\rho_p$), the viscosity of the flow ($\nu$) and the size of the particle (with radius $r$).

$$u_p = u_e \cdot \left[1 - e^{-\frac{t}{\tau}}\right] \qquad \text{with } \tau = \frac{2}{9} \cdot \frac{r^2 \cdot \rho_p}{\nu \cdot \rho_f} \tag{6.12}$$

However, if the particles are too small the scattered light intensity is lowered. The properties of light scattered by small particles or droplets is usually discussed by the Lorenz-Mie theory [56]. Such "Mie-Scattering" is often found in literature. For particles smaller than the wavelength of the light scattered "Rayleigh Scattering" is the common name, mathematically reducing the general multipole interaction to a pure dipole oscillation. For very large drops the Lorenz-Mie theory includes geometrical optics [56], often used to discuss rainbows or two phase flows.
So using a LDA system operating in forward scattering mode is favorable when looking at figure 6.4, as the light in forward direction is scattered 100 times better than in backwards direction. The advantage of systems operating in back scattering mode (see figure 6.5) however is that the systems are of compact build.

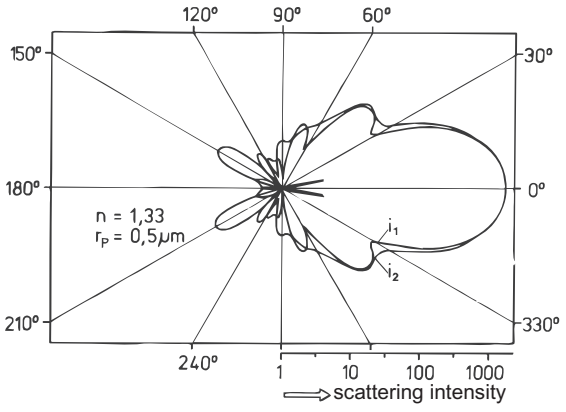


Figure 6.4: Scattering intensity distribution on a water droplet of 1 $\mu$m; [56] modified

The system used in this work is a two-component LDV (DANTEC Fiber-Flow with DANTEC Burst Spectrum Analyser, DANTEC Dynamics, Roskilde, Denmark) fed by an argon ion laser (Coherent Inc., Santa Clara, CA) with wavelengths $\lambda$ =488 nm and 514.5 nm respectively, operating in back-scatter mode. For positioning of the emitting / receiving unit a DANTEC Lightweight traverse was used. Data acquisition and control of the traversing system was done by using DANTEC BSA Flow Software 1.2. Data analysis was done using MATLAB vR2009b (The MathWorks).
For seeding the flow, two seeding generators of type AGF2.OD from PALAS are used. The seeding itself is Diethylhexylsebacate, an oily substance, with a characteristic droplet size of 0.3 $\mu$m. Due to agglomeration in the seeding pipes a droplet size of 0.7 $\mu$m is usually expected.

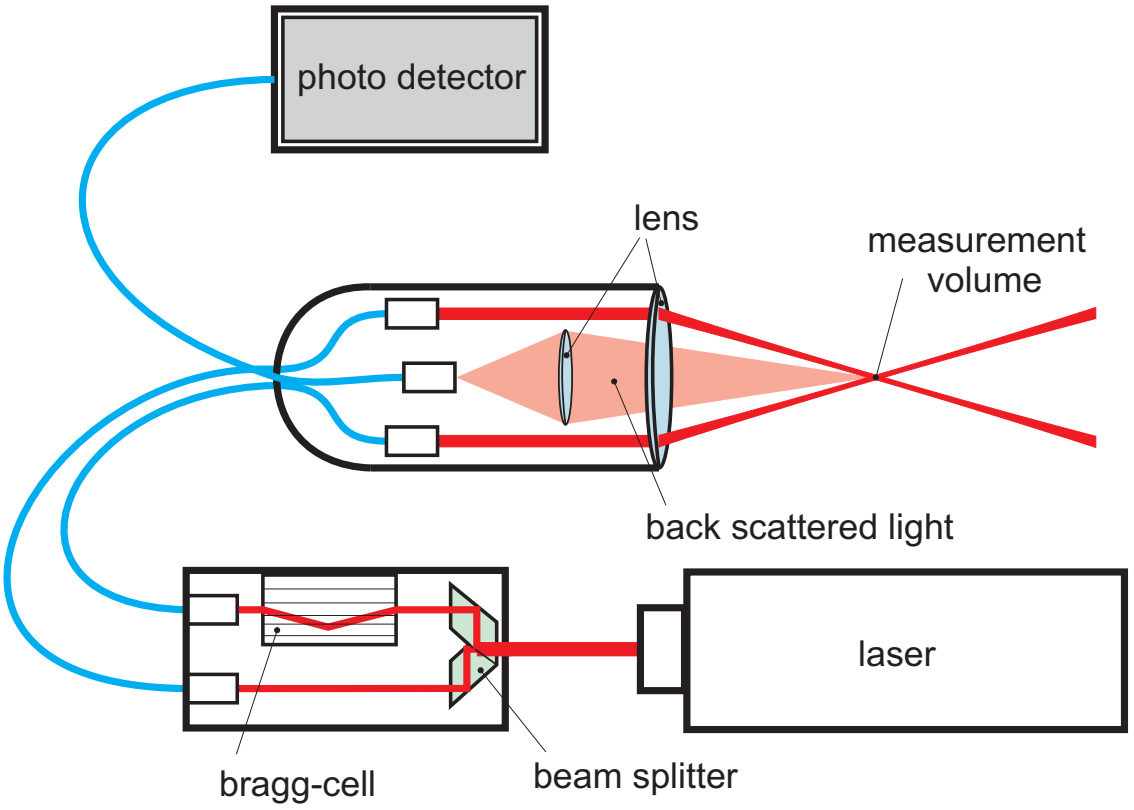


Figure 6.5: Components of a LDA system operating in back scattering mode; by courtesy of Köberl 2011

## 6.2 Laser Vibrometry

To measure the changes in density inside a fluid flow one can either use

- Schlieren or Shadowgraphy
- Differential Interferometry (Shearography)
- Laser Vibrometry

The first method listed above is giving information on the refractive index ($n$) gradient and thus in the gradient of density $\partial\rho/\partial x$.

$$\begin{aligned} n - 1 &= R_G \cdot \rho \\ \frac{\partial n}{\partial x} &= R_G \cdot \frac{\partial \rho}{\partial x} \end{aligned} \tag{6.13}$$

In equation 6.13 $R_G$ stands for the Gladstone-Dale constant (see section 6.4.3). The optical setup needed is rather complex and only qualitative data of density fluctuations can be gathered. Differential Interferometry and Laser Vibrometry are both based on interferometry. As for the interference of light a coherent light source is necessary, both measurement techniques use laser sources. The latter one is using the simplest possible optical setup and spatially and frequency resolved data of density fluctuation can be obtained.
A Laser Vibrometer (LV) is basically a Mach-Zehnder interferometer. To record density fluctuations, the laser beam from the LV passes through the flow investigated, is reflected by a mirror, passes the measurement volume again and reenters the LV. Figure 6.6 shows the setup, including the interior of the LV.

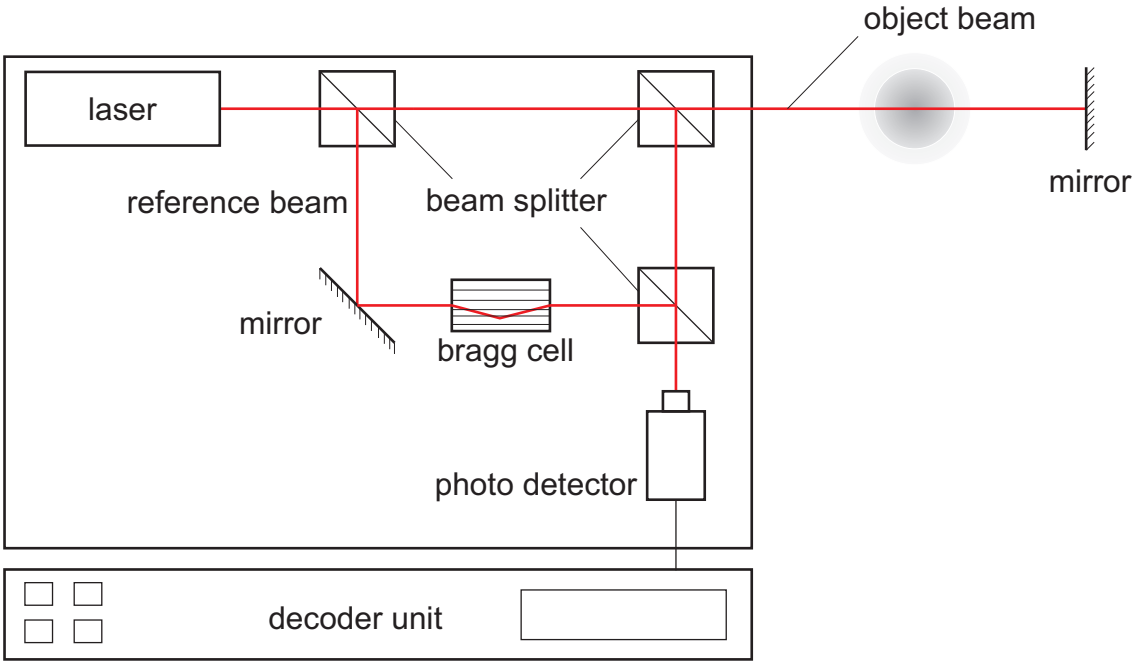


Figure 6.6: Laser Vibrometery (LV) setup, consisting of the LV itself, a decoder unit and a mirror; by courtesy of Köberl 2011

The LV uses a $HeNe$-laser as coherent light source.
By using a beam splitter the laser beam is split into an object beam and a reference beam. The object beam is emitted via a second beam splitter and optic and pointed on a surface. In the common application the surface would be vibrating, but in the application for recording density fluctuations it is a mirror at rest. The reflected object beam passes the measurement volume twice and is superimposed to the reference beam. Thus an interference pattern is generated. This pattern is detected by a photo detector. Here a Bragg cell for modulation of the reference beam is necessary to distinguish a forward from a backwards motion. The beating between the frequency modulated object beam (Doppler shifted) and the frequency modulated reference beam (Bragg Cell shifted) results

in a recording of velocity rather than amplitude.
If now the reflecting surface is at rest the optical path can only be altered by a change in refractive index along the geometrical path [7].

$$l_{opt} = \int_z n(z)\mathrm{d}z \tag{6.14}$$

The phase of such a light wave (see figure 6.7) is thus

$$\phi = \frac{2 \cdot \pi}{\lambda_0} \cdot (2 \cdot l_{opt}) \tag{6.15}$$

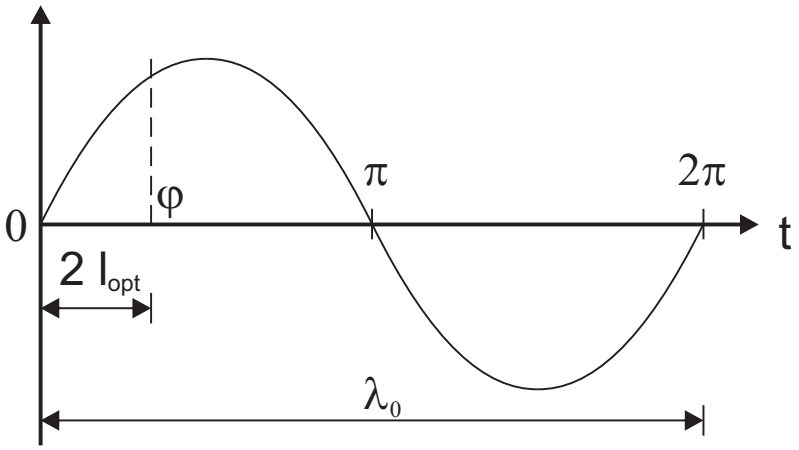


Figure 6.7: Light wave

As the laser beam passes twice the measurement volume the optical path is doubled. Thus the phase difference of object and reference beam can be computed to

$$\Delta\phi(t) = \frac{4 \cdot \pi}{\lambda_0} \left[ \int_{obj} n(z,t)\mathrm{d}z - \int_{ref} n(z)\mathrm{d}z \right] \tag{6.16}$$

The phase lag of the object beam due to changes in refractive index in a homogenous mixture is due to changes in density or composition of the gases [57]. Commonly the use of the Gladstone-Dale relation is used to describe this.

$$R_G = \frac{n-1}{\rho} \qquad \Rightarrow \qquad n = R_G \cdot \rho + 1 \tag{6.17}$$

Therefore equation 6.16 can be written as

$$\Delta\phi(t) = \frac{4 \cdot \pi}{\lambda_0} \left\{ \int_{obj} \left[ R_G \cdot \rho(z,t) + 1 \right] \mathrm{d}z - \int_{ref} \left[ R_G \cdot \rho(z) + 1 \right] \mathrm{d}z \right\} \tag{6.18}$$

For same geometrical path length of object and reference beam, equation 6.18 reduces to

$$\Delta\phi(t) = R_G \cdot \frac{4 \cdot \pi}{\lambda_0} \int_z \Delta\rho(z,t)\mathrm{d}z \tag{6.19}$$

From equation 6.19 it becomes evident that by using LV only density fluctuation can be measured, relative to the density in the reference beam. For absolute values of density one will need a reference measurement with given density. Furthermore the data received are integrals along the geometrical path. To receive local data of density fluctuation, either tomographic reconstruction techniques, or the use of a second LV intersecting locally at the measurement volume would be necessary (dual LV technique) [11].
However, the density fluctuation in equation 6.19 can be split into a long time averaged component and a fluctuating part [7]

$$\Delta\rho(t) = \overline{\Delta\rho} + \Delta\rho'(t) = \overline{\rho} + \rho'(t) \tag{6.20}$$

By using the LV in the Bragg Cell mode, the time derivative of $\rho'$, $\partial\rho/\partial t$, is measured, integral along the line of sight. The change in the optical path $L(z,t)$ is therefore given by

$$L(z,t) = \frac{\Delta l_{opt}}{R_G} = \frac{k \cdot U(t)}{R_G} = \int_z \frac{\partial\rho'}{\partial t}\mathrm{d}z \tag{6.21}$$

with $k$ the instrument gain factor and $U(t)$ the voltage output of the LV decoder. Finally the voltage signal recorded is linked to the time derivative of the density fluctuation by

$$U(t) = \frac{R_G}{k} \cdot \int_z \frac{\partial\rho'}{\partial t}\mathrm{d}z \tag{6.22}$$

As the density fluctuation is continually recorded, an analysis of the time signals as well as the frequency resolved data is possible by using a FFT algorithm on the time signals [11].
With Laser Vibrometry the time derivative of density fluctuation inside the flame can be directly measured without any calibration necessary. Furthermore the continuous recording of the signals allow to compute spatially and frequency resolved maps of density fluctuation (see section 6.4.2).

The system used for experiments is a Polytec OVD 353 Laser Vibrometer, OFV-3001 controller and OVD-02 velocity decoder from Polytec GmbH, Germany.

## 6.3 High temperature resistant pressure transducer

In section 5 it has been shown that density fluctuations can be used as potential marker for combustion instabilities, and that these fluctuations in density can be detected by using LV. However, if no optical accessibility is given, a pressure transducer can be used to detect pressure fluctuations that accompany a combustion instability.
Pressure transducers are based on the direct piezoelectric effect. This means that by an elastic deformation (the force has to be directed) of the piezoelectric crystal an electrical charge will be generated. This happens due to a formation of macroscopic dipoles inside the unit cell of the crystal and thus the center of charge shifts. By accumulating all charges of the electrical field of all unit cells of the crystal, a macroscopic charge can be measured. [58]
As the piezoelectric effect only appears at dielectric materials the sensor has to have a high electric insulation. Furthermore the cable and the charge amplifier have to be good insulated too as the so called electric signal drift will appear otherwise. Charges are getting

lost during the measurement, changing the readout value. This drift is noticeable especially when using low grade materials at increasing temperature. As quartz and especially gallium phosphate ($GaPO4$) crystals are near perfect insulators with almost faultless microstructure the signal to noise ratio of such piezoelectric materials is improved.
However, the problem for such a sensor used in a gas turbine combustion chamber would be the high temperatures it has to face. The usual materials with piezoelectric property used loose the piezoelectric coefficient with increasing temperature (see figure 6.8).

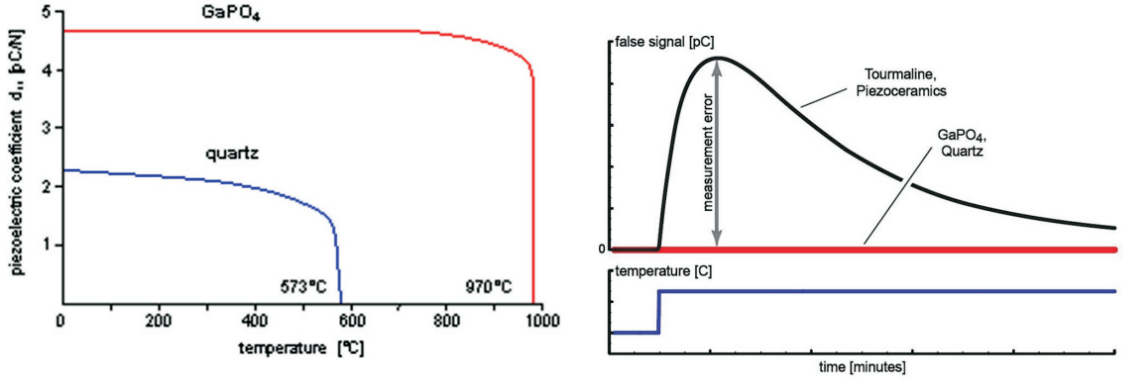


Figure 6.8: Properties of $GaPO4$ crystal, left: piezoelectric coefficient; right: false signal as function of temperature (gradient) and time; [59]

Another problem with increasing temperature is the pyroelectricity of materials such as piezo-ceramics. Pyroelectricity is similar to piezoelectricity, but in this case a charge is generated due to a temperature gradient on the sensor [58]. This charge can not be distinguished from the charges generated due to a elastic deformation of the crystal. Here to $GaPO4$ is non pyroelectric and thus the right choice for use in a pressure transducer for gas turbine application. [59]

The pressure transducer used throughout the experiments in this work is of type CP502 from Piezocryst Advanced Sensorics GmbH, Austria. Its sensitivity is 91 pC/bar with a dynamic range of $0 \div 50$ bar and a frequency response of $2 \div 15,000$ Hz $\pm$ 5 %. The temperature range for this type of sensor is up to $560°C$. For signal conditioning the sensor is connected to a AVL 3057 charge amplifier, set to the appropriate sensitivity.

## 6.4 Specific methods and routines

In this section the routines used to compute the results obtained with the Laser Vibrometry are presented. All data are processed by using MATLAB vR2009b (The MathWorks). First the treatment of data obtained during the scanning for resonant frequencies is presented. That follows a description of the ensemble averaged data analysis for the mapping of density fluctuations. This method was used for the data presented in the articles [60] and [61]. Finally the method of using the correlation of signals is presented, that is used for the data to be discussed in section 9.6.3.
As an additional section the computation of the Gladstone Dale constant is presented as it was necessary to determine this constant for an exhaust gas being built by combustion of ethanol with air.

### 6.4.1 Spectrographical representation of scanning for resonant frequencies

To determine the response of the combustion chamber to perturbation induced by the siren a spectrographical representation has been done.
By operating the siren in an acceleration (or deceleration) mode changing the frequency in steps of several Hertz per second the combustor is scanned for resonant frequencies. The desired spectrogram should show a time resolution of at least one second and a frequency resolution of 5 Hz for graphical representation of the scanning process.
The base of operation are the data with a record length of $n$ samples, sampled at frequency $f_s$. The record time is thus

$$t = \frac{n}{f_s} \tag{6.23}$$

For every channel recorded the data will be reshaped to get the appropriate data structure (shown in figure 6.9). The frequency resolution for the spectrogram $f_{sub}$ will give the smallest time step $t_{sub} = 1/f_{sub}$ so that the sample size $n_{sub}$ for the frequency resolution is given by

$$n_{sub} = \frac{1}{f_{sub}} \cdot f_s \tag{6.24}$$

The raw data are now split into samples of length of $n_{sub}$ giving the direction $i$ of the data matrix (see figure 6.9). The measurement time is given in direction $k$ and the resulting dimension $j$ is given by

$$\frac{n}{n_{sub} \cdot t}$$

representing sub time steps used for averaging of frequency spectra. Re-sampling of the data is also possible by flipping the entries in $i$ and $j$. The signal $S_{jk}$ thus consists of

$$S_{jk} = [x_{1,j,k}, x_{2,j,k} \ldots x_{n_{sub}-1,j,k}, x_{n_{sub},j,k}]$$

signal samples.

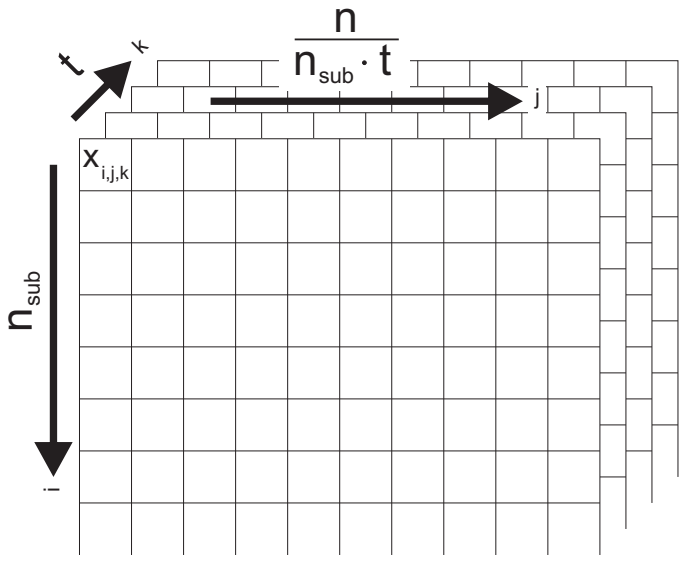


Figure 6.9: Data structure for spectrographical representation

As the first entry in a Fourier Transform (FT) represents the arithmetic average of the signal, the offset for every sub sample is removed next.

$$x_{i,j,k} = x_{i,j,k} - \frac{1}{n_{sub}} \cdot \sum_{i=1}^{n_{sub}} x_{i,j,k} \tag{6.25}$$

Now the FT (using a Fast Fourier Transform - FFT) can be performed along the direction $i$ to receive $n/(n_{sub} \cdot t)$ spectra. Finally an average of the spectra is computed (see equation 6.26) and the amplitude of the signal spectra can be shown in the spectrogram.

$$\overline{FT(S_{jk})} = \frac{1}{\frac{n}{n_{sub} \cdot t}} \cdot \sum_{j=1}^{\frac{n}{n_{sub} \cdot t}} FT(S_{j,k}) \tag{6.26}$$

### 6.4.2 Treatment of data for mapping the density fluctuation inside the combustor

Depending on the experimental setup used, two methods can be applied to receive spatially and frequency resolved information on the density fluctuation inside the measurement volume.
For simple flames using free jet configuration, where the signal to noise ratio is usually in a well bounded order of magnitude, and/or forced excitation of the flame is given, one can do ensemble averaging of the data in the time domain, which will lead to valuable results. If the signal to noise ratio however begins to drop drastically, ensemble averaging will lead to noisy samples thus resulting in large errors, concerning the phasing and frequency of the samples. To overcome this problem one can use the method of correlating signals to find the common (correlated) parts of the signal (phase relationship and signal amplitude). The latter method has also to be used for natural resonances as no reference signal is given for ensemble averaging.

**Ensemble averaging technique** For the ensemble averaging process a reference signal is needed. This can be for example the TTL trigger signal of the flow exciter, a pressure transducer, or a second LV pointing at a fixed location. The latter two signals are usually used for self induced resonant frequencies.
A representative raw time signal (shown are the first 50 ms of the experiment) recorded during a measurements is shown in figure 6.11, giving the siren TTL trigger signal ($S_{TTL}$) first, followed by the signal of the pressure transducer CP502 ($S_{CP502}$) and the Laser Vibrometer ($S_{LV}$). For this example the excitation was set at 176 Hz. The upward front of the sirens TTL trigger can now be used to re-sample the data. As the frequency of the siren can not be assumed as perfectly constant an algorithm is looking for the average period duration of the trigger signal by computing the first derivative of the time signal

$$S'_{TTL} = \frac{\mathrm{d}}{\mathrm{d}t}\left(S_{TTL}\right) \tag{6.27}$$

and determine the upfront edges of the signal by a positive gradient of the derivative. To compute the period duration the distance between two upward fronts is calculated. A histogram is applied to receive a statistical representation of the trigger signal (see for example figure 6.10). The most common period is depicted and the signals of the CP502

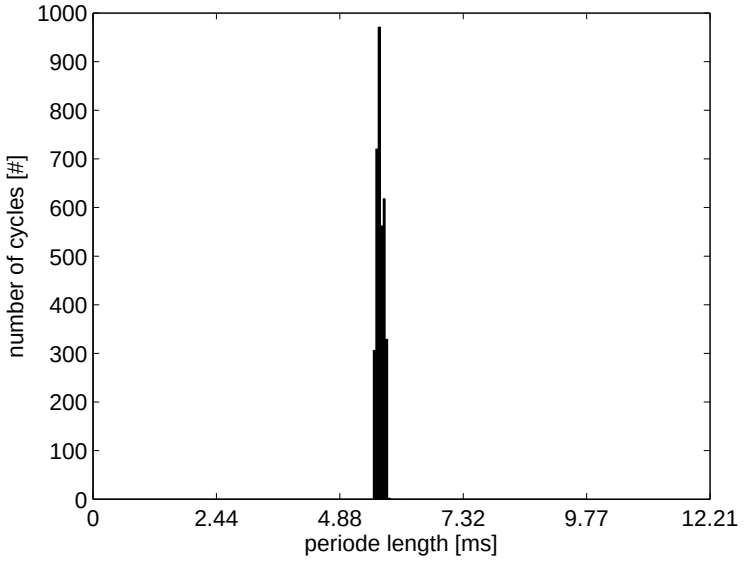


Figure 6.10: Histogram of pulsation periods; at excitation with 176 Hz

and LV are cut accordingly to the beginning of a pulsation cycle and to the length of the cycle. As the data is now phase resolved (at the frequency depicted by the most common period duration) an average of the samples is done after eliminating the offset like done in section 6.4.1 to receive ensemble averaged data.

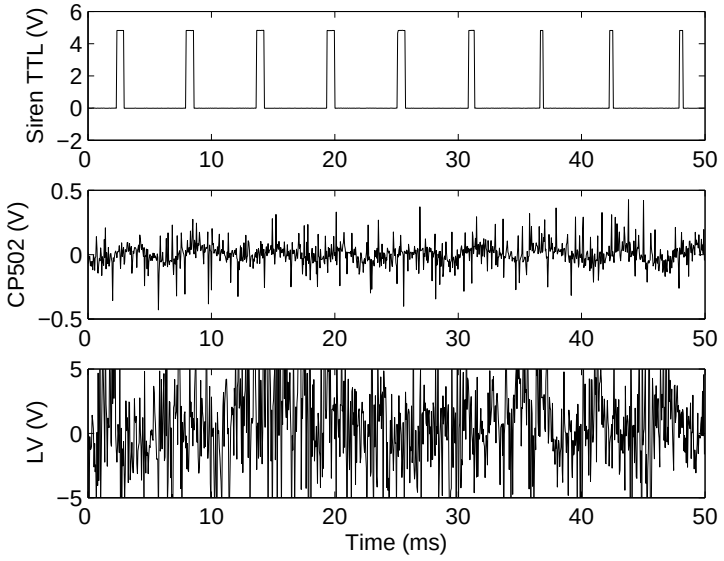


Figure 6.11: Time signals of LV data; recorded during experiments with combustion at forced excitation with 176 Hz

As said before the biggest problem by applying this method is the signal to noise ratio at harsh operating conditions. Figure 6.12 shows two examples for this influence. In (a) the SNR of the LV is fairly good whereas in (b) the LV signal is very noisy and no periodic oscillation can be found. The signal of the pressure transducer is not effected by this as it

is placed inside the air box of the injector. Here in both cases the SNR is excellent.

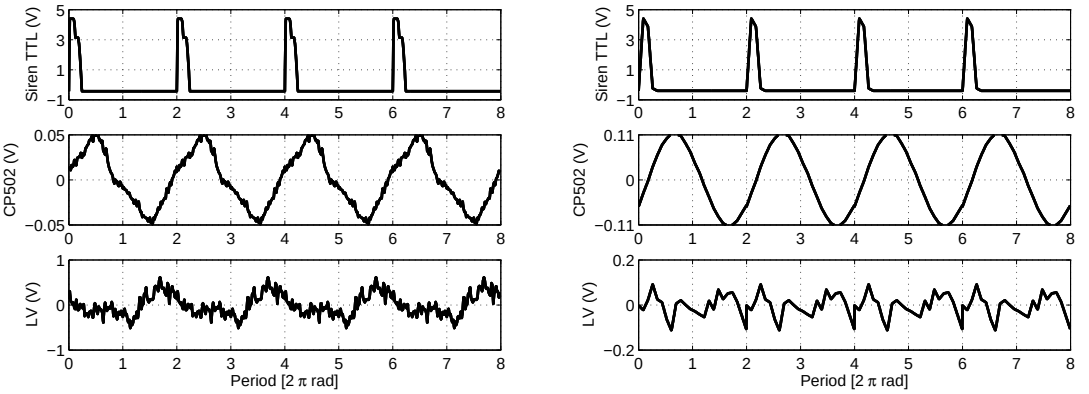


(a) Ensemble averaged time signals at 176 Hz

(b) Ensemble averaged time signals at 900 Hz

Figure 6.12: Phase averaged time signals at good (a) and foul (b) SNR

However, if the SNR allows a further treatment of the signal one can apply a transformation from the voltage signal ($u'_f$), to the density fluctuation $\partial\rho'/\partial t$ by applying equation 6.28.

$$\rho'_f = \frac{k}{G \cdot z} \int u'_f \mathrm{d}t \tag{6.28}$$

After this has been applied to every measurement point, the data has to be organized in respect to their respective coordinates. By using an interpolation method, gaps in the measurement volume are closed and finally the density fluctuation can be plotted in terms of phase angle.

**Correlation technique** If the SNR is too low a correlation of the LV with the reference signal can improve the result. And at the exhaust, where the fluctuations induced by the siren begin to dissipate the result is improved tremendously.
The correlation of two stochastic signals can either be done in the time domain, or more convenient in the frequency domain [8]. For the correlation of signals a time averaging is necessary which is done as an averaging of frequency spectra in the frequency domain. So the raw signals are split into sub samples for this purpose first (similar to the re-sampling done in section 6.4.1).
After removing the offset of the signals, to set the average value to zero, a FFT of all signals is performed.

$$F_{S_i} = FT(S_i) \qquad i = TTL, CP502, LV \tag{6.29}$$

As reference signal the TTL trigger of the siren will be used and the LV signal as well as the CP502 signal will be correlated with this trigger. The correlation itself is than a simple multiplication of one spectrum with the conjugate spectrum of the other signal in the frequency domain and an averaging of them over the sub samples.

$$C_{LV} = \overline{F_{S_{TTL}} \cdot F^*_{S_{LV}}} \tag{6.30}$$

$$C_{CP502} = \overline{F_{S_{TTL}} \cdot F^*_{S_{CP502}}} \tag{6.31}$$

The spectrum obtained by correlating two signals represents physically a power spectrum where the intensity equals the amplitude that is common to both signals and the phase represents the phase angle between the two signals. As in the above shown equations (equation 6.30 and 6.31) two signals are correlated that do not share the same physical quantity. The amplitude of the Laser Vibrometer of the correlated signal is thus substituted by the physical amplitude of the raw LV signal itself. If this would not be done a computation of the density fluctuation is not possible. The Amplitude spectrum of the correlated LV signal is thus compared to the raw LV amplitude spectrum and the correction coefficient $c_c$ can be computed to

$$c_c = \frac{|F_{S_{LV}}|}{|C_{LV}|} \tag{6.32}$$

Attention has to be paid as the correlated spectrum is a power spectrum. So the correction coefficient has to be squared for correcting the amplitude.

$$C_{LV,c_c} = c_c^2 \cdot C_{LV} \tag{6.33}$$

The amplitude of the CP502 sensor will be given in arbitrary units as no correction is done.
As the correlated LV signal now represents a physical density fluctuation, or more precise the time derivative of the density fluctuation, the voltage signal can be used to compute

$$\frac{\partial \rho'}{\partial t} = \frac{k}{G \cdot z} \cdot u'_f \Rightarrow FT\left(\frac{\partial \rho'}{\partial t}\right) = \left(\frac{k}{G \cdot z}\right)^2 \cdot C_{LV,c_c} \tag{6.34}$$

To derive the density fluctuation an integration over time in the frequency domain has to be done. This is a simple multiplication by $1/(2 \cdot \pi \cdot f \cdot i)$. The density fluctuation is thus given by

$$FT(\rho') = \frac{1}{(2 \cdot \pi \cdot f \cdot i)^2} \cdot FT\left(\frac{\partial \rho'}{\partial t}\right) \tag{6.35}$$

By applying this method the density fluctuation is given frequency resolved for the whole frequency domain. Of interest of course is the frequency used to perturb the flow. So by bandpass filtering the signal at the excitation frequency one will get the coherent structures involved in the perturbation. The signals can now be transferred into the time domain.

$$S_{f,i} = |FT(S_i)| \cdot sin[2 \cdot \pi \cdot f \cdot t + \text{angle}(C_i)] \tag{6.36}$$

In equation 6.36 angle stands for the phase angle between the reference signal and the filtered signal. For transformation to the time domain, $t$ has to be split into any subdivision of the period length to receive the desired phase resolution.
With these filtered signals the plotting of the data can be done like described above.

### 6.4.3 Computation of the Gladstone-Dale Constant

For the conversion from the voltage signal of the LV to the time derivative of the density fluctuation on needs to know the Gladstone Dale-Constant $R_G$ [7]. This constant establishes the connection between refractive index changes induced by changes in density and/or changes in the composition of the gas investigated.

$$R_G = \frac{n-1}{\rho} = \sum_{i=1}^{l} R_{Gi} \cdot X_i \tag{6.37}$$

with $R_{Gi}$ being the refractive index of species $i$ and $X_i$ the mole fraction of species $i$ [57]. It is therefore necessary to compute $R_G$ in respect to the exhaust gases as function of equivalence ratio to take into account variation in gas composition.
The reflective index of a species is tabulated for several wave lengths by Gardiner [57], most importantly for 633 nm which is the wave length of the $HeNe$-laser used for Laser Vibrometry.
The composition of the exhaust gases as well as of the fresh mixture was computed by using GASEQ (chemical equilibria in perfect gases, Version 0.79). By applying equation 6.37 the Gladstone-Dale constant was derived and is shown as a function of the equivalence ratio in figure 6.13 for the combustion of ethanol ($C_2H_5OH$ or $C_2H_6O$), with the assumption of a premixed fuel-air-mixture. Appendix F shows the used reflective index per species to compute the Gladstone Dale constant as function of equivalence ratio.

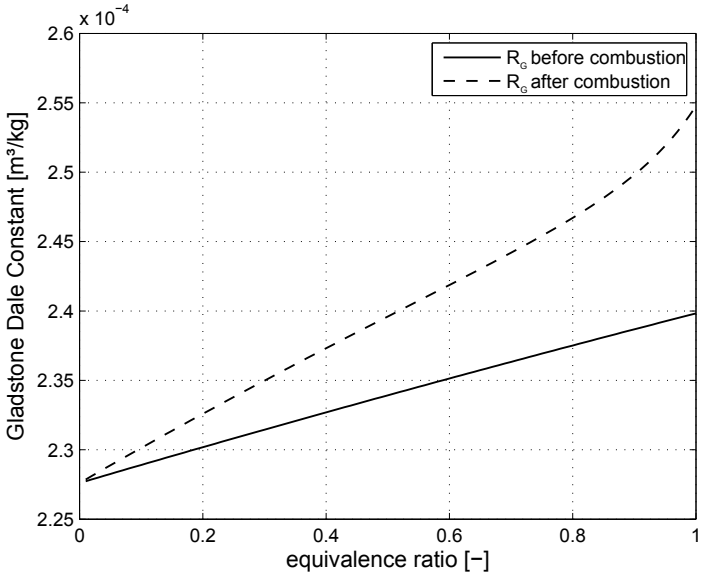


Figure 6.13: Gladstone Dale constant for combustion with ethanol

# Chapter 7

# Model combustor design

It has been shown previously that lean combustion technologies are susceptible to combustion instabilities. To investigate the unsteady combustion phenomena of an oscillating combustion chamber an adequate combustor had to be found. As TU Graz was involved in the analysis of the NEWAC LPP configuration the opportunity to characterize the stability of this combustor was taken.
This configuration is designed in a way that air at high pressure level for combustion is delivered by a radial HPC. But instead of feeding the combustor directly, the air is routed to the exhaust of the engine to be preheated in a recuperator, integrated into the nozzle of the core engine, first. After preheating the air is delivered to the combustor (LPP injectors). To avoid further ducting the air flow is entering the combustor against the main flow direction. Thus the design of the combustor is similar to an annular reverse flow type (see section 4.1). The HPT is located underneath the combustion chamber, which is common to reverse flow type combustors. Figure 7.1 is sketching the IRA engine.

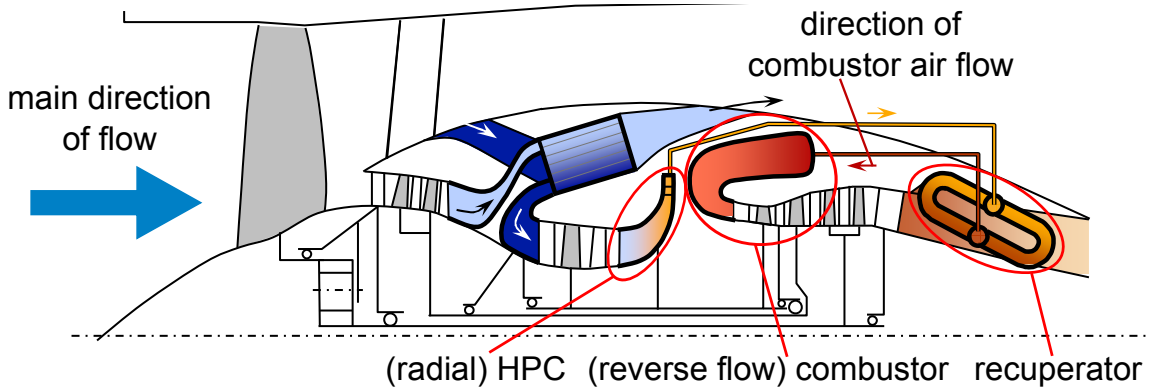


Figure 7.1: Intercooled Recuperative Aeroe Engine scheme; [3] modified

The full annular combustor design was developed by Turbmeca (TM; Group Safran) based on the LOPOCOTEP (LOw POlutant COmbustor TEchnology Project - European funded FP5 project) design by TM and Avio (Propulsione Aerospaziale).
The main task for the ITTM at TUG here is the general investigation of the stability of the LPP injector modules. With this thesis the visualization of combustion instabilities by using a laser based measurement technique (Laser Vibrometry - see section 6.2) shall be adapted to such an industrial type combustion chamber.
However, as optical measurements on a full annular configuration are not feasible, a model combustor with optical accessibility had to be designed. Furthermore to investigate the stability of the combustor in a broad frequency range, a novel flow exciter of the siren type

was developed to force excitation up to 1,000 Hz.
Prior to the development of the sector combustor for this thesis, two simplified combustion chambers had been designed to gain knowledge in combustor design, verify the measurement techniques and perform first experiments with a lower level of complexity.
Finally the sector combustion chamber, equipped with industrial type LPP injectors was designed by the author of this thesis. A sketch of the LPP modules, supplied by TM, is shown in figure 7.2 (the two prototypes delivered are called SER1 and SER2). Each of them consists of two main parts; the premixing tube and the injector itself. The fuel supply is connected to the injector via the fuel supply fitting. As fuel liquid propellants such as kerosene are designated. [redacted] The primary fuel injection can be treated like an air blast.


Figure 7.2: LPP module (by Turbomeca)

To excite the flow a novel designed flow exciter, called TUG siren was designed and will be presented. Afterwards follows a brief description of the first basic dump combustor design used. Finally the industrial type test sector is shown.

## 7.1 Flow Exciter

For the investigation of combustion instabilities it is sometimes necessary to artificially perturb the flow. This can be just because the combustor used for this type of investigation is stable at the operating conditions of the test bench, or several different frequencies of excitations are of interest. The use of a flow exciter gives the researcher the possibility to artificially generate combustion instabilities in a broad frequency range with varying amplitude to artificially excite combustion driven oscillations or amplify natural resonant frequencies related to combustion instabilities.

### 7.1.1 Type of flow exciters

Depending on the combustor under investigation and the infrastructure available, several flow exciters are used in the combustion community. The simplest of all is the loudspeaker. For simple combustor configurations (atmospheric conditions, low power flames) this type of flow exciter is very convenient to use. The loudspeaker is mounted upstream the flame

and attached to the air supply either directly or via an additional membrane. The frequency can be adjusted very simple by converting electronic signals into sound. The sound waves generate pressure perturbations in the flow that are finally interacting with the flame to generate a combustion instability at the frequency of the induced sound waves. It is also possible to induce white noise into the system to find Eigen-frequencies of the system which are strongly related to the frequencies of self induced combustion instabilities. The amplitude of the induced perturbation is related to the size of the loudspeaker and is thus limited for some applications. Experiments performed by using such a device can be found for example in [62, 63].
When more power is necessary thermo-resonators of the Schmidt Rohr type can be used. This exciter uses heat generated by a electronic heater placed inside a straight tube. The heated air lifts depending on the air speed inside the tube. The heat release rate and the air speed are directly coupled thus inducing a thermo acoustic instability [54]. This instability generates pressure perturbations which can be used to excite the air flow of a combustor. Using such a flow exciter adds more complexity to the system because the location of the electric heater is essential for getting into resonance with the tube used [54]. Also the frequency that can be excited is a function of the tube length used. Papers using this type of flow exciter are for example [64].
The most versatile flow exciter is of the siren type. Its principle is based on a rotor/stator configuration. Usually an electrical motor rotates the rotor thus pushing an air flow through the stator. Depending on the rotational speed of the rotor and the number of rotor blades a characteristic noise is generated ("Hiebton"=rotational speed x number of rotor blades). Such a device is given in [65]. The air ducting is more complex compared to a straight flow configuration using a sonic nozzle and a sprocket wheel like given in [66], which is called the ONERA siren. The siren used in [66] was designed for tests at cold flow conditions. The excitation frequency set could not be held precise and it also lacks the feature of an adjustable amplitude of the perturbation.
Thus a new siren for a broad frequency range that can be used in combination with a combustor working at elevated pressure and temperature conditions of the air supply was designed.
A peculiarity of mechanical sirens, the startup, which is a transient process, had also to be overcome. At the very low frequency range the air flow is perturbed quite strongly, meaning that the sonic hole is shut for a rather long time, leading in many cases to a flame out. To cover this problem a possibility to run the siren at full excitation frequency but with low amplitude of perturbation had to be found. This leads to the development of a servo drive for the sprocket wheel. The relative position to the sonic nozzle can now be varied, thus varying the amplitude of perturbation. Figure 7.3 is showing the basic concept of the novel TUG siren.

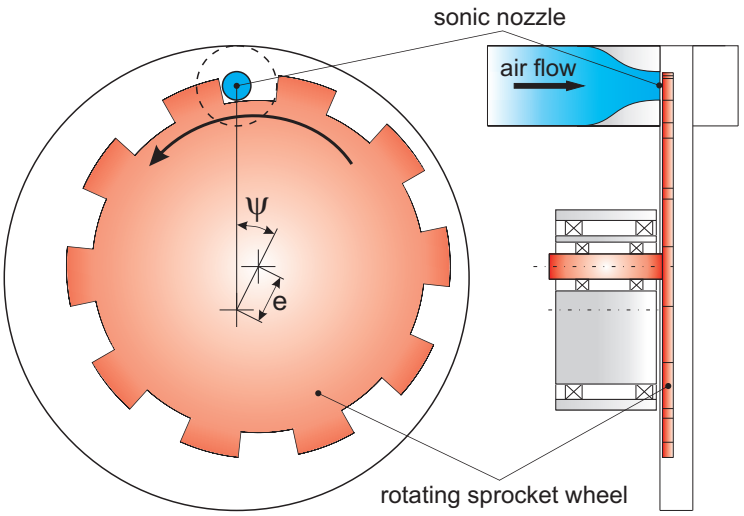


Figure 7.3: Design principle of the TUG siren

### 7.1.2 Design of the TUG siren

The TUG siren is broken down into several modules:

- Sonic nozzle/Sprocket wheel (flow exciting part)
- Drive train (bearing for the sprocket wheel)
- Servo drive (actuator for amplitude variation)
- Casing

Figure 7.4 shows a cross section of the siren with labels for the important parts.

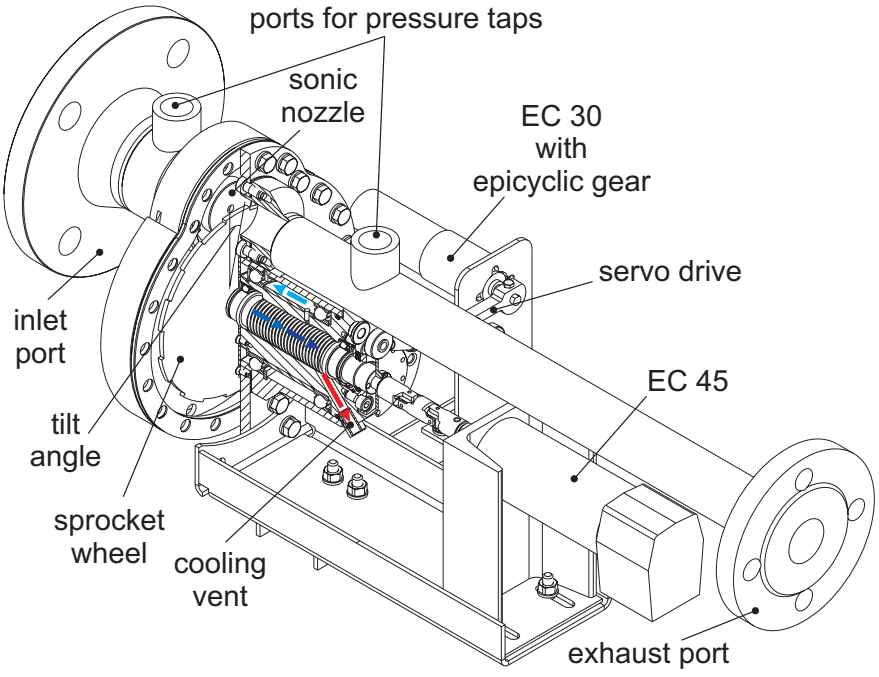


Figure 7.4: Cross section of the TUG siren

The most important module is the combination sonic nozzle/sprocket wheel. The main air flow passes through the sonic nozzle and is sheared by the sprocket wheel to introduce perturbations into the flow. The nozzle is presented in figure 7.5. The diameter at the inlet is given by the piping system used and the inner shape is formed to guarantee a lossless flow.

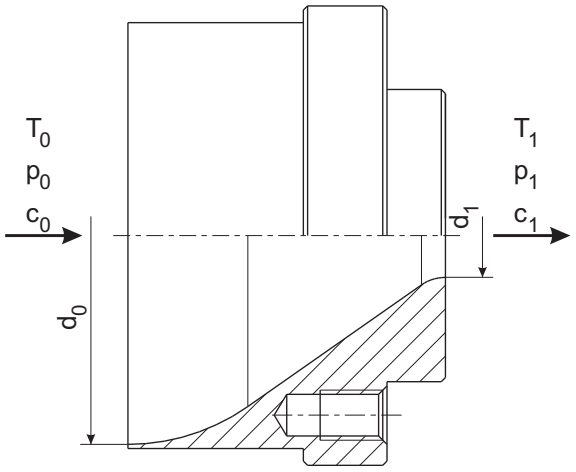


Figure 7.5: Design of the sonic nozzle

The diameter at the outlet was calculated in accordance with the formula given for simple nozzles with overcritical pressure ratio [67]:

$$\dot{m} = \frac{A_1}{v_0} \cdot \sqrt{2 \cdot p_0 \cdot v_0} \cdot \underbrace{\sqrt{\frac{\gamma}{\gamma - 1} \cdot \left[ \left( \frac{p_1}{p_0} \right)^{\frac{2}{\gamma}} - \left( \frac{p_1}{p_0} \right)^{\frac{\gamma+1}{\gamma}} \right]}}_{\psi} \tag{7.1}$$

For ideal gas conditions and two atomic gases like air, the maximum of the function $\psi$, representing a critical state, reaches $\psi = \psi_{max} = 0.484$. After some conversion of equation 7.1 and using a circular area for the outlet condition one will find

$$\dot{m} = \frac{0.685}{R \cdot T_0} \cdot p_0 \cdot r_1^2 \cdot \pi \tag{7.2}$$

With this the mass flow for the siren is only a function of temperature and pressure at inlet conditions. Figure 7.6 shows this graphically. The continuous bold line represents the operating conditions the siren will face during experiments in the test rig at $p$ =5 bar with a nozzle diameter of $d$ =10 mm. This is only valid if the critical pressure ratio, defined by equation 7.3 is reached [68].

$$\frac{p_0}{p_1} = \left( \frac{\gamma + 1}{2} \right)^{\frac{\gamma}{\gamma+1}} \tag{7.3}$$

For an ideal gas with $\gamma = 1.4$ the pressure ratio $p_0/p_1$ has to reach 1.89 so that the above mentioned correlation can be used.

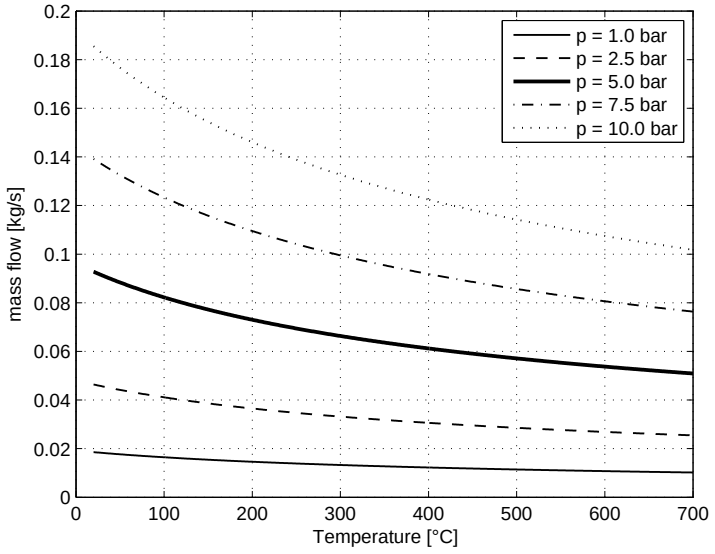


Figure 7.6: Mass flow through a sonic nozzle as function of back pressure ($p = p_0$) and temperature; nozzle diameter $d$ =10 mm

In addition further sets of nozzle/sprocket wheels were manufactured with a nozzle diameter of $d$ =8 mm and $d$ =5 mm respectively. For the design of the sprocket wheels a Matlab tool was developed to investigate the impact of tooth shape on the pulsation. Two types of tooth forms were studied. First a sinusoidal one followed by a simple rectangular shaped tooth. The arrangement nozzle sprocket wheel and the resulting free area of the nozzle as function of rotational angle can be seen in figure 7.7 for four pulsation cycles. It can be seen that the simple geometry gives the best results in terms of homogenous area blockage. Thus the second type of sprocket was used throughout the experiments.

The frequency of excitation of the flow can be set by adjusting the rotational speed of the direct current motor (maxon motor EC45 with 250 W nominal power, equipped with an HEDL 9140 encoder, giving 500 impulses per revolution) that is used. By changing the number of teeth used on the sprocket wheel the upper bound of frequency can be set. The maximum rotational speed set by the motor itself is limited to 6,000 rpm with the specific type used herein and as shown above, 10 teeth are used on the sprocket. By using equation 7.4 the upper limit of frequency is computed to 1,000 Hz.

$$f = \frac{n}{60} \cdot z \tag{7.4}$$

Due to the use of a digital encoder and positioning control, the precision in frequency lies in a narrow band. The uncertainty in frequency can be expressed as

$$\Delta f = f \cdot \tau \tag{7.5}$$

with $\tau$ =50 $\mu s$ response time of the digital encoder used. Figure 7.8 is giving the precision that can be set as function of excitation frequency up to 1,000 Hz, which bound the uncertainty by 5 %.

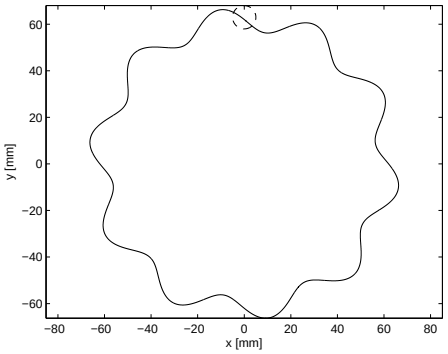


(a) Sinusoidal shaped sprocket

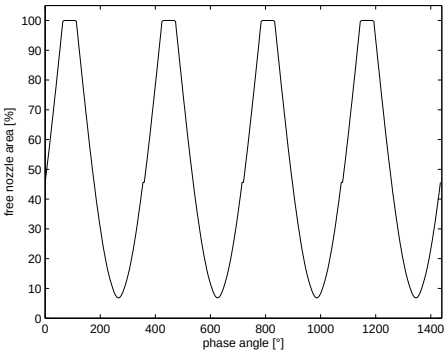


(b) Free area evolution for sinusoidal shaped sprocket

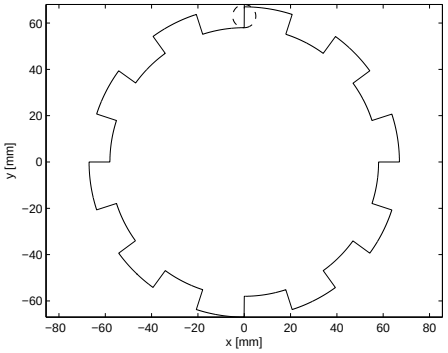


(c) Rectangular shaped sprocket

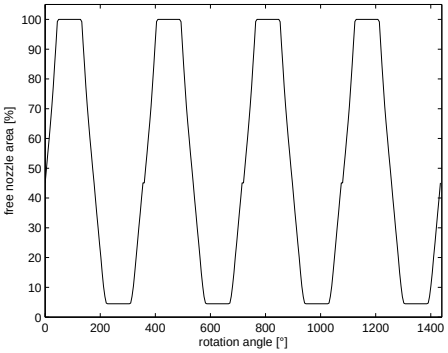


(d) Free area evolution for rectangular shaped sprocket

Figure 7.7: Different ensembles of critical nozzle/sprocket wheel

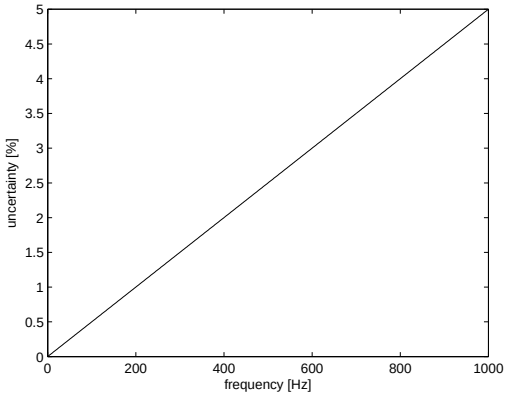


Figure 7.8: Precision of excitation frequency

To not only control the frequency of excitation but also the amplitude, the blocked vs. free nozzle area had to be varied. This was done by changing the relative position of nozzle and sprocket. For the TUG siren the bearing of the siren axle was thus eccentric bedded to the rotation axis of the servo drive by 5 mm. A second servo motor was linked

to the eccentric by a strut. Thus by revolving the servo drive the position of the sprocket was shifted. As drive gear a motor from Maxon motors AG, type EC-max 30, equipped with a HEDL 5540 encoder, supported by an epicyclical gear with a reduction gear $i = 86$ was used. The maximum continuous torque is 6 Nm, which was sufficient to drive the mechanism. The pulsation achievable with this mechanism, expressed as blocked area vs. free area (for the mathematical expression see equation 7.6, where $A_{free}$ denotes the free area of the blocked nozzle and $A_{max}$ is the full free nozzle area) can be seen in figure 7.9 as function of the tilt angle that can be set. The figure shows a combination of a nozzle with 10 mm diameter and a sprocket with 10 teeth for full blockage (outer diameter 134 mm, inner diameter 116 mm). By using the servo drive the sprocket can be tilted for 90° resulting in a perturbation range of 46÷96 %.

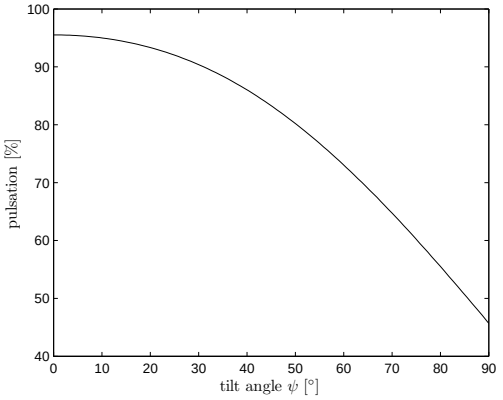


Figure 7.9: Pulsation of the siren as function of tilt angle

$$\text{pulsation} = 100 - min\left(\frac{A_{free}}{A_{max}}\right) \tag{7.6}$$

To use the siren in a harsh environment a cooling system, to cool the bearings for the axle and the positioning of the sprocket, was designed. Pressurized air is first pushed into the outer bearing case. Its direction of flow is against the main flow direction to enhance heat transfer. To cool the bearings of the siren axle, as well as the axle itself, a hole at the front bearings was drilled into the eccentric tappet. The air is entering through this hole to the inner zone of the siren and transports heat away from the bearings to the back of the baring case and leaves the siren through an exit port at the back end (see figure 7.4). The servo motors are coupled to a Maxon Motor EPOS 24/5 motor controller. The controllers are set by using National Instruments LabView 8 routines. Two separate tools were used to set the frequency of excitation and the corresponding amplitude respectively. For the frequency control it was possible to set the desired frequency up to 1,000 Hz in steps of 1 Hz. Furthermore the acceleration and decelerations could be set freely to adjust the desired approach ramp.
Similar inputs could be set for the amplitude controller. The user is free in setting the amplitude in terms of zero position to maximum tilt angle. The corresponding LabView routines were designed by Gradl [69].
Every motor control has a built-in overload protection to prevent overheat of the servo motors.

The positioning system of each motor (Hall sensor plus encoder) reports on the revolution speed and angular position respectively. For the revolution speed an analog output by use of an opto sensor (type photoelectric barrier HOA 2005) was introduced to be able to drive separate instruments (e.g. trigger input for LDA, PIV and so on). To receive a reference signal the output of the photoelectric barrier was transferred to a inverting Hex Schmitt trigger of type SN74HC14. The two threshold levels of this electronic device (0 V and 5 V) steepens the edges of the reference signal an thus improve the quality of the signal [70]. The trigger converter unit was designed by Siebenhofer [71].

## 7.2 Dump Combustor

During the first experiments done by Giuliani et al. [9] the application of the LV measurement technique adapted for combustion experiments has been proved. Experiments were performed at atmospheric conditions only. To further proof the functionality of the LV at elevated pressure conditions, a combustor that can be pressurized was designed.
It was decided to use a dump combustor design in single injector configuration. By doing so the complexity of the system for the first basic experiments at elevated pressure conditions is reduced. A cross section of the combustion chamber, with graphical representation of the main fluid flows, is shown in figure 7.10.

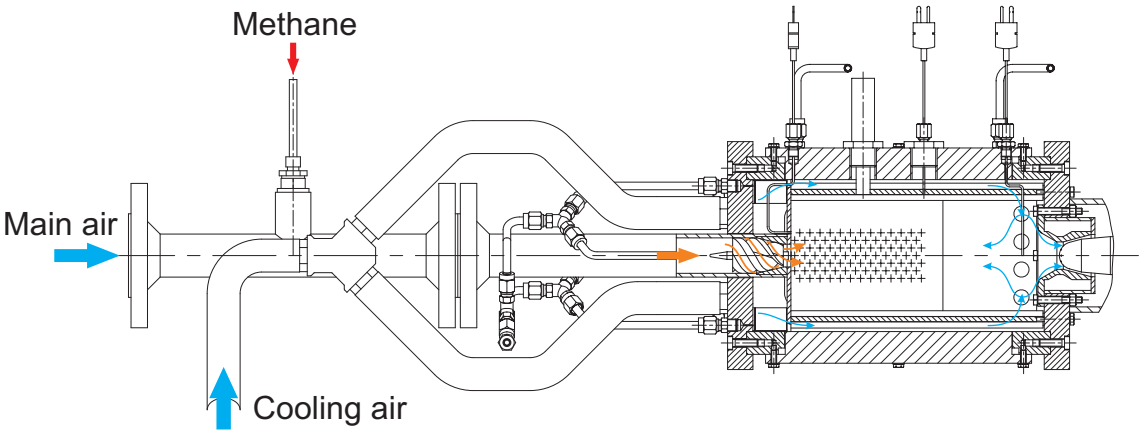


Figure 7.10: Dump combustor design

The injector is based on the design of Wagner [10], being of the axial swirler type. The dimensions of the combustor are in accordance with the combustor designed by Wagner and the design principle is based on an early DLR design of such combustors. More on the design of the combustion chamber can be found in [72].
During first experiments it could be seen that using Robax® for the optical accesses is critical as this ceramic based glass generates speckle patterns when using laser based measurement techniques. However, as it can withstand temperatures up to 873 K, first experiments with LV could be obtained at elevated pressure conditions (see section 9.1).
During the experiments several lessons regarding the design of the combustor and rig were learned and affected the design of the industrial type sector combustor test rig:

- **Optical access**; using quartz glass instead of Robax® to suppress speckle patterns. Furthermore the mounting of the glass had to be redesigned as bending of the fixture

resulted in rupture of the glass. Lateral pressing on the surface of the glass resulted in longer life time of the windows.

- **Flow exciter**; designed especially for eased operation at elevated pressure conditions. During the first experiments using the ONERA siren [66] the problem of flame out during start up procedure of the siren appeared. As the blockage of the nozzle is rather long at low excitation frequency the flame was simply blown out. To overcome this problematic, the TUG Siren with the features presented in section 7.1 was designed.
- **Ignition device**; as the ignition process is not a continuous one (sparks are generated in the order of 10 Hz) the energy release of a spark can be too low or the equivalence ratio of the mixture could be in the wrong conditions for successful ignition. If this happens the combustor is filled with the mixture which can than lead to an explosion. So it was decided to use a torch igniter for smooth ignition (see chapter 7.4.5).

## 7.3 Single LPP combustor

To gain experience in the operation of a single LPP injective fed with liquid fuel, a small combustor was designed. The combustor is basically a simple straight tube with an inner diameter of 80 mm and a length of 200 mm. As it is dedicated for short duration experiments no cooling was implemented. Furthermore this design is in accordance with the primary combustion zone design by TM as this zone also has no cooling holes. Figure 7.11 shows the combustor with installed LPP injector.

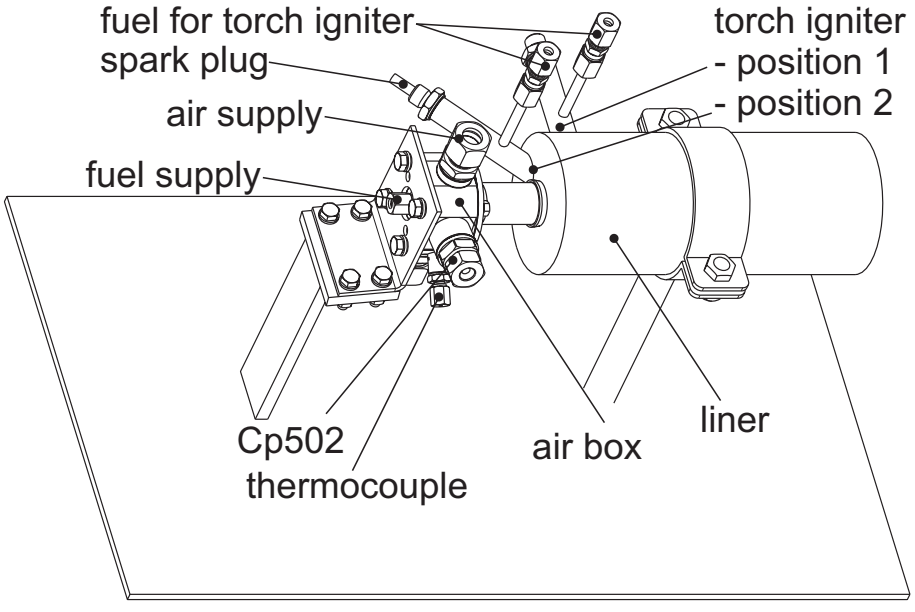


Figure 7.11: Single LPP injector test stand

As previously said the use of a conventional spark plug as ignition device resulted in rupture of the optical accesses. So it was decided to use a torch igniter instead. To investigate the optimum position for the torch this combustor was designed with two mounts for an

ignition system (labeled with torch igniter position 1 and 2 in figure 7.11).
Furthermore the single LPP combustor was used to perform first experiments with LV in a two phase flow environment (see section 9.4).

## 7.4 Industrial type LPP test sector

For the investigation of unsteady combustion phenomena in a industrial type combustion chamber at realistic operating conditions (elevated pressure and temperature), a test sector based on the IRA reverse flow type combustor was designed, with main focus on the primary combustion zone.
The test sector was installed in the combustion laboratory at ITTM, which was adapted to deliver the air feed necessary for the experiments. More on the test facility can be found in [12] and [13].
As only a sector, consisting of 2 main injectors and a pilot stage, were investigated ($7^{th}$ sector of the full annular combustor) the operating conditions in terms of mass flow are scaled to the proper size (see table 7.1 for details of the operating conditions of the full annular combustor).

Table 7.1: Operating conditions of the NEWAC IRA core combustor (full annular combustor setup)

| Condition | p [bar] | T [K] | $\dot{m}_{air}$ [kg/s] | FAR [%] |
|---|---|---|---|---|
| Take Off | 20 | 760 | 4.0 | 2.4 |
| Idle | 6 | 500 | 1.3 | 1.3 |
| Ground Cruise | 13 | 650 | 2.8 | 2.0 |
| Altitude Cruise | 7.7 | 580 | 1.6 | 2.0 |

The pressure level achieved with the configuration was $p = 5\,bar_{abs}$ in the test sector and set by using a throttle at the exhaust of the combustor. Ethanol was used as surrogate fuel for Kerosene. Temperatures of $T = 330 \div 380\,\mathrm{K}$ were sufficient for fuel evaporation. Figure 7.12 is showing a sketch of the hot flow test facility at the ITTM. The combustion chamber is marked by a red circle and labeled with test cell.

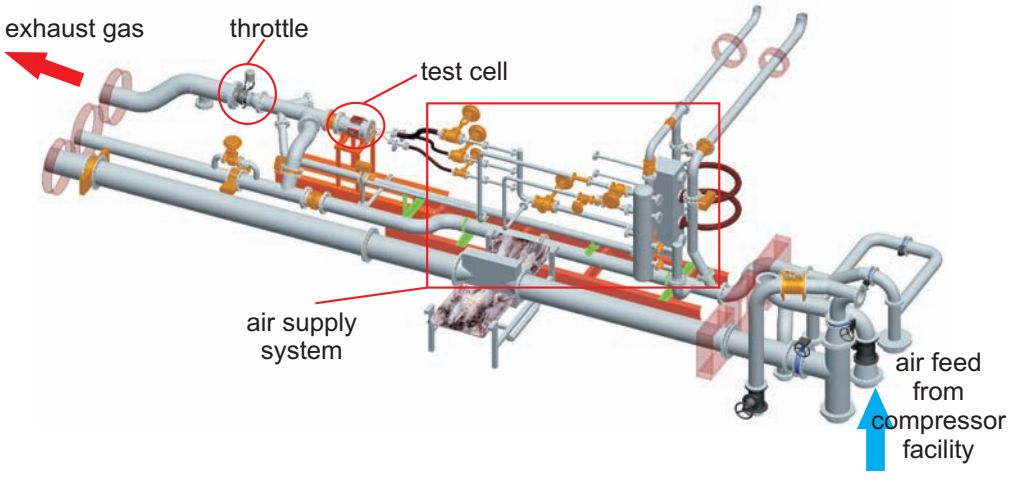


Figure 7.12: Hot flow test facility at the ITTM; by courtesy of Leitgeb 2011

Fuel is supplied via a separate pressure vessel connected to flow controllers for every injection module. More on the setup used for the experiments can be found in the section dedicated for the experimental setup.
The general design criteria for the test sector were as follows:

- **Modular layout**; of the pressure vessel to offer the possibility to use other combustors (liner) in the same test environment.
- **Optical accessibility**; for laser based measurement techniques as well as for monitoring of the experiment ("detection" of flame out).
- **Monitoring of operating conditions**; by using thermocouple, pressure taps and mass flow meters. The liner as well as the pressure vessel are equipped with temperature and pressure probes.

In the following the specific design features of the industrial type LPP test sector are presented. Figure 7.13 is showing a cross section of the test sector with labels for the most important parts.

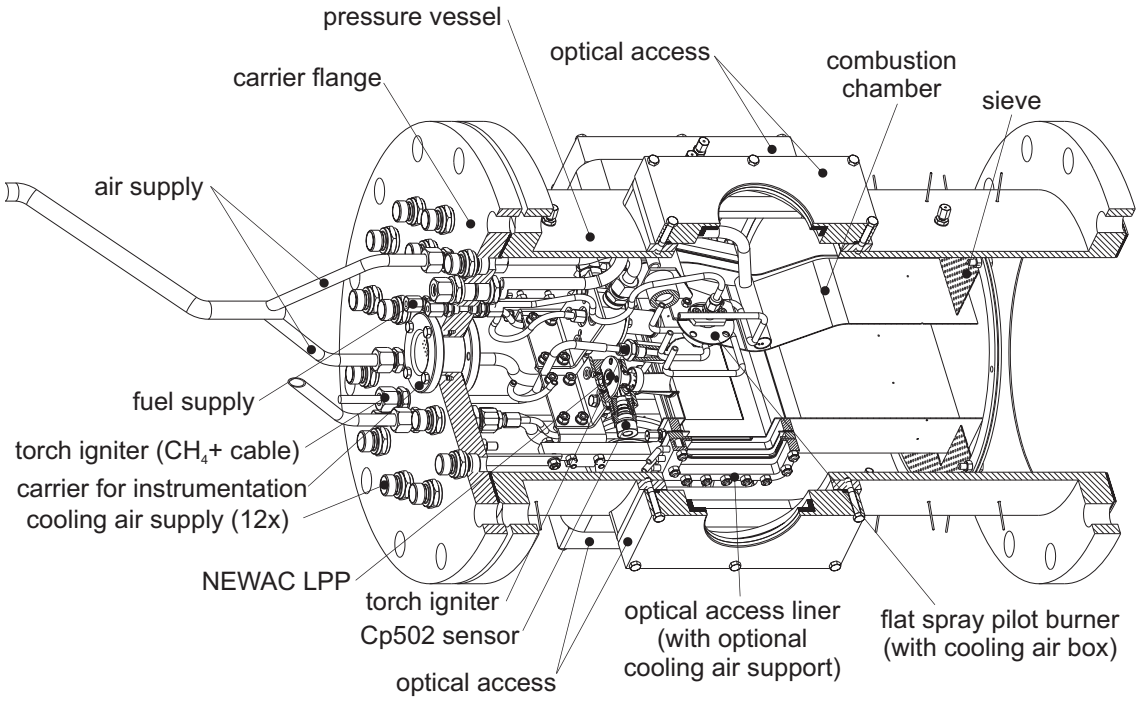


Figure 7.13: Cross section of the industrial type LPP test sector

### 7.4.1 Design guidelines for the LPP test sector

The design guidelines are based on the four drawings shown in figure 7.14, which were provided by TM. The general combustor layout is given in figure 7.14c. A cross section, showing an early design of the IRA core combustion chamber is given in 7.14b. As the combustor is a further development of the LOPOCOTEP combustion chamber, several dimensions are identical and thus are used for the design of the test sector too (figure 7.14a).


(a) Cross section of the LOPOCOTEP combustor


(b) Cross section of the NEWAC combustor (Version 2007)

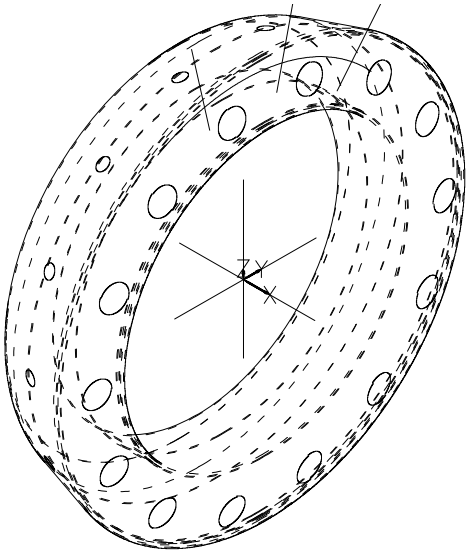

(c) Full annular NEWAC combustor

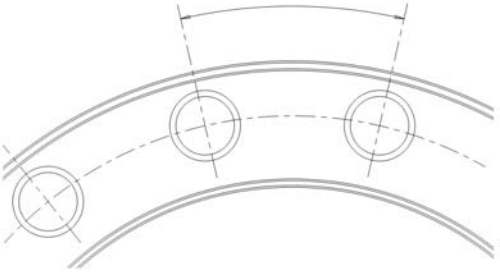

(d) Circumferential injector location at the NEWAC combustor

Figure 7.14: Design input parameter for the NEWAC test sector; provided by TM

The spacing of the injectors is derived from figure 7.14d, by computing the arc length from center point to center point of two LPP injectors. The location of the pilot injector is given in figure 7.14a, showing the first pilot burner concept. During later design stages the pilot shown here was substituted by a flat spray burner type with the same external dimensions.
By the design of the combustor 60 % of the air for combustion is entering through the LPP injectors. This is all the air used in the primary combustion zone. Attention has to be payed that any cooling air for the liner walls does not interfere with the primary air. Additional 2.5 % of air are entering the primary zone via the pilot burner. It was agreed with TM to use dedicated air feeds for the LPP injectors to know the exact amount of air entering the combustion zone.
To perform optical investigation the lateral walls of the test sector have to be cut out and

give the possibility to mount glass panels.
Ignition of the modules should be achieved by using a torch ignition system. The torch will be used to lighten up the pilot burner (the torch should thus face the pilot fuel spray cone) first. The burning kernel of the pilot should than develop towards the LPP modules and finally trigger the combustion process of the LPPs.

### 7.4.2 Liner of the LPP test sector

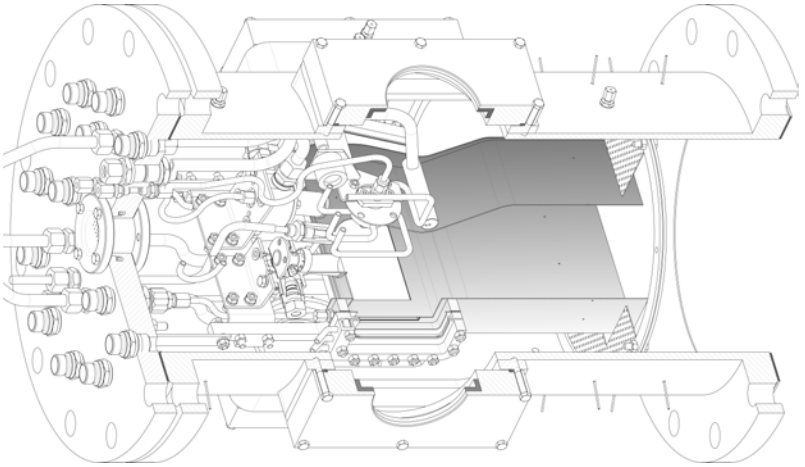

The design of the liner is straight forward. The inner shape of the thermal shield of the primary zone is reproduced in accordance with figure 7.14a and 7.14b. The main combustor layout is given in figure 7.15 and 7.16 respectively. As there is no cooling of the liner intended, the outer liner casing was not designed. As sheet metal steel grade 1.4471 was chosen with a thickness of 1 mm. To represent the bending of the combustor towards the HP turbine the liner walls were elongated to match this cross sectional area. A diffusor was placed after this constriction to receive a larger area ratio to dispense the hot exhaust gases thus lowering the thermal stress of the liner walls.

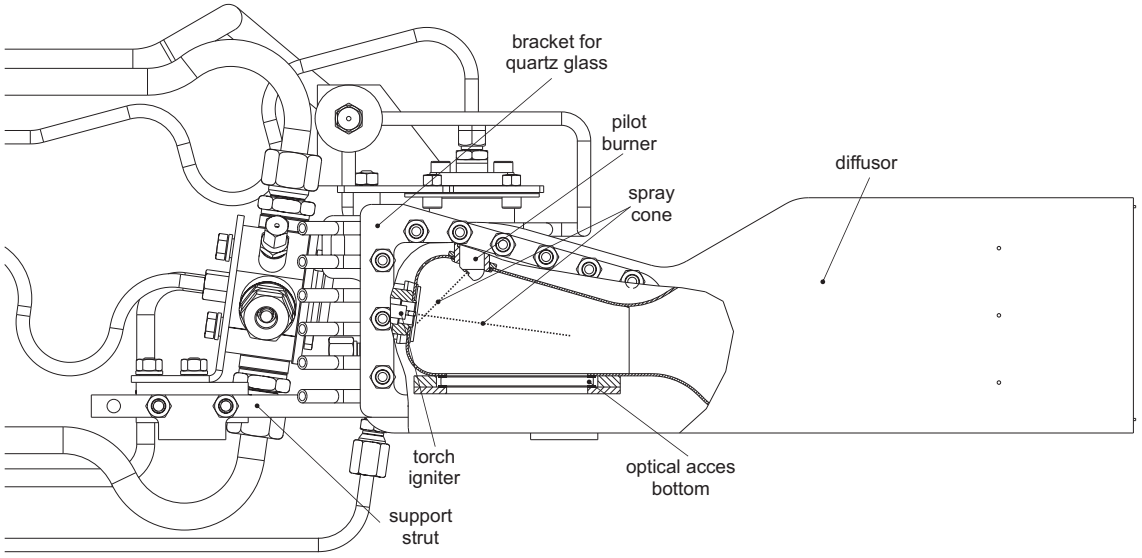


Figure 7.15: 2D cross section through the liner of the NEWAC test sector

Figure 7.15 represents a 2D cross section of the liner. It can be seen that the premixing tube does not have a shoulder to fix it onto the liner. A copper ring is thus used to seal the annulus by pressing the ring against the liner head plate (see also figure 7.2). The pilot burner is fixed in a similar way.

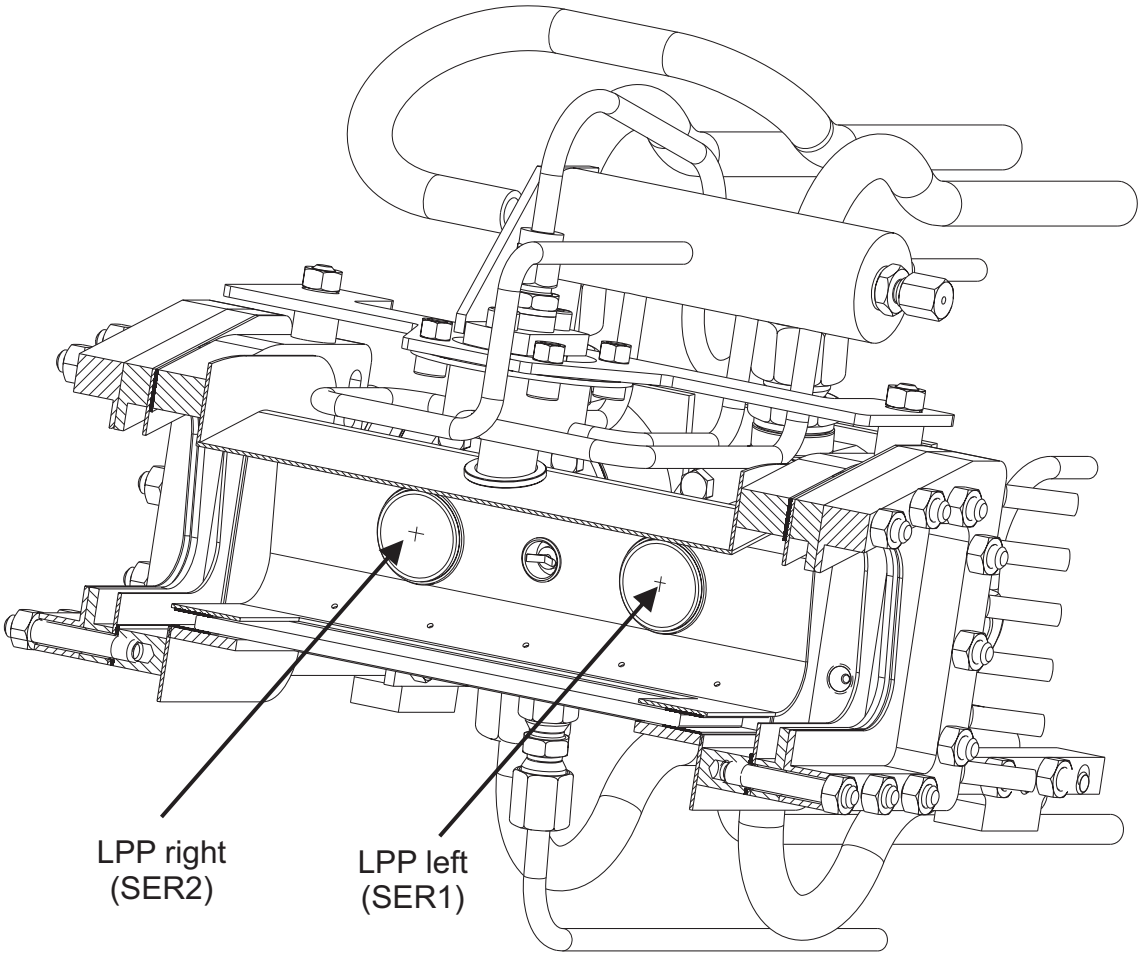


Figure 7.16: 3D cross section through the liner of the NEWAC test sector

The optical accesses are designed such as to ease the replacement of broken quartz glass. The lateral glass is inserted in the supporting struts that also forms the mounting brackets for the liner. Carbon sealing is used as spacer to protect the quartz glass from both sides. Brackets for the optical accesses are installed and hold the glass in place. Attention has to be payed not to over tighten the bolts as the risk of braking glass rises. The glass has to sit snugly so that the elongation of the liner during operation can be compensated. A second system for mounting the quartz glass was also designed (shown in figure 7.15). Its purpose is to offer the possibility of a separate cooling air flow. As no cooling air is allowed in the primary combustion zone the cooling air film is introduced between two windows. During the experiments it was found that it is not necessary to cool the windows separately to protect the from rupture. More of importance is the fact that if the quartz glass is to close to the flame it will locally melt and form pattern as soon as it cools down. Furthermore it was noticed that any residue inside the combustor, or dirt from the compressor facility burns onto the surface. A replacement of the quartz glass after three or more test runs was sufficient.

To also ease the replacement of the bottom glass, the supporting structure is formed to make it possible to replace the glass through the lateral optical access. Here too the supporting structure is designed quite robust as the bottom window is reaching over the whole depth of the combustor (see figure 7.16).
For monitoring purpose the liner was equipped with thermocouple and pressure taps. The instrumentation to monitor the operating conditions can be found in annex D.
During the ignition experiments with the single LPP combustor it was found that it is possible to place the torch igniter on the head plate of the combustor. The ignition device was thus located between both LPP modules of the test sector. By doing so it is possible to ignite the LPP modules even if the pilot burner is out of operation (for reasons of safety a combustion process has to be granted even if one type of injector is not operable).
As the cooling of the liner is done by forced convection from the outside of the liner only, it was intended to further use impingement cooling for the bottom optical access and the strong bend short before the diffuser.

### 7.4.3 Combustor air feed of the LPP test sector

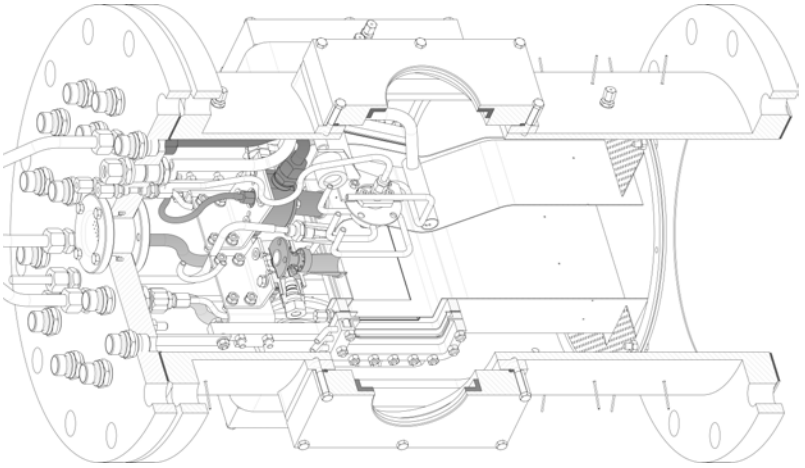

The air for combustion in the primary zone is injected via the LPP modules only (60 % of total air mass flow). To regulate the air feed independently from the cooling air flow and to be able to artificially excite one injector without disturbing the other one, an air box was designed. Figure 7.17 shows the injector SER1 installed in such an air box.
The major constraints for the design of the air box are the dimensions of the combustor, as two LPP modules have to be placed in a rather short distance. As the torch igniter will also be placed between the two LPP modules enough space has to be available for the spark plug and the fuel supply for the torch (for more details see section 7.4.5). The depth of the air box is given by the clearance between the premixing tube and the injector itself (see figure 7.2).
To supply the injector with enough air two hoses are connected to the air box.
For monitoring of operating conditions a pressure tap and a thermocouple are installed. Furthermore the air box for SER1 is designed with a port for a pressure transducer to monitor the stability of combustion.
As the [redacted] flow channels of the injector are aligned with the clearance hole for the attachment bolts the alignment was done in accordance with figure 7.18, showing the injector SER2 on the left and SER1 on the right. The view is against the flow

direction of the combustor. [redacted]

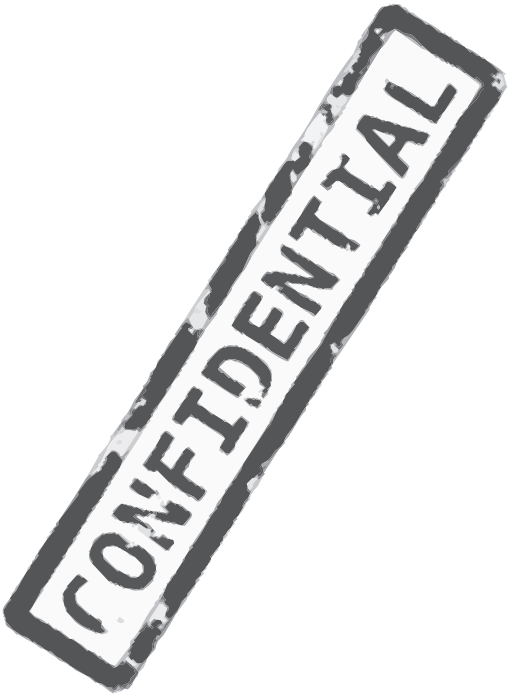


Figure 7.17: Air box with installed NEWAC LPP injector; labels for the major parts and air/fuel feed lines


Figure 7.18: Alignment of the LPP injectors; left: SER2, right SER1; flow direction: out of plane

### 7.4.4 Pressure casing of the LPP test sector

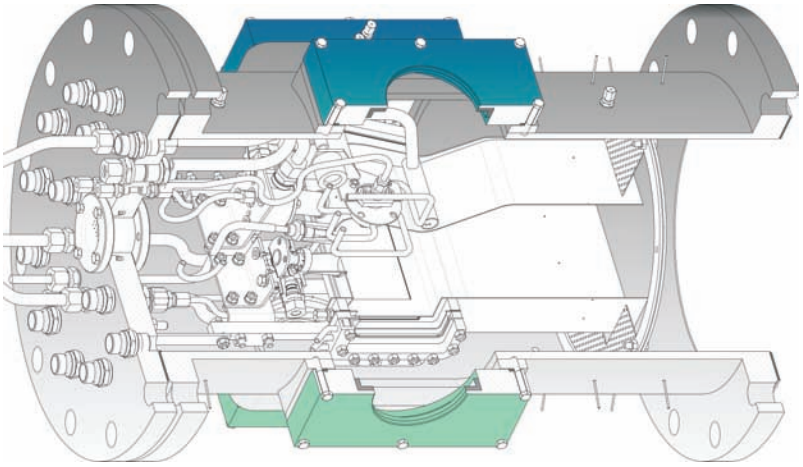

To perform experiments at elevated pressure conditions the combustion chamber has to be pressurized. This is achieved by using the pressure vessel shown in figure 7.19. The vessel consists of a tube with nominal diameter $DN = 300\,\text{mm}$ and a thickness of 10 mm to withstand pressures up to $10bar$ at elevated temperatures (up to $300°C$).

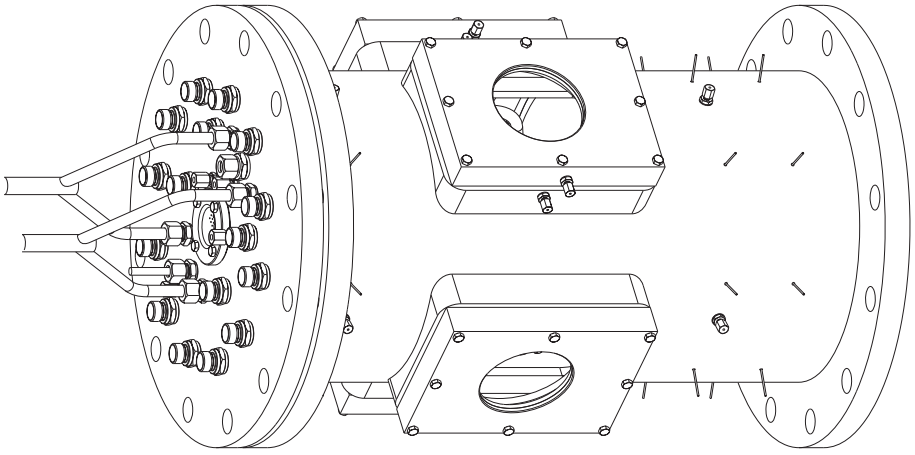

Figure 7.19: Pressure vessel of the LPP test sector

The four optical accesses are in alignment with the ones used in the liner. The design itself is based on the standard for sight glasses (DIN 7080). The chosen dimensions are for a nominal bore of 100 mm and a pressure rating of 16 bar leading to a thickness of the glass of 20 mm. All optical accesses were pressure tested up to 16 bar. Figure 7.20 shows the setup. The glass is embedded in a silicone sealing to avoid any force on the fragile glass. However, it has to sit tight to get a leak proof assembly.

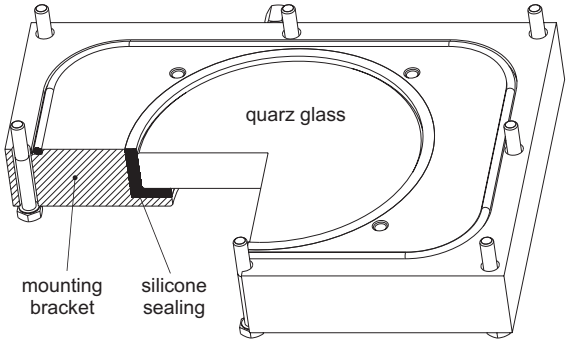


Figure 7.20: Optical access for the pressure vessel

For monitoring of the operating conditions several pressure taps and thermocouple are used. They are located circumferential around one line at the inlet, and in two lines at the exhaust of the vessel. At the exhaust a sieve is installed to generate a pressure drop to ensure that no air can recirculate into the combustion chamber. One line of pressure taps is therefore installed before and one after this sieve for monitoring.
To ensure an easy assemble of the combustor and a versatile design, all measurement leads (thermocouple, pressure taps and pressure transducers) are routed via the mounting flange (see figure 7.13). Furthermore all air and fuel feed lines are linked to this flange too. Also the ignition device is supplied with gas through the flange.
Cooling air to keep the temperatures at the liner and especially at the inner circumferential of the pressure vessel low is supplied via 12 cooling air hoses.

### 7.4.5 Ignition device of the LPP test sector

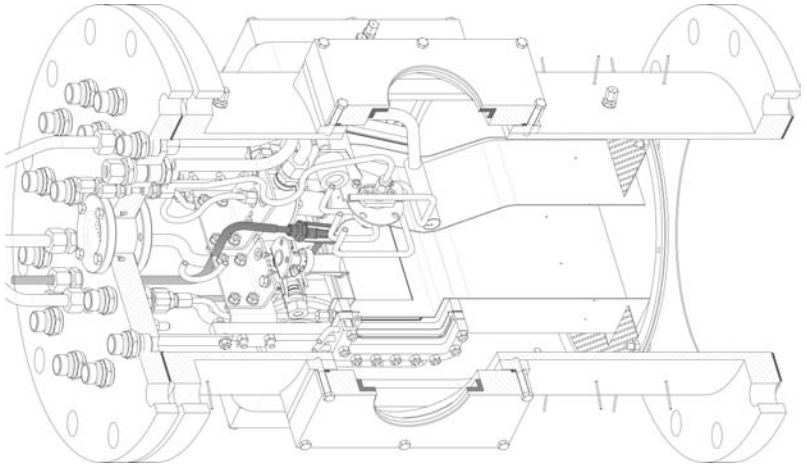

To reduce the measurement time ignition should be possible at elevated pressure conditions. A method had thus to be found to ignite the mixture without endangering the optical accesses.
The usual method of using spark ignition was done during experiments performed with the single gaseous combustion chamber (see chapter 7.2). As the problem of detonation arouse another method had to be found. The most promising method for this purpose is the use of a torch igniter. To further ease the ignition process methane as a combustible

was used for the torch due to the fact that gaseous fuels are more easily to ignite. Liquid fuels have to be evaporated prior to ignition so that more energy is needed. Also a torch is little effected by the location of the device. This gives the possibility to place the torch between the two LPP injectors. The main drawback of such devices however is the problem of cracking and gumming, occuring if the injectors are not operable [34]. During the experiments it was found that the majority of ignition failures were due to coking residue on the grounding of the torch igniter.

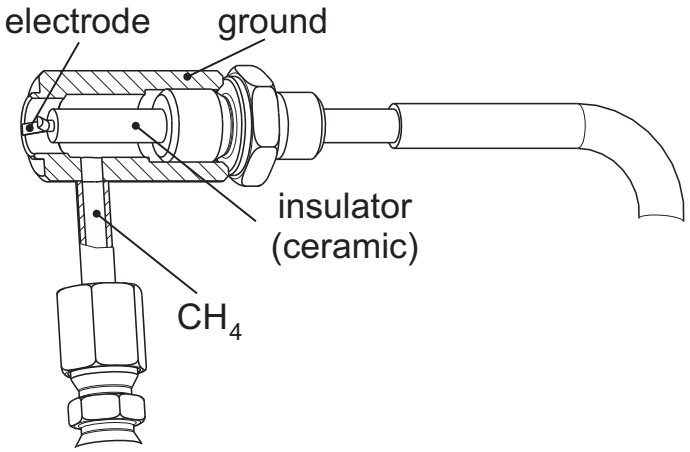


Figure 7.21: Torch igniter

The design of the torch igniter is represented in figure 7.21 showing the ground (acts also as mount for the spark plug), which is welded onto the head plate of the flame tube, the electrode and its insulator made of ceramic as well as the fuel feed line for Methane ($CH_4$). The concept is based on the DLR H2-lance. The first concept was developed by Audrey Camps [73] which was then adapted to the test sector.
During an ignition process methane is routed via the lateral bore to the electrode. The electrode of type *Universal Zündelectrode* (insulator ∅6/55 mm, electrode ∅3/100 mm) is bended towards the ground to receive a tiny gap. If the ignition box (type *Beru Zündgerät*, with a secondary circuit delivering 7.5 kV and 40 mA) is activated the spark produces a continuous arc discharge. The spark plug used delivers a power of 300 W, which is rather low compared to the common spark plugs used in jet engines (common are systems with 2,000 V and 200 A resulting in a power of 0.4 MW [14]).
Through the ignition system only the combustible is routed. The air necessary for combustion is taken from the combustor itself. As soon as the methane is ignited the torch lightens the pilot flame. The LPP's are then ignited via the pilot burner.
As the ground of the ignition device is coupled to the whole test stand attention has to be paid to the overall grounding of the test bench. Furthermore the back end of the torch igniter has to be properly insulated as the space between the air box and the torch igniter is limited.
A *Möller Easy 412-DC-DR* control relay is used for controlling the gas supply and the ignition box. The control panel consists of three solenoid valves, one for methane, one for nitrogen and a 3/2 way valve connected to the torch (see figure 7.22). Nitrogen is used as purge gas for reasons of safety. If ignition is not successful after a few seconds the combustor is purged with nitrogen to prevent detonation of the accumulated fuels in the test cell.

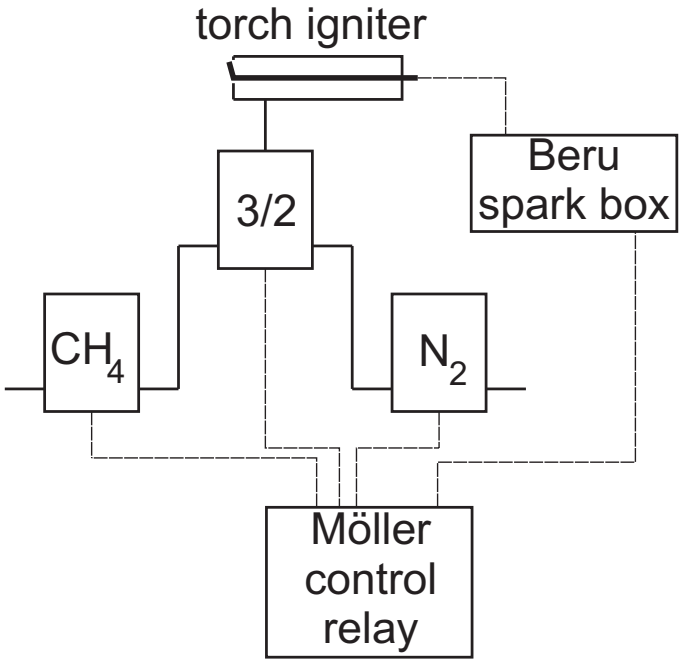


Figure 7.22: Schematic of the ignition control

# Chapter 8

# Experimental Setup

In this chapter the experimental setup, for the various measurements performed, will be presented. The operating conditions for the experiments are also given in this section. If the operating conditions were changed during the experiment, detailed information can be found in the results section at the specific experiment.

## 8.1 Setup for dump combustor experiments

The dump combustor experiments were performed at the combustion laboratory at TU Graz, using the in house air supply. As fuel methane, supplied from a pressure vessel and metered by using an Aalborg flow meter type GFM77A-VGDL2-BoA (Aalborg Instruments & Controls, Inc., New York, USA) was used. For the mapping of density fluctuation the primary combustion zone of the dump combustor was scanned, using a LV (see section 6.2 for more details) mounted on a Leightweight traversing system from Dantec. The measurement grid of the LV measurements is shown in figure 8.1, superimposed by a picture taken from the flame. The field of view used was 40x100 $\mathrm{mm}^2$, consisting of 91 measurement points. Data acquisition was done using National Instruments BNC-2110 I/O device linked to a PXI 1033 chassis and controlled by National Instruments LabView8.0. The data rate was set to 40 kHz collecting $400,000$ samples. During the measurements the ONERA siren was used to artificially excite the flow at 540 Hz. As reference signal a pressure transducer of type CP502 from Piezocryst was used.

Table 8.1: Operating conditions for dump combustor experiments

| | atmospheric | pressurized | |
|---|---|---|---|
| Main air mass flow | 6 | 6 | $[g/s]$ |
| Cooling air mass flow | 25 | 25 | $[g/s]$ |
| Air temperature | 285 | 285 | $[K]$ |
| Reduced overall air mass flow | 0.1 | 0.05 | $[kg/s \cdot \sqrt{T}/p]$ |
| Fuel mass flow | 0.5 | 0.5 | $[g/s]$ |
| Equivalence ratio | 0.7 | 0.7 | $[-]$ |
| Reference velocity | 27.1 | 12.8 | $[m/s]$ |
| Combustor pressure | 1 | 2 | $[bar_{abs}]$ |

Two campaigns have been performed. The first one at atmospheric conditions and the second one at 2 $\mathrm{bar}_{\mathrm{abs}}$. The detailed operating conditions can be found in table 8.1.

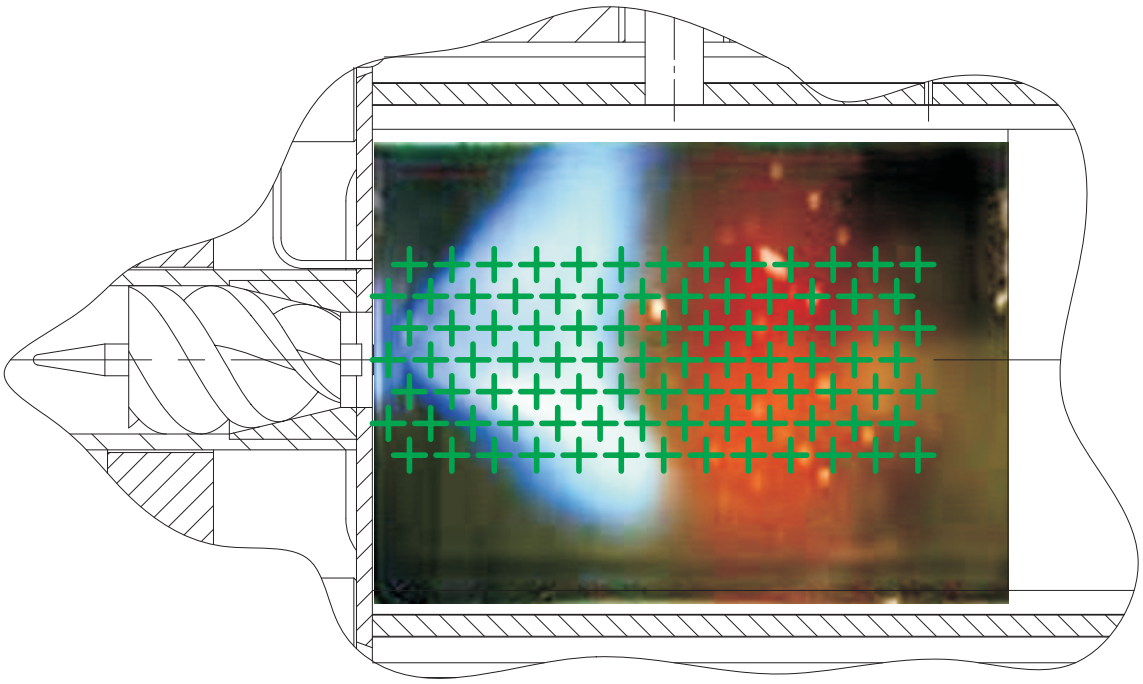

Figure 8.1: LV measurement grid during dump combustor experiments

## 8.2 Setup for isothermal flow characterization

For the isothermal flow characterization LDA measurements at ambient conditions have been performed, using the system described in section 6.1. As the system used is a two-component system, velocities in two perpendicular directions can be measured simultaneously. For a full examination of the flow velocity in three dimensions the probe was thus rotated by 90° to receive the third velocity component too. Figure 8.2 is showing the measurement setup including the orientation of the laser optics. To improve the quality of the measurements the optic was tilted by 45° to detect in both fringe patterns nearly the same velocity magnitude. The positioning of the optical emitter/detector was done with a DANTEC Lightweight traverse. As tracer DEHS (di-ethyl-hexyl-sebacat) with a characteristic size of 0.3 microns was added to flow upstream of the siren. The traverse as well as the acquisition was controlled by DANTEC BSA Flow Software 1. 2. The recorded velocity components were exported to Matlab for further data evaluation. The velocity components $u$, $v$ and $w$ are measured in laboratory coordinates and not the burner's axis (see figure 8.2). However, for computation of the swirlnumber a transformation with respect to the burner's axis has to be done to compute the axial and tangential velocity components.
Operating conditions were set to match a reduced mass flow of $\dot{m}$ =0.25 kg/s$\sqrt{\mathrm{T}}$/p.

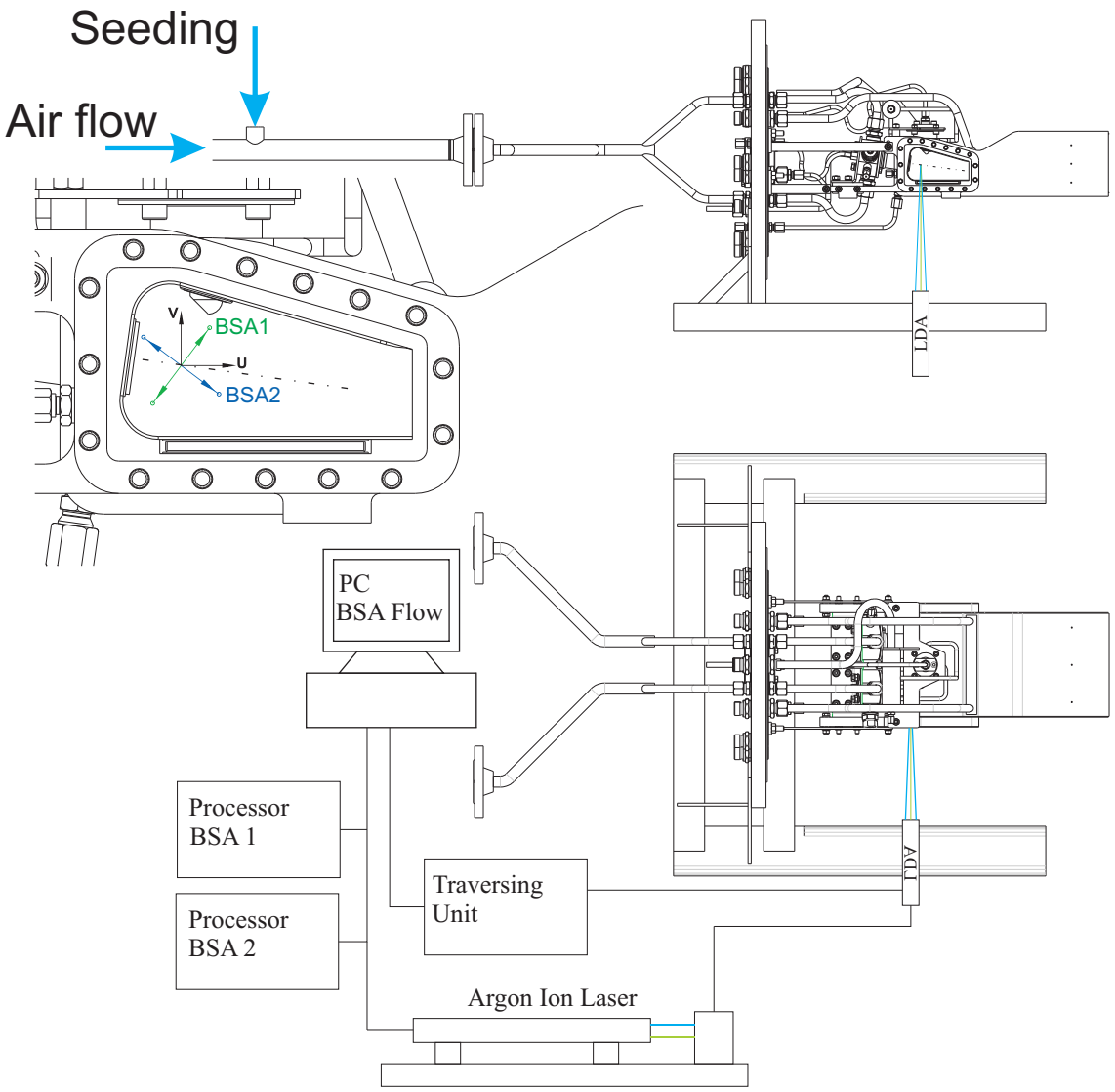


Figure 8.2: Measurement setup during isothermal flow characterization

## 8.3 Setup used to characterize the siren

For these experiments the siren was equipped with the nozzle having an orifice of 10 mm and the sprocket wheel consisting of 10 teeth and giving full blockage of the nozzle. With a smaller sprocket the perturbation was not strong enough to overcome the damping due to the complex ducting.
The operating conditions were set like shown in table 8.2. Figure 8.3 shows the setup used during the experiments.
The opto sensor located on the sirens shaft facing a chopper wheel was used as reference signal and was routed to the BSA processors of the LDA system to acquire phase resolved data.
A pressure transducer from PCB Piezotronics (type PCB106B50) was installed in one of the ports for pressure taps to report on the perturbation and act as a second reference signal.

The air for combustion is fed to the burners via two hoses linked to the air box. Thus damping of any upstream generated perturbation may occur. To determine the damping effect of the hoses and the air box a pressure transducer by Piezocryst (type CP502) is mounted onto the air box.
Inside the combustion chamber flow perturbation are detected by LDA and LV. The LV is used to record frequency spectra of density fluctuations in the perturbed flow. The LV was pointed near the center axis (approximately 4.7 mm above the axis and 3.7 mm downstream of the zero-point) of the left LPP module. During the LDA measurement it was not possible to align both lasers next to each other, so for the data sets recorded simultaneously with LDA, the LV was positioned at the lower left of the combustor. To eliminate the influence of the quartz windows (see section 9.3.2 for details), these were removed for the experiments using LV.
Perturbations in terms of velocity of the flow were measured by using a two-component LDA system. Positioning of the LDA system was done in the same way as previously described. At each of the four measurement positions 80,000 bursts were recorded to measure the velocity. The orientation of the laser beams can be seen in Figure 8.4.

Table 8.2: Operating conditions during evaluation of the siren attached to the NEWAC combustor

| **Modul SER1** | | | **Modul SER2** | | |
|---|---|---|---|---|---|
| $m_{air}$ | 14.50 | $g/s$ | $m_{air}$ | 13.50 | $g/s$ |
| $m_{red}$ | 0.25 | $kg/s \cdot \sqrt{T}/p$ | $m_{red}$ | 0.25 | $kg/s \cdot \sqrt{T}/p$ |
| $m_{fuel}$ | 0.0 | $g/s$ | $m_{fuel}$ | 0.0 | $g/s$ |
| T | 300 | $K$ | T | 300 | $K$ |
| $v_{ref}$ | 31.68 | $m/s$ | $v_{ref}$ | 29.50 | $m/s$ |
| **Pilot** | | | **overall equivalence ratio** | | |
| $m_{fuel}$ | 0.0 | $g/s$ | $\phi$ | 0.00 | [-] |

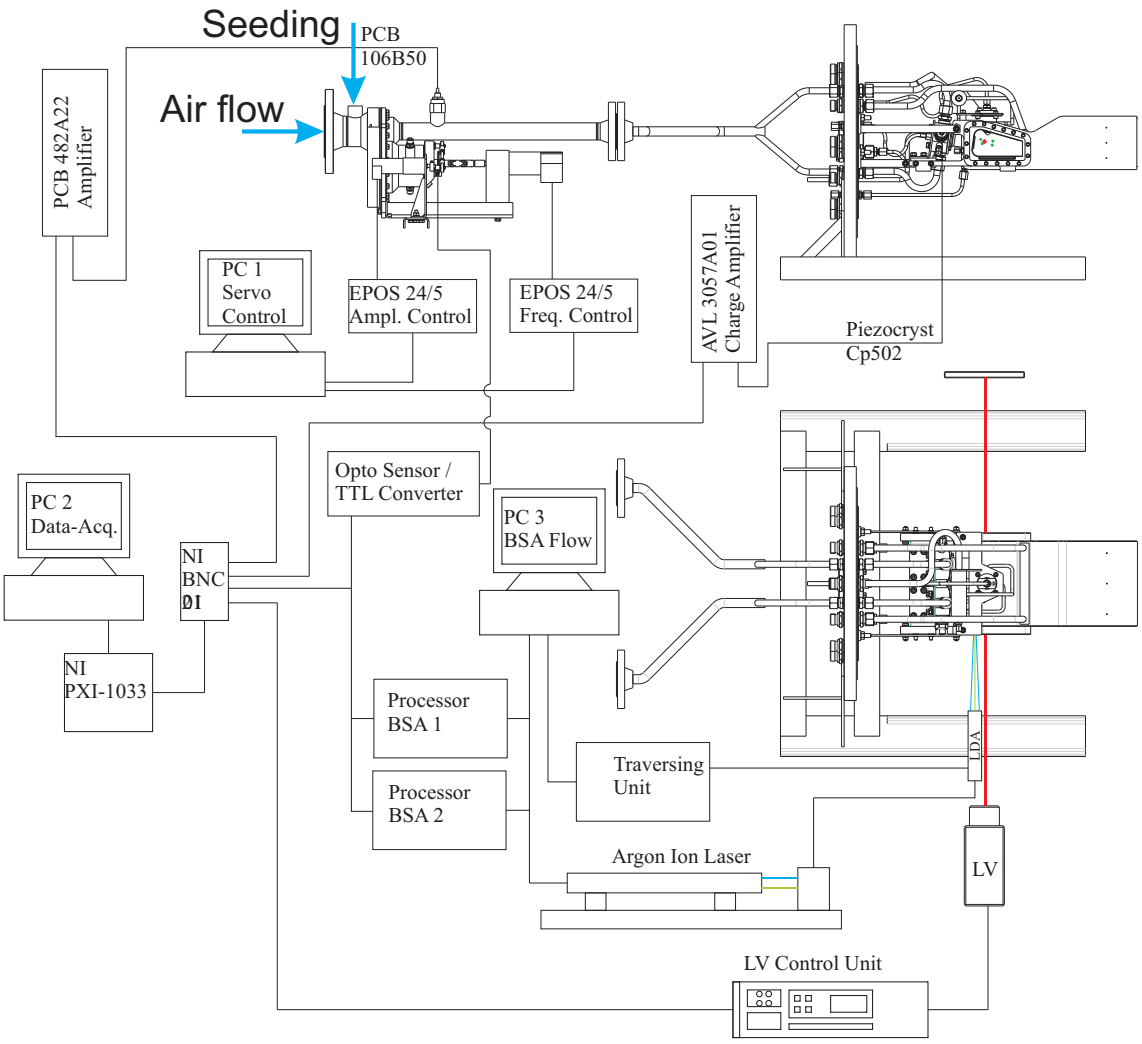


Figure 8.3: Measurement setup during validation of the siren

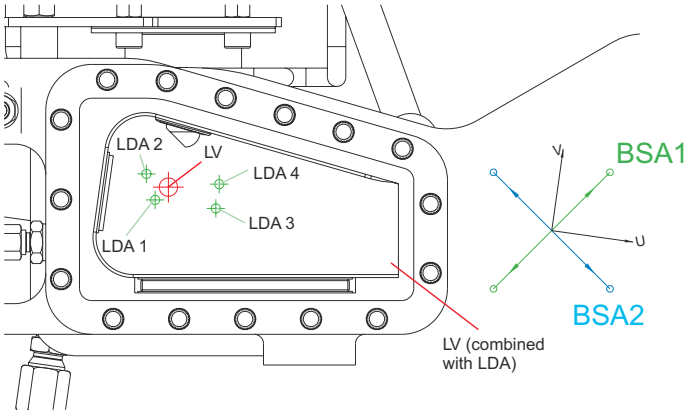


Figure 8.4: Location of measurement points for validation of the siren using LDA and LV

The coordinates for each optical measurement point are given in table 8.3.

Table 8.3: Location of measurement points for optical measurement

| | x [mm] | y [mm] | z [mm][5] |
|---|---|---|---|
| LV | 3.7 | 4,7 | line of sight |
| LDA 1 | 0.0 | 0.0 | 0.0 |
| LDA 2 | -4.0 | 8.0 | 0.0 |
| LDA 3 | 20.0 | 0.0 | 0.0 |
| LDA 4 | 20.0 | 8.0 | 0.0 |

Data acquisition of measurements other than LDA was performed by using National Instruments BNC-2110 I/O device linked to a PXI 1033 chassis. All signals were recorded simultaneously (four channels with sample rate of 40 kHz) by a user-defined routine developed using National Instruments Lab-View 8. 0.
The configuration was as follows:

- **Channel ai_0**: Opto Sensor / TTL Converter (reference signal).
- **Channel ai_1**: PCB106B50 Microphone as an additional reference signal.
- **Channel ai_2**: Piezocryst CP502 sensor to measure the perturbations inside the air box of the left LPP module. Amplifier (AVL 3057) set to 91 pC/bar.
- **Channel ai_3**: Laser Vibrometer to get information on the response of the combustor to perturbations induced by the siren. Controller Unit set to 5 mm/s/V.

## 8.4 Experimental setup during single injector stability analysis

Experiments were performed at ambient conditions using the test rig shown in figure 7.11 (section 7.3). The LPP module SER1 was aligned axially with the tube, surrounded by the air box capable of carrying the pressure transducer CP502. The air feed was given by two hoses connected to the TUG siren. The siren was equipped with a nozzle of 10 mm in diameter and the corresponding toothed wheel, consisting of 10 teeth and a diameter for maximum blockage of the nozzle. The air for combustion was delivered by the in-house pressurized air feed line. The air flow was metered by the use of a V-Cone.
Ethanol was used as fuel and supplied via a pressurized vessel. As pressure gas Nitrogen was used to prevent the formation of a combustible mixture inside the vessel. By making use of the back pressure inside the pressure vessel and the flow number of the specific injector the fuel mass flow was determined.
By using this simplified configuration first experiments with LV in a multi-phase flow were conducted.

As reference signals for the experiments the opto sensor of the siren as well as the CP502 sensor inside the air box were used.
At the exhaust of the combustor one Laser Vibrometer from Polytec of type OFV-353

[5] $z = 0$ is located at the center of the left LPP injector

was placed to detect any flow perturbations.

Data acquisition of the measured signals was done by using National Instruments BNC-2110 I/O device linked to a PXI 1033 chassis. All signals were recorded simultaneously (three channels with sample rate of 10 kHz, collecting 1M samples per channel) by a user-defined routine developed using National Instruments Lab-View 8.0.
The configuration was as follows:

- **Channel ai_0**: Opto Sensor / TTL Converter (reference signal).
- **Channel ai_1**: Piezocryst CP502 sensor to measure the perturbations inside the air box of the LPP module. Amplifier (AVL 3057) set to $95 pC/bar$.
- **Channel ai_2**: Laser Vibrometer to get information on the response of the combustor to perturbations induced by the siren. Controller Unit set to $5 mm/s/V$.

The measurement setup can be seen in figure 8.5.

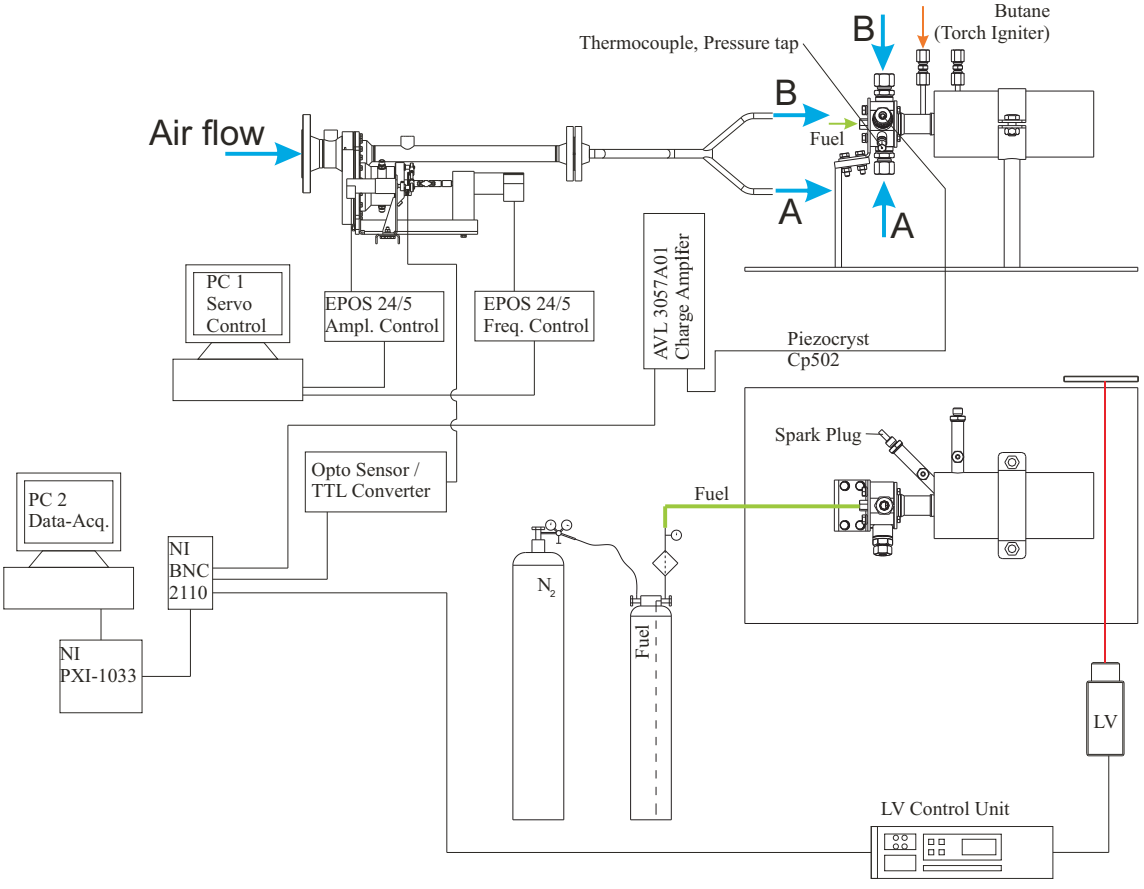


Figure 8.5: Experimental setup for single LPP injector combustion experiments

The operating conditions were set in accordance with table 8.4.

Table 8.4: Operating conditions for single LPP injector experiments

| | | |
|---|---|---|
| Air mass flow | 40.36 | $[g/s]$ |
| Air temperature | 291 | $[K]$ |
| Reduced air mass flow | 0.671 | $[kg/s \cdot \sqrt{T}/p]$ |
| Fuel mass flow | 2.43 | $[g/s]$ |
| Equivalence ratio | 0.54 | $[-]$ |
| Reference velocity | 82.36 | $[m/s]$ |
| Combustor pressure | 1 | $[bar_{abs}]$ |

## 8.5 Setup for isothermal flow stability analysis using the LPP test sector

The NEWAC combustor was installed into the pressure vessel and attached to the compressor facility via the air system. During all experiments the TUG siren was attached to the left LPP module (SER1). LPP SER2 as well as the flat spray burner were not artificially excited. Figure 8.6 shows the setup for the experiments performed during the test campaign. By making use of the throttle at the exhaust of the combustor, the pressure inside the liner was lifted to 5 $\mathrm{bar_{abs}}$.
All data concerning the operating conditions (temperatures, pressures, air mass flows) of the test rig were recorded using a Siemens Simatic S7 device, where the data acquisition is done by using National Instruments LabView. All control valves are controlled using a National Instruments LabView Tool (user defined routines). The control of the siren was done by a separate computer using the routines described in section 7.1.

As reference signals for the experiments the opto sensor of the siren, as well as the CP502 sensor from Piezocryst inside the air box, were used. The proper grounding of the sensor cable is crucial for the experiments to avoid a bad signal to noise ratio.
To detect any flow perturbations inside the combustor a Laser Vibrometer (LV) from Polytec of type OFV-353 was used.
Data acquisition of measurements were performed by using National Instruments BNC-2110 I/O device linked to a PXI 1033 chassis. All signals were recorded simultaneously (three channels with sample rate of 10 kHz, collecting 1M samples per channel) by a user-defined routine developed using Lab-View 8.0.

The configuration was as follows:

- **Channel ai_0**: Opto Sensor / TTL Converter (reference signal).
- **Channel ai_1**: Piezocryst Cp502 sensor to measure the perturbations inside the air box of the LPP module. Amplifier set to 91 pC/bar.
- **Channel ai_2**: Laser Vibrometer to get information on the response of the combustor to perturbations induced by the siren. Controller Unit set to 5 mm/s/V.

The operating conditions were set in accordance with table 8.5. The air flow inside the injection modules was set to 25 g/s so that the operating conditions for the experiments with combustion were matched.

Table 8.5: Operating conditions for isothermal stability analysis

| | | |
|---|---|---|
| Air mass flow | 25.00 | $[g/s]$ |
| Air temperature | 313 | $[K]$ |
| Reduced air mass flow | 0.09 | $[kg/s \cdot \sqrt{T}/p]$ |
| Fuel mass flow | - | $[g/s]$ |
| Equivalence ratio | - | $[-]$ |
| Reference velocity | 11.40 | $[m/s]$ |
| Combustor pressure | 5 | $[bar_{abs}]$ |

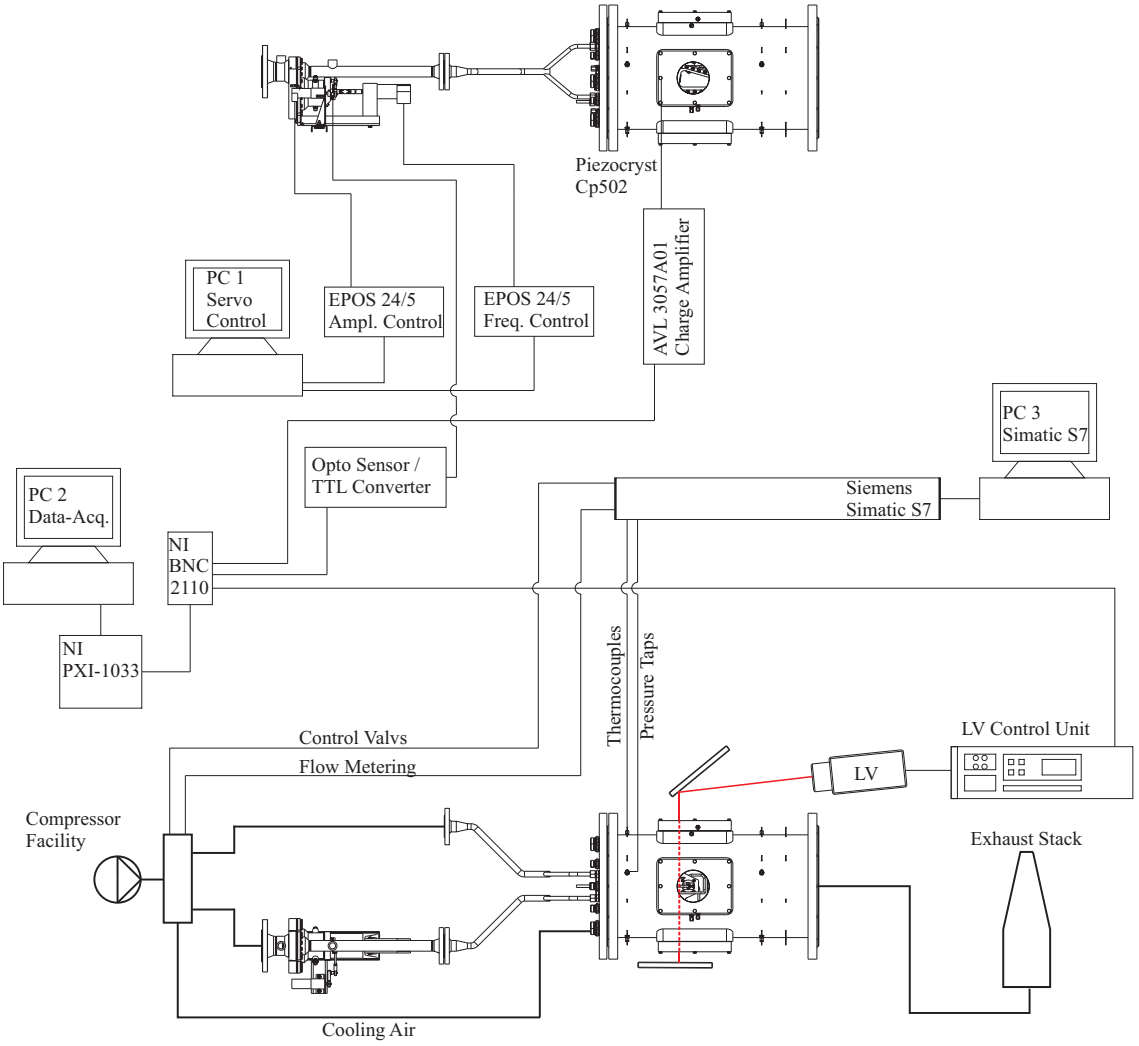


Figure 8.6: Experimental setup during isothermal stability analysis

## 8.6 Setup for reactive flow stability analysis using the LPP test sector

The experimental setup used for reactive flow conditions is similar to the one used for the isothermal stability analysis. As now experiments are performed at reactive conditions a fuel supply is necessary. Also the ignition device, fed with methane, is now used. Figure 8.7 is showing the experimental setup.
To monitor the combustion process a camcorder is used too. In addition for one data set a high speed video has been recorded.
At selected frequencies a mapping of density fluctuations by use of the LV has been done. The setup had thus to be adapted. The laser was aligned perpendicular to the combustor to receive an acceptable data rate. This is shown in figure 8.7 within the dashed box. As the flow field is scanned in two direction, a traversing system of type DANTEC lightweight has been used and controlled with the computer that is doing data acquisition.
The setup for data acquisition, regarding the scanning of the combustor, is the same as in section 8.5. For the mapping of density fluctuations the data acquisition was set to a sampling frequency of 20,480 Hz collecting $409,600$ samples.
During preliminary experiments, that are not shown here, the operating conditions to achieve a stable flame were determined and set during the reactive stability test campaign. The operating conditions set are shown in the results section (section 9.6) as they were changed throughout the various experiments.

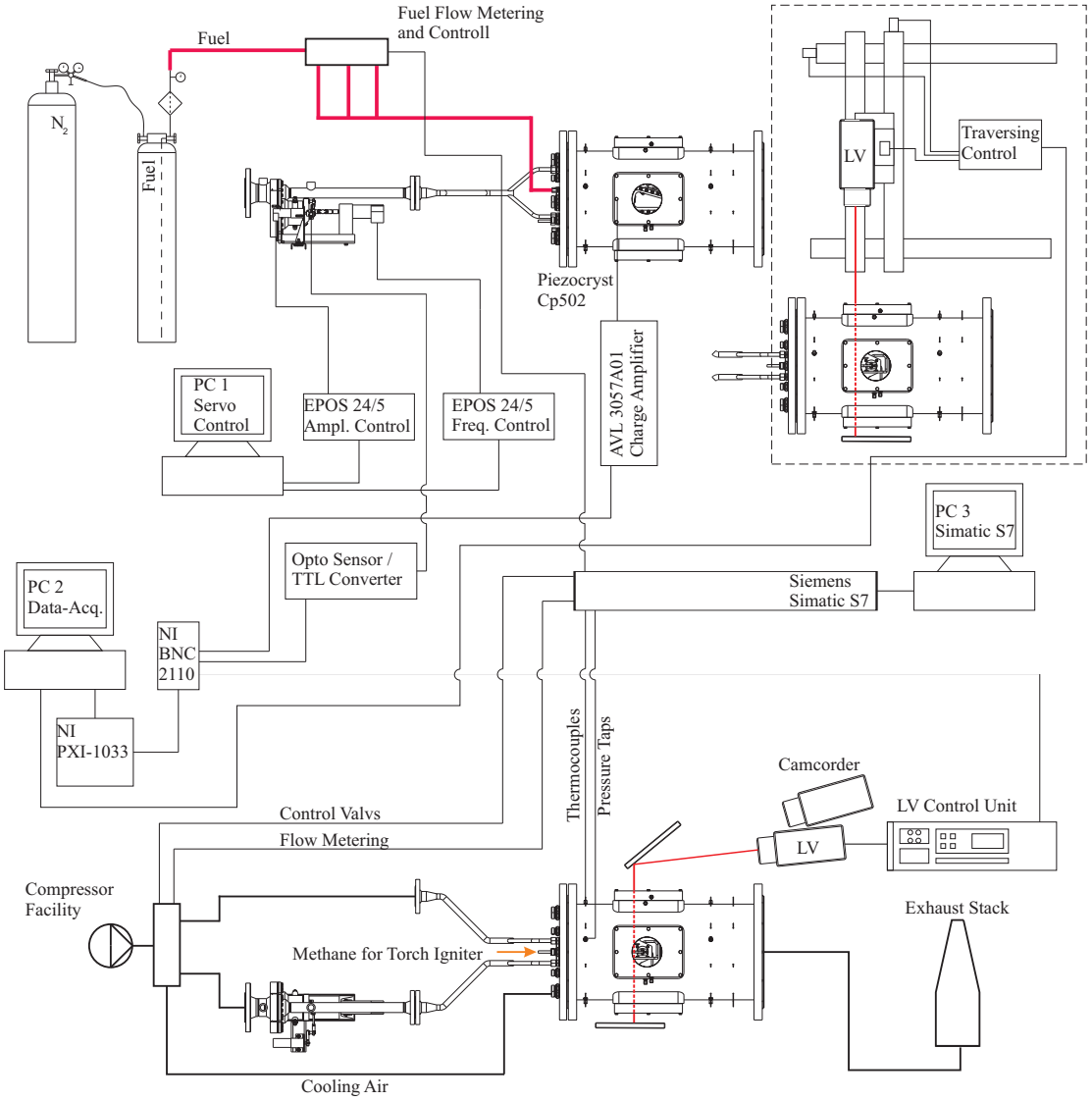


Figure 8.7: Experimental setup during reactive stability analysis

# Chapter 9

# Results and Discussion

This chapter presents and discusses the results obtained throughout the several experiments performed. First the experiments done with the single gaseous injector are presented.
A flow characterization of the test sector at atmospheric conditions by using LDA measurements is presented next.
The operation of the newly developed flow exciter (TUG siren) is then analyzed. First experiments with the siren operating into the ambient are shown, followed by a discussion on the excitation when being attached to the LPP test sector.
The response of a single LPP module installed in the single LPP combustor, using ethanol as fuel, is then given.
Before combustion experiments were performed in the NEWAC test rig, an isothermal stability analysis has been performed.
Finally one injector was artificially excited during combustion processes at elevated pressure and the results obtained are presented.
Table 9.1 shows the test matrix done, indicating which measurement technique has been used for which experiment.

Table 9.1: Measurement techniques used at different experimental setups

| | LDA | LV | | other | comment |
|---|---|---|---|---|---|
| | | cold flow | reactive | | |
| Dump combustor | | | x | PIV | for PIV see [61] |
| Siren | x | x | | | |
| Single LPP injector | | | x | | |
| LPP test combustor | x | x | x | | |

The details concerning the measurement equipment are given in chapter 6 at the appropriate section. The experimental setup for all experiments has been described in the previous section.

## 9.1 Mapping of density fluctuations inside the dump combustor

During the measurement campaign using the dump combustor a characterization of the injector by using techniques such as Particle Image Velocimetry has been performed. A detailed description of the experimental setup and presentation as well as discussion of

the results can be found in [72]. Furthermore the results obtained have been published in [61].
However, as the mapping of density fluctuation inside the LPP test cell are based on the experiments performed with the dump combustor, the results in terms of LV measurement are given here for a further discussion.

For the mapping of density fluctuations the signal of the scanning laser vibrometer was correlated with the pressure transducer as the reference signal of the siren could not be used. For the computation of the data an Abel transform (see e.g. [11]) has been used to receive local information on density fluctuation. Although the injector can be treated as axi-symmetric the restriction for the lack of density gradients at the boundary of the measurement volume results in large errors on the local information.
However, the general information on fluctuating density is valid, beside its real size in terms of amplitude.
Figure 9.1 shows a pulsation period at 540 Hz ($\tau$ =1.85 ms) excitation frequency, subdivided in 8 timesteps of 0.23 ms, during experiments at atmospheric conditions. The pulsation cycle starts at top left, labeled with (a), and has to be read clockwise.
Out of the 91 measurement points recorded, isosurfaces of the phase resolved density data have been computed and are shown. The field of view investigated with the LV is of the size of 40x100 $mm^2$. Data points not physically recorded are interpolated using a Matlab routine to receive smooth isosurfaces.
An increase in density fluctuation is depicted as an isosurface with a bold borderline, whereas a decrease is marked by an isosurface without borderline. The colorbar at center of figure 9.1 gives therefore the magnitude of the Abel-transformed density fluctuation.
Looking at the pulsation cycle it can be seen that pockets of high and low density are advectet from the tip of the injector and travel downstream to the exhaust. The correlated structures are filling the whole height of the field of view and have a depth of 10 to 20 mm. After approximately 30 mm the structures start to break apart and form smaller kernels. 50 mm downstream the injector the structures start to disappear.

The experiment performed at elevated pressure conditions ($p$ =2 $bar_{abs}$) is shown in figure 9.2. The excitation frequency set is still 540 Hz and the pulsation period is divided into the same subdivisions of 0.23 ms. The colorbar indicating the amplitude differs in the maximum intensity, compared to the results obtained at atmospheric conditions. This was done to achieve a "higher contrast" of the images.
It can be seen that correlated structures with alternating density (increasing/decreasing) are advectet from the tip of the injector. However, the breakup of these structures appears to happen short after the point of injection. Smaller unstructured kernels are formed and travel downstream. In addition the structures are packed more dense and start to disappear 30-40 mm downstream the injector.
The velocity of the structures was computed with $v_{conv}$ =11.9 m/s for the atmospheric and $v_{conv}$ =8.1 m/s for the pressurized experiment, resulting in a velocity ratio of $v_{conv}/v_{ref}$ = 0.44 and 0.64 respectively.

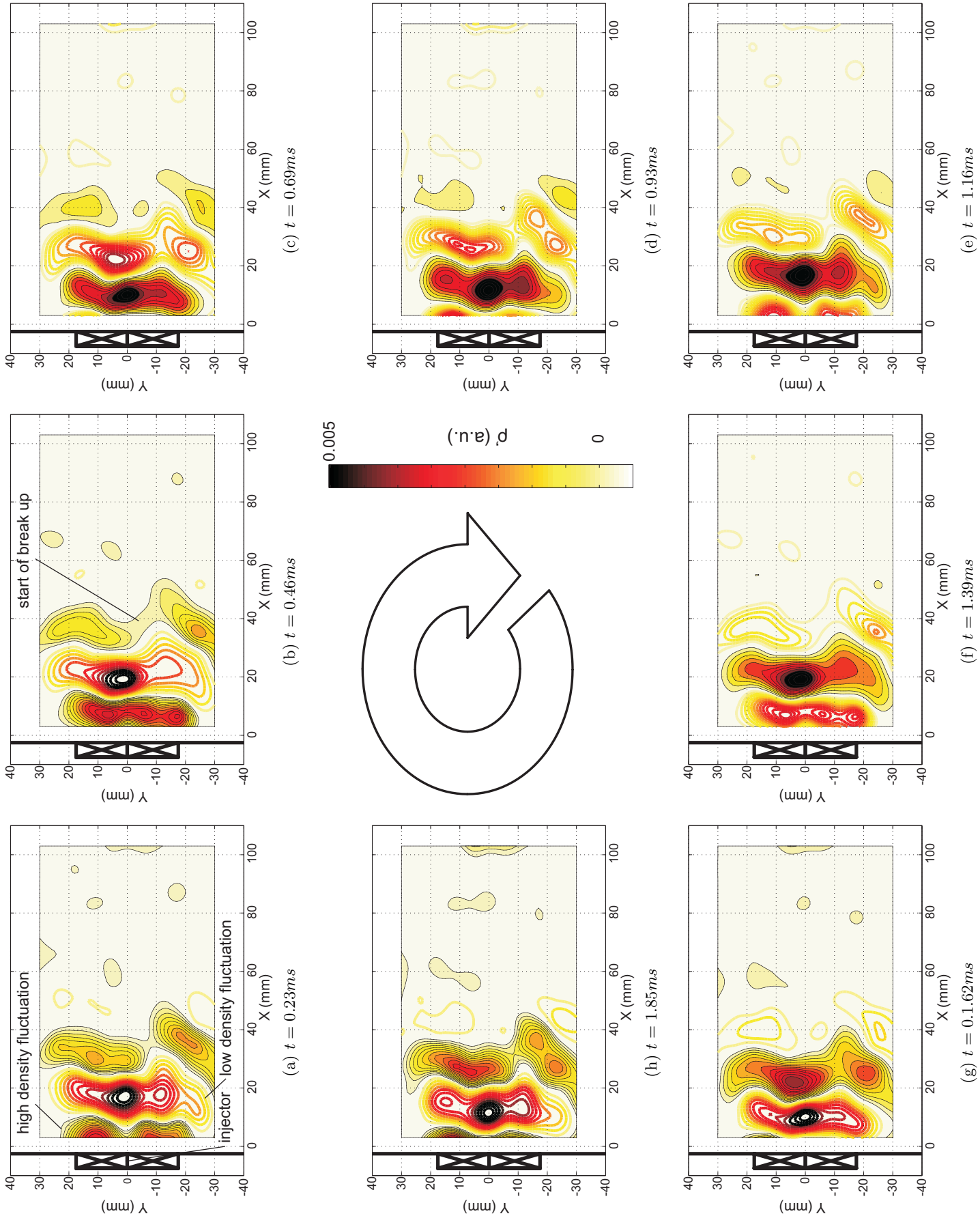


Figure 9.1: Phase resolved density fluctuation at 540 Hz excitation frequency using the dump combustor at atmospheric conditions

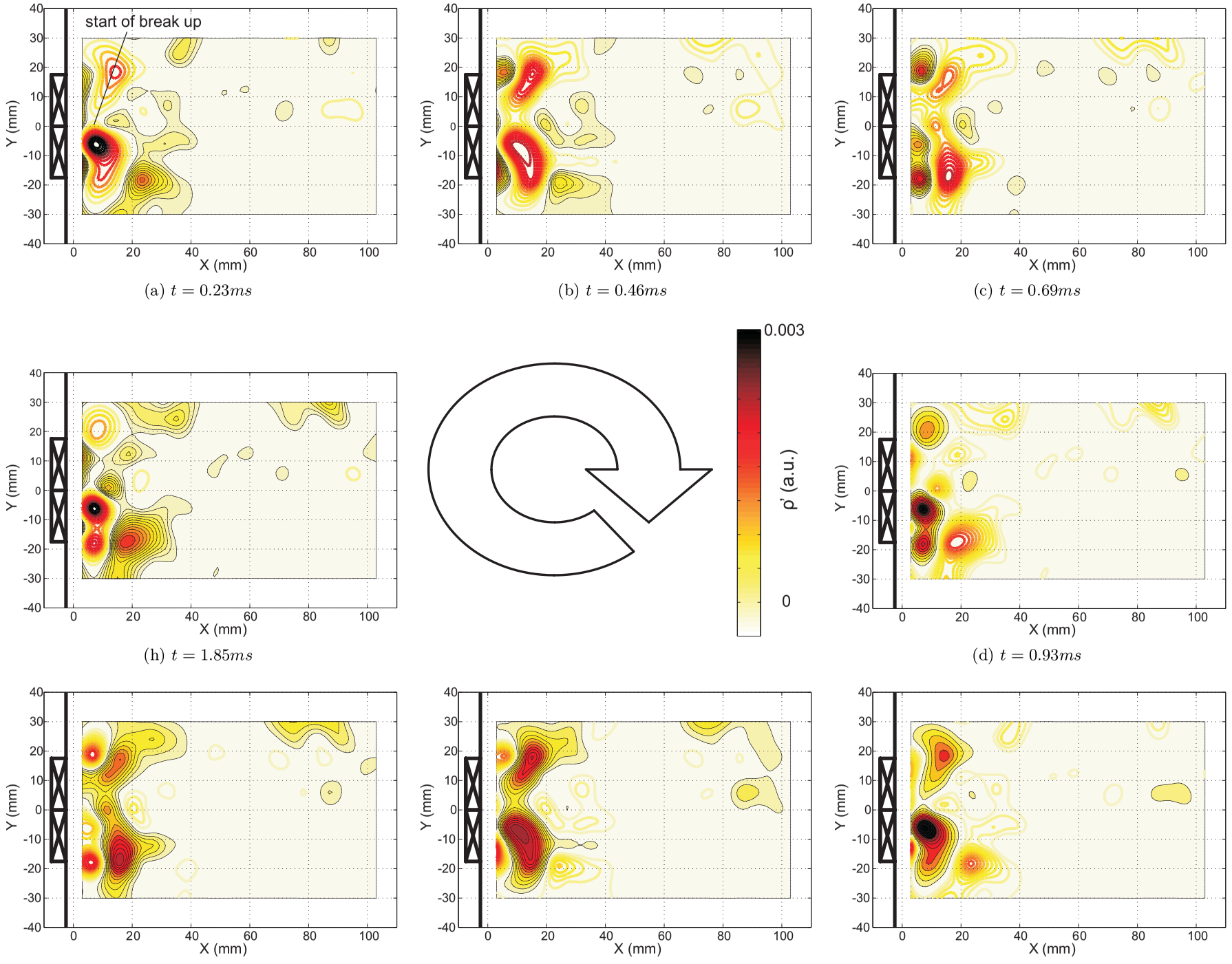


(a) $t = 0.23ms$ (b) $t = 0.46ms$ (c) $t = 0.69ms$

(h) $t = 1.85ms$ (d) $t = 0.93ms$

(g) $t = 1.62ms$ (f) $t = 1.39ms$ (e) $t = 1.16ms$

Figure 9.2: Phase resolved density fluctuation at 540 Hz excitation frequency using the dump combustor at 2 $bar_{abs}$

During the experiments pictures of the flame have been taken. Comparing the picture of figure 9.3a, showing the flame at quasi atmospheric conditions ($p$ =1.1 bar), with the image taken at a pressure of 2 $\text{bar}_{\text{abs}}$ inside the combustor, one will find that the flame at atmospheric conditions (figure 9.3a) is propagating more into the combustor, whereas the flame at elevated pressure is burning more compact (figure 9.3b)

(a) operation at $p$ =1.1 $\text{bar}_{\text{abs}}$

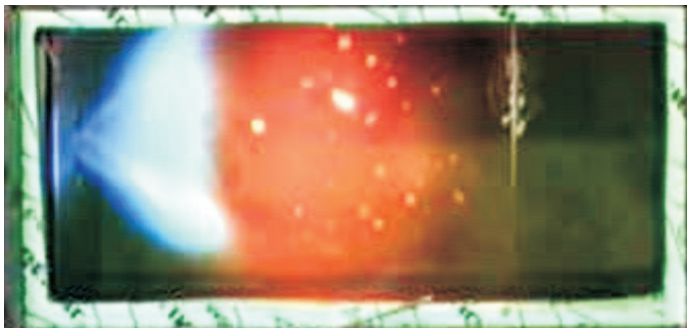

(b) operation at $p$ =2.0 $\text{bar}_{\text{abs}}$

Figure 9.3: Images of flame structure during dump combustor experiments

## 9.2 Isothermal flow characterization of the test sector at atmospheric conditions

Figure 9.4 is showing the lateral view of the combustion chamber. The velocity components were measured in axial and radial direction. The direction of flow is from left to right. As can be seen the measurement grid is fine at the combustor entry and more coarse at the exhaust. LPP left (SER1, figure 9.4a) is showing the tendency to turn the flow downwards whereas the right module (SER2, figure 9.4b) turns the flow upwards. The order of magnitude for the velocity profile is in both cases similar. However, at the right injector the overall flow seams to be a tick faster than in the left one. As for the field of view achievable with the setup it was not possible to investigate the corners of the head plate of the combustor. So the usually present edge vortices could not be determined. However the vectors at roughly $x = -10mm/y = -10mm$ indicate the presence of these vortices. Also a homogenous flow field is established after $x = 20mm$ with the resulting vector pointing along the burners axis.
Of importance for both flow fields is that no recirculation zone is present. The shape of the flow field is similar to the one formed by a Bunsen burner. As shown in the introductory part, recirculation is undesirable as it increases the risk of flashback.

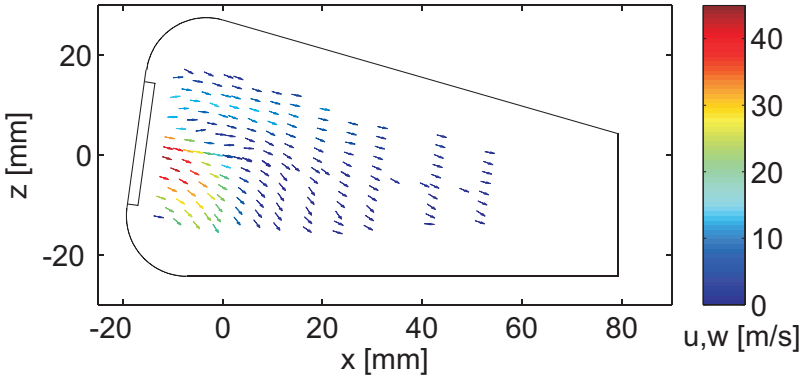


(a) left LPP injector

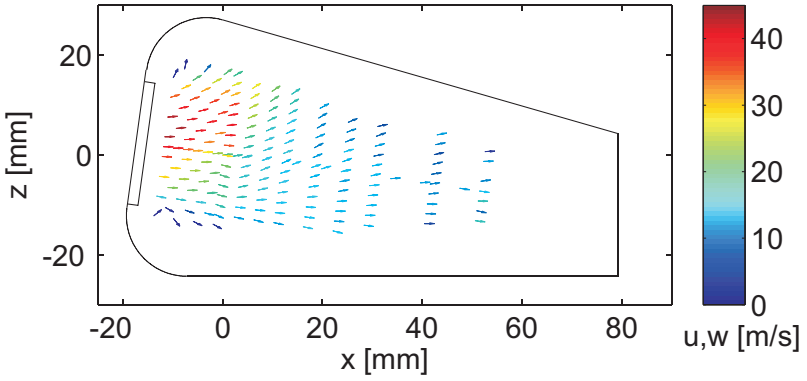


(b) right LPP injector

Figure 9.4: Flow field at lateral view of the combustor; axial and radial velocity components

For a closer investigation of the swirl of the LPP modules figure 9.5 shows the axial velocity as vector plot and the tangential velocity as color map. The direction of view

is from bottom to top. The data is obtained for the same setup, meaning that the LDA probe was aiming through a lateral window to form the measurement volume. The grid is of similar axial spacing. As can be seen both injectors produce a swirl in the same direction (clock wise). LPP right however is forming a more homogenous flow field with a nearly uniform axial velocity component. LPP left seems to tend to blow the air onto the left optical access and the velocity, although higher as for LPP right (due to a slight higher air mass flow), is rather low at the center axis. Also the tangential velocity component is not as uniform as for LPP right.
Due to the depth of the combustor it was not possible to reach with the laser to the center of the combustion chamber. Therefore an investigation of vortical structures formed between the two clockwise swirling air flows was not possible. However, from both figures it can be seen that a rotation between both burners, in the same direction as the swirler turns, is present (figure 9.5a at $y = 1D$ and (b) at $y = -1D$).

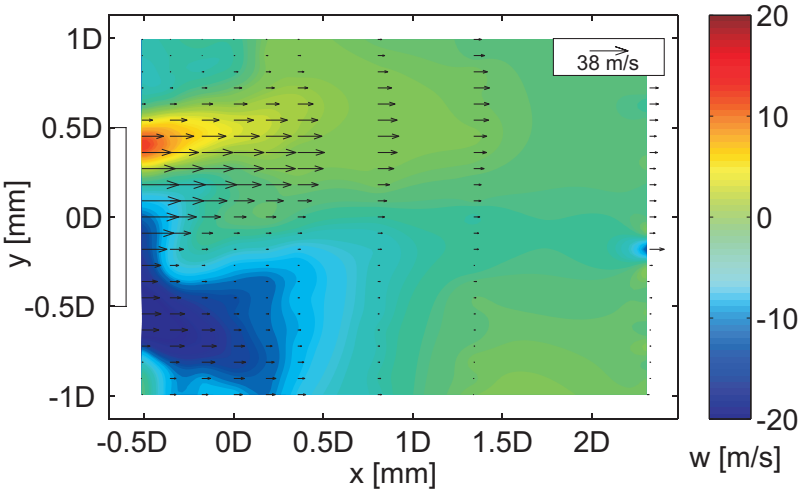


(a) left LPP injector

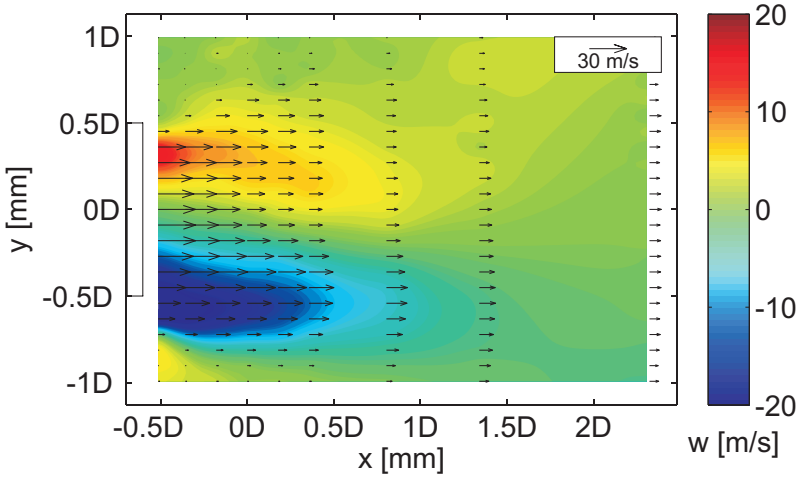


(b) right LPP injector

Figure 9.5: Flow field at bottom view of the combustor; the axial velocity is shown as vector plot and the tangential velocity is given as color map (out of plane component)

For computing the swirl number $S$, the velocity was separated into a component pointing along the burner axis and in a tangential component perpendicular the the axial velocity. Measurements taken at $x/D = 1$ are used to determine $S$ as this is the optimum location to do so. The definition for the swirl number from Beer and Chigier [74] that is used here is given in equation 9.1.

$$S = \frac{2 \cdot \int_0^{2\pi} \int_0^{D_{sw}/2} w \cdot r^2 \cdot \rho \cdot u \mathrm{d}r\mathrm{d}\Theta}{D_{sw} \cdot \left( \int_0^{2\pi} \int_0^{D_{sw}/2} \rho \cdot u^2 \mathrm{d}r\mathrm{d}\Theta + \int_0^{2\pi} \int_0^{D_{sw}/2} r \cdot p \mathrm{d}r\mathrm{d}\Theta \right)} \tag{9.1}$$

As the measurements were done in a cross sectional area, the swirl number was determined for all four quadrants and averaged. The so computed averaged swirl number equals to $S = 0.32$ for both injectors. Figure 9.7 shows the computed swirl numbers in respect to the quadrants where they were measured and the average swirl number.

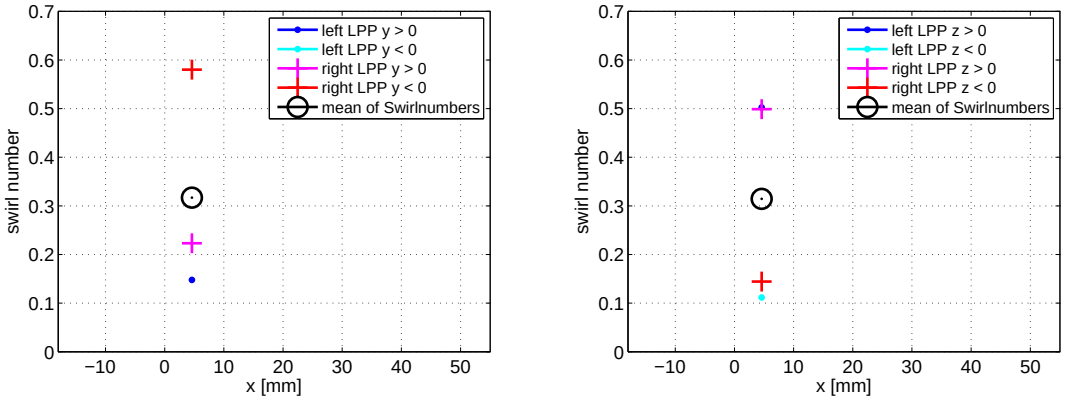


(a) swirl number computed at x-y plane

(b) swirl number computed at y-z plane

Figure 9.6: Swirl number at different cross sectional areas

Finally the flow field at a frontal view is presented. Here all three velocity components are shown. As a two component LDA system was used, the data are determined from two separate measurements. The direction of view is frontal (against flow direction), meaning that the axial flow velocity is out of plane. For clarity the premixing tube of the injectors is depicted as a red circle. It can be seen that the velocity more close to the combustor center is higher than at the outer half to the liner walls. At the center however the axial velocity decreases. This could be due to beginning of some kind of recirculation zone between the injectors. More information on the flow field of the combustor, especially on the Raynolds stress tensor can be found in [75].

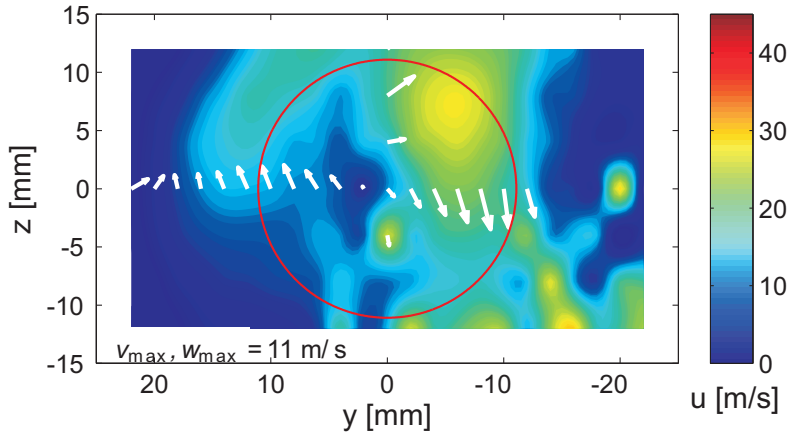


(a) right LPP injector

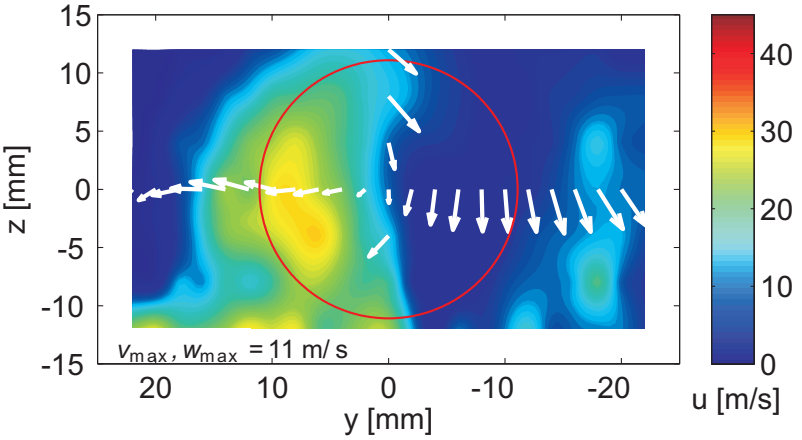


(b) left LPP injector

Figure 9.7: Flow field at frontal view of the combustor; axial, radial and tangential velocity components

## 9.3 Characterization of the flow exciter

Two measurement campaigns were performed. The first one was done to evaluate the siren on its own operating into ambient. After successful testing the siren was fitted to the NEWAC combustor to proof its operating on this device as the ducting of the air flows is rather complex. The siren was therefore linked to the left air box containing the injector SER1.

### 9.3.1 Flow exciter without combustion chamber

For the first tests, the siren was operated without any attached combustor. The measurement were done using a pipe of 1.71 m length connected to the siren to act as a quarter wave resonator. The experiments performed were done to characterize the response of the flow to perturbation induced by frequency modulation as well as amplitude modulation. The results obtained can be found in [76].

### 9.3.2 Flow exciter attached to the NEWAC combustion chamber at atmospheric conditions

**LDA measurement** As shown in the experimental setup four locations were used to detect the flow perturbations inside the combustor. The direction of the laser beams called BSA1 and BSA2 can be seen in figure 8.4. The raw data from BSA1 and 2 were transformed into the coordinate system of the combustor that is tilted by 8°. The tilted velocity components are labeled with $u$ and $v$ respectively. The transformation however is only possible if coincident samples are collected. First the raw data are plotted followed by the transformed coincident axial and radial velocity. Figure 9.8 shows the computed signals for LDA1 and LDA2 positions, at excitation with 452 Hz at highest amplitude possible, where the perturbation was detected quite clearly. Location LDA1 shows a disturbance of the flow in axial as well as in radial direction (figures 9.8a, (b) and (e)). At location LDA2 (figures 9.8c, (d) and (f)) no fluctuation in the radial velocity component was detected and due to the transformation of velocity components it seems that no fluctuation at all is present in this location as the average flow seems to be quasi steady. Measurements at locations LDA3 and LDA4 do not show any perturbations (not shown). However, the mean flow velocity and the minimum and maximum values for both velocity components at all 4 LDA locations are given in table 9.2.

Table 9.2: Mean and min. /max. of velocity components at excitation with 452 Hz at all 4 LDA locations

| | LDA1 | LDA2 | LDA3 | LDA4 | |
|---|---|---|---|---|---|
| $\bar{u}$ | 3.71 | 10.21 | 9.46 | 4.77 | m/s |
| $\bar{v}$ | 12.82 | 10.62 | 9.76 | 8.70 | m/s |
| $u_{min}$ | -3.87 | 5.51 | 7.14 | 2.46 | m/s |
| $u_{max}$ | 10.87 | 14.86 | 12.20 | 7.91 | m/s |
| $v_{min}$ | 9.48 | 6.42 | 7.35 | 4.80 | m/s |
| $v_{max}$ | 16.48 | 14.63 | 13.31 | 12.23 | m/s |

The induced excitation is strongly dependent on the location inside the combustor. At the center axis (location LDA1 and LDA2) the disturbance can be measured near the injector exit and is damped further downstream. Also at a line half a diameter sideways of the injector the perturbation is damped too. However, an excitation of the combustor volume by using the TUG siren is possible. One has also to keep in mind that the frequency of excitation also determines the mode of the wave form inside the combustor so that one might face a node of the wave at a certain point of location.

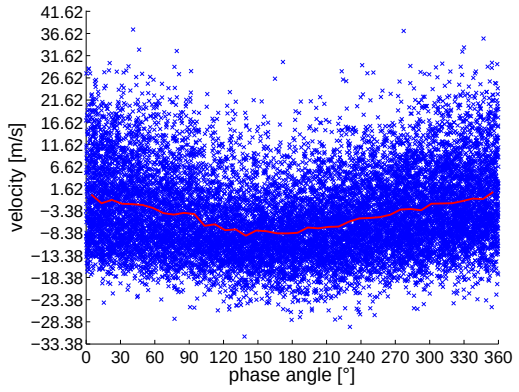


(a) raw axial velocity at LDA1

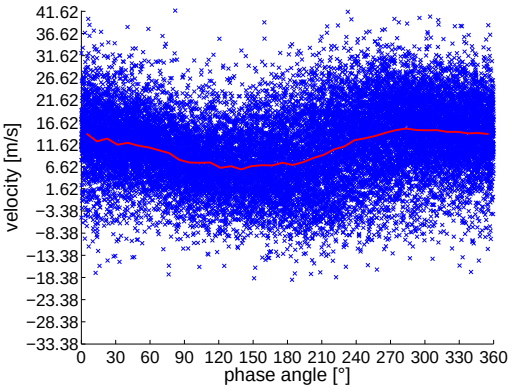


(b) raw radial velocity at LDA1

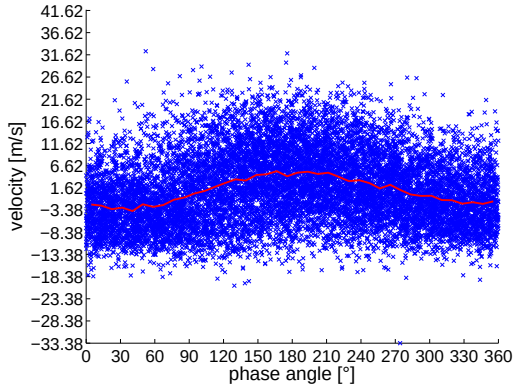


(c) raw axial velocity at LDA2

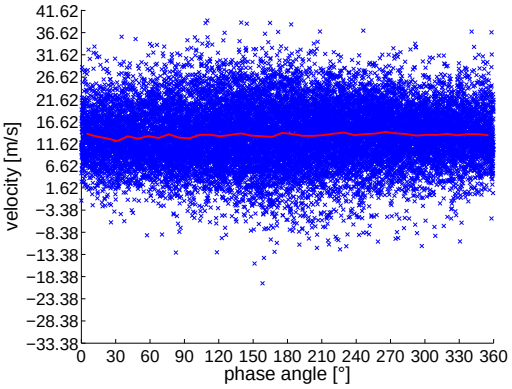


(d) raw radial velocity at LDA2

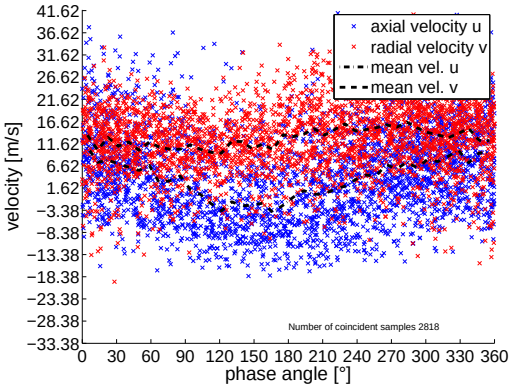


(e) coincident and transformed velocities at LDA1

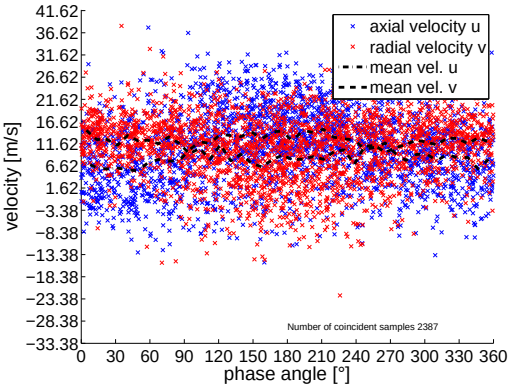


(f) coincident and transformed velocities at LDA2

Figure 9.8: LDA measurement during validation of the siren at 452 Hz; location LDA1 and LDA2

Next the combustor was excited at 226 Hz with varying amplitude to evaluate the influence of the servo drive. In figure 9.9 (location LDA1) and 9.10 (location LDA2) the response of the flow is shown for varying amplitudes, ranging from max. amplitude, denoted as 0° or 95 % perturbation to 74 % perturbation at 60° tilt angle; the tilt angle is the position of the sprocket wheel in respect to the center of the sonic nozzle; see figure 7.4, at a fixed frequency of 226 Hz.

The damping effect can be seen in location LDA1, right after the injector exit, represented by figure 9.9 clearly. In addition a phase shift due to the eccentric movement of the sprocket was identified.

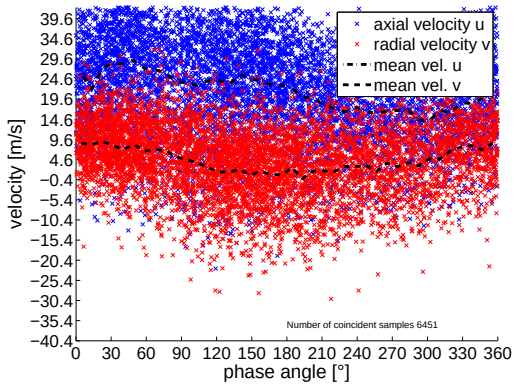


(a) 95% perturbation at 0° tilt angle

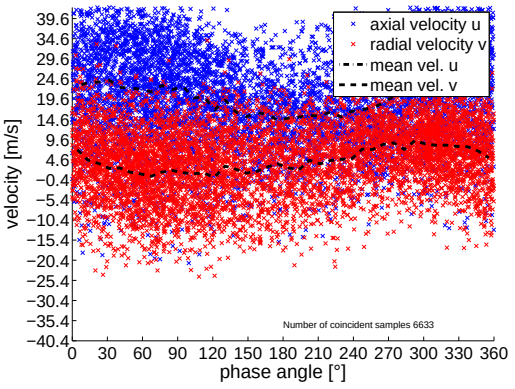


(b) 93% perturbation at 20° tilt angle

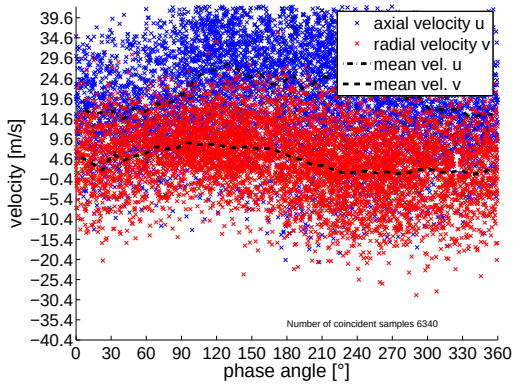


(c) 86% perturbation at 40° tilt angle

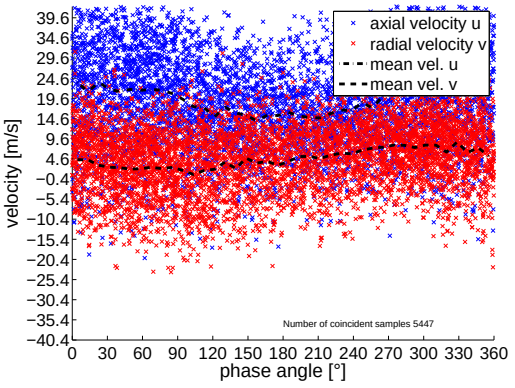


(d) 74% perturbation at 60° tilt angle

Figure 9.9: LDA measurements at LDA1 with varying amplitude of excitation ($f$=226 Hz)

In location LDA2 (figure 9.10) the phase shift gets more pronounced, whereas the damping effect is less developed.

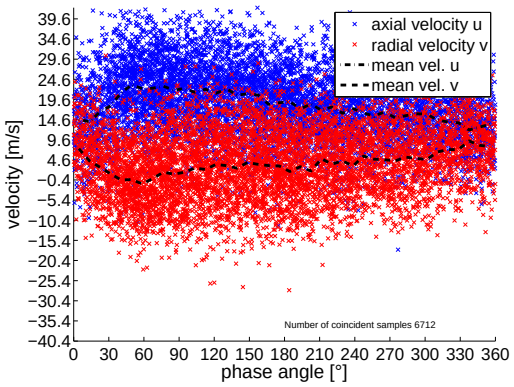


(a) coincident velocities at amplitude 0°

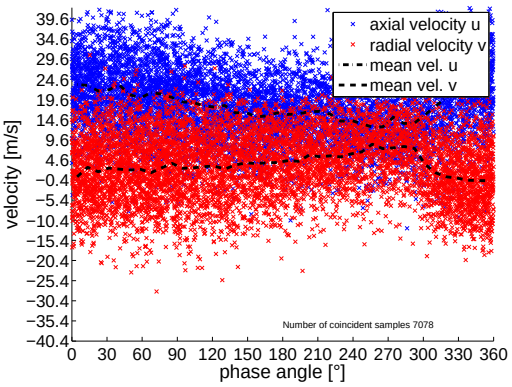


(b) coincident velocities at amplitude 20°

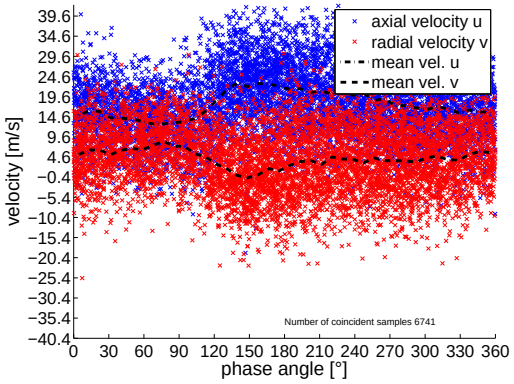


(c) coincident velocities at amplitude 40°

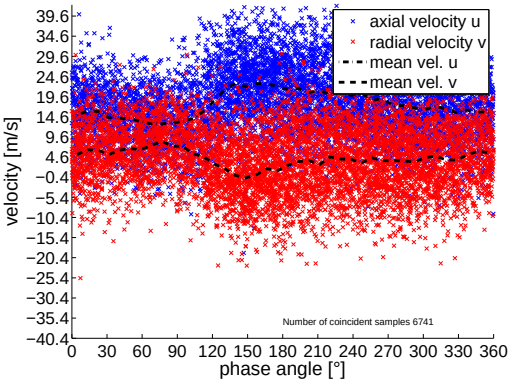


(d) coincident velocities at amplitude 60°

Figure 9.10: LDA measurements at LDA2 with varying amplitude of excitation ($f$=226 Hz)

Here again the mean and minimum/maximum values of velocity are represented in a tabular form (see table 9.3) at location LDA1 and LDA2 respectively.

Table 9.3: Mean and min. /max. of velocity components at excitation with 226 Hz with varying amplitude

| | Location LDA1 | | | | Location LDA2 | | | | |
|---|---|---|---|---|---|---|---|---|---|
| | 95 | 93 | 86 | 74 | 95 | 93 | 86 | 74 | |
| $\bar{u}$ | 21.53 | 20.50 | 20.70 | 19.86 | 17.99 | 18.09 | 17.66 | 17.66 | m/s |
| $\bar{v}$ | 4.38 | 4.28 | 4.16 | 4.64 | 3.69 | 3.49 | 4.278 | 4.28 | m/s |
| $u_{min}$ | 14.19 | 14.34 | 14.49 | 14.00 | 12.02 | 12.72 | 12.82 | 12.82 | m/s |
| $u_{max}$ | 29.27 | 28.38 | 28.26 | 25.20 | 23.25 | 23.45 | 22.96 | 22.96 | m/s |
| $v_{min}$ | -0.08 | 0.27 | 0.74 | 0.70 | -1.38 | -0.60 | -0.59 | -0.59 | m/s |
| $v_{max}$ | 9.06 | 9.29 | 8.63 | 8.75 | 9.30 | 8.48 | 8.55 | 8.55 | m/s |

**Laser Vibrometer and pressure transducer measurement** Concerning the figures shown here, it is of importance that different scales for the ordinate are used, due to the fact that the intensity of the raw signal varies drastically from sensor to sensor. During

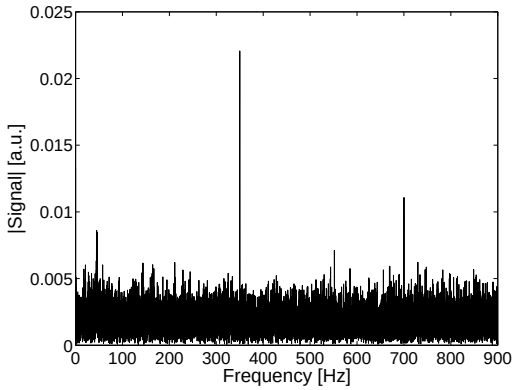


(a) LV signal with quartz glass windows installed

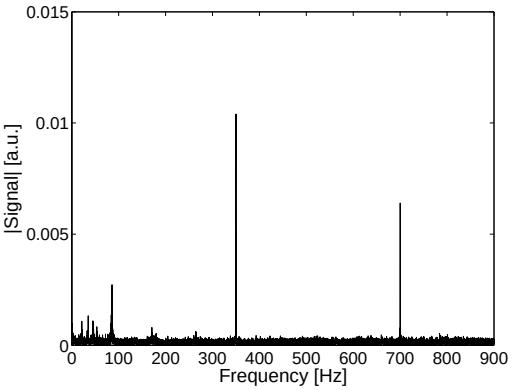


(b) LV signal w/o optical access

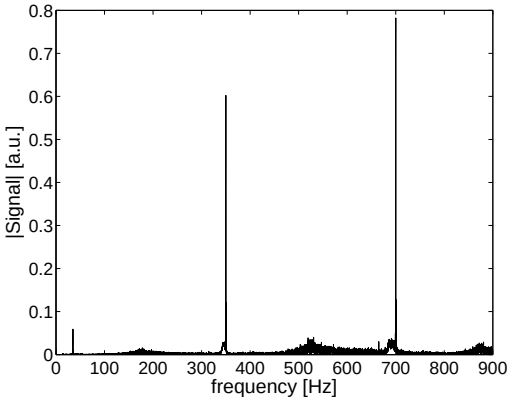


(c) LV signal of the quartz window

Figure 9.11: Influence of the vibrating optical access to the LV measurement; excitation at 350 Hz and max. amplitude

measurements at elevated pressure optical accesses, made of quartz glass windows, have to be used. To determine the influence of the windows on the LV measurement an experiment was performed with and without optical accesses installed. In addition a retroreflective material was put on the quartz glass to detect the vibration of the window itself. The result of this experiment is shown in figure 9.11. The flow is excited at 350 Hz with max. possible amplitude. The chart in figure 9.11a shows the response of the Laser Vibrometer with installed quartz glass. It indicates a resonant frequency at 350 Hz (and the first higher harmonic) corresponding to the excitation set. At same frequency the optical accesses were removed and the experiment repeated. Both signals are in the same order of magnitude. The signal without optical access is lower in signal strength due to the fact that a rather high leakage is generated when the lateral windows are not installed. Figure 9.12b illustrates this. The noise is lower of course, giving a better signal to noise ratio as all disruptive effects are eliminated. Finally figure 9.11c is presenting the vibration of the quartz glass window (a retro foil was used as reflector). The small peak at 35 Hz represents the mechanical vibration induced by the servo motor used, as it revolves at a tenth of the excitation frequency (10 teeth are passing the nozzle per revolution of the motor). The

quartz glass is excited by the flow at this high frequency. But as the signal is two orders of magnitude higher than for the other two cases, the influence of the windows can be neglected. This is due to the fact that by using a retro foil, reflection is achieved for any angle of attack of the laser beam thus leading to a higher signal quality.
Exemplarily figure 9.12 shows three spectra during excitation of the flow with 340 Hz, 350 Hz and 360 Hz respectively. The measurement was performed without optical accesses to neglect any disturbances. It can be seen that the excitation is well detected and the siren operates as expected.

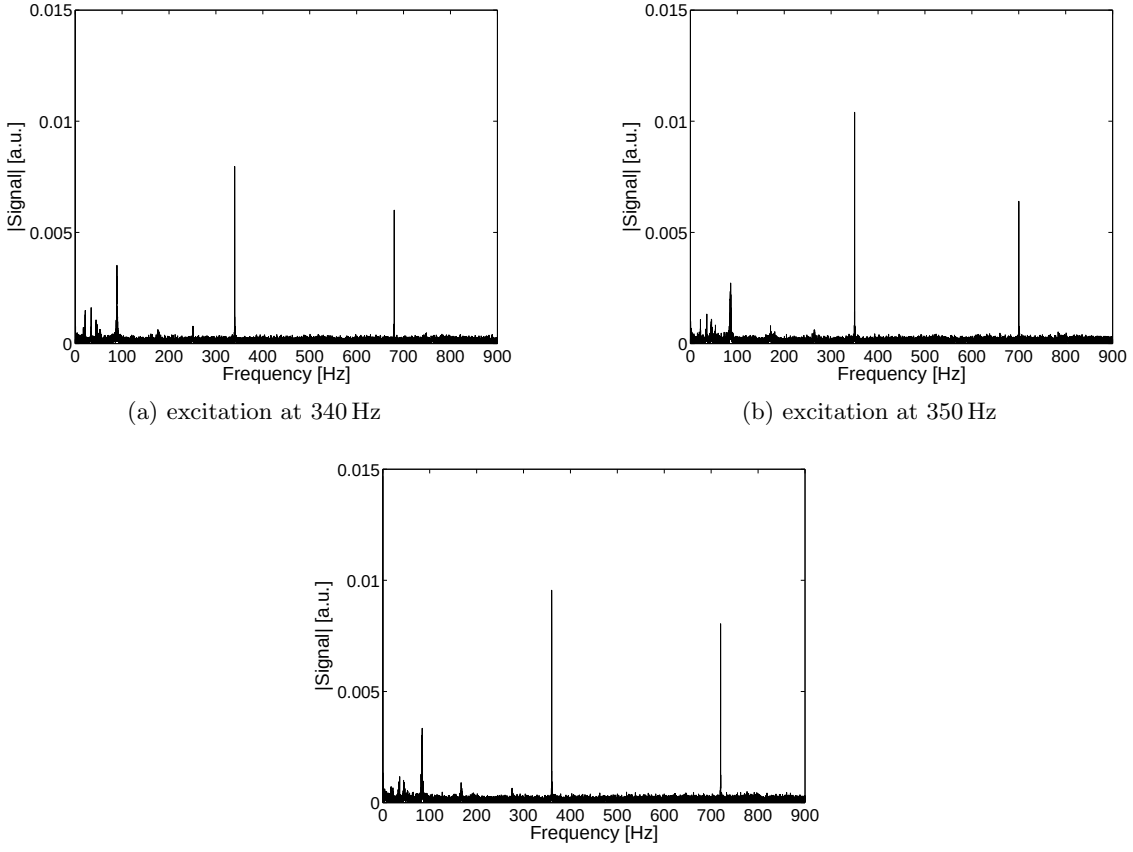


(a) excitation at 340 Hz

(b) excitation at 350 Hz

(c) excitation at 360 Hz

Figure 9.12: Frequency spectra at excitation with 340 Hz, 350 Hz and 360 Hz during validation of the siren

The response of the LV to perturbation induced by the siren at different excitation frequencies has been shown. Next different amplitudes of excitation at fixed frequency are analyzed.
The perturbation was set at a frequency of 226 Hz as done during the LDA measurement. First one will see in figure 9.13 that the signal strength of both sensors is enhanced when moving the wheel out of the nozzle area from 0 to 40 degree. This could be due to a false positioning of the toothed wheel at start of the experiment. Although this is very unlikely it could be an explanation for the observed results. However a reduction in signal strength of 35 % can be observed from maximum amplitude to minimum amplitude. After the experiment the sprocket wheel was aligned to the sonic nozzle once more to eliminate any false positioning.

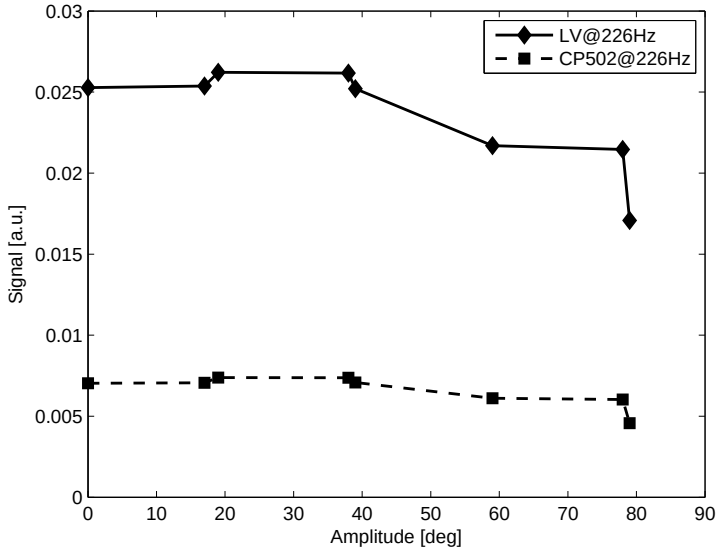


Figure 9.13: Signal strength as function of amplitude for excitation at 226 Hz using Laser Vibrometry and a pressure transducer

The experiments have shown that the siren is capable of exciting the flow inside the LPP test sector in terms of frequency with adjustable amplitude.

## 9.4 Single LPP injector stability analysis

The purpose of the single LPP experiment was to find possible resonant frequencies by operating the siren in a transient mode in the frequency range of 0 Hz to 300 Hz.
Figure 9.14 shows the results obtained. The time signals of the opto sensor (Siren TTL), the high temperature resistent pressure transducer (CP502) and Laser Vibrometer (LV) are shown in figure 9.14a. The time lag in the TTL signal indicates that the siren was not started at start of recording. Thus the highest frequency recorded by the system was 290 Hz although the siren operated up to 300 Hz.
The recorded signals of the opto sensor, the CP502 sensor and the Laser Vibrometer are shown in figure 9.14b to (d).
In the plots the abscissa shows the measurement time in seconds and the ordinate the frequency range of 0 to 500 Hz. The color of the plots is giving the amplitude (in logarithmic scale) of the signal spectra after performing a Fast Fourier Transform (FFT). The algorithm was explained in section 6.4 in detail.
Figure 9.14b shows the acceleration of the siren in steps of 3 Hz/s and the higher harmonics. If the excitation frequency of the siren matches a resonant acoustic frequency inside the combustor the introduced perturbation will be amplified and thus the signal intensity of both sensors (CP502 and LV) will drastically increase. Thus frequencies where a combustion instability can occur will be found by scanning the frequency domain.
The signal of the CP502 sensor indicates that the transient excitation of the air flow induced by the siren could be followed quite easily. This is marked by the light blue line from 9÷290 Hz. The strongest amplification can be found in the low frequency domain of up to 50 Hz. At higher frequencies the excitation can be detected but the amplitudes are

all in the same order of magnitude.
In figure 9.14d the voltage signal of the Laser Vibrometer is shown. Here the signal to noise ratio is not as good as for the CP502 sensor. This is due to the position of the LV at the exhaust of the system. The fluctuations are dissipating towards the end of the liner and so they are harder to detect. However, the response of the LV is still visible from 100 Hz upwards.
As no strong amplification is found one can say that in this configuration no combustion instability will appear in the frequency range of 0 Hz to 300 Hz. The present work shows for the first time that the response of the perturbed flow using a liquid fueled injector can be detected with LV.

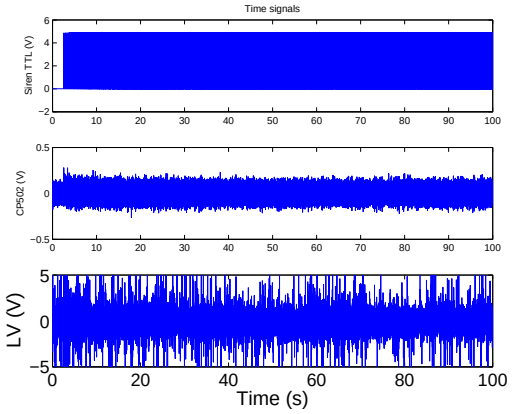


(a) Time signals

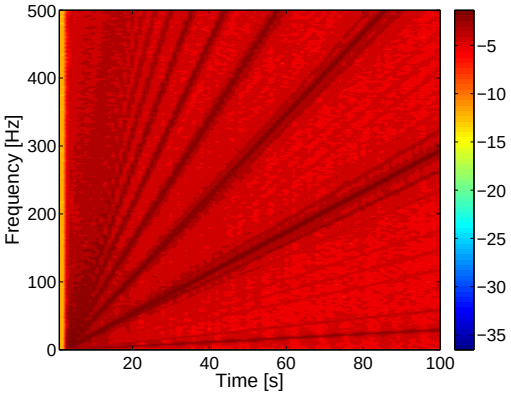


(b) TTL trigger signal as function of time and frequency

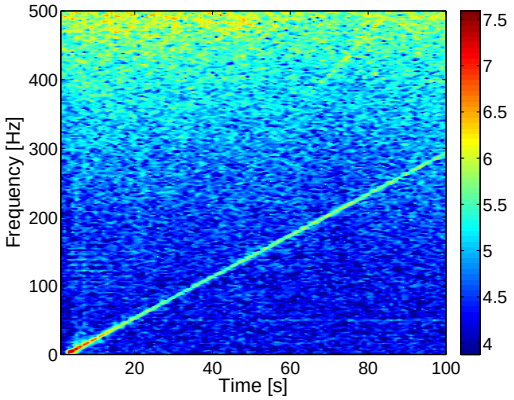


(c) Sound pressure level of CP502 sensor as function of time and frequency

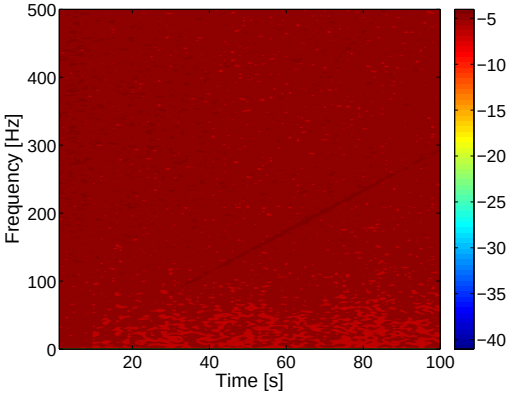


(d) Amplitude of LV signal as function of time and frequency

Figure 9.14: Signals recorded during transient behavior of the single LPP experiment; 0-300 Hz

## 9.5 Isothermal stability analysis of the LPP test sector

After the experiments with a single LPP module, the combustor was equipped with both LPP's and the flat spray pilot burner. Before starting reactive tests, an isothermal stability characterization was performed. The combustor was scanned for possible resonant frequencies in a range from 0 Hz to 900 Hz, using the full frequency range of the siren.

Figure 9.15 shows the recorded signals of the isothermal stability analysis. The time signals are given on top left (figure 9.15a) and the corresponding spectrograms for the trigger signal, CP502 sensor and LV sensor from figure (b) to (d) respectively. For the TTL signal one can see that the siren was operated at 900 Hz at the start of the experiment and constantly decelerated with 9 Hz/s. Thus it took 100 s to perform a measurement.
The signal of the CP502 sensor indicates, that the transient excitation of the air flow induced by the siren could be followed by the sensor easily. More of importance is that 5 regions with high signal intensity could be detected. These are labeled in figure 9.15c. The region with the highest signal of the CP502 sensor can be found from 700 up to 900 Hz.
The LV however did only detect regions of resonant frequencies from 490 to 580 and 700 to 900 Hz respectively. Furthermore two fixed resonant frequencies were detected throughout the whole transient operation of the siren at 120 and 580 Hz.
After scanning the whole frequency domain, possible with the siren, the frequencies with highest signal amplitude in the LV were excited. Figure 9.16 shows the frequency spectra of both sensors during excitation with 526 Hz, 572 Hz and 854 Hz respectively. In this three experiments the right LPP module (SER2) was not supplied with air to cancel out any effect induced by this module.

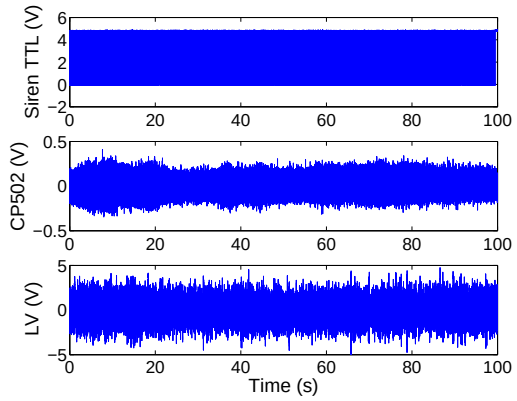


(a) Time signal

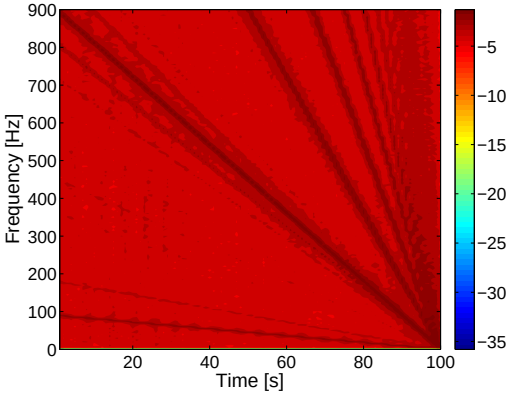


(b) TTL trigger signal as function of time and frequency

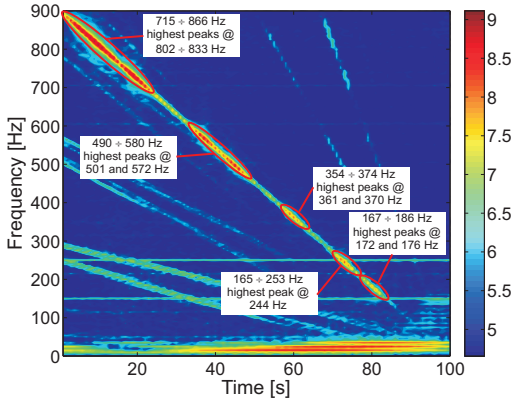


(c) Sound pressure level of CP502 sensor as function of time and frequency

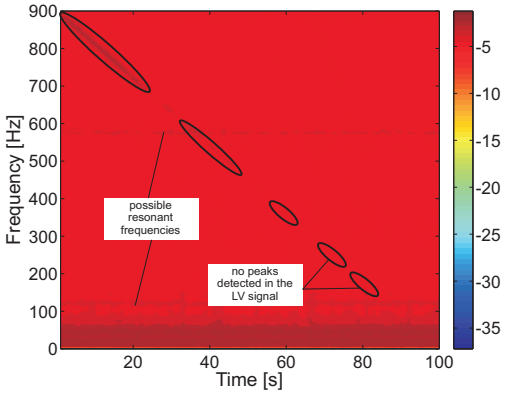


(d) log(Amplitude) of the Laser Vibrometer signal as function of time and frequency

Figure 9.15: Signals recorded during transient isothermal stability analysis; decelerations from 900 Hz to halt at 9 Hz/s

It can be seen that the peaks at 120 Hz and 580 Hz are still in the signal and are not causally linked to the excitation of the siren. These frequencies could be resulting from the piping system of the laboratory. However, as figure 9.15d indicates, a resonant frequency should be found around 572 Hz. This can be confirmed when looking at Figure 9.16d, where the amplitude of the LV signal compared with the excitation at 526 Hz is strongly amplified. As the resonant frequency with the highest amplitude appears to be at 854 Hz (see figure 9.15c and (d)), figure 9.16e and (f) show the results obtained when forcing an excitation at this specific frequency. It indicates that at this specific frequency the highest signal amplitude in the LV could be obtained (amplitude of 0.6 V).
So for the reactive flow stability analysis the frequency range of 490 Hz to 580 Hz and 700 Hz to 900 Hz is of interest, especially around the above mentioned 854 Hz.

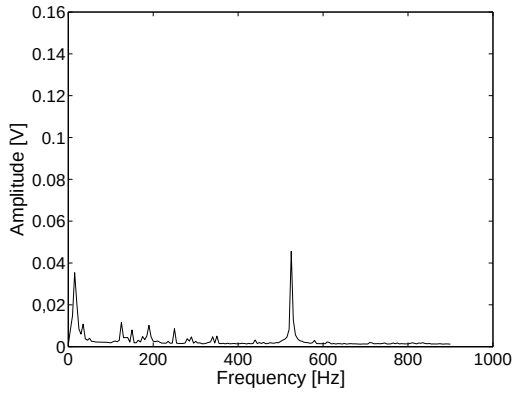


(a) Frequency spectra of CP502 sensor (526 Hz excitation frequency)

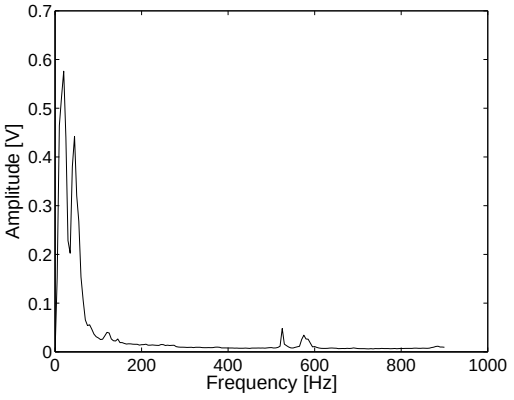


(b) Frequency spectra of the Laser Vibrometer signal (526 Hz excitation frequency)

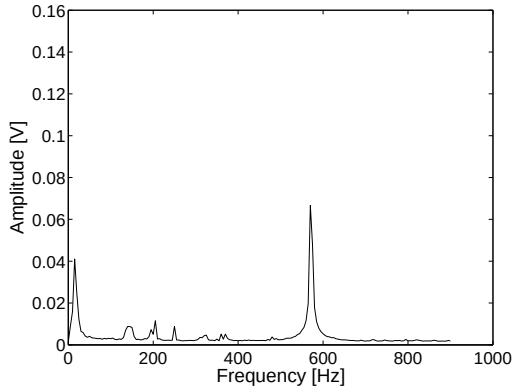


(c) Frequency spectra of CP502 sensor (572 Hz excitation frequency)

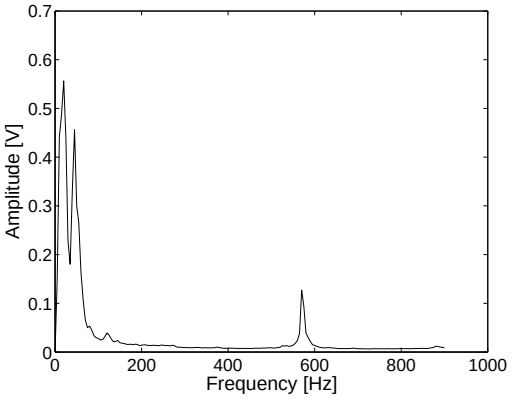


(d) Frequency spectra of the Laser Vibrometer signal (572 Hz excitation frequency)

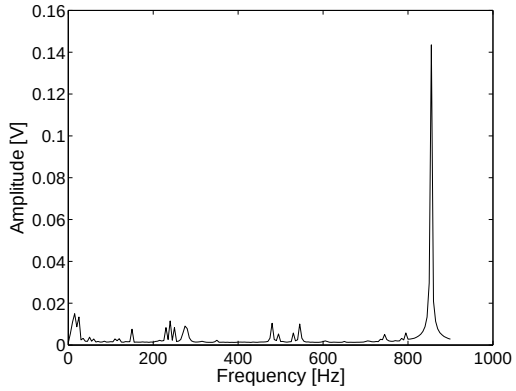


(e) Frequency spectra of CP502 sensor (854 Hz excitation frequency)

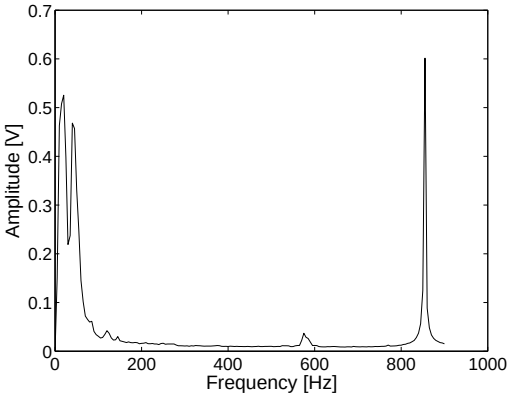


(f) Frequency spectra of the Laser Vibrometer signal (854 Hz excitation frequency)

Figure 9.16: Frequency spectra of CP502 and Laser Vibrometer at excitation frequencies of 526 Hz, 572 Hz and 854 Hz

## 9.6 Reactive stability analysis of the LPP test sector

At reactive flow conditions with all three injectors active the combustor was again scanned for resonant frequencies in the range of 0 Hz to 900 Hz. This was done because the presence of the flame changes the local velocity of sound and thus might change the resonant frequencies of the system. However, attention was paid to the frequencies identified during the cold flow investigations and frequencies identified that act on the flame structure. The operating pressure was set to 5 $bar_{abs}$.

### 9.6.1 Transient stability analysis

First the scanning for resonant frequencies is presented. The operating conditions for this experiment are given in table 9.4. Here only the pilot burner was fed with fuel.
The siren was operated like shown before in deceleration mode from 900 Hz to standstill. The recorded signals are shown in figure 9.17. The time signals of all three sensors are shown in figure 9.17a and the corresponding spectral analysis is shown from figure 9.17b to (d). Again the CP502 sensors follows the transient operation (see figure 9.17c) and gives a hint for resonant frequencies in the range of 700 Hz up to roughly 900 Hz. The highest peaks can be found at 805 Hz and 860 Hz respectively (the resolution of the FTT is in the order of 5 Hz). At the frequencies of 490 Hz and 570 Hz there is also a high response of the pressure transducer to the forced excitation of the siren. In the lower frequency range peaks at 365 Hz and 245 Hz were detected. At 245 Hz the resonance is quite close to an eigenfrequency of the sensor (250 Hz), so this frequency is canceled out. Other eigenfrequencies of the sensor can be found at 20 Hz, 150 Hz and 350 Hz. So generally speaking the sensor detected at reactive and isothermal operating conditions the same resonant frequencies. Still the frequency domain of greatest interest is above 800 Hz.
When looking at the signal gathered from the Laser Vibrometer neither the transient operation of the siren can be detected as a fluctuation of the density inside the flow, nor was a combustion instability in terms of highly resonant density fluctuations detected.
At the operating conditions set the deflection of the laser beam is rather high due to too steep gradients in density. The signal to noise ratio of the FFT performed is low as only five spectra are averaged per frequency step of the siren. Furthermore due to the combustion process itself the signal to noise ratio is getting worse by combustion induced noise. All these facts lead to the hypothesis that for the analysis a larger sample is needed. To check if this changes when using other operating conditions two more experiments have been performed. Both LPP injectors were fed with fuel. First the fuel mass flow was set to match an equivalence ratio of roughly 0.28 (see table 9.5). Next the fuel mass flow was lifted to an equivalence ratio of to 0.36 (table 9.6). In neither of the two experiments an perturbation of the flow could be detected by the LV. The corresponding frequency spectra can be found in annex E as no new information could be extracted.

Table 9.4: Operating conditions for first transient reactive stability analysis; pilot burner fed only

| **Modul SER1** | | | **Modul SER2** | | |
|---|---|---|---|---|---|
| $m_{air}$ | 21.87 | g/s | $m_{air}$ | 22.09 | $g/s$ |
| $m_{red}$ | 0.08 | $kg/s \cdot \sqrt{T}/p$ | $m_{air}$ | 0.08 | $kg/s \cdot \sqrt{T}/p$ |
| $m_{fuel}$ | 0.0 | $g/s$ | $m_{fuel}$ | 0.0 | $g/s$ |
| T | 338 | $K$ | T | 333 | $K$ |
| $v_{ref}$ | 10.77 | $m/s$ | $v_{ref}$ | 10.71 | $m/s$ |
| Pilot | | | overall equivalence ratio | | |
| $m_{fuel}$ | 0.8 | $g/s$ | $\phi$ | 0.16 | $[-]$ |

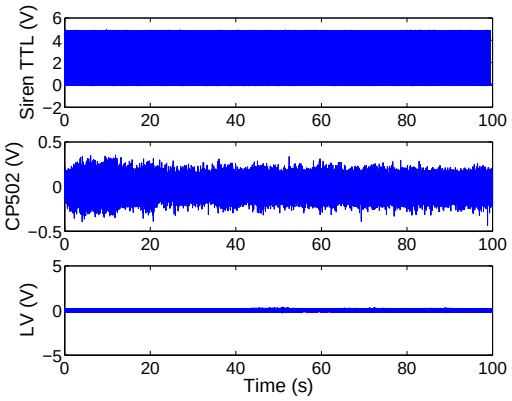


(a) Time signal

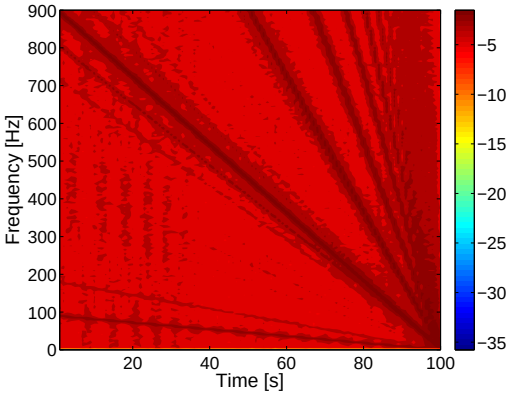


(b) TTL trigger signal as function of time and frequency

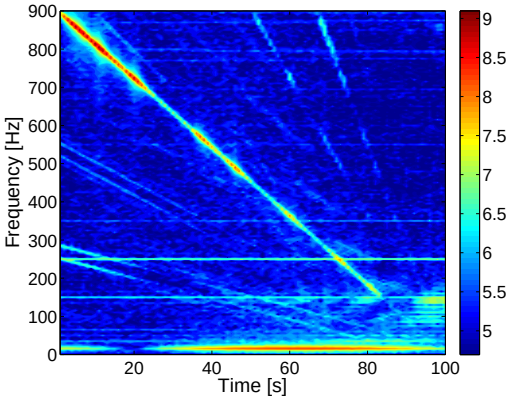


(c) Sound pressure level of CP502 sensor as function of time and frequency

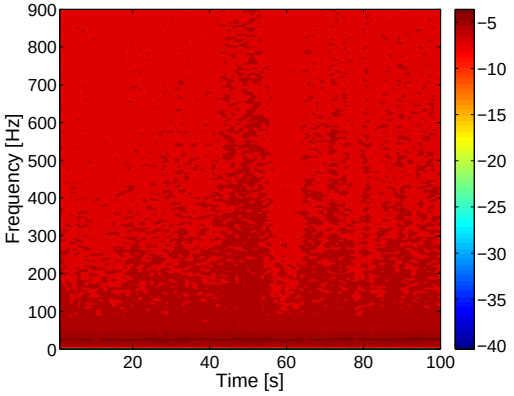


(d) log(Amplitude) of the Laser Vibrometer signal as function of time and frequency

Figure 9.17: Signals recorded during transient reactive stability analysis; decelerations from 900 Hz to halt at 9 Hz/s

Table 9.5: Operating conditions for first transient reactive stability analysis; all injectors active at $\phi = 0.28$

| **Modul SER1** | | | **Modul SER2** | | |
|---|---|---|---|---|---|
| $m_{air}$ | 28.20 | $g/s$ | $m_{air}$ | 28.46 | $g/s$ |
| $m_{red}$ | 0.11 | $kg/s \cdot \sqrt{T}/p$ | $m_red$ | 0.11 | $kg/s \cdot \sqrt{T}/p$ |
| $m_{fuel}$ | 0.5 | $g/s$ | $m_{fuel}$ | 0.5 | $g/s$ |
| T | 366 | $K$ | T | 353 | $K$ |
| $v_{ref}$ | 15.03 | $m/s$ | $v_{ref}$ | 14.63 | $m/s$ |
| **Pilot** | | | **overall equivalence ratio** | | |
| $m_{fuel}$ | 0.8 | $g/s$ | $\phi$ | 0.28 | [−] |

Table 9.6: Operating conditions for first transient reactive stability analysis; all injectors active at $\phi = 0.36$

| **Modul SER1** | | | **Modul SER2** | | |
|---|---|---|---|---|---|
| $m_{air}$ | 27.50 | $g/s$ | $m_{air}$ | 27.7 | $g/s$ |
| $m_{air}$ | 0.11 | $kg/s \cdot \sqrt{T}/p$ | $m_{air}$ | 0.11 | $kg/s \cdot \sqrt{T}/p$ |
| $m_{fuel}$ | 0.7 | $g/s$ | $m_{fuel}$ | 0.7 | $g/s$ |
| T | 384 | $K$ | T | 375 | $K$ |
| $v_{ref}$ | 15.38 | $m/s$ | $v_{ref}$ | 14.86 | $m/s$ |
| **Pilot** | | | **overall equivalence ratio** | | |
| $m_{fuel}$ | 0.8 | $g/s$ | $\phi$ | 0.36 | [-] |

### 9.6.2 Fixed frequency analysis

During the transient operation no perturbation of the flow was detected by the LV because of a too small sample size. To collect a larger sample at a frequency set by the siren, an other operation mode for the siren would have to be designed. As this was not possible, a compromise by doing experiments with a fixed frequency were performed. This analysis has been performed for the frequencies 176 Hz, 624 Hz and 900 Hz. Figure 9.18 shows the spectra obtained. The operating conditions are presented in table 9.7.
As the sample size for a single point measurement was 409,600 it was possible to do an average of 100 spectra. Thus the signal to noise ratio was enhanced.
However, the laser vibrometer detected the perturbation at 176 Hz only. At 624 Hz and 900 Hz only noise was recorded. Comparing the images taken with the camcorder (see annex G), when forcing the excitation with 624 Hz and 900 Hz, one will see that the flame does not stabilize at the primary combustion zone. The flame is established at the end of the combustor. As only a single point measurement close to the tip of the injector was performed, it is possible that either the measurement was performed at a node of the perturbation, or the density change at this location is small as the flame was established at the exhaust.

The frequency at 854 Hz showed the best results in terms of flame stability. Three experiments at different operating conditions were thus performed and are shown separately in figure 9.19. First, only the pilot was operated although the LPP SER1 was excited. Next all three injectors were supplied with fuel and finally only the LPP's were operated at

a rather rich point of operation. The exact set of operating conditions is given in table 9.8.

As the response of the LV at 176 Hz and 854 Hz gave good results, it was decided to map the density fluctuation in the whole combustion chamber. Due to the flame aspect at 624 Hz and 900 Hz mapping was performed here too.

Table 9.7: Operating conditions for perturbations at fixed frequency of 176 Hz, 624 Hz and 900 Hz

| **Excitation at** $176Hz$ | | | | | |
|---|---|---|---|---|---|
| **Modul SER1** | | | **Modul SER2** | | |
| $m_{air}$ | 26.62 | $g/s$ | $m_{air}$ | 27.77 | $g/s$ |
| $m_{red}$ | 0.10 | $kg/s \cdot \sqrt{T}/p$ | $m_{red}$ | 0.10 | $kg/s \cdot \sqrt{T}/p$ |
| $m_{fuel}$ | 0.5 | $g/s$ | $m_{fuel}$ | 0.5 | $g/s$ |
| T | 364 | $K$ | T | 357 | $K$ |
| $v_{ref}$ | 14.11 | $m/s$ | $v_{ref}$ | 14.44 | $m/s$ |
| **Pilot** | | | **overall equivalence ratio** | | |
| $m_{fuel}$ | 0.8 | $g/s$ | $\phi$ | 0.30 | [-] |
| **Excitation at** $624Hz$ | | | | | |
| **Modul SER1** | | | **Modul SER2** | | |
| $m_{air}$ | 26.74 | $g/s$ | $m_{air}$ | 27.87 | $g/s$ |
| $m_{air}$ | 0.10 | $kg/s \cdot \sqrt{T}/p$ | $m_{air}$ | 0.10 | $kg/s \cdot \sqrt{T}/p$ |
| $m_{fuel}$ | 0.5 | $g/s$ | $m_{fuel}$ | 0.5 | $g/s$ |
| T | 369 | $K$ | T | 353 | $K$ |
| $v_{ref}$ | 14.37 | $m/s$ | $v_{ref}$ | 14.33 | $m/s$ |
| **Pilot** | | | **overall equivalence ratio** | | |
| $m_{fuel}$ | 0.8 | $g/s$ | $\phi$ | 0.30 | [-] |
| **Excitation at** 900 | | | | | |
| **Modul SER1** | | | **Modul SER2** | | |
| $m_{air}$ | 22.21 | $g/s$ | $m_{air}$ | 22.36 | $g/s$ |
| $m_{air}$ | 0.09 | $kg/s \cdot \sqrt{T}/p$ | $m_{air}$ | 0.09 | $kg/s \cdot \sqrt{T}/p$ |
| $m_{fuel}$ | 0.7 | $g/s$ | $m_{fuel}$ | 0.7 | $g/s$ |
| T | 371 | $K$ | T | 366 | $K$ |
| $v_{ref}$ | 12.00 | $m/s$ | $v_{ref}$ | 11.92 | $m/s$ |
| **Pilot** | | | **overall equivalence ratio** | | |
| $m_{fuel}$ | 0.5 | $g/s$ | $\phi$ | 0.38 | [-] |

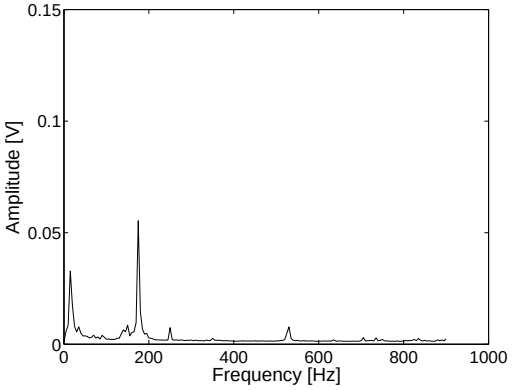


(a) Frequency spectra of CP502 sensor (176 Hz excitation frequency)

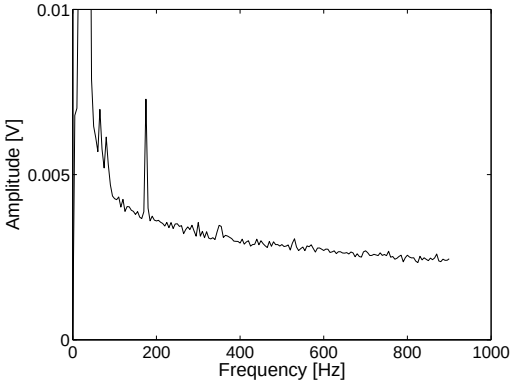


(b) Frequency spectra of the Laser Vibrometer signal (176 Hz excitation frequency)

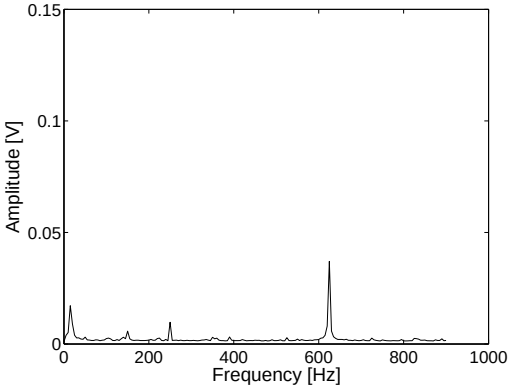


(c) Frequency spectra of CP502 sensor (624 Hz excitation frequency)

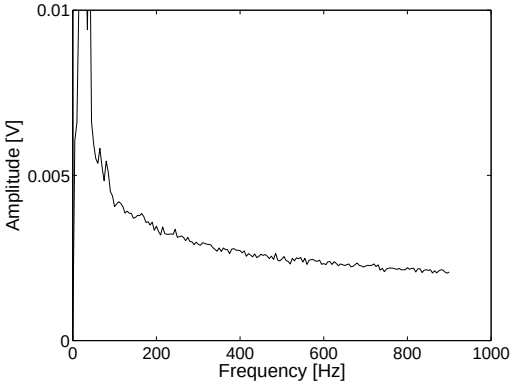


(d) Frequency spectra of the Laser Vibrometer signal (624 Hz excitation frequency)

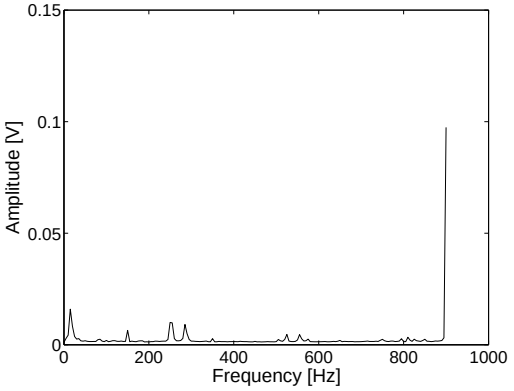


(e) Frequency spectra of CP502 sensor (900 Hz excitation frequency)

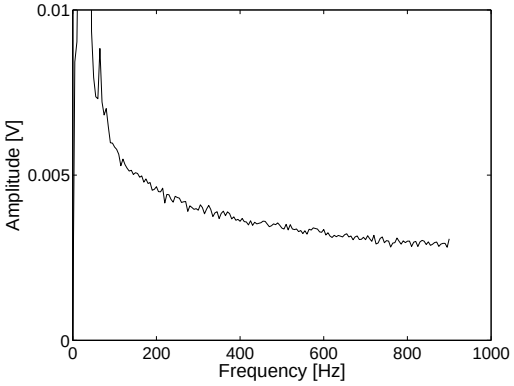


(f) Frequency spectra of the Laser Vibrometer signal (900 Hz excitation frequency)

Figure 9.18: Frequency spectra of CP502 and Laser Vibrometer at excitation frequencies of 176 Hz, 624 Hz and 900 Hz

Table 9.8: Operating conditions during excitation with 854 Hz and different fuel split

| **Pilot burner active only** | | | | | |
|---|---|---|---|---|---|
| **Modul SER1** | | | **Modul SER2** | | |
| $m_{air}$ | 21.30 | $g/s$ | $m_{air}$ | 21.6 | $g/s$ |
| $m_{red}$ | 0.08 | $kg/s \cdot \sqrt{T}/p$ | $m_{red}$ | 0.08 | $kg/s \cdot \sqrt{T}/p$ |
| $m_{fuel}$ | 0.0 | $g/s$ | $m_{fuel}$ | 0.0 | $g/s$ |
| T | 344 | $K$ | T | 336 | $K$ |
| $v_{ref}$ | 10.67 | $m/s$ | $v_{ref}$ | 10.57 | $m/s$ |
| **Pilot** | | | **overall equivalence ratio** | | |
| $m_{fuel}$ | 0.8 | $g/s$ | $\phi$ | 0.17 | [-] |
| **All injectors active** | | | | | |
| **Modul SER1** | | | **Modul SER2** | | |
| $m_{air}$ | 27.67 | $g/s$ | $m_{air}$ | 28.43 | $g/s$ |
| $m_{air}$ | 0.11 | $kg/s \cdot \sqrt{T}/p$ | $m_{air}$ | 0.11 | $kg/s \cdot \sqrt{T}/p$ |
| $m_{fuel}$ | 0.5 | $g/s$ | $m_{fuel}$ | 0.5 | $g/s$ |
| T | 366 | $K$ | T | 353 | $K$ |
| $v_{ref}$ | 14.75 | $m/s$ | $v_{ref}$ | 14.62 | $m/s$ |
| **Pilot** | | | **overall equivalence ratio** | | |
| $m_{fuel}$ | 0.8 | $g/s$ | $\phi$ | 0.29 | [-] |
| **LPP injectors operating only** | | | | | |
| **Modul SER1** | | | **Modul SER2** | | |
| $m_{air}$ | 22.00 | $g/s$ | $m_{air}$ | 22.25 | $g/s$ |
| $m_{air}$ | 0.08 | $kg/s \cdot \sqrt{T}/p$ | $m_{air}$ | 0.08 | $kg/s \cdot \sqrt{T}/p$ |
| $m_{fuel}$ | 1.2 | $g/s$ | $m_{fuel}$ | 1.2 | $g/s$ |
| T | 373 | $K$ | T | 368 | $K$ |
| $v_{ref}$ | 11.95 | $m/s$ | $v_{ref}$ | 11.93 | $m/s$ |
| **Pilot** | | | **overall equivalence ratio** | | |
| $m_{fuel}$ | 0.0 | $g/s$ | $\phi$ | 0.49 | [-] |

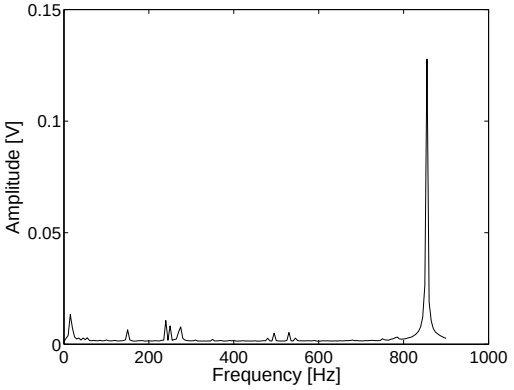


(a) Frequency spectra of CP502 sensor; pilot burner fueled only

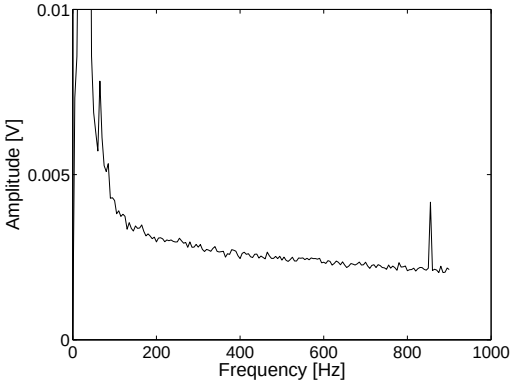


(b) Frequency spectra of the Laser Vibrometer signal; pilot burner fueled only

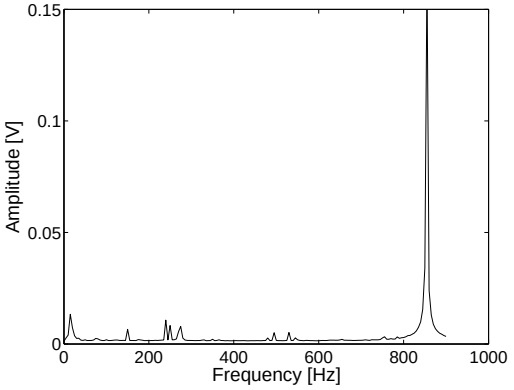


(c) Frequency spectra of CP502 sensor; all injectors active

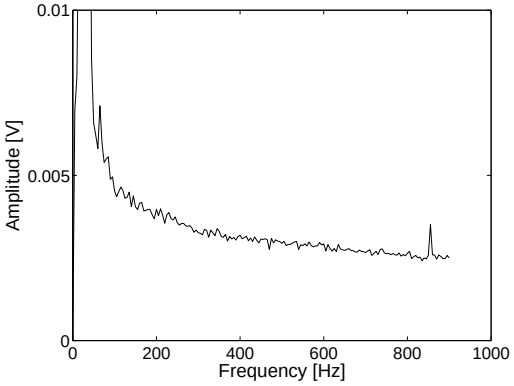


(d) Frequency spectra of the Laser Vibrometer signal; all injectors active

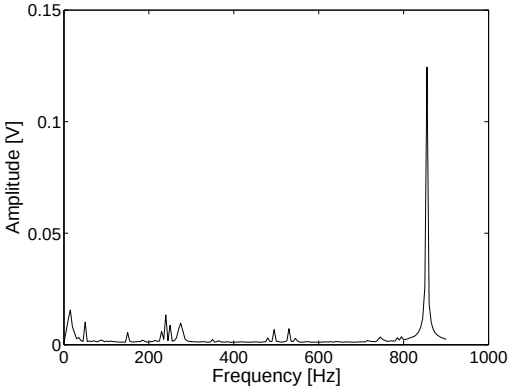


(e) Frequency spectra of CP502 sensor; LPP injectors operating only

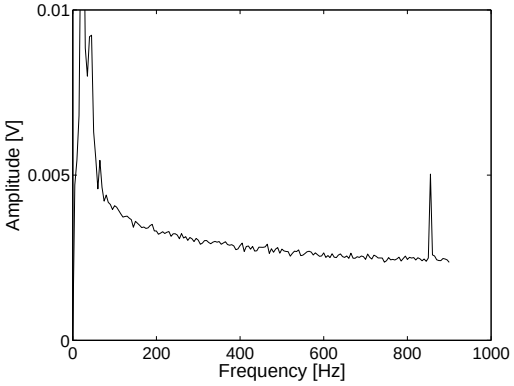


(f) Frequency spectra of the Laser Vibrometer signal; LPP injectors operating only

Figure 9.19: Frequency spectra of CP502 and Laser Vibrometer at excitation frequency of 854 Hz at different operating conditions

### 9.6.3 Mapping of density fluctuations

At 176 Hz, 624 Hz, 854 Hz and 900 Hz a cartography of the whole combustion chamber was performed, in means of density fluctuations. The routines to compute this cartography were presented in chapter 6.

The methodology of presenting the results of the mapping of density fluctuations is similar to the one used at section 9.1. Here the pulsation cycle is divided into 24 subsamples (only 8 are shown here), showing isosurfaces of phase resolved density fluctuation. Here too the figures have to be read clockwise.
During the experiments 93 measurement points were recorded inside the field of view. The measurements were performed along the center axis with a spacing of 5 mm. The lateral spacing was 5 mm too. As the shape of the combustor is not rectangular the measurement plane was tilted. Furthermore the outer boundary have a reduced number of measurement points. The origin of the coordinate system is located at the tip of the pilot burner.
Datapoints were interpolated to receive a finer resolution of the computed data. In the center of each figure a colorbar is given, showing the amplitude of the pulsation. In contrast to the previously shown maps, here the density fluctuation is centered at zero and the colorbar indicates a change in density fluctuation symmetrically to the maximum/minimum. The colorbar changes in magnitude for each figure/experiment.
As no Abel inversion could be performed due to the lack of axi symmetry and the fact that the experiments were performed at $p$ =5 $bar_{abs}$, the density fluctuation shown represents a mean $\rho'$ along the combustor depth.

Figure 9.22 shows the results of the experiment performed at an excitation frequency of 176 Hz ($\tau$ =5.68 ms). The time steps for the subdivisions of the pulsation cycle are 0.24 ms. Shown are frame 1, 3, 6, 9, 12, 15, 18 and 21. The LPP injectors are positioned on the left and the direction of flow is from left to right.
Starting with the first image (figure 9.22a) one will find a large structure with high density fluctuation at the top left corner (see label A). A smaller kernel of low density (label B) is located underneath the larger structure. Both are advectet with the flow downstream to the combustor exit. The direction of flow is along the center axis of the injector, meaning that the trajectory is tilted in respect to the coordinate system. This can be confirmed when looking at the flow visualization presented in section 9.2.
The kernel of low density fluctuation starts to disappear rather quickly (see figure 9.22d), as the amplitude has dropped drastically. However, the structure with increased change in density fluctuation can be tracked until it leaves the field of view, although it looses in intensity too.
After half of the pulsation cycle the kernels change the sign in terms of density fluctuation (figure 9.22e, $t$ =2.84 ms). Although the amplitude for the decreased density fluctuation is at start in the same order of magnitude, it looses quickly in intensity. See the next frame, labeled with (f), at $t$ =3.55 ms.

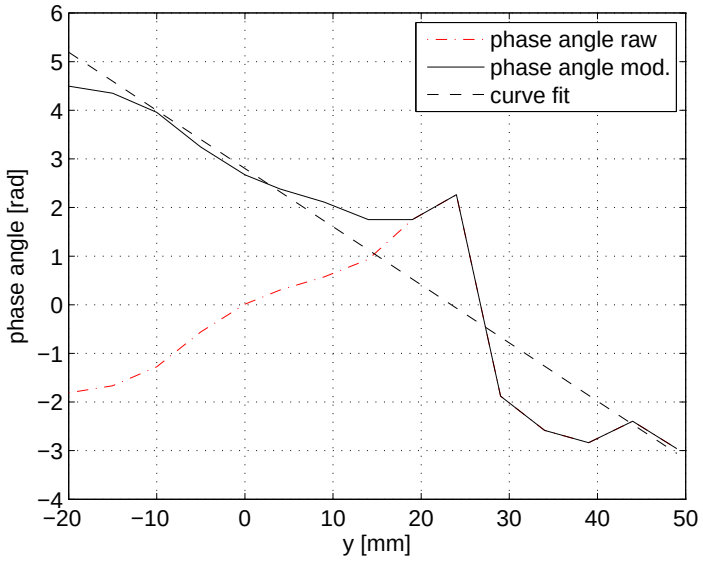


Figure 9.20: Phase plot at center axis during excitation with 176 Hz

An attempt to compute the advect velocity was made by making use of the phase plot at the center line of the injector. Figure 9.20 shows the phase plot at the center line for an excitation frequency of 176 Hz. The ordinate represents the phase angle of density fluctuation in respect to the start of a pulsation cycle. Thus it can be treated as a time scale. The abscissa shows the distance along the jet axis of the injector. By applying equation 9.2 the velocity of the correlated structure can be computed.

$$c = \frac{\Delta s}{\Delta t} \tag{9.2}$$

$t$ is derived from the definition of the phase angle

$$\phi = 2 \cdot \pi \cdot f \cdot t \Rightarrow \Delta t = \frac{\Delta \phi}{2 \cdot \pi \cdot f} \tag{9.3}$$

The resulting advect velocity of the structures at the center axis is computed with 9.2 m/s.

To proof the results obtained, a high speed video has been taken during the experiment. A camera of type Casio Exilim F1 was used, recording images at a frame rate of 600 fps, with a resolution of 432x192 pixels. The images were split into the appropriate RGB channels. The blue channel represents the luminosity of the flame, as due to chemiluminescence ($CH$ chemiluminescence) the flame emits at the blue range of the visible spectrum. After performing a FFT over the whole image plane, figure 9.21 shows a peak at 176 Hz. The measured density fluctuation can thus be correlated with the chemiluminescence of the flame. For more details on the processing see [11].

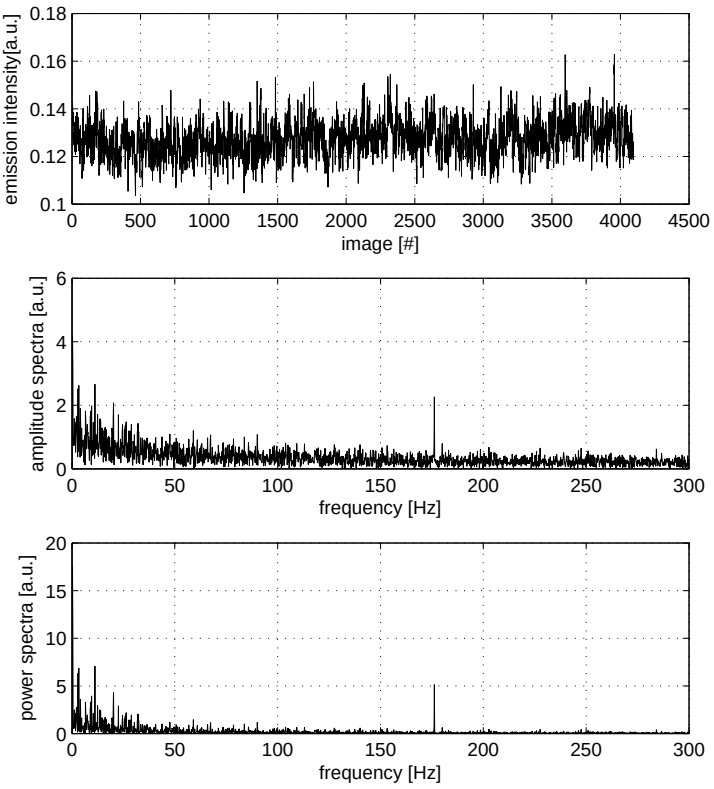


Figure 9.21: Luminosity analysis of a high speed video at 176 Hz excitation frequency

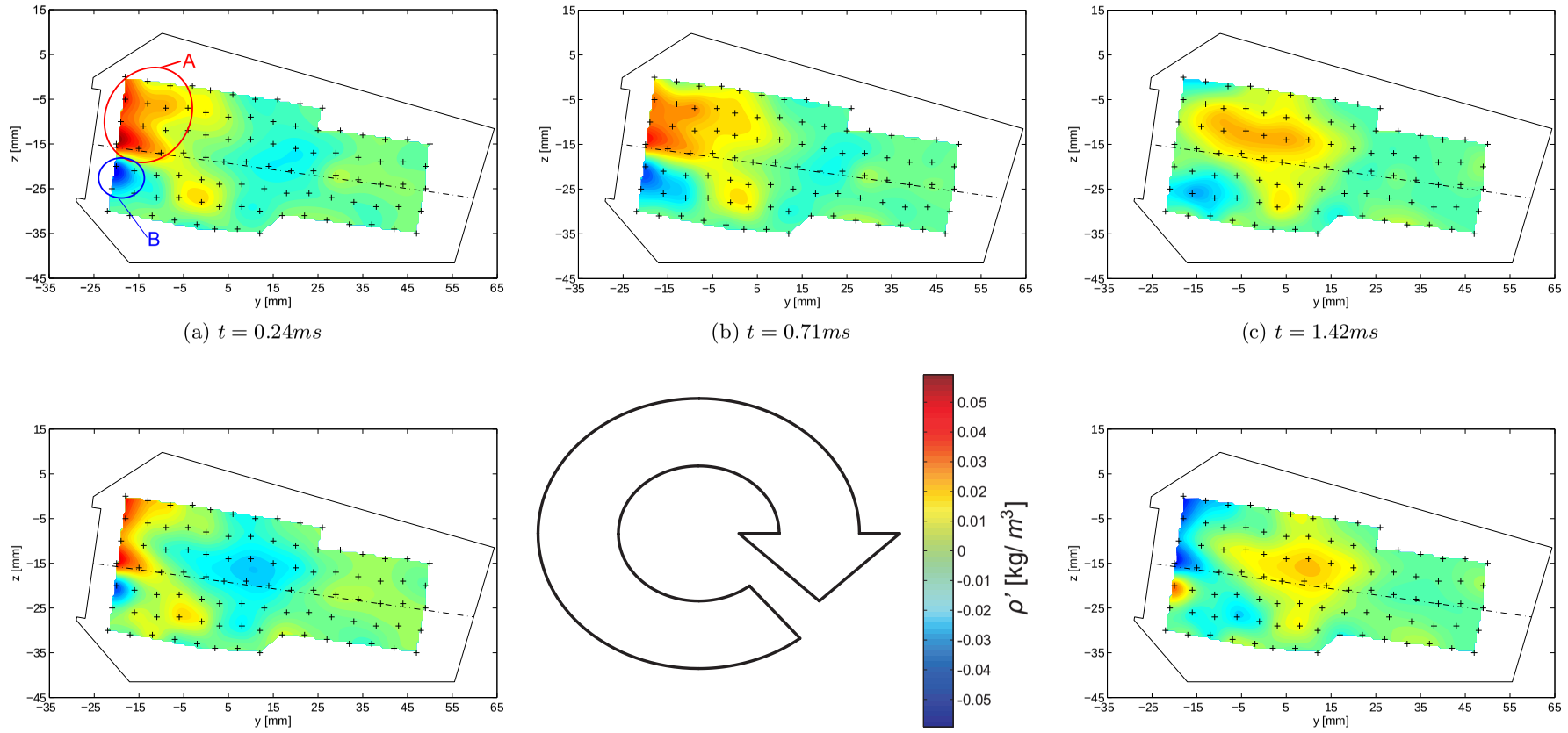


(a) $t = 0.24ms$ (b) $t = 0.71ms$ (c) $t = 1.42ms$

(h) $t = 4.97ms$ (d) $t = 2.13ms$

(g) $t = 4.26ms$ (f) $t = 3.55ms$ (e) $t = 2.84ms$

Figure 9.22: Phase resolved density fluctuation at $176Hz$ excitation frequency

Figure 9.23 shows the density fluctuation recorded at 624 Hz ($\tau$ =1.6 ms) excitation frequency. Frame 1, 3, 6, 9, 12, 15, 18 and 21 of the 24 subperiods (time steps of 0.07 ms) are shown. Notice that the amplitude of excitation (see the colorbar at center of figure 9.23) is only at a fifth of the amplitude during excitation with 176 Hz.
In contrast to the previously shown map at 176 Hz no large structures are advected with the flow. The structures recorded are similar to the ones shown at the dump combustor experiments. A pocket of increased density fluctuation is formed at the combustor entry (see label A). The structure is filling the whole height of the field of view, whereas its widht is in the order of 5 mm. At some frames the oblong shaped structures are split into smaller kernels (e.g. see image (b) and (c)), but combine to one continuous pattern later on. However, the strucutre is then moving towards the exit for half of the distance from one structure with increased density to the next (see the black arrows). After half of the pulsation cycle, kernels with decreased density fluctuation start to appear at the combustor entry (label C). Pockets of higher $\rho'$ are still present at the previously stated location. Towards the exhaust of the combustor (roughly at $y$ =+15 mm) the structures start to disappear and $\rho'$ levels to zero.
The behavior of the flow field in terms of density fluctuation seems to form a wave with its bellies moving with half of the wave length within half of the pulsation period.
Although the single point measurement presented in section 9.6.2 has shown that no perturbation can be detected, the mapping showed the perturbation of $\rho'$ quite easily throughout the whole flow field.
High speed images of the flame could not be taken as the frame rate of the camera available is not high enough. Also the computation of the advect velocity was not possible as the spatial resolution of the measurement is insufficient to track the phase perfectly.

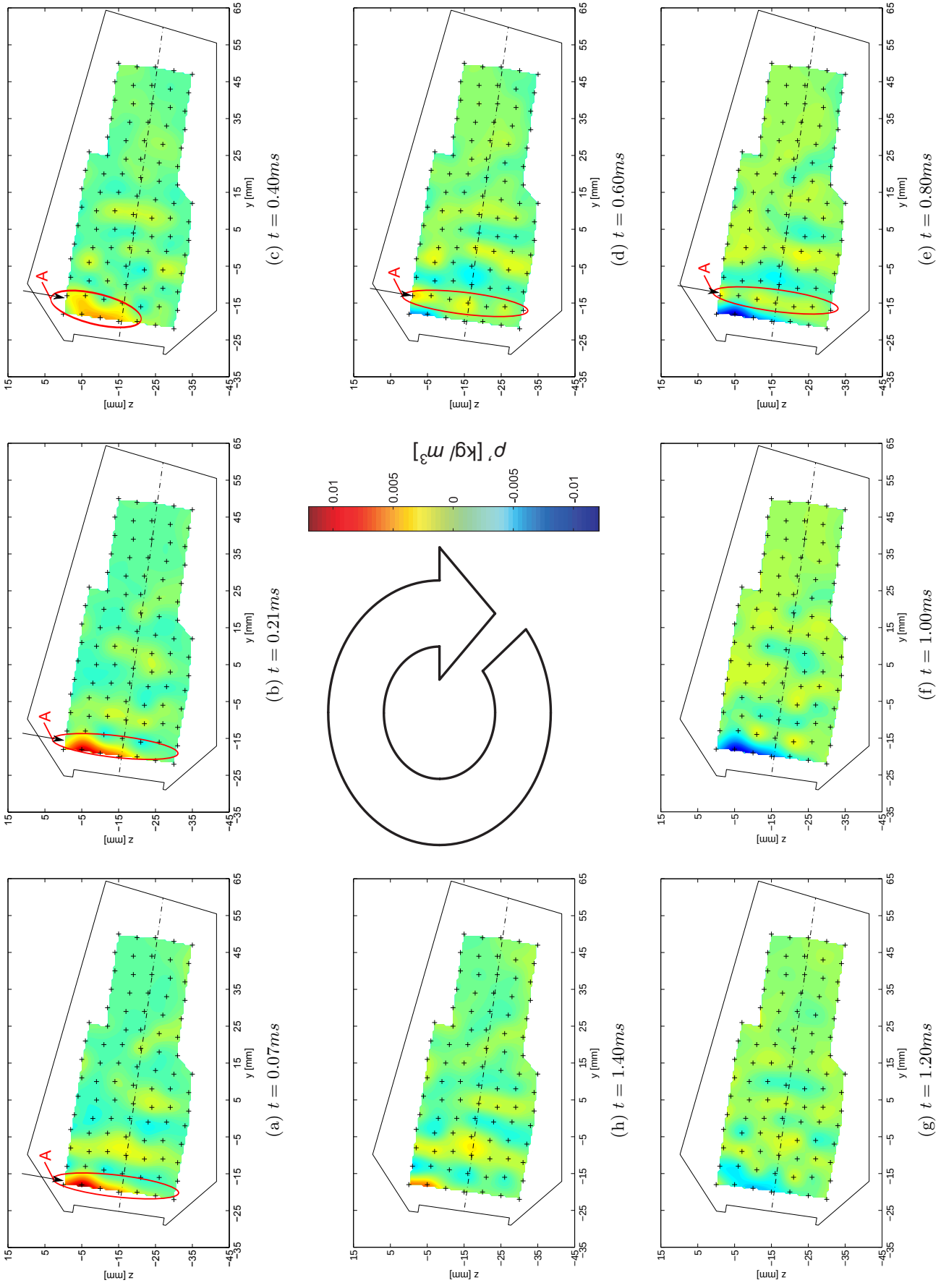


(a) $t = 0.07ms$ (b) $t = 0.21ms$ (c) $t = 0.40ms$

(d) $t = 0.60ms$ (e) $t = 0.80ms$

(f) $t = 1.00ms$ (g) $t = 1.20ms$ (h) $t = 1.40ms$

Figure 9.23: Phase resolved density fluctuation at $624Hz$ excitation frequency

At excitation with 854 Hz ($\tau$ =1.17 ms) the pulsation is given with a resolution of 0.05 ms. Again the image frames 1, 3, 6, 9, 12, 15, 18 and 21 are shown. As the colorbar of figure 9.24 indicates, the amplitude is less than half of the amplitude at 176 Hz, but doubled compared to the excitation at 624 Hz.
Similar to the previously shown excitation the structures are narrow in lateral direction. The width is smaller (below 5 mm) compared to the structures as 624 Hz. The structures almost fill the whole height of the field of view. At bottom of the combustor the density levels to zero. Here too a structure with increased density fluctuation is formed at the tip of the LPP injector and advected with the flow (label A; see black arrows for tracking). Between the bellies with high density fluctuation, smaller kernels of decreasing $\rho'$ can be found. At image (c) the structures almost disappear (label B) and change from increasing to decreasing density fluctuation in the next frame (label C).
For the second half of the pulsation cycle a similar behavior is found. Following the whole pulsation cycle it seems that a standing wave with several bellies inside the combustor volume is formed.

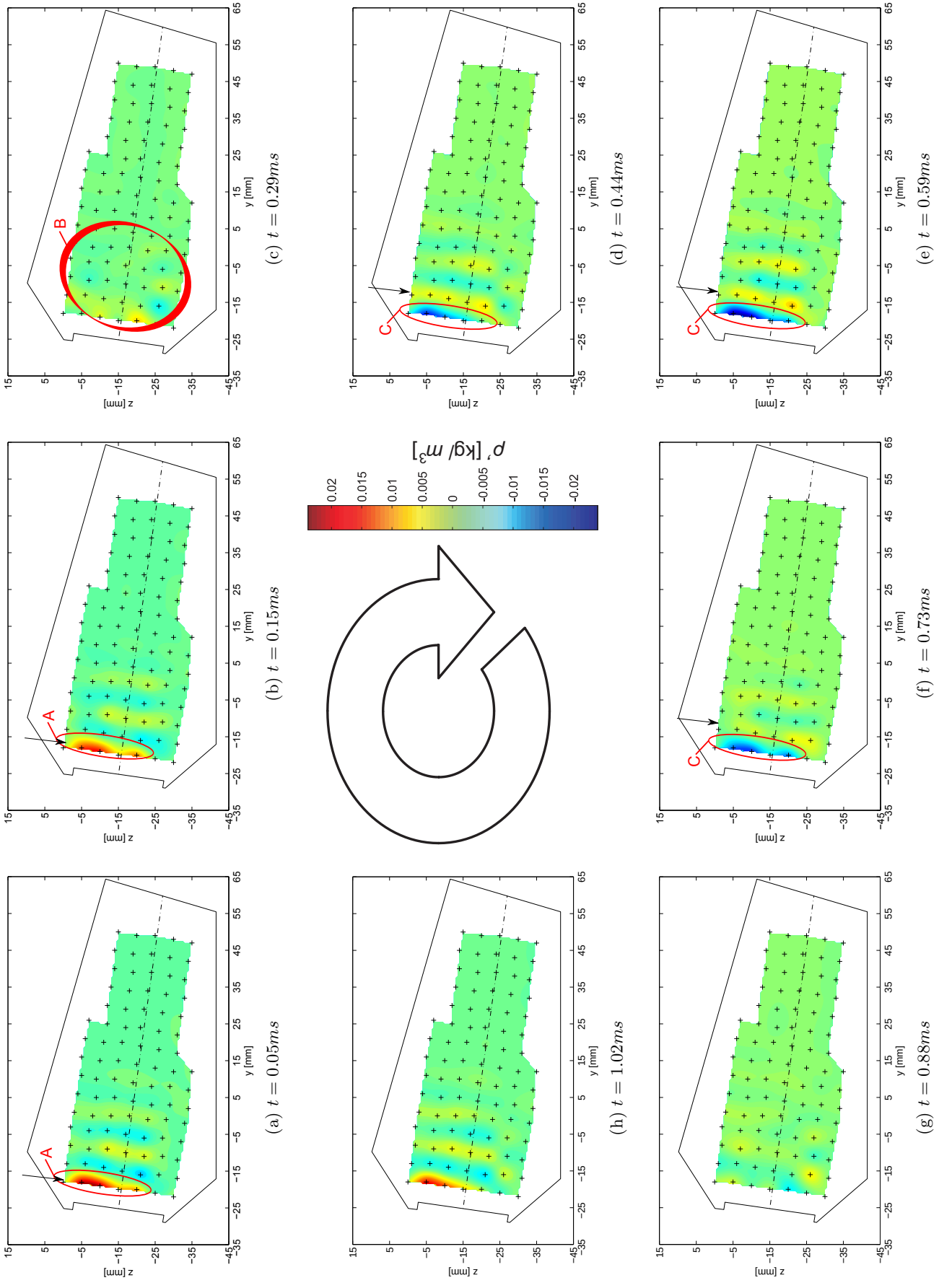


(a) $t = 0.05ms$ (b) $t = 0.15ms$ (c) $t = 0.29ms$ (d) $t = 0.44ms$ (e) $t = 0.59ms$ (f) $t = 0.73ms$ (g) $t = 0.88ms$ (h) $t = 1.02ms$

Figure 9.24: Phase resolved density fluctuation at $854Hz$ excitation frequency

For the excitation with 900 Hz ($\tau$ =1.11 ms) the established field in terms of density fluctuation is different from the previously shown. The intensity of the pulsation is lower than the one at 176 Hz and 854 Hz, but still higher than when perturbing with 624 Hz. The correlated structures formed tend to be located at the top left of the field of view. Furthermore are the structures trackable only up to roughly $y$ =5 mm. The flow field further downstream is centered at $\rho' = 0$. The detached structures do not reach below the center axis of the LPP injectors and only proceed till the location of the pilot injector. The structures are labeled with A in figure 9.25 and seem to be causally linked to the fuel injection via the pilot burner. The pulsation of the LPP modules seems to be less effective here, but a feedback on the pilot seems to be given.

Comparing the results obtained during experiments using ethanol, to the results obtained when using methane, it will lead to the fact that the LV can be used for measurements in two phase flows at elevated pressure conditions. Although no tomographic reconstruction technique could be used due to the setup, the integral data along the line of sight still lead to reasonable results.

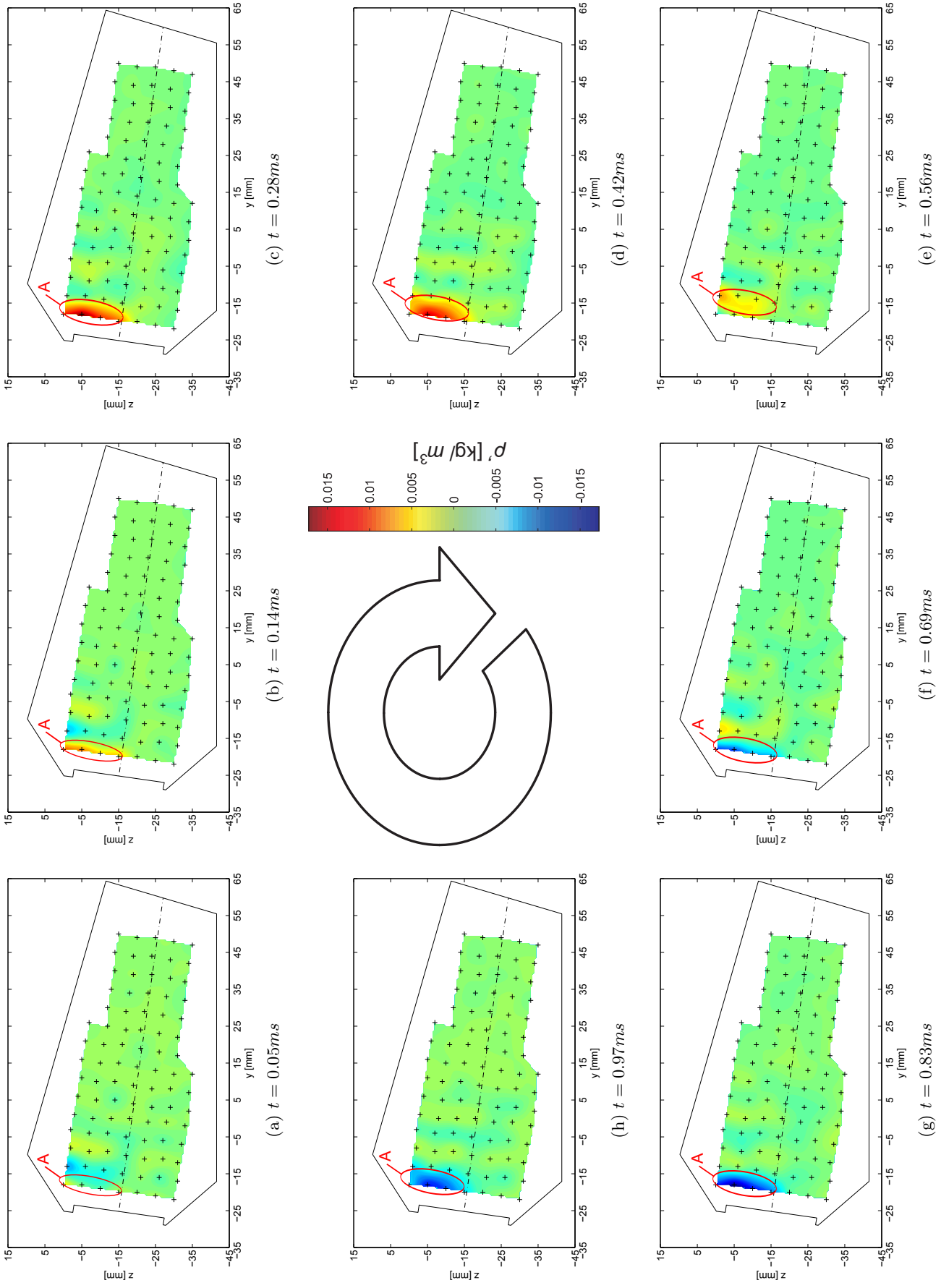


(a) $t = 0.05ms$ (b) $t = 0.14ms$ (c) $t = 0.28ms$

(d) $t = 0.42ms$ (e) $t = 0.56ms$ (f) $t = 0.69ms$

(g) $t = 0.83ms$ (h) $t = 0.97ms$

Figure 9.25: Phase resolved density fluctuation at $900Hz$ excitation frequency

# Chapter 10

# Summary and Conclusion

In this work unstable combustion was investigated with regard to two aspects. A wanted discontinuous combustion in possible future aero engine combustion chambers and secondly the unwanted effect in actual combustion chamber systems.
First during the literature survey the use of pulse detonation combustors was shown, where the regularly used deflagrative combustion was replaced by a detonation process. The thermodynamical background of such a device acting in a hybrid turbo fan engine was gathered from the literature, new improved aspects were introduced and compiled into a performance computation tool. The developed performance computation tool was validated using test cases from the literature with success. Two engine configurations have been designed and their performance was estimated.
Both test cases have in common that a part of the high pressure core was replaced by a pulse detonation combustor. The first test case however intended to build a lighter engine at same thrust specific fuel consumption by making use of the pressure gain during the detonation process. A reduction in engine weight of 6 % could be achieved (see reference [29]), giving an operational area for short range air crafts. For the second test case an engine with an increased pressure ratio was modeled. Here again, by using the pressure gain combustion, the OPR of the engine was further lifted. Thus at same thrust a decrease in thrust specific fuel consumption of 5.4 % could be claimed, giving a penalty of an increase in 13 % engine weight. This will result in an engine configuration for long range application.
In the presented study it was shown that for the scope beyond 2020 of the ACARE goals a technology is waiting in the wings to further enhance the reduction in pollutant emissions and fuel burn.

However, as the technology of pulsed combustion, although very promising, is just at the start of development, close attention was paid on the topic of avoiding pulsed combustion in terms of combustion instabilities.
As especially in modern low $NO_x$ combustors the problem of combustion instabilities arises, a laser based measurement technique, the so called Laser Vibrometery, was adapted to combustors operating at elevated pressure and temperature conditions.
Several combustion chambers were designed. The first one was used for preliminary experiments. Its development was based on a laboratory design. The purpose of the device was to gain experience in combustor and test rig design for elevated pressure and temperature conditions and to perform first experiments using Laser Vibrometry at such operating conditions. In addition the optical investigation of forced combustion instabilities was accompanied by a pressure transducer of type CP502 by Piezocryst. With the experiments performed on the test bench it was shown that this type of sensor can detect combustion oscillations, when being installed near the flame at the combustor

liner wall, thus facing elevated pressure and temperature conditions. The sensor was thus also used for later experiments and integrated into the monitoring system of the combustors used.
After experiments with a combustor built with one liquid fueled injector for experiments at ambient conditions using Laser Vibrometry, a industrial type combustor test sector was designed and built. It consists of two Low-$NO_x$ injectors of the Lean Premixed Prevaporized type and a pilot burner stage. All modules were operated using ethanol as propellant.
To artificially excite the flow field, a siren type flow exciter was designed, build and fully validated.
The test campaign of the industrial type combustor started with an isothermal flow characterization done at ambient conditions using LDA. The measurements performed have shown that the flow field inside the combustor is not establishing a recirculation zone. Although this is common to aero engine combustors, LPP combustors are designed not to form such a zone. The flow field is designed more to appear like seen on Bunsen burners. The flow field of the test sector does also have such an appearance. Next the combustor was operated at elevated pressure at isothermal conditions to scan for possible resonant frequencies. Two strips of frequencies with high response of the combustor to the introduced perturbation were found. One at 490÷580 Hz and one at 700÷900 Hz. The latter one being of greatest interest as the strongest response was given there.
The scanning for resonant frequencies was repeated at reactive flow conditions. Although the response of the pressure transducer was the same as at isothermal conditions, the LV was not able to detect any excitation. It was found out that due to the operating conditions the sample size of the recording was not sufficient enough to result in a good signal to noise ratio. Thus experiments at fixed frequencies were performed to collect a larger signal sample. This resulted in a higher quality of the computed Laser Vibrometer data. The perturbation could now be detected easily. Finally a mapping of the density field perturbed by the siren was done. It was shown that at the low frequency range (176 Hz) correlated structures are transported with the mean flow downstream the combustor. At higher pulsation frequencies the combustion instabilities form standing waves with several bellies inside the combustor. At 900 Hz it was found that the introduced perturbations mainly act on the pilot burner.
During experiments with the first combustion chamber the method of ensemble averaging was possible to show phase averaged spatially resolved density fluctuations. Due to the low signal to noise ratio during experiments with the liquid fueled combustor, correlation techniques had to be used. It has been shown that by using the siren trigger as correlation signal, the information in terms of phase could be gained. The signal amplitude of density fluctuation however was obtained by simply using the signal amplitude of the LV itself.
So for the first time LV was successfully applied to a liquid fueled combustor operating at elevated pressure and temperature conditions to map density fluctuations in such an environment, induced by a siren type flow exciter.

With the help of the Laser Vibrometry it is now possible to use a non intrusive fast working measurement technique on the test bench during first combustor sector rig tests to look for combustion instabilities. For first shots by making use of the developed siren it is possible to scan for resonant frequencies and finally cartograph combustion instabilities in a wide field of view. The results obtained (density fluctuations) are spatially (at least two dimensional) and frequency resolved without the need for calibration of the device or correction of the measured data.

For further experiments it would be of interest to investigate the impact of different amplitudes of excitation at the above stated frequencies. To use all the capabilities of the testing facility at the ITTM at TUG, the use of kerosene as fuel would be of interest too. Concerning the Laser Vibrometry the use of a second LV in the dual mode, as used by Köberl [11], in an industrial type combustor would be interesting to receive local information (spatially resolved in three dimensions) of the density fluctuation. However, as this was not possible with the actual combustor design a newly designed combustor is necessary. A first attempt towards such a new combustor was made with the design of a LPP type injector (see [77] for details).

# Chapter 11

# Published articles

## 11.1 Articles on Pulse Detonation engines

Fabrice Giuliani, Andreas Lang, Mohammad Irannezhad, Tomas Grönstedt. Effects of a Controlled Phase-Shift on the Outlet Conditions of a Set of Pulse Detonators. In *Proceedings of the 18th ISABE Conference*, number ISABE-2009-1315, 2009

Fabrice Giuliani, Andreas Lang, Mohammad Irannezhad, Anders Lundbladh. Pulse Detonation as an Option for Future Innovative Gas Turbine Combustion Technologies: A Concept Assessment. In *27th International Congress of the Aeronautical Sciences*, 2010.

## 11.2 Articles on Laser Vibrometry Measurements

Andreas Lang, Thomas Leitgeb, Jakob Woisetschläger, Alain Strzelecki, Pierre Gajan, and Fabrice Giuliani. Analysis of a Pulsed Flame at Intermediate Pressure. In *Proceedings of the 13th International Symposium on Flow Visualization and 12th French Congress on Visualization in Fluid Mechanics*, 2008.

Fabrice Giuliani, Thomas Leitgeb, Andreas Lang, and Jakob Woisetschläger. Mapping the Density Fluctuations in a Pulsed Air-Methane Flame Using laser-Vibrometry. In *Proceedings of ASME Turbo Expo 2009: Power for Land, Sea and Air*, GT2009-59682

Fabrice Giuliani, Thomas Leitgeb, Andreas Lang, and Jakob Woisetschläger. Mapping the Density Fluctuations in a Pulsed Air-Methane Flame Using laser-Vibrometry. In *Journal of Engineering for Gas Turbine and Power*, 132

Fabrice Giuliani, Andreas Lang, Thomas Leitgeb, Jakob Woisetschläger, Franz Heitmeir. Using Dual Laser Vibrometry to Monitor the Stability of Gas Turbine Combustion. In *3rd European Combustion Meeting*, 2007

## 11.3 Others

Fabrice Giuliani, Alexander Schricker, Andreas Lang, Thomas Leitgeb, Franz Heitmeir. High-Temperature Resistant Pressure Transducer for Monitoring of Gas Turbine Combustion Stability. In *Proceedings of the 16th ISABE Conference*, number ISABE-2007-1111, 2007.

Fabrice Giuliani, Andreas Lang, Klaus Johannes Gradl, Peter Siebenhofer, Johannes Fritzer. Air Flow Modulation for Refined Control of the Combustion Dynamics Using a Novel Actuator. In *Proceedings of ASME Turbo Expo 2011: Power for Land, Sea and Air*, GT2011-45700

Fabrice Giuliani, Andreas Lang, Klaus Johannes Gradl, Peter Siebenhofer, Johannes Fritzer. Air Flow Modulation for Refined Control of the Combustion Dynamics Using a Novel Actuator. In *Journal of Engineering for Gas Turbines and Power*, in press

Andreas Lang, Renaud Lecourt, Fabrice Giuliani. Statistical Evaluation of Ignition Phenomena in Turbojet Engines. In *Proceedings of ASME Turbo Expo 2010: Power for Land, Sea and Air*, GT2010-23229

# Appendices

# Appendix A

# Thermodynamical expressions for pulse detonation engine modeling

This annex describes the mathematical expressions used for the performance model to represent detonative combustion. The expressions presented are generally in accordance with Kentfield [41]. Special notes are given where appropriate.
As said in chapter 3 the specific heat and thus the isentropic exponent $\gamma$ is iterated on an energy balance between the station points $X$ ($T_X$) and $Z$ ($T_{0z}$).

The Mach-Number of the stationary shockwave at start of detonation is given by

$$M_x = \left[2 \cdot \left(1 + \frac{\gamma + 1}{T_X \cdot c_p \cdot AFR_{st}} \cdot \phi \cdot H_f\right)\right]^{1/2} \tag{A.1}$$

The pressure raise due to the normal shock is determined by making use of the NACA normal shock tables (equations are used)[42]

$$\frac{p_Y}{p_X} = \frac{2 \cdot \gamma \cdot M_x^2 - \gamma + 1}{\gamma + 1} \tag{A.2}$$

The temperature ratio of the normal shock is also derived from the normal shock tables

$$\frac{T_Y}{T_X} = \frac{[2 \cdot M_x^2 - (\gamma - 1)] \cdot [(\gamma - 1) \cdot M_x^2 + 2]}{(\gamma + 1)^2 \cdot M_x^2} \tag{A.3}$$

The Mach-Number at the end of the normal shock (stationary shockwave) equals

$$M_Y = \left(\frac{M_x^2 \cdot (\gamma - 1) + 2}{2 \cdot M_x^2 \cdot \gamma - (\gamma - 1)}\right)^{1/2} \tag{A.4}$$

The stagnation temperature ratio after the normal shock is given by equation A.5. The equation is representing the relationship between static and stagnation temperature as function of the Mach-Number of the fluid (isentropic; the missprint in [41] is corrected here)

$$\frac{T'_{0Y}}{T_X} = \frac{T_Y}{T_X} \cdot \left(1 + \frac{\gamma - 1}{2} \cdot M_Y'^2\right) \tag{A.5}$$

Similar for the stagnation pressure after the normal shock

$$\frac{p'_{0Y}}{p_X} = \frac{p_Y}{p_X} \cdot \left(1 + \frac{\gamma - 1}{2} \cdot M_Y'^2\right)^{\frac{\gamma}{\gamma - 1}} \tag{A.6}$$

The pressure ratio of the detonation process itself, meaning a normal shock with a following Rayleigh heat addition can be computed as

$$\frac{p_Z}{p_X} = \frac{1}{2} \cdot \left( \frac{p_Y}{p_X} + 1 \right) \tag{A.7}$$

For the Rayleigh heat addition, which is defined as a steady, one dimensional flow process with addition or removal of heat without any mechanical work, viscous stress or body force involved; Foa [40]. However, by setting the specific heat of the detonation process constant, one can apply the following equation

$$p_0 \cdot G = \text{const.} \tag{A.8}$$

with

$$G = \frac{1 + \gamma M^2}{\left(1 + \frac{\gamma - 1}{2} \cdot M^2\right)^{\frac{\gamma}{\gamma - 1}}} \tag{A.9}$$

Furthermore

$$\frac{N}{\sqrt{T_0'}} = \text{const.} \tag{A.10}$$

with

$$N = \frac{M \left(1 + \frac{\gamma - 1}{2} \cdot M^2\right)^1 2}{1 + \gamma \cdot M^2} \tag{A.11}$$

By applying the equations A.8 and A.10 to the flow at a known state one can determine the flow conditions at another station when knowing the amount of heat added or removed. These equations are now applied to station $Y$ to compute the constants. First equation A.9 is solved

$$G_Y = \frac{1 + \gamma M_Y'^2}{\left(1 + \frac{\gamma - 1}{2} \cdot M_Y'^2\right)^{\frac{\gamma}{\gamma - 1}}} \tag{A.12}$$

and applied to equation A.8

$$\text{const}_p = p_{0Y} \cdot G_Y \tag{A.13}$$

For the temperature relation the same methodology is applied

$$N_Y = \frac{M_Y' \left(1 + \frac{\gamma - 1}{2} \cdot M_Y'^2\right)^1 2}{1 + \gamma \cdot M_Y'^2} \tag{A.14}$$

$$\text{const}_T = \frac{N_Y}{\sqrt{T_{0y}}} \tag{A.15}$$

At the end of the detonation process the Mach-number $M_Z'$for the stationary shock wave is unity. So equation A.11 is once more used

$$N_Z = \frac{\left(1 + \frac{\gamma - 1}{2}\right)^1 2}{1 + \gamma} \tag{A.16}$$

and thus the stagnation temperature ratio after the heat addition for the stationary shock wave is

$$\frac{T_{0Z}'}{T_X} = \left( \frac{N_Z}{\text{const}_T} \right)^2 \cdot \frac{1}{T_X} \tag{A.17}$$

The static temperature ratio is than as follows

$$\frac{T_Z}{T_X} = \frac{T'_{0Z}}{T_X} \cdot \left(1 + \frac{\gamma - 1}{2} \cdot\right)^{-1} \cdot \frac{1}{T_X} \tag{A.18}$$

For the pressure ratio one will find

$$G_z = \frac{1 + \gamma}{\left(1 + \frac{\gamma - 1}{2}\right)^{\frac{\gamma}{\gamma - 1}}} \tag{A.19}$$

$$\frac{p_{0Z}}{p_X} = \frac{\text{const}_p}{G_Z \cdot p_X} \tag{A.20}$$

The pressure ratio $p_Z/p_X$ can now be checked for consistency by using

$$\frac{p_Z}{p_X} = \frac{p_{0Z}}{p_X} \cdot \left(1 + \frac{\gamma - 1}{2}\right)^{-\frac{\gamma}{\gamma - 1}} \tag{A.21}$$

The stationary shock wave has now to be transformed into a moving one. Therefore the speed of sound is evaluated at the initial state and is deducted from the Mach-numbers at state point $Y$ and $Z$. Thus the Quantities at $Y$ and $Z$ have to be evaluated once more. First the velocity of the flow at $X$ is computed

$$a_X = \sqrt{\gamma \cdot R \cdot T_X} \tag{A.22}$$

$$c_X = M'_x \cdot a_X \tag{A.23}$$

The Mach-number at $Y$ for the moving shock wave is than as follows

$$a_Y = \sqrt{\gamma \cdot R \cdot T_Y} \tag{A.24}$$

$$M_Y = \frac{c_X}{a_Y} - M'_Y \tag{A.25}$$

Doing the same for state $Z$

$$a_Z = \sqrt{\gamma \cdot R \cdot T_Z} \tag{A.26}$$

$$M_Z = \frac{c_X}{a_Z} - M'_Z \tag{A.27}$$

Thus the stagnation temperature and pressure ratios can be computed by applying equations A.6 and A.5 once more

$$\frac{T_{0Y}}{T_X} = \frac{T_Y}{T_X} \cdot \left(1 + \frac{\gamma - 1}{2} \cdot M_Y^2\right) \tag{A.28}$$

$$\frac{p_{0Y}}{p_X} = \frac{p_Y}{p_X} \cdot \left(1 + \frac{\gamma - 1}{2} \cdot M_Y^2\right)^{\frac{\gamma}{\gamma - 1}} \tag{A.29}$$

$$\frac{T_{0Z}}{T_X} = \frac{T_Z}{T_X} \cdot \left(1 + \frac{\gamma - 1}{2} \cdot M_Z^2\right) \tag{A.30}$$

$$\frac{p_{0Z}}{p_X} = \frac{p_Z}{p_X} \cdot \left(1 + \frac{\gamma - 1}{2} \cdot M_Z^2\right)^{\frac{\gamma}{\gamma - 1}} \tag{A.31}$$

To account for the nonuniform flow field inside the PDE device, leading to an average pressure and temperature, both being much lower than the peak values computed so far, the energy required to drive the shock wave is computed, thus lowering the pressure and

temperature at the exhaust of the tube.
So the temperature at the end of the detonation process will finally drop to

$$T_D = T_{0Z} - \Delta T_{finalexp} \tag{A.32}$$

To compute the temperature needed in the final expansion process an energy balance has to be provided. One will therefore consider the following.
First the temperature increase due to constant area combustion is given by

$$\Delta T_{gain} = T_{0Z} - T_{0Y} \tag{A.33}$$

The energy spill-over due to heat release by the combustion reduced by the temperature increase due to constant area combustion will be used to power the shock wave. Thus

$$\Delta T_{work} = \frac{\Delta q}{c_p} - \Delta T_{gain} \tag{A.34}$$

On the other hand, the work needed to drive the shock wave from $X$ to $Y$ is

$$\Delta T_{shock} = T_{0Y} - T_X \tag{A.35}$$

So the temperature difference for the final expansion is therefor the work that is required to drive the shock wave reduced by the work obtained and employed to it

$$\Delta T_{finalexp} = \Delta T_{shock} - \Delta T_{work} \tag{A.36}$$

For the pressure after the detonation process one can use the isentropic relationship

$$p_D = p_{0z} \cdot \left( \frac{T_D}{T_{0z}} \right)^{\frac{\gamma}{\gamma - 1}} \tag{A.37}$$

Figure A.1 is illustrating the computation to find the end temperature and pressure of the detonation.

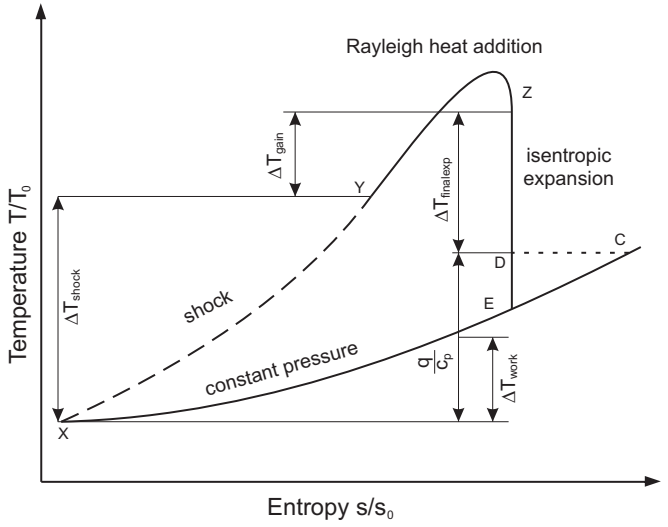


Figure A.1: Detailed Temperature Entropy Diagram of the Detonation Process with Enthalpy Changes

Also quite obvious from the previous description of the process is that the heat addition during the detonation process will result in an temperature increase that would be achieved during a constant pressure combustion, but at a lower entropy increase.

$$\Delta T_{finalexp} = \Delta T_{shock} - \Delta T_{work} \tag{A.38}$$

$$T_{0Z} - T_D = T_{0Y} - T_X - \frac{q}{c_p} + T_{0Z} - T_{0Y} \tag{A.39}$$

$$\frac{q}{c_p} = T_D - T_X \tag{A.40}$$

# Appendix B

# Results on second test case evaluation

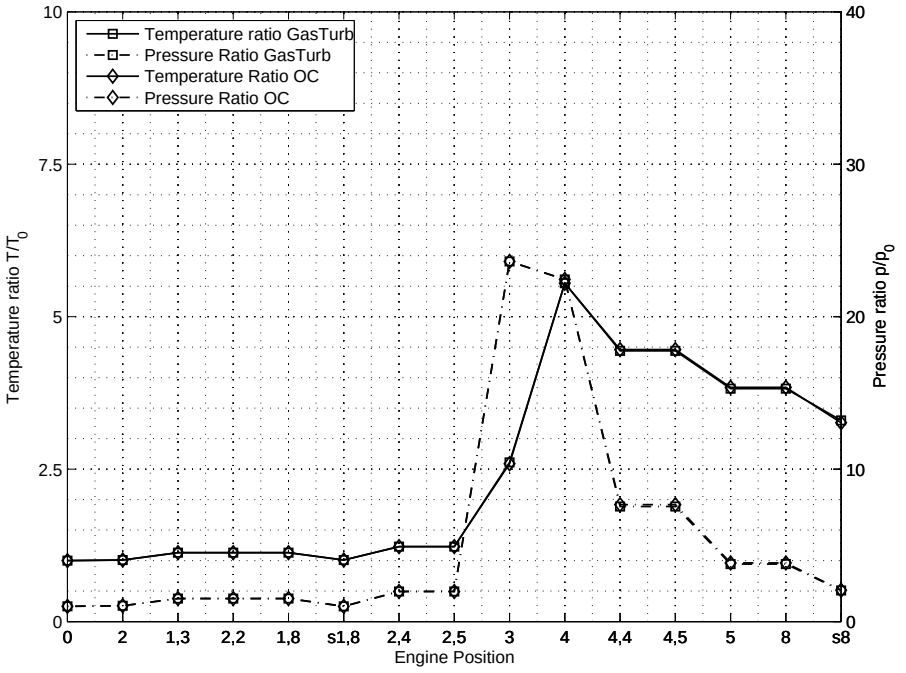


Figure B.1: Results obtained from computation of reference engine (case 1)

Table B.1: Results of cycle evaluation for conventinal turbofan engine reference case 2; comparison of PM to GasTurb11

| | | **GasTurb11** | **PM** | **deviation [%]** |
|---|---|---|---|---|
| $FN$ | [kN] | 133.28 | 133.63 | 0.26 |
| $w_f$ | [kg/s] | 2.092 | 2.077 | -0.72 |
| $TSFC$ | [mg/Ns] | 15.696 | 15.541 | -0.98 |
| $\eta_{th}$ | [-] | 0.3041 | 0.3095 | 1.75 |
| $\eta_{prop}$ | [-] | 0.3698 | 0.3691 | -0.19 |
| $\eta_o$ | [-] | 0.1258 | 0.1269 | 0.95 |
| $\eta_{core}$ | [-] | 0.4911 | 0.4981 | 1.42 |
| $\eta_{trans}$ | [-] | 0.6151 | 0.6213 | 1.01 |

# Appendix C

# Hybrid Engine Concepts

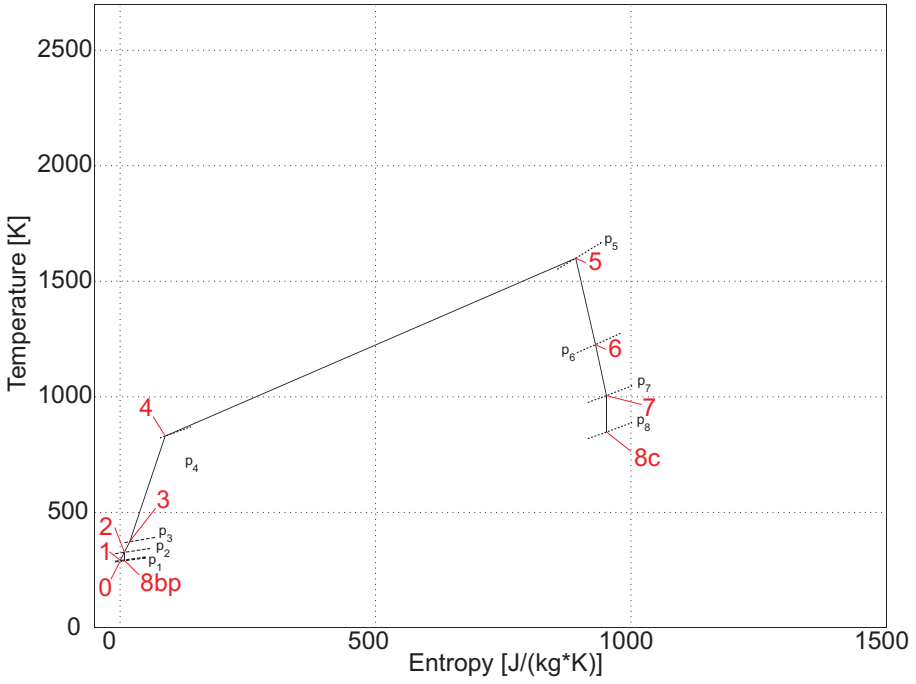


Figure C.1: Temperature Entropy Diagram of reference engine: same as reference case 1 for PM validation

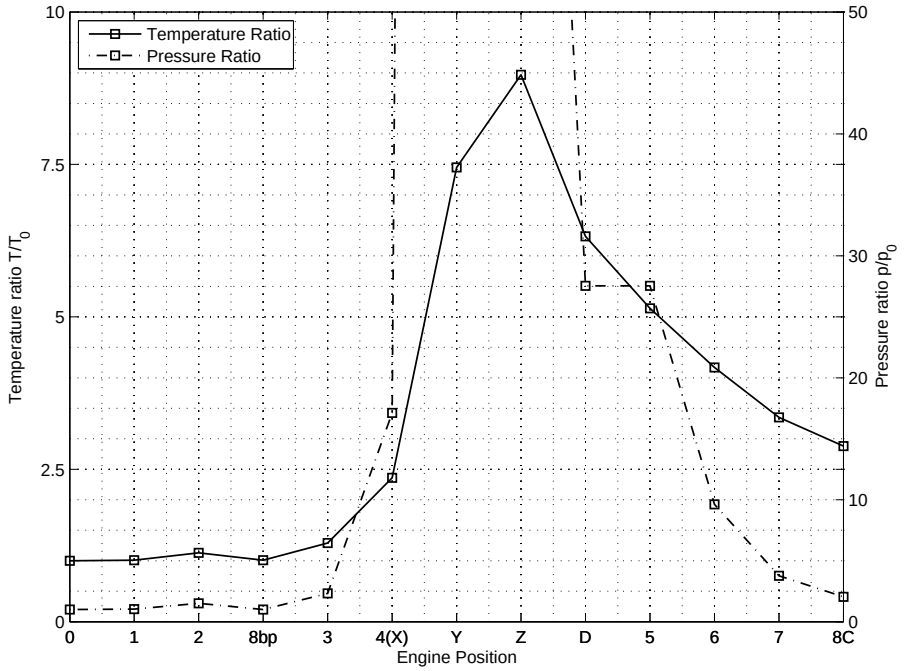


Figure C.2: Temperature and pressure history for HTE concept 1: lighter engine at lower OPR

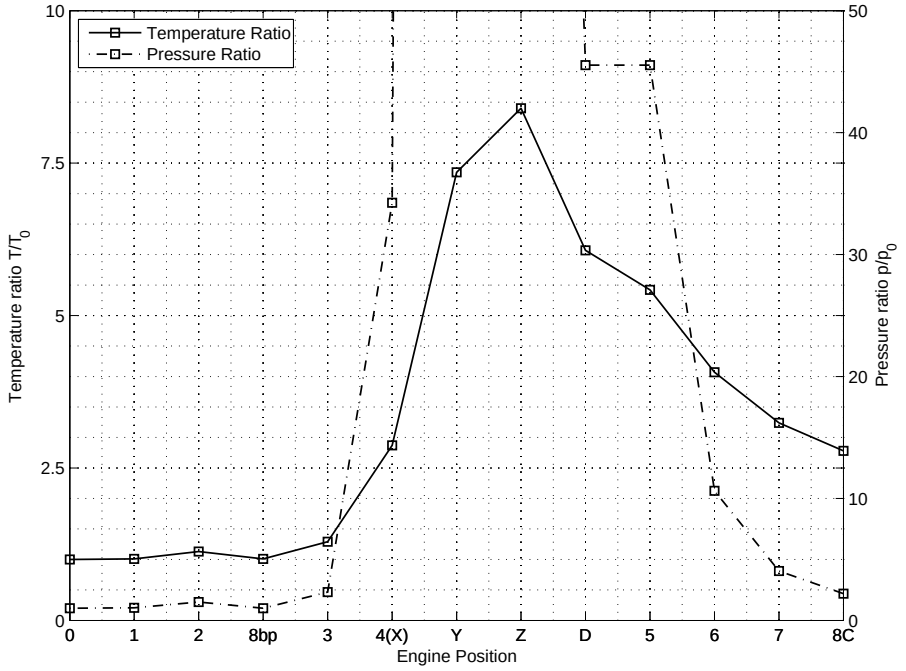


Figure C.3: Temperature and pressure history for HTE concept 2: improved efficiency at higher OPR

Table C.1: PDE stats at configuration HTE1

| | T [K] | p [bar] |
|---|---|---|
| X | 680 | 17.35 |
| Y | 2173 | 755.47 |
| Z | 2584 | 132.36 |
| D | 1823 | 27.97 |
| $\tilde{q}$ | 5.07 | [-] |

Table C.2: PDE stats at configuration HTE2

| | T [K] | p [bar] |
|---|---|---|
| X | 828 | 34.70 |
| Y | 2119 | 860.31 |
| Z | 2421 | 193.42 |
| D | 1750 | 46.13 |
| $\tilde{q}$ | 4.06 | [-] |

# Appendix D

# Instrumentation of the flame tube of the NEWAC combustor

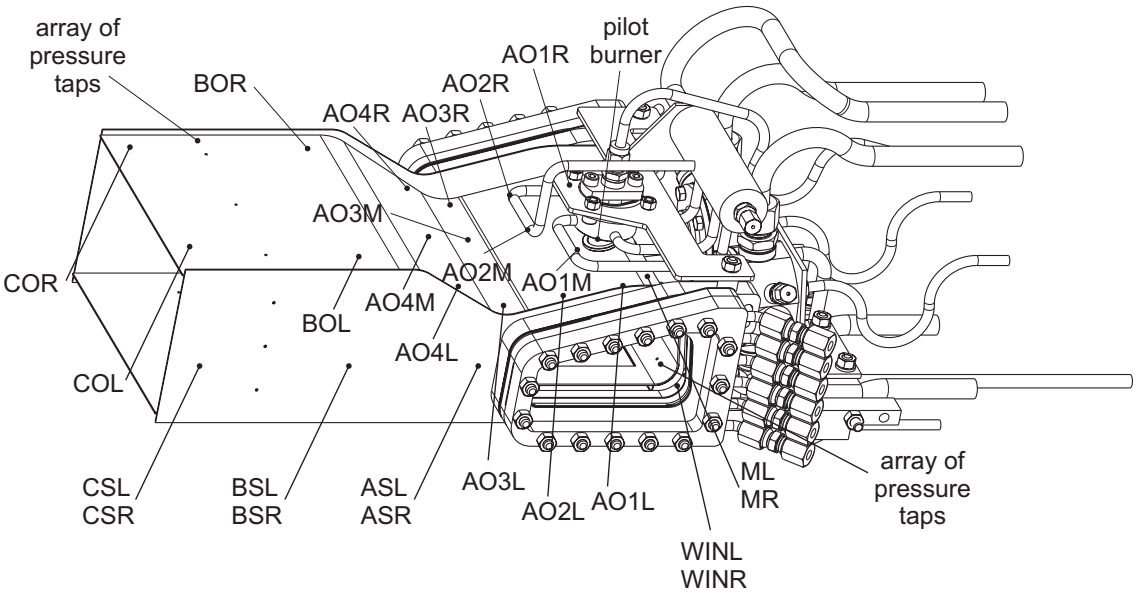


Figure D.1: Instrumentation of the NEWAC liner, top view; labeled are thermocouples and pressure taps

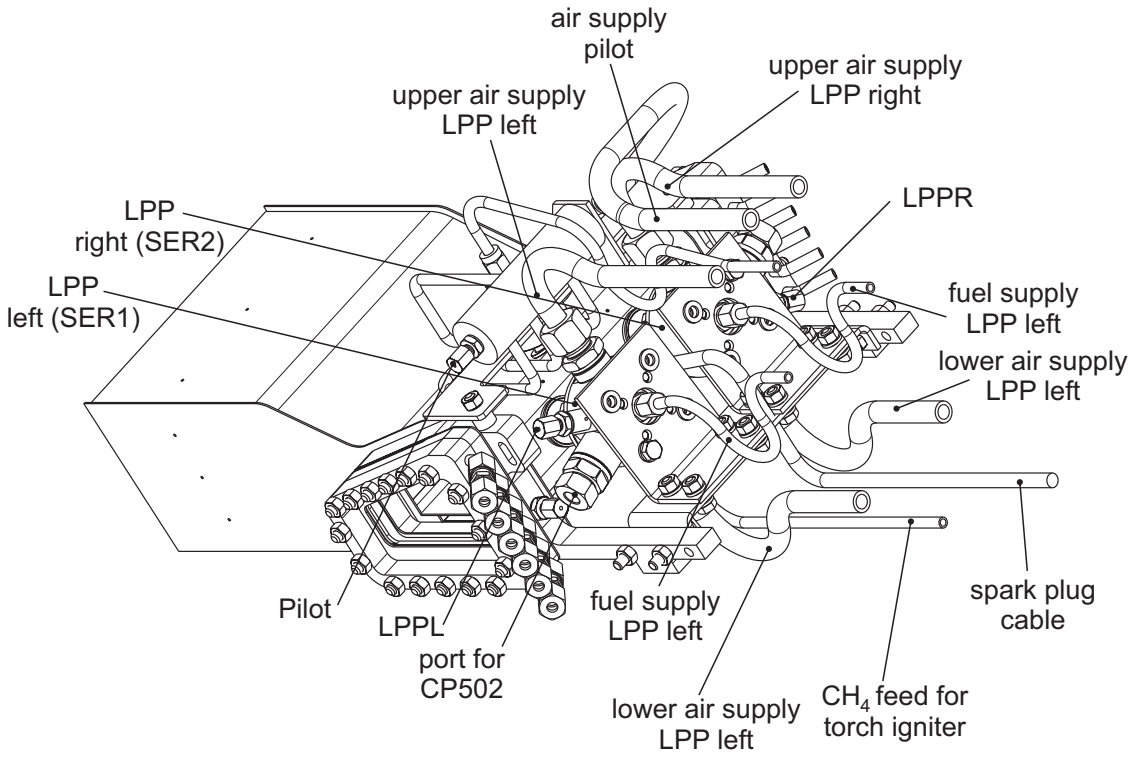


Figure D.2: Instrumentation of the NEWAC liner, back view; labeled are attached parts such as the injectors and dedicated feed lines

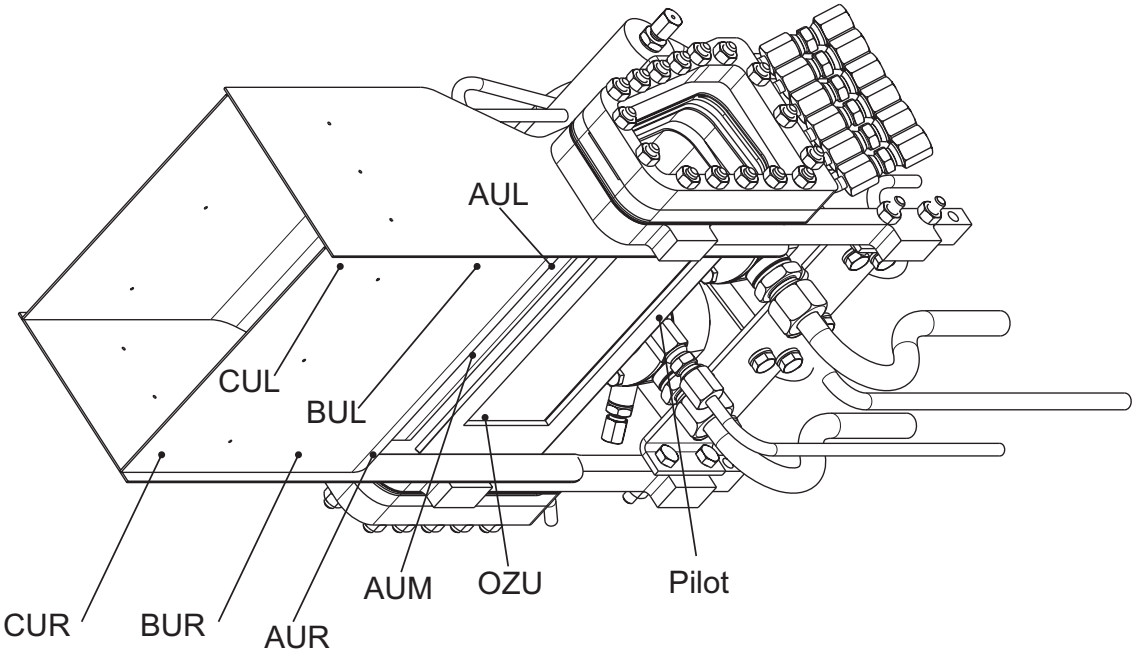


Figure D.3: Instrumentation of the NEWAC liner, bottom view; labeled are thermocouples only

# Appendix E

# Additional results on reactive stability analysis

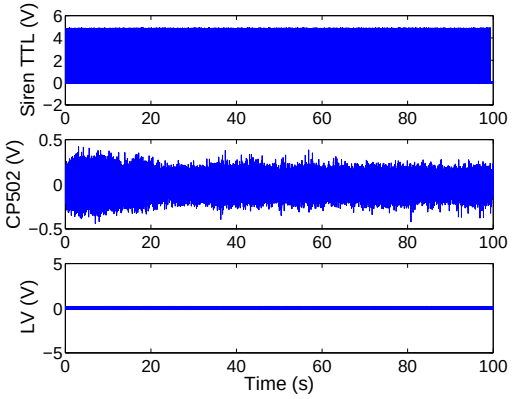


(a) Time signal

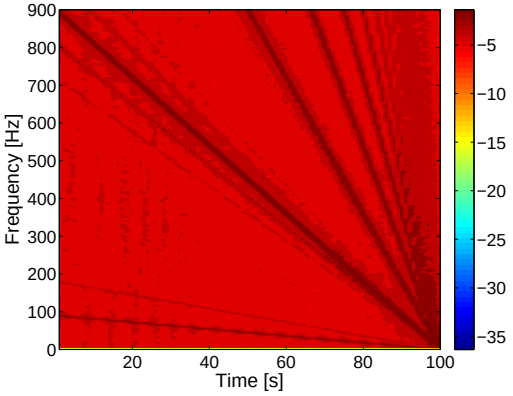


(b) TTL trigger signal as function of time and frequency

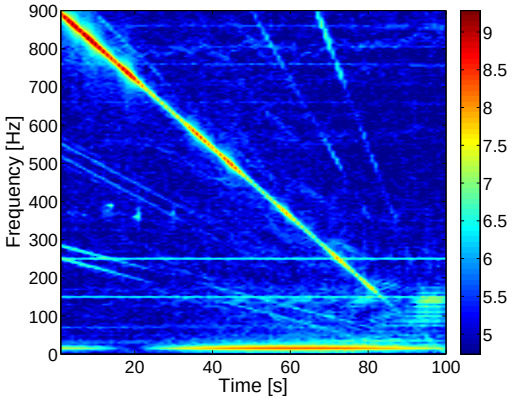


(c) Sound pressure level of CP502 sensor as function of time and frequency

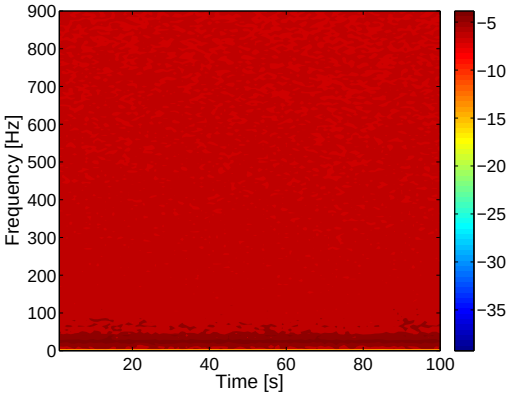


(d) log(Amplitude) of the Laser Vibrometer signal as function of time and frequency

Figure E.1: Signals recorded during second transient reactive stability analysis; decelerations from 900 Hz to halt at 9 Hz/s

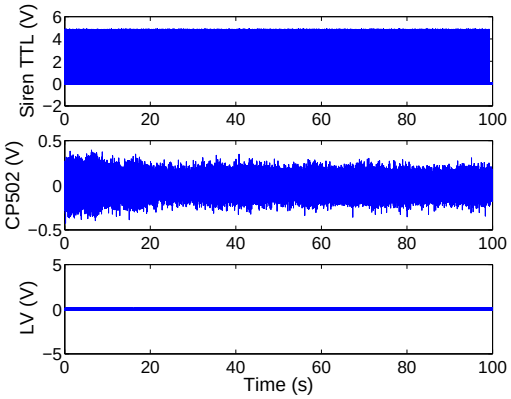


(a) Time signal

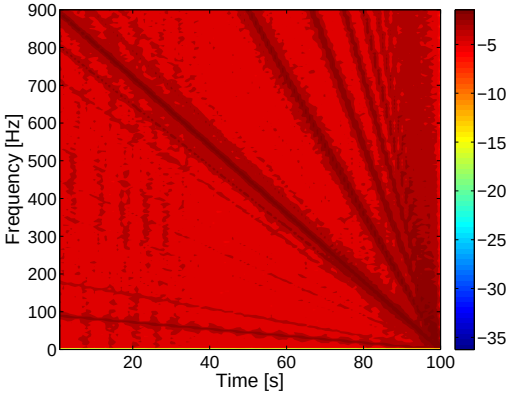


(b) TTL trigger signal as function of time and frequency

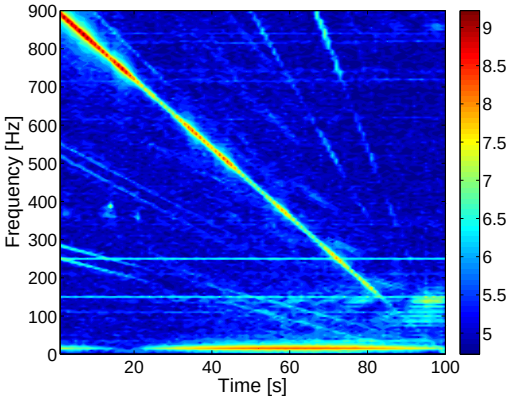


(c) Sound pressure level of CP502 sensor as function of time and frequency

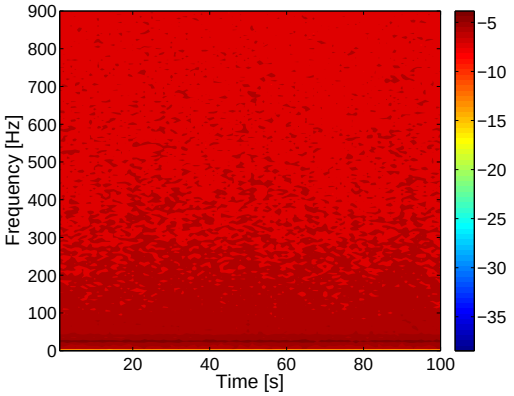


(d) log(Amplitude) of the Laser Vibrometer signal as function of time and frequency

Figure E.2: Signals recorded during third transient reactive stability analysis; decelerations from 900 Hz to halt at 9 Hz/s

# Appendix F

# Refractive indices for computation of the Gladstone-Dale constant

The refractive indices (at wavelength of 633 nm) for the combustible ethanol $C_2H_6O$ (in addition also for $CH_4$) and the species for air as well as the products are given in table F.1.

Table F.1: Refractive indices for several species [57]

| **Species** | $R_{Gi}$ |
|---|---|
| $C_2H_6O$ | $19.112 \cdot 1e-6$ |
| $CH_4$ | $9.864 \cdot 1e-6$ |
| $N_2$ | $6.689 \cdot 1e-6$ |
| $O_2$ | $6.053 \cdot 1e-6$ |
| $Ar$ | $6.298 \cdot 1e-6$ |
| $H_2O$ | $5.623 \cdot 1e-6$ |
| $CO_2$ | $9.968 \cdot 1e-6$ |
| $CO$ | $7.487 \cdot 1e-6$ |
| $OH$ | $8.010 \cdot 1e-6$ |
| $H$ | $2.583 \cdot 1e-6$ |
| $O$ | $2.769 \cdot 1e-6$ |
| $H_2$ | $3.106 \cdot 1e-6$ |
| $NO$ | $6.581 \cdot 1e-6$ |

# Appendix G

# Images of the flame during reactive experiments

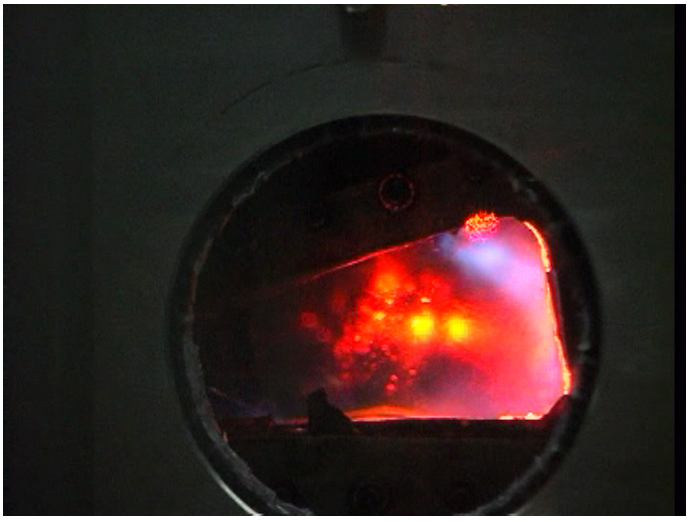

Figure G.1: Flame structure during excitation with 176 Hz

Figure G.2: Flame structure during excitation with 624 Hz

Figure G.3: Flame structure during excitation with 854 Hz

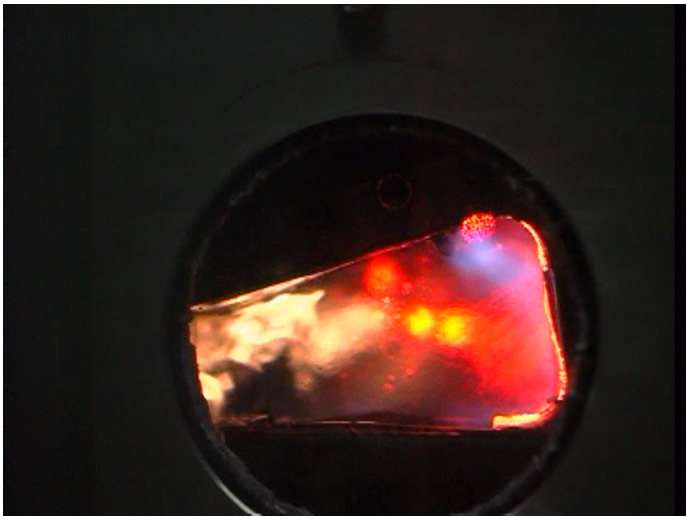

Figure G.4: Flame structure during excitation with 900 Hz

# Appendix H

# Characterization of the LPP injectors

## H.1 Flow number

During several experiments the flow number and the pressure loss of both LPP injectors (SER1 and SER2) were measured.
For the flow number of the injectors the back pressure at the injector connector was set and the fuel mass flow recorded. By applying equation H.1, with the mass flow $\dot{m}$ in $kg/h$ and the pressure $p$ in $bar$ the flow number can be computed.

$$FN = \frac{\dot{m}}{\sqrt{p}} \tag{H.1}$$

Figure H.1 is giving the flow number as function of back pressure, when ethanol as fuel is used.

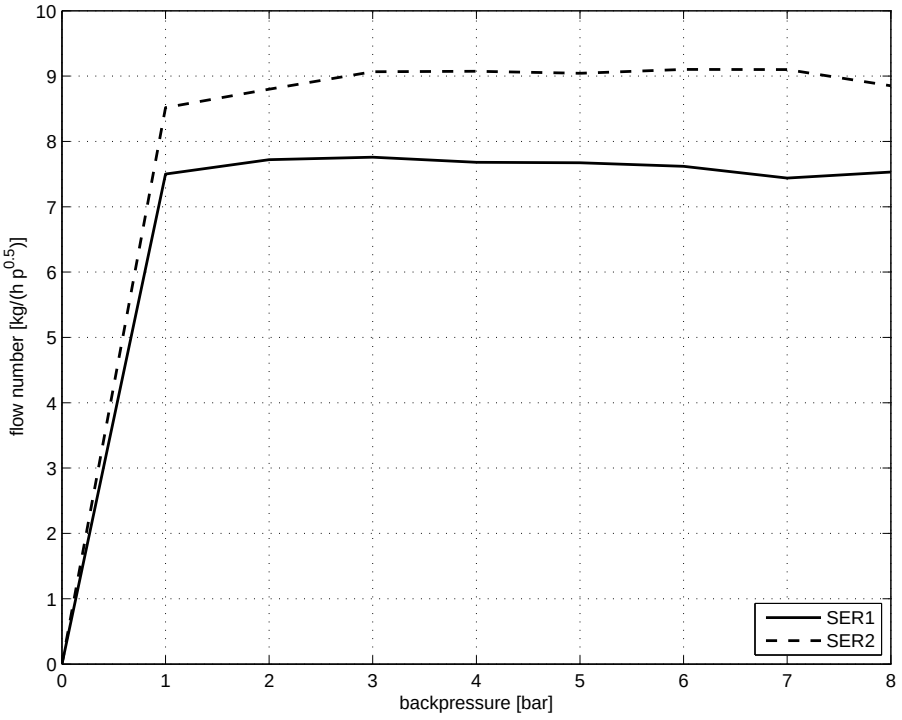


Figure H.1: Flow number of the NEWAC LPP's

## H.2 Pressure loss coefficient

For the determination of the pressure loss of both LPP injectors the single LPP injector test bench at atmospheric conditions has been used.
The pressure loss, or the differential pressure between the static pressure upstream of the injector and the pressure after the premixing tube (in this case ambient), is based on the dynamic pressure multiplied with the pressure loss coefficient $\zeta$.

$$\Delta p = \zeta \cdot \rho \cdot \frac{v^2}{2} \tag{H.2}$$

When using the equation for continuity the pressure loss coefficient can be computed by using equation H.3.

$$\zeta = \frac{2 \cdot \rho \cdot (p_{up} - p_{down})}{\left(\frac{\dot{m}}{A}\right)^2} \tag{H.3}$$

Figure H.2 is giving the mass flow as well as the pressure loss coefficient for both LPP modules (SER1 and SER2) as function of back pressure set.

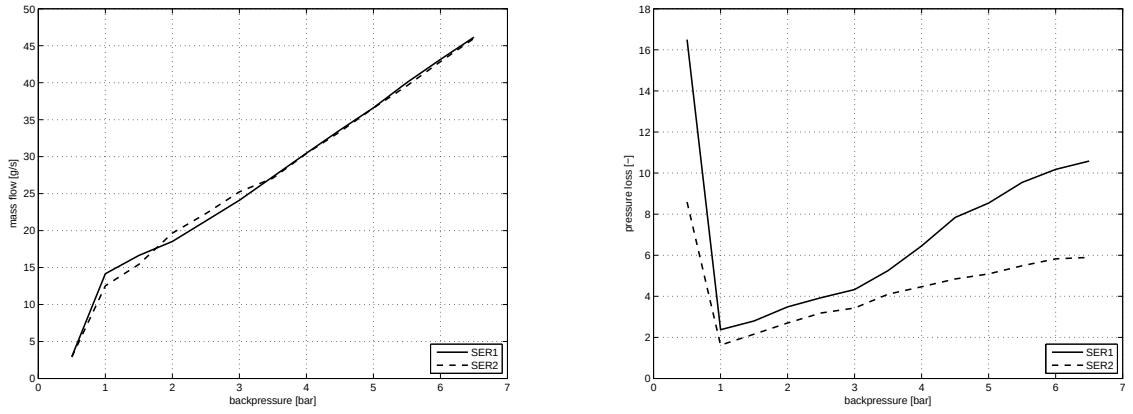


(a) Mass flow

(b) pressure loss coefficient

Figure H.2: Characterization of the NEWAC LPPs; (a): mass flow rate; (b): pressure loss coefficient

# Appendix I

# Mathematical derivation of the time derivative of the density fluctuation

Equation 5.33 is given once more for an easy to follow explanation.

$$\frac{\mathrm{D}\rho}{\mathrm{D}t} = \underbrace{\frac{\mathrm{d}\rho}{\mathrm{d}t}}_{\rho'} = \left.\frac{\partial\rho}{\partial p}\right|_s \cdot \underbrace{\frac{\mathrm{d}p}{\mathrm{d}t}}_{p'} + \left.\frac{\partial\rho}{\partial s}\right|_p \cdot \underbrace{\frac{\mathrm{d}s}{\mathrm{d}t}}_{s'} \tag{I.1}$$

The partial derivative of density by pressure at constant entropy can be transformed by using the isentropic relation for an ideal gas.

$$p \cdot v^\gamma = \text{const.} \tag{I.2}$$

The deviation of the above given equation will result in

$$\gamma \cdot p \cdot v^{\gamma-1}\mathrm{d}v + v^\gamma \cdot \mathrm{d}p = 0 \tag{I.3}$$

with the density being the inverse of the specific volume

$$\begin{aligned} \frac{1}{v} &= \rho \\ -v^{-2} \cdot \mathrm{d}v &= \mathrm{d}\rho \\ \mathrm{d}v &= -\mathrm{d}\rho \cdot v^2 \end{aligned} \tag{I.4}$$

Substituting equation I.4 into eq. I.3 will result in

$$\begin{aligned} \gamma \cdot p \cdot v^{\gamma-1} \cdot \left(-v^2 \cdot \mathrm{d}\rho\right) &= -v^\gamma \cdot \mathrm{d}p \\ \frac{\mathrm{d}\rho}{\mathrm{d}p} &= \frac{v^\gamma}{v^{\gamma+1} \cdot p \cdot \gamma} \\ &= \frac{1}{\gamma \cdot p \cdot v} = \frac{1}{\gamma \cdot R \cdot T} = \frac{1}{c^2} \end{aligned} \tag{I.5}$$

For the partial derivative of density by entropy at constant pressure one can make use of the reversible heat given when using a heat addition at constant pressure.

$$\mathrm{d}q_{rev} = T \cdot \mathrm{d}s = \mathrm{d}h - v \cdot \mathrm{d}p \tag{I.6}$$

As said the heat is added at constant pressure, resulting in $v \cdot \mathrm{d}p = 0$, leading to

$$T \cdot \mathrm{d}s = \mathrm{d}h = c_p \cdot \mathrm{d}T \tag{I.7}$$

with $\mathrm{d}h$ the enthalpy change, $c_p$ the specific heat at constant pressure.
Using the derivative of the ideal gas equation at constant pressure

$$\begin{aligned} p \cdot v &= R \cdot T \\ T &= \frac{p \cdot v}{R} = \frac{p}{R \cdot \rho} \\ \mathrm{d}T &= \frac{p}{R} \cdot \left(-\rho^{-2}\right) \cdot \mathrm{d}\rho \end{aligned} \tag{I.8}$$

Equation I.7 can now be written as

$$\begin{aligned} -c_p \cdot \frac{p}{\rho^2 \cdot R}\mathrm{d}\rho &= \frac{p}{\rho \cdot R}\mathrm{d}s \\ \frac{\mathrm{d}\rho}{\mathrm{d}s} &= -\frac{\rho}{c_p} \end{aligned} \tag{I.9}$$

For the specific heat at constant pressure ($c_p$) one can give the following expression

$$\begin{aligned} \gamma &= \frac{c_p}{c_v} = \frac{c_p}{c_p - R} \\ c_p &= (c_p - R) \cdot \gamma \\ &= R \cdot \frac{\gamma}{\gamma - 1} \end{aligned} \tag{I.10}$$

Thus $\mathrm{d}\rho/\mathrm{d}s$ can be written as

$$\frac{\mathrm{d}\rho}{\mathrm{d}s} = -\frac{(\gamma - 1) \cdot \rho}{\gamma \cdot R} \tag{I.11}$$

Finally the density fluctuation can be written as

$$\rho' = \frac{1}{c^2} \cdot p' - \frac{(\gamma - 1) \cdot \rho}{\gamma \cdot R} \cdot s' \tag{I.12}$$

By using the (derivative of the) reversible heat given in equation I.6 once more

$$\begin{aligned} \rho' &= \frac{1}{c^2} \cdot p' - \frac{(\gamma - 1) \cdot \rho}{\gamma \cdot R} \cdot \frac{q'}{T} \\ &= \frac{1}{c^2} \cdot p' - \frac{(\gamma - 1) \cdot \rho}{c^2} \cdot q' \end{aligned} \tag{I.13}$$

The time derivative of the density fluctuation is thus

$$\frac{\partial \rho'}{\partial t} = \frac{1}{c^2} \cdot \frac{\partial p'}{\partial t} - \frac{(\gamma - 1) \cdot \rho}{c^2} \cdot \dot{q}' \tag{I.14}$$

which represents the equation given by Dowling [49] for the mathematical expression of a combustion instability.

# Bibliography


[1] ICAO. Forecasts of scheduled passenger traffic - medium-term traffic passenger forecasts. `http://www.icao.int/icao/en/atb/eap/Eap_FP_ForecastMed.htm`, 2010.

[2] ICAO. Forecasts of scheduled passenger traffic - long-term traffic and aircraft movement forecasts. `http://www.icao.int/icao/en/atb/eap/Eap_FP_Forecast_LongTerm.htm`, 2010.

[3] Joerg Sieber. Newac overview. Power point presentation, MTU Aero Engines, 2010.

[4] Unknown. Esa technology readiness level summary. Technical report, European Space Agency, 2010.

[5] Group of Personalities. European aeronautics: A vision for 2020, January 2001.

[6] NEWAC. Newac – aero engine technology for environmentally friendly aircraft (broschur).

[7] Norbert Mayrhofer and Jakob Woisetschläger. Frequency analysis of turbulent compressible flows by laser vibrometry. *Experiments in Fluids*, 31:153–161, 2000.

[8] Bernd Hampel and Jakob Woisetschläger. Frequency- and space-resolved measurement of local density fluctuations in air by laser vibrometry. *Measurement in Science and Technology*, 17:2835–2842, 2006.

[9] Fabrice Giuliani, Bernhard Wagner, Jakob Woisetschläger, and Franz Heitmeir. Laser vibrometry for ral-time combustion stability diagnostic. In *Proceedings of the ASME Turbo Expo 2006: Power for Land, Sea and Air*, number GT2006-90413, 2006.

[10] Bernhard Wagner. Anpassung der messmethoden an die stationäre und instationäre verbrennung. Master's thesis, Graz University of Technology, 2005.

[11] Stefan Köberl. *Development and Application of Interferometric Measurement Techniques for Multi-Flame Gas Turbine Combustion.* PhD thesis, Graz University of Technology, 2011.

[12] Thomas Leitgeb, Fabrice Giulinai, and Franz Heitmeir. Design and adaption of a versatile test facility for turbines and combustion chambers. In *Proceedings of the 8th European Turbomachinery Conference*, 2009.

[13] Thomas Leitgeb, Fabrice Giuliani, and Andreas Niederhammer. Computer aided dimensioning and validation of a versatile test facility for combustion chambers and turbines. In *Proceedings of the ASME Turbo Expo, Gas Turbine Technical Congress & Exposition*, 2009.

[14] Willy J. G. Bräunling. *Flugzeugtriebwerke.* Springer, 3 edition, 2009.

[15] Anders Lundbladh. Final evaluation for future innovative core architectures. Technical report, Volvo Aero, 2011.

[16] Tp400 engine cutaway. `http://eaglesgate.com/TP400.htm`, 2011.

[17] V2500 engine cutaway. `http://www.pw.utc.com/Products/Commercial/V2500`, 2011.

[18] Ej200 engine cutaway. `http://www.eurojet.de/en/`, 2011.

[19] Olympus 593 mk. 610 engi cutaway. `http://www.rjc-technical.co.uk/Pages/olympus.htm`, 2011.

[20] Emil Göttlich. Research on the aerodynamics of intermediate turbine diffusors. *Progress in Aerospace Sciences*, -:–, 2001.

[21] Rolls royce trent 1000. `http://www.rolls-royce.com/civil/products/largeaircraft/trent_1000/technology.jsp`, 2011.

[22] NEWAC. Sixth framework programme priority 4 - aeronautics and space (fp6-2005-aero-1) - description of work r3.0.

[23] X. He and A. R. Karagozian. Numerical simulation of pulse detonation engine phenomena. *Journal of Scientific Computing*, 19:201–207, 2003.

[24] C.F. Smith, P.H. Snyder, and M.R. Nalim. Impact of the consant volume combustor on a supersonic turbofan engine. In *AIAA/ASME/SAE/ASEE Joint Propulsion Conference and Exhibit*, number AIAA 2002-3916, 2002.

[25] Pezhman Akbari, Razi Nalim, and Norbert Müller. A review of wave rotor technology and its applications. In *Proceedings of IMECE04*, number IMECE2004-60082, 2004.

[26] Razi Nalim and Kerem Pekkan. Internal combustion wave rotors for gas turbine engine enhancement. In *Proceedings of the International Gas Turbine Congress*, number IGTC2003Tokyo FR-303, 2003.

[27] P. Snyder, B. Alparslan, and M. Nalim. Gas dynamic analysis of the constant volume combustor, a novel detonation cycle. In *38th AIAA/ASME/SAE/ASEE Joint Propulsion Conference & Exhibit*, 2002.

[28] Fabrice Giuliani, Andreas Lang, Mohammad Irannezhad, and Tomas Grönstedt. Effects of a controlled phase-shift on the outlet conditions of a set of pulse detonators. In *Proceedings of the 18th ISABE Conference*, number ISABE-2009-1315, 2009.

[29] Fabrice Giuliani, Andreas Lang, Mohammad Irannezhad, and Anders Lundbladh. Pulse detonation as an option for future innovative gas turbine combustion technologies: A concept assessment. In *27th International Congress of the Aeronautical Sciences*, 2010.

[30] Jeffrey Goldmeer, Venkat Tangirala, and Anthony Dean. System-level performance estimation of a pulse detonation based hybrid engine. *Journal of Engineering for Gas Turbines and Power*, 130:–, 2008.

[31] Joachim Kurzke. *GasTurb11 - Design and Off-Design Performance of Gas Turbines.*

[32] Philip P. Walsh and Paul Fletcher. *Gas Turbine Performance*. Blackwell Science Ltd, 2 edition, 2004.

[33] Alexander Burcat and Branko Ruscic. Third millennium ideal gas and condensed phase thermochemical database for combustion with updates from active thermochemical tables. Technical report, ARGONNE National Laboratory, TECHNION Israel Institute of Technology, 2005.

[34] H. Lefebvre, Arthur. *Gas Turbine Combustion*. Taylor & Francis, 1999.

[35] Wildon Fickett and William C. Davis. *Detonation: Theory and Experiment*. Dover Publications Inc., 1979.

[36] E. Wintenberger. *Application of Steady and Unsteady Detonation Waves to Propulsion*. PhD thesis, California Institute of Technology, 2004.

[37] Unknown. Perspectives on detonation-based propulsion. *Journal of Propulsion and Power*, 22:–, 2006.

[38] E. Wintenberger and J.E. Shepherd. A model for the performance of air-breathing pulse detonation engines. In *AIAA/ASME/SAE/ASEE Joint Propulsion Conference and Exhibit*, number AIAA 2003-4511, 2003.

[39] William H. Heiser and David T. Pratt. Thermodynamic cycle analysis of pulse detonation engine. *Journal of Propulsion and Power*, 18:68–76, 2002.

[40] Joseph Victor Foa. *Elements of Flight Propulsion*. John Wiley & Sons, Inc., 1960.

[41] J.A.C. Kentfield. Thermodynamics of airbreathing pulse-detonation engines. *Journal of Propulsion and Power*, 18:1170–1175, 2002.

[42] Ames Research Staff. Equations, tables, and charts for compressible flow. Technical Report 1135, Ames Aeronautical Laboratory, 1953.

[43] Yuhui Wu, Fuhua Ma, and Vigor Yang. System performance and thermodynamic cycle analysis of air breathing pulse detonation engines. *Journal of Propulsion and Power*, 19:556–567, 2003.

[44] Bonnie J. Gordon, Sanford and. McBride. Computer program for calculation of complex chemical equilibrium compositions and applications i. analysis. Technical Report NASA-1311, National Aeronautics and Space Administration, Lewis Research Center, 1994.

[45] NEWAC. Newac - new aero engine core concepts. `http://www.newac.eu/`, 2010.

[46] Franz Joos. *Technische Verbrennung*. Springer, 2006.

[47] Rudolf Pischinger, Manfred Kell, and Theodor Sams. *Thermodynamik der Verbrennungskraftmaschine*. Springer, 2009.

[48] Tim Lieuwen, H. Torres, C. Johnson, and Ben T. Zinn. A mechanism of combustion instability in lean premixed gas turbine combustors. *Journal of Engineering for Gas Turbines and Power*, 123:182–189, 2001.

[49] Ann P. Dowling and Aimee S. Morgans. Feedback control of combustion oscillations. *Annual Review of Fluid Mechanics*, 37:151–182, 2005.

[50] Thomas Leitgeb, T. Schuller, D. Durox, Stefan Köberl, Jakob Woisetschläger, and Fabrice Giuliani. Interferometric determination of heat release in a periodic flame. *Combustion and Flame*, -:–, submitted.

[51] Tim Lieuwen. Introduction: Combustion dynamics in lean-premixed prevaporized (lpp) gas turbines. *Journal of Propulsion and Power*, 19:721, 2003.

[52] J. W. S. Rayleigh. *The Theory of Sound*. Dover Publications, 1945.

[53] Abbott A. Putnam. Combustion driven oscillations in industry. *Fuel and Energy Science Series*, -:–, 1971.

[54] Shekhar Sarpotdar, N. Ananthkrishnan, and S.D. Sharma. The rijke tube - a thermo-acoustic device. Technical report, Indian Academy of Sciences, 2003.

[55] T. Arts, H. Boerrigter, M. Carbonaro, J-M. Charbonnier, G. Degrez, D. Olivari, M.L. Riethmuller, and R.A. Van den Braembussche. *Measurement Techniques in Fluid Dynamics - An Introduction*. von Darman Institute, 1994.

[56] Bodo Ruck. *Laser-Doppler-Anemometrie*. AT-Fachverlag, 1987.

[57] W.C. Gardiner, Y. Hidaka, and T. Tanzawa. Refractivity of combustion gases. *Combustion and Flame*, 40:213–219, 1981.

[58] tbd. *Physik für Ingenieure*. Springer-Lehrbuch, tbd.

[59] Fabrice Giuliani, Alexander Schricker, Andreas Lang, Thomas Leitgeb, and Franz Heitmeir. High-temperature resistant pressure transducer for monitoring of gas turbine combustion stability. In *Proceedings of the 16th ISABE Conference*, number ISABE-2007-1111, 2007.

[60] Fabrice Giuliani, Thosmas Leitgeb, Andreas Lang, and Jakob Woisetschläger. Mapping the density fluctuations in a pulsed air-methane flame using laser-vibrometry. In *Proceedings of the ASME Turbo Expo 2009: Power for Land, Sea and Air*, number GT2009-59682, 2009.

[61] Andreas Lang, Thomas Leitgeb, Jakob Woisetschläger, Alain Strzelecki, Pierre Gajan, and Fabrice Giuliani. Analysis of a pulsed flame at intermediate pressure. In *Proceedings of the 13th International Symposium on Flow Visualisation and 12th French Congress on Visualization in Fluid Mechanics*, 2008.

[62] Adrian Spencer Jochen Rupp, Jon Carrotte. Methodology to identify the unsteady flow field associated with the loss of acoustic energy in the vicinity of circular holes. In *Proceedings of ASME Turbo Expo 2010*, number GT2010-22178, 2010.

[63] Paul Palies. Swirling flame instability analysis based on the flame describing function methodology. In *Proceedings of ASME Turbo Expo 2010*, number GT2010-22294, 2010.

[64] Jonas P. Moeck. Thermoacoustic instabilities in an annular rijke tube. In *Proceedings of ASME Turbo Expo 2010*, number GT2010-23577, 2010.

[65] A. Müller. Performance of prefilming airblast atomizers in unsteady flow conditions. In *Proceedings of ASME Turbo Expo 2006*, number GT2006-90432, 2006.

[66] Fabrice Giuliani. *Analysis on the behaviour of an aeroengine air-blast injection device with forced entries*. PhD thesis, Institut Supérieur de l'Aéronautique et de l'Espace, 2002.

[67] R. Pischinger. *Thermodynamik*. Skriptenshop der HTU Graz, tbd.

[68] Günther Zhuber-Okrog. *Grundlagen der Strahlantriebe*. Institut für Thermische Turbomaschinen der TU Graz, -.

[69] Klaus Johannes Gradl. Ansteuerung einer sirene zur modulation der frequenz und amplitude eines luftmassenstroms. Technical report, Graz University of Technology, 2010.

[70] Dieter Sautter and Hans Winerth. *Elektronik und Mikroelektronik*. VDI Verlag, 1993.

[71] Peter Siebenhofer. Umsetzung eines inkrementgebers zur drehzahl- und frequenzmessung 3. Technical report, Graz University of Technology, 2010.

[72] Andreas Lang. Konstruktion eines brennkammer-prüfstandes und messungen unter mittlerem druck. Master's thesis, Graz University of Technology, 2007.

[73] Audrey Camps. Automated ignition for safe start at intermediate pressure conditions. Technical report, Graz University of Technology, 2008.

[74] J. Beer and N. Chigier. *Combustion Aerodynamics*. Applied Science Publishers Ltd., 1972.

[75] Christian Faustmann. Experimental investigations of the igniting and flow characteristics in a combustion chamber in the context of the newac-project. Master's thesis, Technische Universität Darmstadt, 2010.

[76] Fabrice Giuliani, Andreas Lang, Klaus Johannes Gradl, Peter Siebenhofer, and Johannes Fritzer. Air flow modulation for refined control of the combustion dynamics using a novel acutator refined control of the combustion dynamics using a novel actuator. *Journal of Engineering for Gas Turbines and Power*, -:–, in press.

[77] Markus Stütz. Konstruktion eines... Technical report, Graz University of Technology, 2011.